The Dissertation Committee for Liubin Pan
certifies that this is the approved version of the following dissertation:

Turbulent Mixing of Chemical Elements in Galaxies

Committee:

John Scalo, Supervisor

Eiichiro Komatsu

Pawan Kumar

Paolo Padoan

Paul Shapiro

J. Craig Wheeler

Turbulent Mixing of Chemical Elements in Galaxies

by

Liubin Pan, B.S., M.S.

Dissertation

Presented to the Faculty of the Graduate School of

The University of Texas at Austin

in Partial Fulfillment

of the Requirements

for the Degree of

Doctor of Philosophy

The University of Texas at Austin

May 2008

Dedicated to my parents

Acknowledgments

I first wish to thank John Scalo for directing my scientific maturation. I want to thank Craig Wheeler for advice on supernova science and on graduate studies. I would like to thank Paolo Padoan for support when the thesis was written at UC San Diego. I would also like to thank Eiichiro Komatsu for teaching me the early universe. Continuous kind help from Stephanie Crouch is deeply appreciated.

Liubin Pan

The University of Texas at Austin
May 2008

Turbulent Mixing of Chemical Elements in Galaxies

Publication No. ____________________

Liubin Pan, Ph.D.
The University of Texas at Austin, 2008

Supervisor: John Scalo

Chemical elements synthesized in stars are released into the interstellar medium (ISM) from discrete and localized events such as supernova (SN) explosions and stellar winds. The efficiency of transport and mixing of the new nucleosynthesis products in the ISM determines the degree of chemical inhomogeneity in the galaxy, which is observable in objects of the same age, such as coeval stars and the ISM today. It also has implications for the transition from metal-poor to normal star formation in high-redshift galaxies.

We develop a physical mixing model for chemical homogenization in the turbulent ISM of galaxies using modern theories and methods for passive scalar turbulence. A turbulent velocity field stretches, compresses and folds tracers into structures of smaller and smaller scales that can be homogenized faster by microscopic diffusivity, the only physical process that truly mixes. From a model that incorporates this physical process, an evolution equation for the probability distribution of the tracer concentration is derived. Including the processes of new metal release, infall of low metallicity gas and incorporation of metals into new stars in the equation, we establish a new approach to investigate chemical inhomogeneity in galaxies: a kinetic equation for the metallicity probability distribution function, containing all the 1-point statistical information of the metallicity fluctuations.

Motivated by a recent interpretation of ultraviolet properties of high-redshift Lyman Break Galaxies, we apply this approach to study mixing of primordial gas in these galaxies and find that primordial gas can survive for ~ 100 Myr in the presence of continuous metal sources and turbulent mixing if the unlikely efficient mixing in SN shells is excluded.

Recent observations show that the Galaxy has been extremely homogeneous during most of its history. In an attempt to understand the homogeneity using our approach, we find that standard chemical evolution models without infall give metallicity scatters consistent with observations while all the infall models produce scatters at least 5 times larger than observed. To avoid this discrepancy and to remain a valid solution to the G-dwarf problem, the main motivation for infall models, the infall gas is required to primarily consist of small clouds of size less than ~ 5 pc.

Fluctuations in the carbon to oxygen abundance ratio are of astrobiological interest: regions with C>O are likely to be devoid of water, which is thought to be essential for life. A small degree of inhomogeneity in the ratio gives a finite probability for the existence of regions with C>O even when the average ratio is smaller than unity. As the mean C/O ratio increases, as supported by observations and theoretical models, the Galaxy will eventually make a transition from mostly

oxygen-rich to mostly carbon-rich. To the extent that life requires liquid water, the formation of habitable planets would no longer be possible. Adopting a negative Galactic C/O radial gradient, the transition appears as an outward-moving dehydration wave from the inner regions of the Galaxy.

Finally we examine the effect of turbulent stretching on nuclear flames in Type Ia Supernova (SN Ia) progenitors. Turbulent stretching exhibits strong intermittency at small scales where its probability distribution shows a broad tail, corresponding to intense but rare stretching events. These events have important implications for the flame burning state and thus for the deflagration to detonation transition (DDT) in SN Ia explosions. Current DDT models require a critical turbulent intensity or stretching over a flame region that is sufficiently large. We find that including local intermittent stretching in these models results in a shift toward larger transition densities at which the DDT occurs.

Contents

List of Tables

List of Figures

Chapter 1

A new approach for inhomogeneous chemical evolution models

Chapter Synopsis: The degree of chemical inhomogeneity in galaxies is determined by the efficiency of transport and mixing of metal sources, such as supernova explosions and stellar winds, in the interstellar medium (ISM). A theoretical model for chemical mixing in the turbulent ISM is needed to explain the observed scatters in elemental abundances or abundance ratios in objects of the same age, such as coeval stars and the ISM today, and to investigate the transition from primordial to normal star formation in high-redshift galaxies. Despite its importance, the physics of turbulent mixing is not explicitly included in current inhomogeneous chemical evolution models where the mixing efficiency is simply parametrized. A physical model for mixing in the ISM turbulence is yet to be developed. We establish a physical mixing model in the turbulent interstellar medium using a kinetic equation to evolve the probability distribution function (pdf) of metallicity. The model recognizes the fact that the microscopic diffusivity, although slow by itself, is the only physical agent that really mixes and that the ISM turbulence, which does not mix by itself, significantly enhances the mixing efficiency by generating concentration structures at small scales where the microscopic diffusivity can operate fast. The mixing timescale in the model is characterized by the time for the ISM turbulence to stretch the concentration field to the diffusion scale where the microscopic diffusion becomes faster than the turbulent advection. We use a closure approximation to model the turbulence-enhanced diffusivity term, which is justified by considerations of generation and interaction of small scale sheet- like metallicity structures by turbulent stretching and microscopic diffusivity, respectively. In addition to the homogenization process by the ISM turbulence, all other processes that change the metallicity pdf, such as infall of low metallicity gas, release of new nucleosythesis products from supernovae and stellar winds, metal lockup in low-mass stars, are consistently incorporated in the kinetic equation. As a direct application, we derive an equation for the evolution of the unpolluted gas fraction in the ISM, which is important for metal-free star formation in high redshift galaxies. We also give a pdf formulation for a previous inhomogeneous chemical evolution model, which assumes efficient mixing of newly generated metals with the interstellar gas swept up in supernova (SN) or superbubble (SB) shells. We point out that this assumption probably overestimates the mixing rate in SN or SB shells.

1.1 Introduction

Inhomogeneous chemical evolution models (ICEMs) are concerned with the degree to which the interstellar medium (ISM) is mixed during the history of galaxies, which controls the degree of metallicity variations in objects formed at the same time. The interesting questions that cannot be answered by the mean-field chemical evolution models but require ICEMs include: 1) how and when the primordial gas in early galaxies was polluted by products of nucleosynthesis and when the transition from metal-free star formation to the normal star formation occurred (Tumlinson 2005, Pan & Scalo 2007), 2) understanding the observed scatter in elemental abundances and ratios in objects of the same age, e.g., coeval stars, the present-day ISM (e.g., Reeves 1972; Edwards 1975; White and Audouze 1983; Roy and Kunth 1995; van den Hoek and de Jong 1997, Oey 2000, 2003; Pan and Scalo 2008a), 3) how chemical inhomogeneity in the ISM affects the predicted stellar metallicity distribution function from mean-field chemical evolution models (e.g., Oey 2000) and hence perhaps the solution to the G-dwarf problem (e.g., White and Audouze 1983).

ICEMs were first motivated by the second question when it was thought that the metallicity scatter of coeval stars was large (e.g., White and Audouze 1983; see van den Hoek and de Jong 1997 for a review). Recent years have seen a remarkable change in the observational point of view: the metallicity scatter of coeval objects is extremely small, usually below the observation uncertainties, in the Galactic disk. The compelling evidence comes from the HST/FUSE UV observation of abundances over many different lines of sights in the ISM (e.g., Cartledge 2006), the metallicity scatter of stars in open clusters (e.g., DeSilva et al. 2006) and the metallicity ratio in field stars (Reddy et al 2004, 2006). A detailed review of evidence for small observed metallicity scatter in various objects is given in chapter 3.

In contrast, no significant theoretical progress has been made to physically model the process of metal transport and mixing in the ISM. A physical mixing model for the ISM must consist of two important components, the microscopic diffusivity and a catalyzing velocity field. Although small in most regions thus slow by itself except in the hot bubbles, microscopic diffusivity is the only process that truly mixes while the velocity field alone, no matter how complex, does not mix at all, but can greatly enhance mixing by feeding the microscopic diffusivity with small scale structures. We will rigorously prove this statement, which is unrecognized in most ICEMs. A careful and explicit consideration of the combined action of the advecting velocity field and the microscopic diffusivity is essential for a physical mixing model.

Most ICEMs use supernova (SN) or superbubble (SB) (we will use SN to represent both SN and SB for convenience) shocks as the catalyzing velocity and make the assumption that the ejected metals from a SN explosion are well mixed with interstellar gas swept up in the SN shells (Shigeyama & Tsujimoto 1998, Argast et al. 2000, Saleh et al. 2006). We will call this model a SN sweepup model. Models that use the volume overlap argument first given by Edmunds 1975 (e.g., Roy and Kunth 1995, Oey 2000) are equivalent to the SN sweepup models. In that argument it is assumed that the probability of a gas parcel being polluted by a SN event is equal to the volume filling factor of the SN remnant (SNR) , i.e., the ratio of the final volume of a SNR to the total volume of the galaxy. The appropriate value for this probability in compressible flows should be the mass fraction of gas polluted by each SN event with respect to the total gas mass. The volume filling factor is equal to the mass fraction only if the ejected metals can be spread into the shell and mix with the gas there; otherwise it overestimates the mixing efficiency. Therefore efficient mixing of the swept-up mass in SN shells with ejected metals is implicitly assumed in overlap models using the volume filling factor. This contrasts to the claim that no mixing is included in overlap models (e.g., Oey 2000).

The validity of the assumption of efficient mixing in shells is not obvious. Thornton et al. (1998) argued that metals in the hot cavities of SNe or SBs cannot easily catch up with the fast moving supersonic shock and thus it is unlikely that the gas swept up in the shells can mix with new metals. Tenorio-Tagle (1996) pointed out that a dense shell that is separated from the hot cavity by a contact discontinuity has such a small molecular diffusivity (due to the low temperature and the high density) that it cannot efficiently mix with the metal-rich gas inside. Only the shell gas evaporated into the hot cavity by thermal conduction and dense clouds that can penetrate the SN shell and crush into the cavity can mix with the metals inside. Tenorio-Tagle estimated that through these mechanisms only a small fraction (about 10%) of the swept-up mass can enter the hot cavity and mix with the newly produced metals. High mixing efficiency, assumed in the sweepup models, requires the existence of hydrodynamic instabilities to accelerate the action of microscopic diffusivity by producing small scale structures in the shells and enhance mixing.

Various shell instabilities, such as the overstability of a radiative shock (Chavalier & Imamura 1982) and the thin shell instability (Vishniac 1982) have been found in different evolution stages of a SN shock both analytically (e.g., Kimoto & Chernoff 1997) and numerically (e.g., Blondin et al. 1998). However none of the studies considered the shell evolution at very late time just before it stalls, when most gas is swept up. The existence of instabilities at this very late stage remains to be confirmed by further numerical studies. If instabilities do exist in this stage, they can probably enhance mixing across the small shell thickness (see §1.4). However, we show that they are not capable of giving perfect mixing over the entire shell sphere. Gas parcels at different directions in a shell move apart from each other as the shell expands, making mixing between them more difficult with time. In §1.4, we show that gas within only a small solid angle in a shell can be well mixed by instability- enhanced diffusivity. Depending on the length scale of the metallicity fluctuations in the ISM, this radial-only mixing results in different equations for the metallicity fluctuations. If instabilities do not exist in the late stage of the shell evolution, an alternative mixing process for the new metals with the shell gas, e.g., mixing by the ISM turbulence, is required for significant homogenization in the ISM.

The ISM turbulence is expected to play an important role in chemical homogenization in galaxies (Scalo & Elmergreen 2004). If mixing in SN shells is not as efficient as assumed in the sweepup models, the ISM turbulence would be the main agent that mixes the newly produced metals with the dense shells and later with the ambient ISM. If the shells are well mixed by instabilities (if they exist), turbulence would give rise to a second mixing phase that homogenizes the already enriched shells with the ambient ISM. This phase of mixing is usually neglected in the SN sweepup models. Despite its importance, turbulent mixing in the ISM has not received much investigation perhaps because of the intricacy of the physics involved (known as passive scalar turbulence) as a consequence of the nonlinear stochastic turbulent velocity field. Turbulence enhances mixing by providing a strain field that stretches the sources of metals into smaller and smaller structures until a scale is reached at which the diffusivity term can operate at a rate exceeding the strain rate of the velocity field. Karlsson (2005) assumed turbulent mixing to be a diffusion process for the second phase mixing in addition to mixing in shells implicit in his model with volume overlap. This treatment that transports metals in well-mixed shells as a smooth expansion into the ambient ISM using an eddy diffusivity for the expansion rate is not adequate and overestimates the turbulent mixing efficiency. Turbulence does not smoothly spread sources of metals; instead while transporting and dispersing the sources it also stretches them into filamentary or sheet-like structures (de Avillez and Mac Low 2002, see §1.3 and Fig.1.1). We will present a turbulent mixing model that incorporates this physical process.

Other ICEMs typically either treat mixing processes in a purely parametrized way or choose mixing parameters from an observational point of view without considerations of physical mixing processes. White and Audouze (1983) parametrized the polluted gas mass after each solar mass of stars formed. If the parameter is set to be the gas mass incorporated into shells by SN shocks produced by unit mass of stars, the model becomes identical to the sweepup models and the free parameter then obtains an interpretation as the sweepup mass by a unit mass of stars. van den Hoek and de Jong (1997) choose the mixing timescale to be the dispersion time of a star-forming cloud (i.e., the time before the cloud breaks up), for which they take a value based on observational considerations. After this timescale, it is assumed that ejecta produced in the cloud are homogeneously mixed with inactive clouds without ongoing star formation events. In order to account for the sequential enrichment effect, they use another parameter, the fraction of metals produced in an active cloud that are transported to and mixed with gas in the cloud hosting the next star formation event. Pilyugin and Edmunds (1996) adopted an observational approach to the mixing problem. They choose the amount of gas with which the metals released by each star formation event in a cloud mix in such a manor that the metallicity difference between the-first formed stars and the last-formed in the cloud is consistent with the observed metallicity spread in a local star-forming cloud.

There are also models that are mainly concerned with estimates of mixing timescales and do not give quantitative calculations of the metallicity fluctuations, e.g., the cloud collision model by Batesman and Larson (1993) and the fountain and spray model by Tenorio-Tagle (1996).

The mathematical tools used in various ICEMs are summarized as follows. Two special cases with sweepup mixing, a closed-box model without infall (Oey 2000) and an infall model with constant infall rate balancing the star formation rate (SFR) (White and Audouze 1983), have analytical solutions, where the metallicity probability distribution function (pdf) is derived using a binomial distribution $P(n|N)$ for the probability that a certain gas parcel is polluted n times and is not incorporated into stars after N SN explosion/star formation events. Most ICEMs use Monte Carlo simulations. For example, Shigeyama & Tsujimoto (1998) and Selah et al. (2006) studied the chemical patterns for metal-poor halo stars using SN-induced star formation and sweepup mixing; Pilyugin and Edmunds (1996) and van den Hoek de Jong (1997) studied the infall effects on the metallicity scatter using parametrized mixing models. Hydrodynamic numerical simulations cannot resolve dispersal and mixing processes in the ISM because of the huge range ($\sim 10^5$) of scales involved, with largest scales up to ~ 1 kpc associated with the dispersal of metals by SB and SN shocks and the smallest scale of ~ 0.1 pc where microscopic diffusivity dominates the strain of the advecting velocity field. Existing simulations are concerned with either the dispersal of particles by ISM turbulence and not mixing (Klesson and Lin 2003) or the decay of concentration variations by turbulent mixing without continuing sources of metals (de Avillez and Mac Low 2002).

In this chapter, we develop a new approach for ICEMs: kinetic equations of the metallicity probability distribution function. We concentrate on the derivation of a physical model for turbulent mixing in the ISM, based on the following physical picture. Turbulence stretching produces smaller and smaller 2D (sheet-like) structures which are, at the same time, brought closer to each other by turbulent folding at larger scales. As the sheet thickness and separation decrease to the diffusion length scale, neighboring sheets can exchange tracer materials by microscopic diffusivity and homogenize. The mixing timescale is characterized by the time for stretching to reduce the sheet length scale to the diffusion length scale. Note that, different from previous ICEMs, our derived mixing timescale is physically based and thus not a free parameter. We find that, in the decaying case without continuous sources, this model gives an exponential variance decay with a timescale in excellent agreement with the numerical simulation results by de Avillez and Mac Low (2002). In addition to homogenization by the ISM turbulence, lockup of metals in stars, the infall of low-metallicity gas and the outflow of metal-rich gas, release of new metals from SN sources and stellar winds are all self-consistently incorporated in the kinetic equation. We also give a kinetic equation formulation for the SN sweepup model.

In §1.2, we use the pdf equation for a metallicity field subject to advection by a general stochastic velocity field and the molecular diffusivity, derived in Appendix A, to show that that the velocity field does not mix at all by itself. In §1.3, we give a phenomenological theory for turbulent mixing, based on which we develop a closure method for the diffusivity term in the pdf equation. We derive the pdf equation for the sweepup models in §1.4.

1.2 The pdf approach: Mixing catalyzed by velocity

The evolution of a metallicity field $Z(\mathbf{x},t)$ is generally given by an advection- diffusion equation,

$$\frac{\partial Z(\mathbf{x},t)}{\partial t} + \mathbf{u}(\mathbf{x},t) \cdot \nabla Z(\mathbf{x},t) = \frac{1}{\rho}\nabla \cdot (\rho\kappa\nabla Z(\mathbf{x},t)) + S(\mathbf{x},t) \tag{1.1}$$

where κ is the microscopic diffusivity (cm^2 s^{-1}), $\mathbf{u}(\mathbf{x},t)$ represents an arbitrary velocity field, e.g., random SN shocks and instabilities (if present) in the SN shells or the ISM turbulence, and S denotes various metal contributions from SN sources, stellar winds, infall of low- metallicity gas, outflow of metal- rich gas etc. The mixing rate is determined by the two important components, the advecting velocity and the microscopic diffusivity.

Before presenting the general equation for the metallicity probability distribution, we first show that the diffusivity alone is too slow to homogenize the ISM. We obtained microscopic diffusivities in different phases of the ISM using standard calculations. In a neutral medium, the molecular diffusivity is given by $\kappa \sim \lambda c = c/(n\sigma)$, where λ is the mean free path, c is the thermal speed, n is the density and σ is the collision cross section. Taking $\sigma \simeq 4 \times 10^{-15}$ cm^2 for oxygen in neutral gas, we have $\kappa \sim 1 \times 10^{19}(T/10^2)^{1/2}n^{-1}$ cm^{2}s. In an ionized medium $\kappa \sim 2 \times 10^{18}(Z_1Z_2)^{-2}(T/10^4)^{5/2}(n/0.1)^{-1}$ cm^{2}s (Kulsrud 2004), where Z_1 and Z_2 are the charges of the background ions and the diffuser. The interested readers are referred to papers by Tenorio-Tagle (1996) and Oey (2003) for details. Our result is very similar to that given in Table 1 of Oey (2003). The phase with most efficient mixing is the hot ionized medium, i.e., hot cavities of SNRs or SBs, which has a large diffusivity, $\sim 5 \times 10^{23}$cm^{2}s, due to its high temperature and low density. With this diffusivity, the mixing length scale during the life time of SNRs or SBs is about 2-10 pc, which is a little smaller than the stall size of SNRs or SBs. Considering that, at early stages of SNR and SB evolution, the size was smaller and the diffusivity was significantly larger due to higher temperature, we assume that gas in hot cavities are perfectly mixed throughout the paper (Rayleigh-Taylor instabilities at early time can also make mixing faster). However, this hot phase occupies a negligible mass fraction and most mixing has to occur in other phases. HII regions also contain a small fraction of gas and have a very small diffusivity $\sim 10^{18}$ cm^{2}s, therefore repeated photoionization does not contribute much to mixing (see, however, Tenorio-Targo (1996) who assumes mixing primarily occurs in HII regions based on a completely different homogenization picture for the ISM). The warm neutral medium and the cool neutral medium contain most of the gas mass. Using their typical temperatures and densities, we obtain $\kappa = 5 \times 10^{20}$ cm^{2}s^{-1} for the warm neutral medium and $\kappa = 10^{19}$ cm^{2}s^{-1} for the cold neutral medium, respectively. For the mean diffusivity in the neutral medium, an average weighted by the residence time in different phases is appropriate. We assume that the residence- time is proportional to the mass fraction in different phases so that we can instead use a mass-weighted average for the mean. Assuming the WNM contains a significant fraction ($\geq$ 20%) of the ISM mass, the mean diffusivity in the ISM is $\kappa \sim 10^{20}$ cm^{2}s^{-1}. This diffusivity can mix over only about 1 pc in 10 Gyr. To see the severity, the timescale to erase inhomogeneity with a moderate length scale of $\sim$ 10 pc is $\sim 10^3$ Gyr. Therefore mixing by the microscopic diffusivity alone is too slow.

Clearly, to mix the Galaxy, a velocity field represented by the second term in eq (1.1) is required. Since the velocity field $\mathbf{u}(\mathbf{x}, t)$ in the ISM is stochastic, a probabilistic approach is necessary for our problem. We define a metallicity probability distribution function (pdf) $f(Z, \mathbf{x}, t)$ such that $f(Z, \mathbf{x}, t)dZ$ is the mass fraction of material in the metallicity range $(Z, Z + dZ)$ at position $\mathbf{x}$ and time t. A detailed derivation of the equation for $f(Z, \mathbf{x}, t)dZ$ from equation (1.1) is given in appendix A using an ensemble average technique. It can also be found in Janicka et al. (1979), Pope (2000) and Fox (2003). The resulting equation can be understood as a statement of conservation of probability in phase space $(Z, \mathbf{x})$, similar to the Liouville equation in kinetic theory.

$$\frac{\partial f}{\partial t} + \nabla \cdot (f \frac{\langle \rho \mathbf{v} | Z \rangle}{\langle \rho | Z \rangle}) = -\frac{\partial}{\partial Z}(f \frac{\langle \nabla \cdot (\rho \kappa \nabla Z) | Z \rangle}{\langle \rho | Z \rangle}) + (\frac{\partial f}{\partial t})_{src} \tag{1.2}$$

where $\langle ... | ... \rangle$ denotes the conditional ensemble average as defined and explained in Appendix A. The density averaging is needed for a compressible flow where mass fraction is more important. The term $(\frac{\partial f}{\partial t})_{src}$ represents all the contributions from various sources.

With this equation, we can show that, although it assists the action of microscopic diffusivity and enhances mixing (see below), the velocity field itself does not mix at all. To prove this, we first consider an idealized case with statistically homogeneous velocity field and metallicity field, i.e., where $f\frac{\langle\rho\mathbf{v}|Z\rangle}{\langle\rho|Z\rangle}$ is not a function of space, and thus its divergence is zero. The advection term then has no contribution to the metallicity distribution at any local place, suggesting that the velocity field does not mix.

In general, the advection term in equation (1.2) can change local metallicity distributions. However, this change, caused by transport of fluid parcels with different metallicities across a local place, is completely different from that by true mixing, represented by the diffusivity term in eq (1.2). We show that the transport effects over all space cancel out, giving no contribution to the global metallicity distribution. This indicates that the advecting velocity does not mix at all since true mixing has a general trend to make the global distribution narrower. The global metallicity distribution can be written as $f_g(Z,t) = \int_V f(Z;\mathbf{x},t)dV$ where V is the volume of the system. Integrating equation (1.2), we find that the contribution from the advection term to the global distribution $f_g(Z,t)$ is $\int_V \nabla\cdot(f\frac{\langle\rho\mathbf{v}|Z\rangle}{\langle\rho|Z\rangle})dV = \int_S(f\frac{\langle\rho\mathbf{v}|Z\rangle}{\langle\rho|Z\rangle})\cdot d\mathbf{S}$ where S is the surface of the volume V and we have used Gauss divergence theorem. The surface integral vanishes for periodic boundary conditions or if $f(Z;\mathbf{x},t)$ decreases to zero fast when $\mathbf{x}$ approaches infinity as applies to any realistic system. Therefore the advection term conserves the global pdf, rigorously proving that a velocity field, no matter how complex it is, does not mix at all. Intuitively this result means that a velocity field just moves fluid parcels around, and displacement of fluid parcels only changes their relative position and does not affect the mass fraction of fluid parcels with a given metallicity, leaving the distribution in the metallicity space unchanged.

Although conceptually distinct from mixing, changes in spatial configuration of a metallicity field by advection have profound effects on the diffusivity term in eq (1.2), which depends on spatial gradients of the metallicity field. The advecting velocity plays an implicit but very important role in mixing. Complex velocity fields, e.g., turbulence, tend to increase metallicity gradients thus enhance mixing by stretching and folding metallicity parcels into small scale structures such as filaments and sheets. Therefore a velocity field works as a catalyst, feeding the microscopic diffusivity with small scale structures. This cooperation results in a much higher mixing efficiency than the case with diffusivity only. The mixing timescale essentially depends on how fast the velocity field generates small structures that the microscopic diffusivity can homogenize quickly. In the following two sections, we consider two enhancing velocity fields, the ISM turbulence and the instabilities, if present, in SN shells. We will estimate the mixing timescales and develop pdf equations for the two models.

As mentioned above, the advection term can change local metallicity distributions through transport of fluid parcels. This can have important consequences for local metallicity fluctuations. For example, a large-scale metallicity gradient, if it exists, can provide a source of local fluctuations, when combined with a stochastic velocity field that brings gas from different places to the vicinity of an observer. In §1.3, we will give an approximation for this term which can be used to study the effect of large-scale gradients on local fluctuations.

In summary, although it does not mix at all, the velocity field plays two important roles. First it disperses and transports the localized "pollutant" sources. Second it stretches the sources and generates small scale gradient structures to feed microscopic diffusivity and thus enhances the mixing efficiency. The process is well illustrated in Fig 1.1, which is a particle simulation using a synthetic stochastic velocity field designed to have a Kolmogorov spectrum to simulate a real turbulent flow. The 4 panels correspond to snapshots of the spatial distribution of particles at 2, 5, 10 and 20 times the flow correlation time after release of a particle parcel at the origin.

We point out that our pdf approach is a 1-point formulation, where spatial structures can not be accounted for explicitly. The structures will be built in when modeling the diffusivity term and estimating the mixing timescale using important length scales of the metallicity fluctuations. We assume that the SN sources are completely random and that infall gas continuously flows onto the galaxy disk and participates in any mixing event immediately upon landing. This assumption gives an upper limit for the mixing rate since it minimizes the need of transport between different SN sources and between SN sources and infall. In reality, complicated spatial structures such as clustering of SN sources, the spatial separation between the infall gas and the sources exist. Therefore we need a more sophisticated treatment, perhaps a 2-point formulation, which, however, is out of the scope of this study.

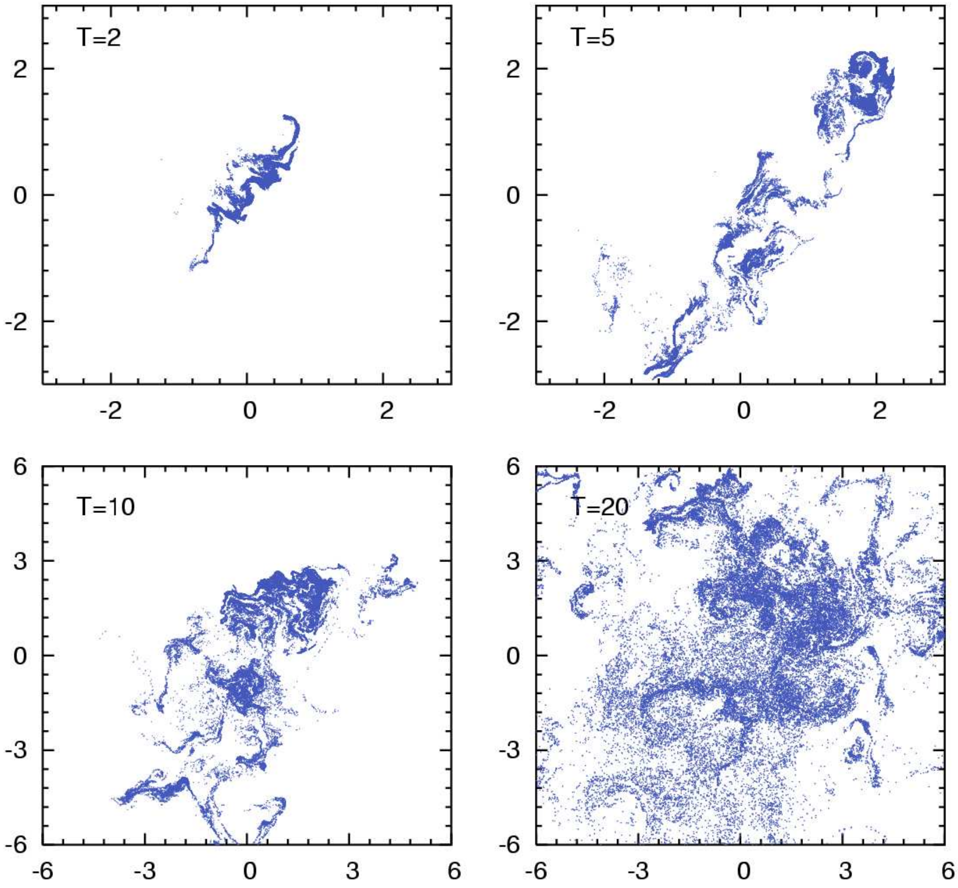

Figure 1.1 Illustration for turbulent transport and mixing

Blue particles, representing heavy elements deposited by SN sources or stellar winds, are advected by a stochastic synthetic velocity field with a Kolmogorov spectrum to mimic a real turbulent flow. A particle parcel, initially released at the origin, is spread and transported by the flow in a non-smooth way. Small-scale structures in the concentration field are generated by the strain field. The velocity field enhances mixing because concentration structures at smaller scales can be erased by the microscopic diffusivity faster. In this flow realization, the parcel accidently encounters a large-scale shear when it is released. Note that this process is completely different from diffusion where particle parcels are spread smoothly and no small-scale fluctuations appear. The four panels correspond to snapshots at 2, 5, 10 and 20 times the correlation timescale of the flow after the particle release. See §1.2, 1.3.2, 1.3.3.

1.3 A turbulent mixing model

In this section we develop a model for mixing by ISM turbulence, using the general pdf equation (1.2) with $\mathbf{v}(\mathbf{x};t)$ being a stochastic nonlinear turbulent velocity. We will analyze the terms in eq (1.2) one by one. The difficulty for turbulent mixing is the so-called closure problem for the advection term and the diffusivity term. Exact forms for these two terms essentially require the knowledge of the full multi-point statistics of the velocity field and the concentration field. The multi-point statistics, which certainly contains all information about the 1-point statistics that we pursue, is of course unknown. Therefore some phenomenological theories have to be used to approximate the multi-point statistics to obtain a solution for the 1-point probability distribution.

This problem can be clearly seen in the diffusivity term, which depends on the 2-point pdf of the metallicity field due to the metallicity gradient in the conditional mean. The conditional mean can be explicitly expressed as a function of the 2-point pdf in the limit of zero separation. For simplicity, we use incompressible flows with constant density and diffusivity as an example. In this case, the diffusivity term can be written as,

$$-\partial_C(f\langle\kappa\nabla^2 Z|Z=C\rangle) = -\kappa \lim_{\mathbf{x}'\to\mathbf{x}} {\nabla_{\mathbf{x}'}}^2 \int C'\partial_C f^{(2)}(C,C';\mathbf{x},\mathbf{x}')dC' \tag{1.3}$$

with $f^{(2)}(C,C';\mathbf{x},\mathbf{x}';t)$ denoting the probability that at time t the metallicities at $\mathbf{x}$ and $\mathbf{x}'$ are C and C', respectively. Similarly for compressible flows with varying density and diffusivity, it can also be shown that the diffusivity term, in a more complicated way, depends on the 2-point pdf. To obtain a form for the diffusivity term to solve the pdf equation, one may try to derive an equation for the 2-point pdf $f^{(2)}(C,C';\mathbf{x},\mathbf{x}')$ from the advection-diffusion equation. However, the 2-point pdf equation turns out to have terms dependent on 3-point pdfs, and so on. Therefore we have no closed form for the diffusivity term unless some approximation is applied to truncate this hierarchy of multi-point pdf equations. This is the closure problem mentioned above. We will model the diffusivity term using a recent phenomenological theory (e.g., Villermaux 2004) for the mixing timescale and an integral closure by Janicka et al. (1979) for the form of the diffusivity term in §1.3.2.

A similar problem exists for the advection term, which, due to the conditional mean, depends on the 1-point density weighted (necessary for compressible flows) joint probability distribution $P_\rho(\mathbf{V}, Z; \mathbf{x}, t)$ of the velocity and the metallicity at $\mathbf{x}$. The closure problem arises again when we derive an equation for the unknown joint pdf $P_\rho(\mathbf{V}, Z; \mathbf{x}, t)$ using the momentum equation for $\mathbf{v}$ and the advection-diffusion equation for Z. In the resulting equation there are four terms that contribute to the joint pdf evolution. Only the one related to advection of the joint probability is in a closed form, given by $\mathbf{V} \cdot \nabla_{\mathbf{x}} P_\rho(\mathbf{V}, Z; \mathbf{x}, t)$. The other three terms associated with pressure, viscosity and diffusivity all depend on 2-point pdfs, whose own equations in turn involve 3-point pdfs and so on. We again encounter the closure problem. We give an approximation to close the advection term in §1.3.1.

The source term needs no approximation and has an exact form, which we give in §1.3.3.

1.3.1 The advection term

A commonly used closure for the advection term is the diffusion approximation (Pope 2000),

$$\nabla \cdot \left(f(Z; \mathbf{x}, t) \frac{\langle \rho \mathbf{v} | Z \rangle}{\langle \rho | Z \rangle}\right) = -D \nabla^2 f(Z; \mathbf{x}, t) \tag{1.4}$$

where D is called the turbulent eddy diffusivity. Usually D is estimated by $D \sim v_{rms} L \sim v_{rms}^2 T$ where v_{rms} is the rms velocity, L and T are the correlation length scale and time scale respectively.

We stress that this diffusion approximation for the metallicity *pdf* equation is completely different from the diffusion approximation for the metallicity field Z *itself* as used by Karlsson (2006). The latter, modeling the turbulent advection by a Laplacian operator directly on the metallicity field with a large effective diffusivity D, conceptually confuses the role of advection with true mixing which only occurs through microscopic diffusivity. It corresponds to a fast smooth spread of metallicity parcels with size increasing as $\sim (Dt)^{1/2}$, contradicting the realistic picture of turbulent mixing, where structures such as filaments and sheets are created by the strain of the advecting velocity field and thus the transport is not smooth (see Fig. 1.1). As the structures become thinner and their separations get smaller, the space between them is gradually filled up and then smoothed out by the microscopic diffusivity (see §1.3.2). A diffusion approximation for the metallicity itself gives rise to artificial mixing that synchronizes the transport process and the homogenization process. Without the time delay between the two processes accounted for, the model overestimates the turbulent mixing efficiency. For more specific arguments against this approximation, see de Avillez & Mac Low (2002).

The diffusion operator on the distribution $f(Z,t)$, on the other hand, models the transport effect of advection without causing artificial smearing of the metallicity field. As can be shown with the same technique in §1.2, the approximation eq (1.3) retains the property of advection: the conservation of the global metallicity distribution. Therefore the metallicities in fluid parcels are kept intact when transported by this term. Physically this closure means that the probability for a fluid element to be transported to a place at a distance of d from its original position in time t is given by $1/(4\pi Dt)^{3/2} exp(-d^2/4Dt)$ assuming D is constant. This closure is based on the Taylor's theorem (see, e.g., Monin & Yaglom 1976), which says that the probability distribution of the distance, over which a passive particle (or a fluid element) travels in an isotropic and stationary turbulent flow in time t is Gaussian with variance $\sim v_{rms}^2 Tt$ for t much larger than the (Lagrangian) velocity correlation time scale T. At large time, the total distance can be thought of as a sum of independent steps of duration $\sim T$ each, therefore $D \sim v_{rms}^2 T$ at $t \gg T$ from the central limit theorem. At $t \ll T$, particles move ballistically, so the variance of their displacement goes like $\sim v_{rms}^2 t^2$. The distribution of the displacement is also close to Gaussian since the 1-point statistics of a turbulent velocity field is approximately Gaussian. This suggests that for $t \ll T$ the closure form remains valid and we only need to set $D \sim v_{rms}^2 t$. Therefore a good model would have a time-dependent D that captures behaviors both in the long-time and short-time limits. We will postpone a detailed discussion on a proper choice of D to a future study.

We point out that this advection term only deals with how metallicity parcels can be statistically transported and does not depend on, or give any information about, the characteristics of structures created during the transport, which is, however, very important to the diffusivity term that we consider next.

1.3.2 The diffusivity term

The essential part of the pdf formulation for turbulent mixing is to model the diffusivity term on the rhs of eq (1.2). This term depends on the metallicity gradients, thus implicitly depends on the velocity field, which reduces the length scale of the gradients. An appropriate model for this term has to account for the combined effects of the velocity field and the microscopic diffusivity.

The basic features of turbulent mixing in incompressible flows can be captured by a model in which the velocity field stretches, folds and twists the concentration field and thus brings the fluctuations into small scales where the microscopic diffusivity can operate fast (see Fig. 1.1). Tracers are stretched into filaments by the turbulent velocity field at places where the strain tensor has two negative eigen values or into sheet-like structures where only one eigen value is negative. It has been found that sheets are the dominant tracer structures in simulations (e.g., Watanabe and Gotoh 2004) and experiments (Villermaux 2004). We will use "sheets" or "sheet-like structures" to represent both filaments and sheets. As sheets are stretched thinner and thinner, their surface area becomes larger and larger, resulting in an increase of the contact area between different metallicities and thus an enhancement in the mixing efficiency. At the same time, these laminated and extended structures are subject to turbulent folding and twisting at larger scales that bring them closer to each other and reduce their mean separation. This stretching and folding process continues until the thickness of the sheets and their mean separation reach a length scale at which diffusivity can operate faster than advection. We will call this length scale the diffusion scale. In §1.3.2.1, we use a simple argument to calculate the timescale for the stretching process to bring the structures to the diffusion scale. The folding process occurs with a similar same timescale, which we justify by a simple calculation.

In addition to the timescale, we need a model for homogenization between sheets of different metallicities by diffusivity. We will only consider metal transfer between neighboring layers or sheets and neglect the metal transfer over separated structures. This assumption is justified by the fact that diffusivity probably cannot operate fast enough over distances between separated sheets before the velocity field stretches and folds further and brings them into contact. In §1.3.2.2, we use a closure model by Janicka et al. (1979) to formulate this interaction process between neighboring sheets by microscopic diffusivity.

Although the models we use here were initially proposed for mixing in incompressible turbulence, we assume that they can be applied to supersonic turbulence, characteristic of the interstellar medium, considering the large solenoidal energies found even in highly supersonic turbulence simulations (Elmergreen and Scalo 2004) and the fact that shock wave compressions are analogous to the incompressible stretching in the sense of bringing tracers from large to small scales.

1.3.2.1 The mixing timescale

The conventional conception of turbulent mixing is a cascade of tracer fluctuations through many successive scales step by step. This picture has recently been replaced by a new one in which tracers are stretched into the diffusion scale in a single step with a constant strain rate. This gives an exponential decrease in the scale of tracer structures. This "short circuit" cascade is consistent with observed properties in turbulent mixing experiments for jets (Villermaux 2004) and is similar to results based on path integral Lagrangian models (Schraiman and Siggia 2000). It is also closely related to theories of pollutant mixing in stochastic and weakly turbulent flows (Ottino 1991, Voth et al. 2002). The model is conceptually simple and allows a direct calculation of the characteristic mixing timescale.

The characteristic timescale for turbulent mixing is the time for the turbulent velocity field to deliver scalar fluctuations from the scale of the sources L_s to the diffusion length scale l_d. The source length scale here corresponds to the sizes of SNRs/SBs, the length scales of infall clouds etc. Different sources may have different length scales, thus a realistic calculation needs to account for a spectrum of source sizes. For simplicity we will use a single size for L_s as if all the sources had the same length scale. We take it to be the average size of different kinds of sources.

As shown in Appendix C, the stall radii of isolated SNe have a quite weak dependence on the density and metallicity in the ISM gas to be swept up. We will adopt an average radius of 50 pc and set L_s to be the diameter 100 pc for isolated SNe. The final size of a SB depends on the mechanical luminosity or equivalently, the number of exploding massive stars it contains. We derived the final size as a function of the number of SNe powering the SB in Appendix C. Using empirical mechanical luminosity functions, we find that the average radius of a SB is about 200 pc. The mean source size including both SBs and SNe depends on the weighting factor used for averaging. If we weight the source size by the number frequency, the resulting average for L_s is about 110 pc, very close to the size of an isolated SN. This is because isolated SNe are much more frequent than SBs (although a majority of SNe are clustered in SBs, the number frequency of SBs is small since each SB contains a larger number, ~ 30, of SNe). However, if the source size is weighted by the amount of metals each source produces, the average turns out to be about 300 pc, closer to the radii of a SB because most of SNe and thus most fresh metals are in SBs. We will adopt $L_s = 100$ pc for the average source size of SBs and SNe, which is obviously a lower limit. We keep in mind that this may underestimate L_s by a factor of 3.

The size of infall clouds is not observationally constrained since there is no direct observational evidence for infall. The most investigated candidate for infall gas is high velocity clouds (HVCs), which have a large range of sizes from ~ 100 pc to ~ 10 kpc (see, e.g., Putman 2006). Considering that the large clouds probably need to be disrupted and fragmented by instabilities before completely entering the disk, we assume the average size of infalling blobs when landing on the disk is not much larger than the disk scale height of 100 pc. It is still uncertain whether HVCs are the infall gas needed to fuel star formation in some chemical evolution models while the derived mass flux from the observed HVCs is too low to account for the total star formation rate in the Galaxy (Putman 2006). Therefore the infall gas, if indeed exists, probably has other forms than the HVCs. An idealized situation is that the infall gas continuously dumps at the top layer of the galactic disk. In order for the infall gas to enter the central disk plane, instabilities are required to produce "finger" like structures so that infall gas can penetrate the disk. We expect these structures to have a length scale of the scale height, which is ~ 100 pc. It seems likely that the source size for infall gas is not larger than the scale height. However, no constraints can be put on the lower limit for the length scale of infall gas. We cannot exclude the possibility that the infall gas is mainly in the form of compact clouds of sizes beyond current detection limit. In fact, in chapter 3, we show that the small observed scatter in the Galactic disk favors the form of tiny clouds for the infall gas if it exists. Here we will adopt 100 pc for the size of the infall gas. Since the sizes of both SN/SB sources were also the taken to be 100 pc, the final average for L_s would be 100 pc.

We obtain l_d by calculating the scale at which the diffusivity term begins to exceed the advection term. At a given scale l, the advection term is $\sim u_l Z_l / l$ and the diffusion term is $\sim \kappa Z_l / l^2$ where u_l and Z_l denote the velocity and concentration at the scale l, respectively. Assuming a linear scaling for velocity difference $u_l \sim l$, consistent with assumed exponential stretching (see below), the advection term is equal to UZ_l/L_s where U is the rms turbulent velocity on the scale of the sources. Equating the advection term and the diffusion term gives the diffusion scale,

$$l_d = (\frac{\kappa L_s}{U})^{1/2} \tag{1.5}$$

For κ, we use the residence-time average for the neutral medium estimated in §1.2, i.e., $\kappa = 10^{20}$ cm^2/s. Then we have $l_d \sim 0.06$ $(\kappa_{20}L_{100}/U_{10})^{1/2}$ pc where κ_{20} is $\kappa/10^{20}$ cm^{2}s^{-1}, L_{100} is $L_s/100$ pc, and U_{10} is U in unit of 10 km/s (Kulkarni & Heiles 1987). Noting that l_d enters the mixing time only logarithmically, and the uncertainty in the estimate caused by that in the diffusivity is negligible.

The evolution of the dimension or length scale l of tracer structures, e.g., the thickness of tracer sheets, under stretching by a turbulent velocity field can be written as,

$$dl/dt = -\gamma l \tag{1.6}$$

where γ is the stretching rate at length scale l. In the single-step picture, the stretching rate γ is constant all the way down to the diffusion scale and independent of the scale l of the structure being stretched. With the assumption, γ can be evaluated at the source scale, $\gamma = U/L_s$. The constancy of the strain rate $\sim u_l/l$, is equivalent to a linear velocity scaling, i.e., $u_l \sim l$, during a stretching event. With constant γ, eq (1.6) gives,

$$l = L_s exp(-\gamma t) \tag{1.7}$$

The exponential decrease of the structure scale is supported by a series of papers (Batchelor 1952, Girimaji & Pope 1990, Goto and Kida 2003) which have demonstrated that the length of infinitesimal line elements released in a turbulent flow grows exponentially in time. Following Shraiman and Siggia (2000), we obtain the timescale to stretch sources from L_s to l_d by setting l to l_d in eq (1.7),

$$\tau = \gamma^{-1} ln(\frac{L_s}{l_d}) = \frac{L_s}{2U} ln(\frac{UL_s}{\kappa}) = \frac{L_s}{2U} ln(Re) \tag{1.8}$$

where we used eq (1.5) for the diffusion length scale and UL_s/κ, the diffusivity analogue of the Reynolds number, is called the Peclet number Pe. Numerically, $Pe \sim 3 \times 10^7$ $(U_{10}L_{100}/\kappa_{20})$. The formula is consistent with the mixing timescale found in experiments by Villermaux (2000). For a typical source size of 100 pc, we have $\tau = 75$ Myr.

The result eq (1.8) is in excellent agreement with the numerical simulations by de Avillez and Mac low (2002); thus the adopted phenomenological theory here gives an physical explanation to their results. Setting the source size to that chosen by de Avillez and Mac low for their initial checkerboards, i.e., $L_s = 25$ and 50 pc in eq (1.8), we get mixing timescales of 16 and 36 Myr respectively, which are very close to the variance decay timescales they found, i.e., 21 Myr and 37 Myr. Note that eq (1.8) explains the almost linear scaling of the timescale with the source size. Using the numerical result by Dib and Burkert (2005) that the rms velocity in the ISM scales with the SN rate as $U \sim \nu_{SN}^{1/2}$, eq (1.8) also explains the scaling of the decay timescale with the SN rate $\tau \sim \nu_{SN}^{-1/2}$ found in de Avillez and Mac low (2002). We point that the SN/SB source size is likely to be larger than 25 pc or 50 pc used by de Avillez and Mac Low (2002). We choose a standard value of $\tau = 75$ Myr corresponding to $L_s = 100$ pc.

Finally we show that the timescale for turbulent folding to decrease the mean distance between sheets is approximately equal to the timescale for stretching to reduce their thickness if the source size is close to the integral length scale L of the flow, which is expected to be about the scale height in the ISM. We prove this statment for incompressible flows and assume it applies to supersonic ISM turbulence where a significant fraction of kinetic energy is in the solenoidal mode. In incompressible flows, the conservation of total metal mass implies that the volume of a metal parcel is conserved before the microscopic diffusivity comes in. As the strain field stretches the sources into thin sheets at a constant rate γ, the total area of the sheets, A, increases at the same rate to conserve the volume,

$$A = A_s exp(\gamma t) \tag{1.9}$$

where $A_s \sim L_s^2$ is the total initial area of the sources. The mean distance d between sheets can be estimated by,

$$d \sim \frac{L^3}{A} = \frac{L^3}{A_s^2} exp(-\gamma t) \tag{1.10}$$

Setting d to l_d gives the timescale τ_d to reduce the mean distance between sheets to the diffusion scale,

$$\tau_d = \gamma^{-1} ln(\frac{L^3}{A_s l_d}) \qquad (1.11)$$

Clearly, if the source size L_s is close to the integral scale L, $L^3/A_s \sim L_s$ and we have $\tau_d \sim \tau$ by comparing eqs (1.8) and (1.11). Since τ_d depends on the integral scale and the source size logarithmically, $\tau_d \sim \tau_v$ as long as L and L_s are close in order of magnitude. This is satisfied in the case we are studying: both the integral scale L in the ISM turbulence and the source size L_s are $\sim$ 100 pc. This justifies our assumption that the stretching process and the folding process have the same timescale.

1.3.2.2 The closure formulation

A mixing timescale is insufficient to give a quantitative prediction of the probability distribution of gas metallicity. A function form is needed to model the diffusivity term, for which there is no standard or accepted closure technique. We adopt the closure model by Janicka et al. (1979). When this model was proposed, the turbulent mixing process was thought to be a cascade process of scalar fluctuations from large eddies to small eddies. Based on this picture, Janicka et al. modeled the diffusivity term as an interaction process of metals in tracer "eddies" of similar sizes, that are generated and brought into contact by the velocity field. As mentioned earlier, this picture is challenged by recent experiments and simulations and a new picture emerges where small-scale structures are generated in single-step stretching events and the dissipative structures are 2-dimensional sheets. We reformulate the model by Janicka et al. in the new picture and interpret the model in terms of interactions between sheets. We expect that the timescale from the production of dissipation structures to the completion of interactions to be similar to that for the stretching and folding process since the diffusive interaction between sheets at smallest scales is fast. We will consider the tracer exchange between two neighboring tracer sheets by microscopic diffusivity.

Interactions give new values of metallicity to neighboring tracer sheets in contact. Since the diffusivity always transfers metals from the high-metallicity sheet to the low-metallicity one, the final metallicities Z_1' and Z_2' must be between the initial values Z_1 and Z_2 (assuming $Z_1 \le Z_2$), i.e., $Z_1 \le Z_1', Z_2' \le Z_2$. The conservation of the total mass of metals requires the sum of metallicities in the two interacting sheets unchanged by the interaction, i.e., $Z_1' + Z_2' = Z_1 + Z_2$. Here the interacting sheets are assumed to be of similar sizes; otherwise Z_1 and Z_2 need to be weighted by gas mass in each sheet. We define a transition function $P(Z_1, Z_2; Z)$ as the probability that one of the sheets ends up with a metallicity Z as a result of an interaction between two sheets with initial metallicities of Z_1 and Z_2. The metallicity in the other sheet is fixed by the conservation of metals. From the arguments above, the transition probability distribution satisfies the the following conditions:

$$\begin{aligned} P(Z_1, Z_2; Z) &\geq 0 \quad Z_1 \leq Z \leq Z_2 \\ &= 0 \quad \text{otherwise} \end{aligned} \tag{1.12}$$

and

$$P(Z_1, Z_2; Z) = P(Z_1, Z_2; Z_1 + Z_2 - Z) \tag{1.13}$$

because the emergence of a sheet with metallicity Z from an interaction is always accompanied by another sheet with metallicity $Z_1 + Z_2 - Z$. The normalization of P is given by,

$$\int_{Z_1}^{Z_2} P(Z_1, Z_2, Z) dZ = 2 \tag{1.14}$$

where the factor of two accounts for the fact that two new values of metallicities result in one interaction.

There is no exact form for the transition function, which depends on the details of tracer exchange between two sheets at interaction. The choice of the form for $P(Z_1, Z_2, Z)$ is unconstrained and characterizes a specific model. We will consider two special forms for the transition function. Janicka et al. (1979) set $P(Z_1, Z_2; Z)$ to be uniform between Z_1 and Z_2,

$$P(Z_1, Z_2; Z) = \frac{2}{Z_2 - Z_1} \quad Z_1 \leq Z \leq Z_2 \tag{1.15}$$

and Curl (1963) assumes that the final metallicity is equal to the average of the initial metallicities so that P is given by a delta function,

$$P(Z_1, Z_2; Z) = 2\delta(Z - \frac{Z_1 + Z_2}{2}) \tag{1.16}$$

This process is in close analogy to particle collisions in the kinetic theory with $P(Z_1, Z_2; Z)$ playing the role of the cross section of particle interactions. The conservation of metal mass corresponds to the conservation of momentum. However, the metallicity square in this model, which corresponds to the kinetic energy in particle collisions, is not conserved. In fact, $Z_1'^2 + Z_2'^2 \leq Z_1^2 + Z_2^2$, which results in monotonically decreasing metallicity variance as shown in Appendix B. Therefore unlike the Boltzmann equation for elastic collisions, the equation we will derive below for this mixing model has no equilibrium solution for the decaying case without continuing sources.

We derive the diffusivity term by counting the mass fraction of gas that enters and leaves a given infinitesimal metallicity bin through interactions. We split the metallicity space into N bins $[0, \Delta Z)$, $[\Delta Z, 2\Delta Z)$, ..., $[(N-1)\Delta Z, N\Delta Z]$ with the bin size $\Delta Z = Z_u/N$ where the upper limit $Z_u \leq 1$ is determined by the maximum source metallicity. Assuming the total gas mass is M and the mass of gas under interactions during $(t, t+\Delta t)$ is ΔM_i with the subscript "i" standing for "interaction", the mass fraction of gas whose metallicity changes in Δt is then $\Delta M_i/M$. The fraction of gas that gets into the metallicity bin $[I\Delta Z, (I+1)\Delta Z)$ by interactions is given by,

$$\Delta_+ f(I)\Delta Z = \frac{\Delta M_i}{M}(\sum_{J=0}^{I} f(J)\Delta Z \sum_{K=I}^{N-1} f(K)\Delta Z P(J, K; I)\Delta Z) \tag{1.17}$$

and the mass fraction that leaves this bin is,

$$\Delta_- f(I)\Delta Z = \frac{\Delta M_i}{M}(\sum_{J=0}^{I-1} f(I)f(J)\Delta Z^2 + 2f(I)^2\Delta Z^2 + \sum_{J=I+1}^{N-1} f(I)f(J)\Delta Z^2) \tag{1.18}$$

where the factor 2 before $f(I)^2\Delta Z^2$ is due to the fact that two elements in the bin $[(I-1)\Delta Z, I\Delta Z]$ are involved in an I-I interaction. Using the normalization of f, we have

$$\Delta_- f(I)\Delta Z = \frac{\Delta M_{si}}{M}(f(I)\Delta Z + f(I)^2\Delta Z^2) \tag{1.19}$$

The second term is of second order and can be dropped in the limit $\Delta Z \to 0$ if $f(I)$ is not singular. However if $f(I)$ is singular so that $\lim_{\Delta Z \to 0} f(I)\Delta Z$ is finite, this term cannot be neglected (for an example, see the derivation for the primordial fraction equation below).

Subtracting $\Delta_- f(I)\Delta Z$ from $\Delta_+ f(I)\Delta Z$ and taking the limit $\Delta Z \to \infty$ and $\Delta t \to 0$, we have,

$$(\frac{\partial f}{\partial t})_{mix} = \frac{1}{\tau_{mix}}[\int\limits_0^Z dZ_1 f(Z_1) \int\limits_Z^{Z_u} dZ_2 f(Z_2) P(Z_1, Z_2; Z) - f(Z)] \tag{1.20}$$

where the sheet interaction timescale is defined as,

$$\tau_{mix} = \lim_{\Delta t \to 0} \frac{M}{\Delta M_i / \Delta t} \tag{1.21}$$

Note that the $f(I)^2 \Delta Z^2$ term in eq (1.19) disappears if $f(I)$ is non-singular and is correctly incorporated into the double integral if it is singular. Therefore eq (1.20) is a correct continuous representation of the discrete eqs (1.17) and (1.19) for both cases. In Appendix B, we show that this closure term exactly conserves the total probability and the mean as required of any mixing model.

To complete the model, we specify the timescale τ_{mix}, which can be understood as the timescale for all the tracer elements to be stretched into sheets and to experience interactions. As discussed earlier, this timescale is dominated by the time for turbulence to stretch the tracers to the diffusion scale, therefore we expect $\tau_{mix} \simeq \tau$ with τ given by eq (1.8). In this case, as shown in Appendix B, the variance of metallicity fluctuations decays exponentially with timescales of $\sim 3\tau$ or 2τ for the transition functions given by Janicka et al. (1979) and Curl (1963) respectively.

We point out the uncertainty in taking $\tau_{mix} \simeq \tau$ above. This relation should be understood as an order-of magnitude estimate since it is not obvious how the interaction timescale exactly relates to the streching timescale. An uncertainty factor of 2-3 is expected. For example, if we interpretate the stretching timescale τ as the variance decaying timescale, motivated by the excellant agreement of eq (1.8) with the variance decaying timescale obtained in simulations by de Avillez and Mac Low (2002), we need to determine τ_{mix} by deriving a variance equation for eq (1.20) and setting the timescale in the obtained equation to τ. This is done in Appendix B where we find the timescales in the variance equations are $3\tau_{mix}$ and $2\tau_{mix}$, respectively, for Janicka et al's and Curl's nodels. Therefore setting them to be τ, we have $\tau_{mix} = \frac{\tau}{3}$ and $\tau_{mix} = \frac{\tau}{2}$ and for the two models. This means that τ_{mix} could be smaller than τ by a factor of $2 - 3$. We expect that the smallest possible value for τ_{mix} is $\tau/3 \simeq 25$ Myr.

Finally we point out the interactions in the metallicity space represented by the transition function in this model are nonlocal. Pope (2000) claimed that models with nonlocal interactions in the metallicity space give unphysical results based on studies of turbulent combustion flows. We agree that, in reality, interations due to microscopic diffusivity should be local. To recognize this fact is very important for combustion flows, where flames separate the ash and fuel regions. Models with nonlocal interactions may give instantaneous mixing between ash and fuel, which is prohibited by flames and thus may cause unphysical results. Howerer, modeling a nonreactive passive scalar where a fast mixing between neighboring structures is not prohibited is quite different. A nonlocal model for interactions between tracer sheets with different metallicities is justified for passive scalars by the fact that the tracer exchange between neighboring sheets occurs with a very small timescale compared to the timescale at the integral length scale.

Primordial fraction. The fraction of primordial gas, which controls the formation of POP III stars, as a function of time in a galaxy has important effects on chemical and dynamical evolution. Here we study how mixing affects the primordial fraction in the model developed above. We define the primordial fraction as

$$P = \lim_{\epsilon \to 0} \int_0^{\epsilon} f(Z) dZ \tag{1.22}$$

which is nonzero when $f(Z)$ is singular at $Z = 0$, e.g., $f(Z) = \delta(Z)$ at $t = 0$ assuming galaxies start with entirely primordial gas. An equation of P can be derived exactly from eq (1.20). Here we derive it from the discrete form, i.e., eqs (1.17) and (1.19), since it is physically more transparent. An outline for the derivation directly and exactly from eq (1.20) is given below.

In the discrete form, the primordial fraction is given by,

$$P = \lim_{\Delta Z \to 0} f(0)\Delta Z \tag{1.23}$$

Setting $I = 0$ in eq (1.17) gives

$$\Delta_{+}P = f(0)\Delta Z f(0)\Delta Z P(0,0,0)\Delta Z \tag{1.24}$$

where we have neglected interactions between sheets with **finite** metallicities and unpolluted primordial sheets because any such interaction gives an infinitesimal contribution to the primordial bin as the bin size approaches zero if $P(0, Z_2; Z)$ is not singular at $Z = 0$ for any finite Z_2, which we assume to be the case (this is true for models both by Janicka et al. and and by Curl). In other words, primordial sheets are destroyed once they interact with any sheet with finite metallicities. From the normalization eq (1.14) of the transition function, $P(0, 0, 0)\Delta Z = 2$ and we have,

$$\Delta_+ P = \frac{1}{\tau_{mix}}(2f(0)^2 \Delta Z^2) \tag{1.25}$$

Eq (1.19) at $I = 0$ gives,

$$\Delta_- P = \frac{1}{\tau_{mix}}(f(0)\Delta Z + f(0)^2 \Delta Z^2) \tag{1.26}$$

Subtracting $\Delta_- P$ from $\Delta_+ P$ and taking the limit $\Delta Z \to 0$ and $\Delta t \to 0$, we obtain

$$\frac{dP}{dt} = -\frac{1}{\tau_{mix}} P(1 - P) \tag{1.27}$$

The equation is exact for any transition function $P(Z_1, Z_2; Z)$ as long as it is non-singular at $Z = Z_1$ for $Z_2 \neq Z_1$. This has been confirmed numerically for the two special transition functions by Janicka et al. and by Curl.

Equation (1.27) has a simple physical explanation: the primordial fraction decreases whenever fluid elements containing primordial gas, with mass fraction P, and all gas that has been polluted by sources or previous mixing events, with mass fraction $1 - P$, are stretched sufficiently to interact with each other, which occur with a frequency of τ_{mix}^{-1}.

We outline the mathematical derivation of the equation for P from eq (1.20). Integrating eq (1.20) from $Z = 0$ to ϵ and taking the limit $\epsilon \to 0$ gives,

$$\frac{dP}{dt} = \frac{1}{\tau_{mix}}(\lim_{\epsilon \to 0} \int_0^{\epsilon} dZ \int_0^{Z} dZ_1 f(Z_1) \int_Z^{Z_u} dZ_2 f(Z_2) P(Z_1, Z_2; Z) - P) \tag{1.28}$$

As the integral range for Z approaches 0, the contribution to the triple integral is only from the infinitesimal range $Z_1 \in (Z, Z^-)$ and $Z_2 \in (Z, Z^+)$, i.e., Z_1 and

Z_2 in the infinitesimal vicinity of Z, where $P(Z_1, Z_2; Z) \rightarrow 2\delta(Z - (Z_1 + Z_2)/2)$ is singular. For ranges of Z_1 and Z_2 not in the vicinity of Z, $P(Z_1, Z_2; Z)$ is nonsingular as assumed. In this case, integrations over those ranges of Z_1 and Z_2 give a nonsingular function of Z and then the integration of this nonsingular function in the infinitesimal range $(0, \epsilon)$ gives 0. As $\epsilon \rightarrow 0$, Z approaches 0, thus in the limit, $f(Z_1)$ and $f(Z_2)$ are singular in the vicinity of Z: $f(Z_1) \rightarrow P\delta(Z_1 - Z)$ and $f(Z_2) \rightarrow P\delta(Z_2 - Z)$ with P being the primordial fraction. We therefore have 3 delta functions in the triple integral,

$$\frac{dP}{dt} = \frac{1}{\tau_{mix}}(\lim_{\epsilon \rightarrow 0} \int\limits_0^\epsilon dZ \int\limits_{Z^-}^{Z} dZ_1 P\delta(Z_1 - Z) \int\limits_{Z}^{Z^+} dZ_2 P\delta(Z_2 - Z) 2\delta(Z - \frac{Z_1 + Z_2}{2}) - P) \tag{1.29}$$

Using the properties of delta functions that $\int\limits_0^Z \delta(Z' - Z)dZ' = 1/2$ and $\delta(Z/2) = 2\delta(Z)$, we can perform this integral and rigorously prove eq (1.27).

1.3.3 The source term

The source term can be derived by directly considering how various sources affect the metallicity distribution. Given the metallicity distribution $f(Z, t)$ at time t, we calculate the metallicity distribution at time $t + dt$ as if it had only been affected by sources during dt. We will denote this function as $f_{src}(Z, t + dt)$. The source term is then given by

$$(\frac{\partial f}{\partial t})_{src} = \lim_{dt \rightarrow 0} \frac{f_{src}(Z, t + dt) - f(Z, t)}{dt} \tag{1.30}$$

We start the derivation with the mass change $dM_{src}(Z, t)$ of gas with metallicity Z caused only by sources in dt. By definition, $dM_{src}(Z, t) = M_g(t + dt) f_{src}(Z, t + dt) - M_g(t) f(Z, t)$ with $M_g(t)$ being the gas mass at time t in the Galaxy. Considering the effects of incorporation of gas and metals into stars, SN ejecta, stellar winds, infall and outflow gas (if present), $dM_{src}(Z, t)$ can be formally written as

$$\begin{aligned} dM_{src}(Z, t) &= -B(t) f_s(Z, t)dt + e(t) f_{ej}(Z, t)dt + W(t) f_w(Z, t)dt \\ &\quad + I(t) f_I(Z, t)dt - E(t) f_E(Z, t)dt \end{aligned} \tag{1.31}$$

where $B(t)$, $e(t)$, $W(t)$, $I(t)$ and $E(t)$ are, respectively, the rate of gas incorporated into stars (the star formation rate), the mass return rate from SN ejecta, the mass return rate from winds, the accretion rate of the infall gas and the rate at which the ISM gas is expelled to the intergalactic medium, and f_s, f_{ej}, f_w, f_I and f_E are the metallicity distributions in the corresponding gases. Using mass conservation, $M_g(t+dt) = M_g(t) - B(t)dt + e(t)dt + W(t)dt + I(t)dt - E(t)dt$, and eq (1.31) we obtain a formula for $f_{src}(Z, t+dt)$ expressed in quantities at time t. Inserting it into eq (32), we get the source term,

$$\begin{aligned}(\tfrac{\partial f}{\partial t})_{src} \quad = \quad & -\tfrac{B(t)}{M_g}(f_s(Z,t) - f(Z,t)) + \tfrac{e(t)}{M_g}(f_{ej}(Z,t) - f(Z,t)) + \\ & \tfrac{W(t)}{M_g}(f_w(Z,t) - f(Z,t)) + \tfrac{I(t)}{M_g}(f_I(Z,t) - f(Z,t)) \\ & -\tfrac{E(t)}{M_g}(f_E(Z,t) - f(Z,t))\end{aligned} \tag{1.32}$$

We analyze the terms in eq (1.32) one by one.

The metallicity distribution $f_s(Z,t)$ in gas incorporated into stars is in general determined by the metallicity distribution $f(Z,t)$ in the ISM and the dependence of the star formation efficiency on metallicity. Given that dependence, $f_s(Z,t)$ can be obtained by a conversion from $f(Z,t)$. For simplicity, we will assume that the star formation rate is independent of metallicity in star formation clouds, thus at given time, gas going into stars completely samples the metallicity distribution in the ISM, i.e., $f_s(Z,t) = f(Z,t)$. It follows immediately from eq (1.32) that incorporation of gas and metals into stars gives no direct contribution to the source term in the pdf equation.

The SN ejecta term includes both thermonuclear SNe (SNe Ia) and core-collapse SNe (SNe II, SNe Ib, Ic). We derive formulae for them separately. The gas return rate $e_{cc}(t)$ from core-collapse SN ejecta can be related to the star formation rate using the stellar initial mass function (IMF) $\phi(m)$,

$$e_{cc}(t) = B(t) \int_{m_{SN}}^{m_u} M_{ej}(m)\phi(m)dm \tag{1.33}$$

where m_{SN} and m_u are the mass limit for core-collapse SN explosions and the upper limit of stellar masses, $M_{ej}(m)$ is the ejected mass from a core-collapse SN produced by a progenitor star of mass m. The initial mass function is normalized by mass, $\int_{m_l}^{m_u} m\phi(m)dm = 1$ with m_l being the low limit of stellar masses.

As discussed earlier, while efficient mixing between ejecta with gas swept up in SN shells is unlikely to occur (§1.1), ejected material itself is probably well mixed due to the large diffusivity in the hot cavity (§. 1.2). Therefore the metallicity distribution in the ejecta of a single SN is a delta function. Consider a progenitor star of mass m, which produces a significant mass, $M_Z(m)$, of the element of interest (e.g., oxygen). When it explodes, the abundance distribution of the element in the ejecta is given by $\delta(Z - M_Z(m)/M_{ej}(m))$ We have neglected the mass of the element of interest that has been in the envelope of the star since the star formed. This mass is probably much smaller than $M_Z(m)$. The metal mass M_Z and the ejecta mass M_{ej} as functions of m can be taken from nucleosynthesis calculations. The contribution from this SN to $dM_{src}(Z,t)$ is then $M_{ej}\delta(Z - M_Z/M_{ej})$. Including all the core-collapse SNe exploded during $(t, t+dt)$, we have,

$$e_{cc}(t) f_{ccej}(Z,t) = B(t) \int_{m_{SN}}^{m_u} M_{ej}(m)\delta(Z - \frac{M_Z(m)}{M_{ej}(m)})\phi(m)dm \tag{1.34}$$

We can obtain a function form for f_{ccej}, given the IMF and the nucleosynthesis results for $M_Z(m)$ and $M_{ej}(m)$. For simplicity, we replace the distribution f_{ccej} by a delta function $\delta(Z - Z_s)$ at its mean Z_s in our calculations. This is equivalent to assuming all the core-collapse SN sources are identical. Ignoring the fluctuations due to SN source variations, this approximation gives a narrower distribution $f(Z,t)$ than calculated exactly from eq (1.34).

For an element not considerably produced in core-collapse SNe, its abundance distribution in the ejecta basically samples that in the gas out of which the progenitor stars formed. Since gas going into stars is assumed to sample the abundance distribution in the ISM and the lifetime of massive stars is negligible, we have $f_{ccej}(Z,t) = f(Z,t)$ for this element, implying that the abundance distribution of this element is not affected by SNe cc.

For type Ia SNe, we have to calculate their number rate $\nu_{Ia}(t)$ from a prescription for their progenitors, generally believed to be binary systems with a white dwarf as the main star and a red giant or a main sequence star as the companion. We will adopt the prescription by Kobayashi et al (2000) for our calculations in chapter 4. We are particularly interested in the iron yield by SNeIa. According to Theilemann, Nomoto and Hashimoto (1993), each type Ia SN produces almost the same amount, M_{IaZ}, of iron, independent of the progenitors. Assuming the ejecta mass M_{Iaej} is also identical for each SNIa, the contribution to the source term is simply $\nu_{Ia}(t)M_{Iaej}(\delta(Z - M_{IaZ}/M_{Iaej}) - f(Z,t))$.

The main difference of the term for stellar winds from that for core-collapse SNe is the time delay of stellar winds due to the long lifetimes of low-mass stars. The derivation is otherwise the same. The wind rate is given by,

$$W(t) = \int_{m_l}^{m_{SN}} W(m)B(t - \tau(m))\phi(m)dm \tag{1.35}$$

where $W(m)$ and $\tau(m)$ are, respectively, the wind mass from and the lifetime of a star of mass m. For an element that is significantly produced in low-mass stars (e.g., carbon), we have

$$W(t)f_w(Z,t) = \int_{m_l}^{m_{SN}} M_w(m)\delta(Z - \frac{M_Z(m)}{M_w(m)})B(t - \tau(m))\phi(m)dm \tag{1.36}$$

where $M_Z(m)$ is the mass of the element produced in the wind of a star of mass m. Again we assumed that the wind itself is well mixed and that the mass of the element in the wind that was originally incorporated into the star when it formed can be neglected compared to the newly produced mass $M_Z(m)$.

As in the case of core-collapse SNe, we will assume that stellar winds do not affect the abundance distribution of elements that they do not produce, i.e., $f_w(Z,t) = f(Z,t)$. We point out that this approximation is less well justified than the case for core-collapse SNe due to significant lifetimes of low-mass stars. The abundance distribution of elements not significantly produced in the winds samples the ISM gas long time ago when the stars formed, thus it has a lower mean than that in the ISM at the time of the wind release. The effect of winds in this case is therefore to give a larger low-metallicity tail to $f(Z,t)$ and a larger metallicity variation in the ISM since they are a continuous source of variations. However, our assumption is made reasonable by the fact that, in most chemical evolution models, the gas returned from winds at a given time is mainly from stars formed within less than one billion years ago thus the abundance distribution $f_w(Z,t)$ of this element in the winds is probably not very different from $f(Z,t)$.

The distribution $f_I(Z,t)$ of the infall gas has to be obtained from observations or theoretical models of galaxy formation. Since there is currently no direct observational evidence for the infall gas and no theoretical studies on the infall metallicity distribution available, we simply assume the infall gas is chemically homogeneous with a single-valued metallicity Z_i. Therefore the metallicity distribution in the infall gas is a delta function, $f_I(Z) = \delta(Z - Z_i)$. The infall metallicity could be a function of time. Chemically inhomogeneous infall would result in a broader $f(Z,t)$ than we obtain. For primordial infall gas, $Z_i = 0$ and we have $f_I(Z) = \delta(Z)$.

The metallicity distribution $f_E(Z,t)$ of the outflow gas has also to be prescribed. Although outflow may have important consequences to the metallicity distribution in dwarf and irregular galaxies, throughout the paper we will neglect outflow for the Galaxy, as most Galactic chemical evolution models do.

According to the discussions above, the source term for oxygen, which is mainly produced in core-collapse SNe, is given by,

$$(\frac{\partial f}{\partial t})_{src} = \frac{B}{M_g} \int\limits_{M_{SN}}^{M_u} M_{ej}(m)(\delta(Z - \frac{M_Z(m)}{M_{ej}(m)}) - f(Z,t))\phi(m)dm + \frac{I}{M_g}(\delta(Z - Z_i) - f(Z,t)) \tag{1.37}$$

For iron, we include the contribution from SNe Ia,

$$\begin{aligned}(\tfrac{\partial f}{\partial t})_{src} \;=\; & \tfrac{B}{M_g} \int\limits_{M_{SN}}^{M_u} M_{ej}(m)(\delta(Z - \tfrac{M_Z(m)}{M_{ej}(m)}) - f(Z,t))\phi(m)dm \\ & + \tfrac{\nu_{Ia} M_{Iaej}}{M_g}(\delta(Z - \tfrac{M_{IaZ}}{M_{Iaej}}) - f(Z,t)) \\ & + \tfrac{I}{M_g}(\delta(Z - Z_i) - f(Z,t))\end{aligned} \tag{1.38}$$

If we are interested in the carbon abundance distribution, we need to add the contribution from the winds of low mass stars, which is $\frac{1}{M_g} \int\limits_{m_l}^{m_{SN}} M_w(m)(\delta(Z - \frac{M_Z(m)}{M_w(m)}) - f(Z,t))B(t - \tau(m))\phi(m)dm$. Note that the infall term is a delta function at a small metallicity and the metal source terms are essentially another delta function at a large metallicity. These two different sources therefore continuously force two spikes in the probablility distribution at low and high metallicities.

In these equations, the gas mass, the star formation rate, the infall rate etc will be taken from chemical evolution models. In chapter 3 and 4, we will consider models by Naab & Ostriker (2006), Chiappini et al. (1997), exactly using their infall rates and star formation rates etc.

If a small fraction of gas mass swept up by SN shells can enter the hot ejecta and get mixed with the new metals, as pointed out by Tenorio- Tagle (1996), we need to use the total mass that mixes with the new metals in the derivation above. If the amount of metals contained in the gas to enter the cavity and mix with new metals is much less than M_Z, we only need to replace M_{ej} by the total gas mass to be mixed. Otherwise, we need to include in eq (1.36) the total mass of metals already in the gas before entering the cavity and mixing with the ejecta, as is the case for the sweepup model which we will discuss in §1.4.

1.3.4 The numerical method and a schematic example

In this subsection, we outline our difference scheme to integrate the integro-differential equation for the metallicity probability distribution, especially for the integral kernel in the diffusivity closure term eq (1.20). We adopt a simple difference method, which is first order in both metallicity space and time space. The method is a straightforward implementation of the physical process involved in the kernel as described in §1.3.2.2. In each simulation cell, we subtract the probability loss due to interactions of this cell with other cells and add the probability increase from interactions of two cells, above and below the cell of interest respectively, that result in a metallicity within the cell. Our difference scheme, by design, conserves the total probability and the mean. The numerical solution from this code agrees well with the analytical result of exponential variance decay in the absence of continuous sources derived in Appendix B. We tested the convergence of the code and found that the numerical solution converges for a resolution larger than 200 in the metallicity space and a time step smaller than 0.2 times the timescale τ_{mix}.

We use a simple example to illustrate the schematic behavior of the integral kernel. In the example, we set the initial pdf to be two spikes at $Z = 0$ and $Z = 0.1$. The $Z = 0$ spike corresponds to the metal-free gas in a galaxy at the time when it forms and the $Z = 0.1$ spike is used to represent the metal release from SN or SB ejecta. For simplicity, we do not impose a continuous forcing by SN sources or infall in this illustrating example. The solution behaviour is sketched in Fig 1.2. Mixing erases the two spikes and pushes the probability toward the central region around the average metallicity where a peak forms. With time the heights of the two spikes decrease and the central peak gets narrower. This indicates that the ISM becomes

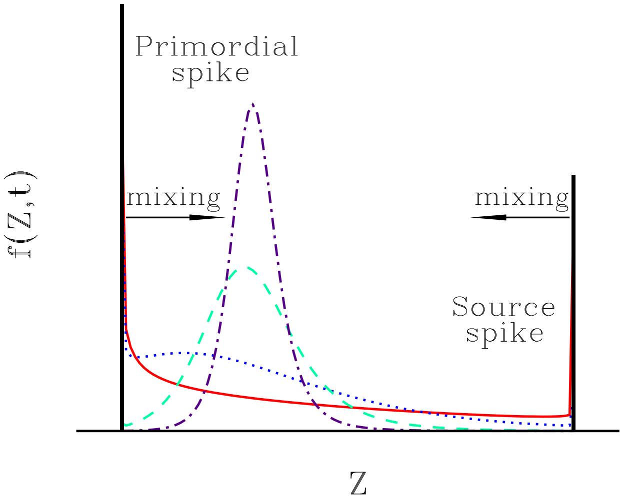

Figure 1.2 Schematic evolution of the metallicity probability distribution

The metallicity probability distribution in the turbulent mixing model we developed for the interstellar medium. The source spike at high metallicity is forced by continuous release of high metallicity gas from SN sources or stellar winds. The primordial spike corresponds to the interstellar gas that has not been polluted by metals. In a closed-box chemical evolution model, this primordial spike, representing the initially primordial gas when the galaxy forms, decays with time due to metal sources and mixing. In chemical evolution models with primordial infall gas, the spike can be maintained by continuous infall. Mixing tends to erase the spikes, push the probability toward the center and form a peak around the average metallicity. In the figure the central peak gets narrower with time (from solid curve to dotted, dashed and dot-dashed), indicating the ISM becomes more and more homogeneous. See §3.4.

more and more homogeneous due to mixing. In this decaying case, the pdf first evolves from a bimodal form to basically trimodal with two spikes and one central peak and finally becomes unimodal when both spikes are erased.

In the forcing case with continuous infall of primordial gas and metal sources, the pdf evolution is similar. However, the pdf does not arrive at a final unimodal state, instead it evolves toward a quasi-steady state where forcing by fresh sources balances mixing. In the steady state, the pdf keeps a trimodal form: the heights of the spikes and the thickness of the central peak achieve finite steady-state values. In a chemical evolution model with preenriched infall, the infall gas forces a spike distinct from the primordial spike. The primordial spike, representing the initial chemical condition in the galaxy, gets destroyed while the infall spike finally arrives at a quasi-steady state. The final trimodal pdf thus consists of a source spike, an infall spike and a central peak.

1.4 The pdf equation for SN sweepup models

We give a pdf formulation for the SN sweepup models mentioned in §1.1. As discussed there, newly produced metals probably cannot mix with ISM gas swept in SN shells. In this section we make assumptions at different levels to obtain the upper limit for maximum mixing efficiency available in SN shells.

We first assume that metals in SN ejecta could catch up with the supersonic shock so that it is possible that newly produced metals can be deposited to the sweepup gas in the SN shells by microscopic diffusivity. However we show that microscopic diffusivity, by itself, cannot mix new metals across the shell thickness by calculating the diffusion timescale. Using the diffusivity formula for an ionized medium given in §1.2, we find the time scale is $50(H/\mathrm{pc})^2(Z_1Z_2)^2(n/10\mathrm{cm}^{-3})(T/10^5\mathrm{K})^{-5/2}$ Gyr where H is the thickness of the shell and Z_1, Z_2, n and T have their standard meanings. At the late stages of SNR evolution, $H \sim 1$ pc (read from figures in Thorton et al. 1998); the temperature in the shell increases from $\sim 10^2$ K in the preshock region to $\sim 10^6$ K behind the shock and we use a generous value of 10^5 K for T; the shell density has a peak of more than 100 cm^{-3} and we take a moderate value $n \sim 10$ cm^{-3} (Thornton et al. 1998). Clearly the diffusion timescale is much larger the SNR lifetime and the molecular diffusivity itself cannot mix across the shell thickness. Since the gas density in the shell $n \sim 1/H$ from mass conservation, the timescale goes linearly with H, thus the thickness has to be less than $\sim 10^{-4}$ pc for diffusivity to mix across the shell in a shell expansion time of ~ 1 Myr. Noting that shell radius is of order 50 pc, much larger than the thickness, considerable mixing in azimuthal directions by the diffusivity itself is impossible. Therefore efficient mixing in shells assumed in previous ICEMs using SN shocks as the catalyzing velocity field relies on the existence of shell instabilities to enhance mixing.

We next assume instabilities do exist in SN shells while keeping in mind that they may be absent at the late stages of the SNR evolution when most of the gas is swept up (Thornton et al. 1998, see §1.1). We show that the assumed instabilities can only efficiently enhance mixing across the shell thickness but not over the entire shell sphere. Instabilities induce turbulent motions that enhance mixing by producing small scale metallicity structures. The mixing process by instabilities can therefore be described by the turbulent model given in §1.3.2. The mixing timescale is mainly determined by the characteristic length scale λ_{in} and velocity scale v_{in} of the instabilities. It is expected that λ_{in} and v_{in} are of the same order as the shell thickness H and the shock speed v_{sh} respectively. Since $\lambda_{in} \sim H$, the timescale for instabilities to mix across the shell would be the time for instabilities to stretch the metallicity field from scale H to the scale at which diffusivity can operate fast, which can be calculated using eq (1.8). Inserting the thickness H for L_s and the rms velocity v_{in} due to instabilities for U in eq (1.8), we obtain a time scale of several 10^5 yrs if $v_{in} \sim v_{sh}$ is several tens of km/s at the late stage shell evolution. Therefore instabilities, if they exist, can give fast mixing in the radial direction.

The mixing time in the azimuthal directions, on the other hand, is very different from the stretching timescale estimated above because the shell radius is much larger than the instability length scale. The timescale mainly depends on the tangential transport of gas parcels by instabilities to bring the gas in different directions on the shell sphere into contact. As discussed in §1.3.1, during the transport, small scale structures are created, enhancing mixing between parcels brought into contact. We estimate the distance over which instability-induced motions can transport during the lifetime of a SNR and calculate the corresponding solid angle $\Delta\Omega$ it extends around a direction Ω. The transport is diffusive over distance much larger than the characteristic length scale of the instabilities and the transport rate can therefore be approximated by an effective diffusivity $D_{sh} = v_{in}\lambda_{in}$ (see §1.3.1). Then the tangential transport distance on the shell during the expansion time τ_{SNR} of a SNR is given by $(\lambda_{in} v_{in} \tau_{SNR})^{1/2} \lesssim (H v_{sh} \tau_{SNR})^{1/2} \sim (HR)^{1/2}$ where $R \sim v_{sh}\tau_{SNR}$ is the stall radius of the SNR. We assumed a planar geometry in this estimate, which is justified by the resulting distance $(HR)^{1/2}$ being much smaller than the shell radius R. The solid angle corresponding to the distance $(HR)^{1/2}$ is $\sim HR/R^2 = H/R$. Clearly we have $\Delta\Omega \lesssim H/R \ll 1$. This proves that only gas within a small solid angle can be mixed by shell instabilities, i.e., a perfect azimuthal mixing does not occur in reality even if instabilities exist, as pointed out in the introduction. In the rest of this section, we will adopt the picture for the SN sweepup model: instabilities can help mix across the shell thickness but essentially do not give rise to considerable azimuthal mixing.

We consider the metallicity probability distribution in the gas to be swept up by a SN shock and evaluate the change in the distribution caused by mixing of new metals from the ejecta with the shell primarily in the radial direction. The metallicity distribution in the gas to be swept up measures the chemical variations of the ISM gas within the stall radius of a SN. The amplitude of the variations depends on how this radius compares with the characteristic length scale of the overall abundance fluctuations in the ISM. The stall radius R of a SNR is typically ~ 50 pc, so the length scale of the ISM gas to be incorporated into a shell is about 100 pc. The length scale of local abundance variations, expected to be approximately the scale height of the thin disk, is also about 100 pc. The coincidence of the two length scales suggests that the gas to be swept up by a SN shock probably has metallicity variations that sample the distribution $f(Z,t)$ in the ISM. We will assume the metallicity distribution in the gas to be swept up by any SN shock is equal to $f(Z,t)$.

New metals from a SN are deposited into the sweep-up gas through radial mixing by instabilities. In the mean time, azimuthal inhomogeneities exist on scales larger than the angle size $\Delta\Omega$, over which instabilities cannot help mix. We split the shell into $4\pi/\Delta\Omega$ well-mixed parts, each of which extends a small solid angle $\Delta\Omega$. The metals in each shell part are from two sources: the new metals released by the SN and metals existing in the ISM gas before being swept into the part of the shell. Since the ejecta is probably well mixed early in the SNR evolution (see §2), we assume that the new metals are isotropically spread into the parts, giving the same amount of increase in metallicity, $M_Z/(M_{sw} + M_{ej}) \approx M_Z/M_{sw}$, in each part where $M_{sw} \gg M_{ej}$ is the total gas mass swept into the shell. We will refer to M_{sw} as the sweepup mass. The metallicity in a shell part corresponding to a solid angle $\Delta\Omega$ then becomes $M_Z/M_{sw} + Z_{\Delta\Omega}$, where $Z_{\Delta\Omega}$ is the average metallicity of the ISM gas in the solid angle prior to being swept into the shell part. The average here is due to radial mixing and azimuthal mixing within the solid angle. When the shell stalls, the metallicity distribution in the swept-up gas is then determined by the distribution $f_{\Delta\Omega}$ of $Z_{\Delta\Omega}$ over all the parts of size $\Delta\Omega$ in different directions. Namely, it is given by an upshift of $f_{\Delta\Omega}$ by M_Z/M_{sw}, i.e., $f_{\Delta\Omega}(Z - M_Z/M_{sw}, t)$.

The distribution $f_{\Delta\Omega}$ depends on the metallicity distribution in the pre-sweepup gas, which was assumed to sample $f(Z,t)$, and the spatial metallicity fluctuations in a solid angle $\Delta\Omega$, which are to be erased by mixing. Since spatial structures in a solid angle cannot be explicitly included in our 1-point pdf formulation, $f(\Delta\Omega)$ cannot be exactly specified. We consider two extreme limits for $f_{\Delta\Omega}$ and the actual distribution is between the limits. In the first limit, we assume that there are no metallicity fluctuations in the gas within each solid angle to be swept by a SN shell. In this case, the metallicity in each solid angle is single-valued and the distribution over all the angles is equal to $f(Z,t)$. Therefore $f_{\Delta\Omega} = f(Z,t)$. No averaging effect exists. Mixing is not needed to homogenize the gas to be swept up into each shell part; the effect of mixing is just for new metals to upshift the metallicity in each part. We find, by numerically integrating the pdf equation derived below, that the model in this limit is equivalent to the models using the overlap argument (Edmunds 1975, Oey 2000, and also White and Audouze 1983). Therefore our discussion above provides a physical picture implicitly asssumed in these overlap models. Clearly, from the various assumptions leading to this model, it is unlikely the conditions under which the overlap formulation can give valid results are met in reality. The other extreme limit is that the gas within any solid angle $\Delta\Omega$ samples the entire distribution $f(Z,t)$ so that the average metallicity $Z_{\Delta\Omega}$ in every solid angle is the same and equal to $\int Z f(Z,t) dZ = \langle Z \rangle$. In this case, $f_{\Delta\Omega} = \delta(Z - \langle Z \rangle)$. This is equivalent to assuming perfect mixing in all the sweepup gas. It gives an upper limit for the fastest mixing available in the sweepup model, which is unlikely to occur.

We point out both limits are not realistic. For the first limit, fluctuations in each solid angle do exist since gas in each shell part is swept over a distance of 50 pc, comparable to the characteristic scale for inhomogeneities in the ISM. For the second limit, due to large scale fluctuations in the ISM, the metallicity averaged in each solid angle is expected to vary with directions. Therefore the form for $f_{\Delta\Omega}$ is between the two limits. Finally, considering that the conditions for significant mixing in shells may not be satisfied at all in reality, even the first limit should probably be taken as an upper limit for mixing efficiency in SN shells.

The pdf equation for the sweep-up model can be derived in the same way as for the source term in §1.3.3 assuming that the SN sweeping and mixing process is instantaneous. The assumption is justified by the fact that the SNR evolution timescale $\tau_{SNR} \sim 1$ Myr is negligible in comparison with the chemical evolution timescale. With the same analysis as in §1.3.3, we find that for the pdf equation of the sweep-up model, we just need to replace M_{ej} by the total mass $M_{sw} + M_{ej}$ and the source delta functions in eq (39) by the metallicity pdf $f_{\Delta\Omega}(Z - M_Z/M_{sw})$ in the swept-up gas enriched by the new metals. In the first limit discussed above, $f_{\Delta\Omega} = f(Z, t)$, we have a pdf equation for the oxygen abundance,

$$\begin{aligned} \frac{df(Z,t)}{dt} &= \frac{B}{M_g} \int_{m_{SN}}^{m_u} M_{sw}(f(Z - \frac{M_Z(m)}{M_{sw}}, t) - f(Z,t))\phi(m)dm \\ &+ \frac{I}{M_g}(f_I(Z) - f(Z,t))dt \end{aligned} \tag{1.39}$$

where the effects of stellar winds and the outflow are neglected. We assumed the sweepup mass is the same for each SN. See appendix C for a treatment to account for variations in sweepup mass by SNe. An implicit assumption in the equation is the independence of the SN explosions when including multiple sources, which ensures that the metallicity distribution in the gas to be swept up by every SN samples $f(Z, t)$. This is not true for the case with SN clustering. In that case a SN shell tends to sweep up gas that has just been enriched by a previous SN event, i.e., the sweepup gas by a new SN shock tends to sample the high metallicity tail of $f(Z, t)$ instead of the entire $f(Z, t)$. Strong clustering of SNe, i.e., SBs, are studied in Appendix C. We find that the presence of SBs do not considerably affect the formulation and results. Here we neglect the case with intermediate degree of clustering and just point out it would give a broader metallicity distribution due to the accumulation of high metallicity tails.

The meaning of the infall terms is as follows. The infall gas enters the Galactic disk with a metallicity distribution $f_I(Z, t)$ and becomes part of the disk gas M_g. It keeps the original distribution until swept up by a SN shell, i.e., incorporated into the sweep-up mass M_{sw} and gets enriched through the first two terms in eq (1.39). We do not introduce any arbitrary mixing (e.g., White and Audouze 1983) for the infall gas before it participates in a sweep-up event.

We find that eq (1.39) gives same results as Oey (2000) for a chemical evolution model without infall and as White and Audouze (1983) for infall models without artifically adding extra mixing for the infall gas.

Including the contribution from SNe Ia for iron, we have,

$$\begin{aligned} \tfrac{df(Z,t)}{dt} &= \tfrac{\nu_{Ia} M_{sw}}{M_g}(f(Z - \tfrac{M_{ZIa}}{M_{sw}}, t) - f(Z,t)) \\ &+ \tfrac{B}{M_g}\int\limits_{m_{SN}}^{m_u} M_{sw}(f(Z - \tfrac{M_Z(m)}{M_{sw}}, t) - f(Z,t))\phi(m)dm \\ &+ \tfrac{I}{M_g}(f_I(Z) - f(Z,t))dt \end{aligned} \tag{1.40}$$

where we again assumed that each type Ia SN releases the same amount of iron, M_{ZIa}.

If all the gas swept up in a shell is perfectly mixed (equivalent to the second extreme limit above; both unlikely), the swept-up gas has a unique metallicity and $f(Z - M_Z/M_{sw}, t)$ in eqs (1.39) and (1.40) is replaced by a delta function $\delta(Z - \langle Z \rangle - M_Z/M_{sw})$.

The equation for the fraction of primordial gas in this model can be easily derived. Integrating eq (7) from $Z = 0$ to ϵ and taking the limit $\epsilon \to 0$ gives,

$$\frac{dP}{dt} = \frac{(\nu_{cc} + \nu_{Ia})M_{sw}}{M_g}P + \frac{I}{M_g}(1 - P) \tag{1.41}$$

where we have assumed that the infall gas is primordial, i.e., $f_I(Z) = \delta(Z)$. For non-primordial infall, the last term becomes $-\frac{I}{M_g}P$. Note that this equation applies to any function form for $f_{\Delta\Omega}$.

Clearly, the mixing efficiency in the sweepup model is determined by the the gas mass M_{sw} swept up by a SN or SB event. We give a detailed derivation for M_{sw} in Appdendix C where we consider both isolated SNe or superbubbles. For isolated SNe, we obtain the sweepup mass from the dynamical calculations of the SNR evolution (e.g., Cioffi and Schull 1991, Thornton et al. 1998) taking into account the effect of magnetic fields (Hanyana and Tomita 2006) and the density fluctuations of the interstellar gas. We find that the sweepup mass per isolated SN is about $9000 M_\odot$. For SBs, we derive the sweepup mass as a function of the number

N of SNe powering the bubble by following the expansion history of SBs under the effects of the scale height of the galactic disk, the radiative cooling and the magnetic fields. We integrate the function over the empirical distribution of N to calculate the average sweepup mass per SN in SBs. Allowing for uncertainties, we obtained a range from $5000M_\odot$ to $20000M_\odot$ for this average sweepup mass per SN. Assuming that 70% of SNe explode in clusters as SBs and 30% are from runaway stars in the field, we adopt a range from $6000-16000M_\odot$ for the sweepup mass per SN averaged over both isolated SNe and SBs.

Chapter 2

Mixing of primordial gas in Lyman Break Galaxies

Chapter Synopsis: This chapter is a direct application of the approach developed in chapter 1 to investigate the fraction of primordial gas in high redshift galaxies, which controls the formation of primordial stars. The study was motivated by a recent interpretation of ultraviolet properties of $z \sim 3$ objects, mainly high-SFR Lyman break galaxies (LBG), as due to an intermediate fraction of primodial stars by Jimenez and Haiman(2006). A primordial fraction different from 1 or 0 requires microscopic diffusion catalyzed by a velocity field with timescale comparable to the duration of star formation. We find that in LBGs the turbulence-enhanced mixing induced by exponential stretching of metal-rich ejecta, formulated in chapter 1, satisfies this requirement without fine-tuning. The time-dependence of the primordial fraction in this model is calculated. On the other hand, efficient mixing in supernova (SN) shells, assumed in SN sweepup models, erases the primordial gas in only one percent of the star formation duration in LBGs and hence is much too fast. We show that conclusions for all the models discussed here are virtually independent of the IMF, including extremely top-heavy IMFs.

2.1 Introduction

Galaxies begin their lives with entirely primordial gas. As they age, metal production and mixing reduce the primordial gas fraction. We explore the predicted time dependence of the primordial fraction for various types of mixing and chemical evolution processes using the kinetic equations for the abundance probability distribution function developed in Chapter 1. In particular, we address the question of whether any models for mixing and chemical evolution predict that this transformation occurs at an accessible redshift.

Jimenez and Haiman (2006) (hereafter JH) showed that several UV properties of a variety of objects, mostly Lyman break galaxies (LBGs), at redshift $z \sim 3$, can all be understood if these objects contain a substantial fraction, about 10 to 50 percent, of massive stars with essentially zero metallicity ($Z \lesssim 10^{-5}\ Z_{\odot}$; we use Z and metallicity indiscriminantly here). These UV properties cannot all together be explained by a top-heavy IMF, and essentially require $Z = 0$ stars while with a considerable fraction of primordial stars a top-heavy IMF is not required. Massive stars have short lifetimes, so their metal abundances reflect that of the concomitant gas. Therefore if JH are correct, a substantial fraction of the interstellar medium of these galaxies, with star formation ages a few hundred million years, has not been polluted by any products of nucleosynthesis[1].

Motivated by JH and other suggestions for the existence of $Z = 0$ stars (Malhotra and Rhoads 2002; Shimasaku et al. 2006) at accessible redshifts, and the fact that during some early period in the lives of *all* galaxies a transformation from primordial to non-primordial must occur, leaving spectrophotometric signatures (JH; see Schaerer 2003), we examine a number of models for this transformation in Lyman break galaxies.

In §2.2, we review the properties of LBGs and point out that SN sources alone cannot signicantly reduce the primordial fraction below 1 and mixing by diffusivity is required. In §2.3. We consider several models with catalyzed diffusivity by several velocity fields especially, the ISM turblence and the instabilities in SN shells studied in Chapter 1. Our results are discussed in §2.4.

2.2 Lyman Break Galaxies at z ~ 3

2.2.1 Star formation age, star formation rate and the gas mass

We consider the important properties in LBGs associated with their chemical status. The most important quantity to determine the primordial fraction is the star formation (SF) age or duration, the time since SF began. This is the time during which the interstellar gas is exposed to pollution and mixing by stellar nycleosythesis products. The existence of a primordial gas fraction $P(t)$ that is not nearly unity or zero, i.e., both $P(t)$ and $1-P(t)$ are significantly larger than zero, a condition we refer to as a "significant" or "intermediate" primordial fraction, requires a mixing or depletion process with a characteristic timescale comparable to the star formation (SF) age. If the mixing timescale is much smaller, $P(t)$ will be nearly zero; if it is much larger, $P(t)$ will remain near unity. SF ages for LBGs and likely-related objects at somewhat different redshifts have been estimated by Papovich et al. (2001), Shapley et al. (2001), Erb et al. (2006) and others, using galaxy evolution models

---

[1] The existence of $Z = 0$ gas requires an IMF deficient in stars with $M \lesssim 1\ M_\odot$. Otherwise the number of low- mass stars observable today with $Z = 0$ would be large, contradicting observational limits on the star fraction with very small Z (see Oey 2003) by several orders of magnitude. We discuss the effects of different IMFs below. We show that all our conclusions are independent of the IMF.

that assume an exponentially decreasing SFR that began at some time in the past. Although there is much variation, median SF ages are 3×10^8 yr.

The SF ages for the LBGs cannot be significantly different for a number of reasons. The lookback times of about 11.5 Gyr for z=3 imply a strict upper limit to the SF age of 2 Gyr, and a more likely upper limit of 1.5 Gyr (corresponding to $z \sim 8$). The irregular morphologies of the LBGs (Giavalisco 2002) suggest that LBGs are in the process of formation, accumulating large fragments of gas and stars through mergers (Conselice 2006), and probably undergoing one of their first major bursts of SF; starburst populations have durations, estimated from statistics (Kennicutt et al. 1987; Nikolic et al. 85), modeling of integrated light features (Marcillac et al. 2006), and theoretical arguments (Leitherer 2001), that are similar to the estimates in LBGs. Finally, ages much greater than 3×10^8 yr would produce greater metallicity than observed (Giavalisco 2002).

We assume star formation has been a continuous function of time. If instead the SFR preceding or during the present episode consists of bursts of shorter duration, most of our arguments remain unchanged if the SF age is replaced by the accumulated duration of SF (see below).

We next consider the star formation rate in LBGs, which determines the rate at which newly produced metals are deposited into the interstellar gas. A large range of SF rates exists in LBGs at z $\sim$ 3. For example, SF rates derived from the UV luminosity vary from 10 to 10^3 $M_\odot$/yr (Giavalisco 2002). We will adopt a median SFR of $100 M_\odot$/yr. Note that these SF rates are calculated assuming a Salpeter IMF with a low mass limit of 0.1 $M_\odot$. To be consistent with the SFR adopted, we will also mainly use a Salpeter IMF in our calculations (other shapes of IMFs proposed for normal stars in the Galaxy will also be discussed). However, since the question of interest here is about the formation of primordial stars, which are currently thought to have an IMF with lower mass cutoff larger than that for normal stars forming today, a careful consideration of IMFs with different lower mass limits on the derived SF rates is particularly important.

There are two nonstandard IMFs which are especially important. First, intermediate primordial fractions require that the IMF lower limit $M_l \gtrsim 1$ $M_\odot$ to avoid too many $Z = 0$ stars observable today. Such a cutoff increases the empirically derived SFRs, based on integrated light from massive stars corrected for the rest of the IMF. For example, the SFR would increase by a factor of 1.7 if the low mass cutoff is at 1 $M_\odot$ instead of at 0.1 $M_\odot$ for a Salpeter IMF. However, this change in the cutoff mass does not affect chemical evolution in the LBGs because the (massive) stars responsible for the observed UV luminosity or other SF indicators are exactly those that release heavy elements. The star formation history in these galaxies is so short that the metal contamination from low mass stars or thermonuclear SNe (Type Ia) is negligible (thus we will use "SN" or "SNe" to denote only core-collapse SNe without including Type Ia in this chapter). With a larger lower mass limit, the number of core-collapse SNe or the ejected mass per unit mass of stars formed increases. This increase exactly compensates the decreases in the SFR. This means that the rate of SNe or the metal release, which can be essentially obtained by a direct conversion from the UV observed flux, is independent from the assumed lower mass limit of the IMF. This IMF-independence of τ_{src} holds for any cutoff smaller than the lower mass limit for SNe, $\sim 8\ M_\odot$. Therefore we will not discuss this type of IMF in the following calculations since it does not change our conclusions.

Second, a perennially popular IMF for $Z = 0$ star formation consists of only very massive stars (VMS) due to the Jeans mass resulting from H_2 cooling (Hutchins 1976; see Bromm and Larson 2004) although it has been questioned on a number of grounds (Silk and Langer 2006). Comparing $H\alpha$ emission per unit SFR for a VMS IMF (50-500) $M_\odot$ of $Z = 0$ stars in Schaerer (2003) with the same quantity for a (0.1-100) $M_\odot$ IMF in Kennicutt (1998), both for a Salpeter IMF (for illustration only), the SFR for a VMS IMF is 26 times smaller. We will address the effect of a VMS IMF on every calculation below.

Finally we need the total mass of gas in the interstellar medium, i.e., the amount of gas to be polluted by metal sources. This is the most uncertain quantity in our calculations because it cannot be directly measured by observations. We take the total gas mass M_g to be $5 \times 10^{10}\ M_\odot$, extrapolated from gas masses estimated in the $z \sim 2$ UV-selected sample of Erb et al. (2006). An uncertainty of a factor of a few exists in this estimate and will be discussed whenever it might affect our results.

2.2.2 Depletion of the Primordial Fraction by Sources

The JH result of 10-50% primordial gas at $z \sim 3$ seems surprising, but actually galaxies are expected to remain almost completely primordial for billions of years if microscopic diffusivity is neglected. This can be understood from the evolution of the metallicity probability distribution in the metallicity space in the absence of mixing. The reader is referred to the primordial spike and the source spike in Fig 1.1 for an illustration (ignoring for now the curves representing the turbulence-enhanced mixing that fills up the space between the two spikes). SN metal production slowly depletes primordial gas by transferring it from a $Z = 0$ delta function in the metallicity distribution to another delta function at a much larger Z, the source metallicity Z_s averaged over the IMF (~ 0.1 assuming the hot ejecta are well mixed, see below). Intermediate values of Z cannot be reached without mixing by diffusivity .

This suggests the simplest explanation for an intermediate primordial fraction in LBGs: 50 to 90% of the primordial gas passed through stars that became SN ejecta. We call the timescale for this process the source timescale, $\tau_{src} = M_g/BR_{SN}$, where B is the star formation rate and R_{SN} is the returned fraction from core-collapse SNe averaged over the IMF. As discussed in §2.1, we take the total gas mass $M_{gas} \simeq 5 \times 10^{10}\ M_\odot$ and adopt a median SFR of 100 $M_\odot$/yr for the case with the IMF lower limit $M_l = 0.1$ (Papovich et al. 2001, Shapley et al. 2001, Giavalisco 2002, Erb 2006, Yan et al 2006). For this M_l, we calculate $R_{SN} \approx 0.1$ for both the Salpeter IMF and an IMF with slope indices of -0.4 and -1.7 below and above 1 $M_\odot$ respectively (which we will call a (-0.4, -1.7) IMF), using the ejected masses given in Woosley & Weaver (1995), Meynet & Maeder (2002) and Nomoto et al. (2006). We find that R_{SN} has little dependence on metallicity, including $Z = 0$, and there is only 20-30% variation between studies. Variations in the form of the IMF change the SFR by ∼50%, with only a slight effect on R_{SN}. The source timescale is then $\tau_{src} = 5$ Gyr, much larger than the star formation age in LBGs. Even considering the combined uncertainty in the SFR and the gas mass M_g that may decrease the τ_{src} by a factor of, say, 5, the sources alone are still too slow to decrease the primordial fraction below 70%. Thus the simplest assumption does not work.

We derive the source timescale τ_{src} for a VMS IMF. For this IMF, we obtained a SFR smaller than from a nomal Salpeter IMF by a factor of 26 (§2.2). Here we estimate the returned fraction from SNe II for this IMF. Assuming only stars in the range 130-260 $M_\odot$ explode as pair instability SNe (Wooley et al. 2002), we find $R_{SN} = 0.27$, a few times larger than for a normal IMF. Combining the two factors, we have $\tau_{src} = 50$ Gyr, an order of magnitude larger than the normal IMF case. This result strengthens our conclusion that the formation of massive stars is far too slow to deplete primordial gas significantly in the available time.

2.3 Depletion of Primordial Gas by Mixing

As shown in §2.2.2, without a process to spread metals into the "gap" between the Z_s peak and the primordial $Z = 0$ peak, $P(t)$ would remain near unity for billions of years. The only physical process that can fill this gap is microscopic diffusivity (Chapter 1). However, using the average molecular diffusivity in the neutral ISM obtained in §1.2 (see also Oey 2003) for the rate at which the random sources could pollute primordial gas in LBGs, we find that the fraction of the interstellar mass mixed in time t is only $\sim 10^{-5}(t/0.5 \text{ Gyr})^{5/2}$. Therefore diffusivity by itself cannot pollute more than a tiny fraction of the primordial gas over the estimated SF ages. This is consistent with the estimate of the mixing timescale by diffusivity alone in §1.2. To reduce the primordial fraction, a velocity field is required to catalyze the microscopic diffusivity. We consider several catalyzing velocity fields.

2.3.1 Turbulence-Enhanced Mixing

We apply the approach developed in §1.3 for turbulent mixing in the ISM to LBGs. Since we are interested in the integrated primordial fraction (only global quantities in these distant objects are observable due to lack of spatial resolution), the advection term in the pdf equation (1.2) vanishes and has no effect (§1.2). Because of the short star formation history, we consider only core-collapse SN sources. We neglect outflow and infall in these galaxies, whose effects will be discussed later. From eqs (1.20) and (1.34), the metallicity distribution function is then given by,

$$\begin{aligned} \frac{\partial f(Z)}{\partial t} = & \frac{1}{\tau_{mix}}\Big(\int_0^Z dZ_1 f(Z_1) \int_Z^{Z_s} dZ_2 \frac{2}{Z_2 - Z_1} f(Z_2) - f(Z)\Big) \\ & - \frac{\nu_{SN} M_{ej}}{M_{gas}} f(Z,t) + \frac{\nu_{SN} M_{ej}}{M_{gas}} \delta(Z - Z_s) \end{aligned} \tag{2.1}$$

where we assumed all SN sources are identical with ejecta mass of M_{ej} and metallicity in the ejecta $Z_s = M_Z/M_{ej}$. We take M_{ej} and Z_s to be the average over the assumed IMF using nucleosynthesis results mentioned earlier. This assumption about the metallicity of sources, which is far away from the primordial spike in the metallicity space, does not affect the predicted primodial fraction at all. The core-collapse

SN rate ν_{SN} (denoted as ν_{cc} in Chapter 1) is converted from the SFR, the IMF and the mass limit for core-collapse SNe. We have $\nu_S N M_{ej}/M_{gas} = 1/\tau_{src} = 0.2$ Gyr^{-1} for an IMF with lower mass limit less than the SN mass limit, $\sim 8\ M_\odot$. The timescale τ_{mix} has a standard value of 75 Myr with an uncertainty of a factor of ~ 3.

With these parameters, we solved eq (2.1) numerically with the initial condition $f(Z,0) = \delta(Z)$, representing an entirely primordial galaxy at $t = 0$. The result is shown in Fig. 2.1. The curves show the metallicity probability distribution at different times as labelled. As expected, turbulent mixing erases the primordial and the source spikes and pushes the distribution toward the central region. The decrease in the height of the primordial spike can be more clearly seen in the inset where the cumulative probability with metallicity smaller than Z is plotted. The cumulative probability at $Z = 0$ represents the fraction of gas not yet polluted by metal sources. We see that, for the parameters chosen, the primordial fraction at the star formation age of 0.3 Gyr is about 60%, consistent with the result by JH.

As shown in Chapter 1, an equation for the primordial fraction can be derived from the equation of the metallicity distribution function. Therefore it is not necessary to solve the integro-differention equation numerically for the primordial fraction; instead it can be obtained directly from its own equation. The equation for the primodial fraction corresponding to eq (2.1) is

$$\frac{dP}{dt} = -\frac{1}{\tau_{mix}} P(1-P) - P/\tau_{src} \tag{2.2}$$

which is solved by,

$$P = (1 + (\tau_{mix}/\tau_{src}) exp(t/\tau_{mix}))^{-1} \tag{2.3}$$

where we have used the fact that $\tau_{mix} \ll \tau_{src}$.

From the solution, the primordial fraction P decreases exponentially on a timescale τ_{mix} after a delay time $\sim \tau_{mix}\ ln(\tau_{src}/\tau_{mix})$, which is $\sim 3 \times 10^8$ yr for $\tau_{mix} = 75$ Myr and $\tau_{src} = 5$ Gyr assuming an IMF with $M_l \lesssim 8\ M_\odot$. The delay time is the time for sources to provide enough non-primordial gas to make P depart from unity, but the dependence on τ_{src} is only logarithmic, and so is nearly independent of IMF, even for the extreme case of a VMS IMF where the source timescale is 10 times larger. In that case, the delay time is only 50% larger.

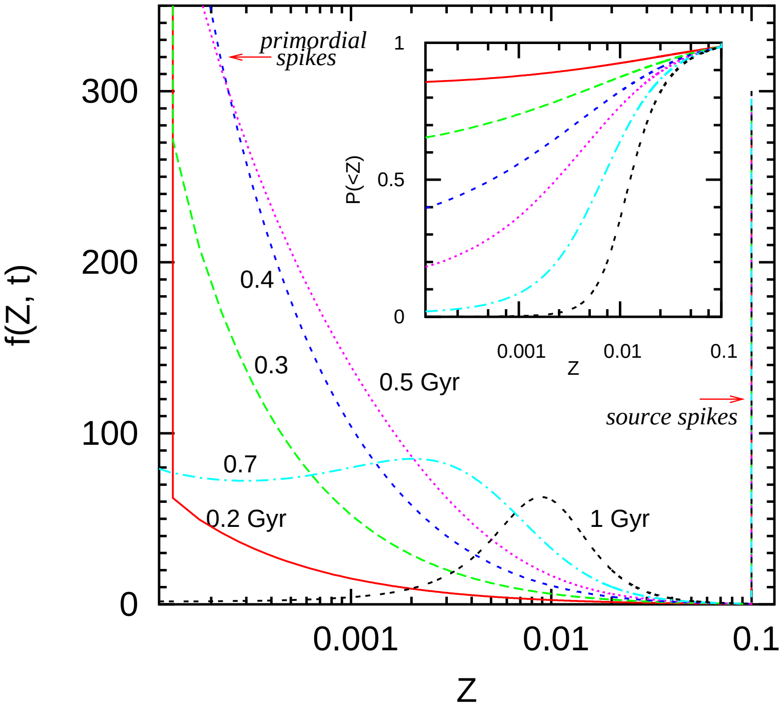

Figure 2.1 Metallicity probability distribution as a function of time.

Evolution of metallicity distribution function in the LBGs solved from eq (2.1). The empirical value for τ_{src} of about 5 Gyr is adopted. The timescale τ_{mix} is set to be 75 Myr. The source metallicity Z_s is taken to be 0.1. Clearly, turbulent mixing reduces the height of the primordial spike and thus decreases the primordial fraction. The inset shows the cumulative probability with metallicity no larger than Z. The primordial fraction at given time can be read from the cumulative probability at $Z = 0$.

The behavior of P as a function of time for different τ_{mix} and τ_{src} is illustrated in Fig. 2.2. To account for the uncertainty in τ_{mix} (§1.3.2.1), we picked two other values 25 Myr and 150 Myr. The mixing timescale could be even smaller if the velocity dispersion is larger than 10 km/s in these galaxies due to larger SFRs. Our major result is that $P(t)$ declines on a timescale similar to SF ages inferred from empirical modeling, without adjustment of parameters. Note that the result from the primordial fraction equation generally agrees with that from the numerical solution of the metallicity pdf equation by compring Fig. 2.1 to the curve with the corresponding parameters in Fig. 2.2. However, there is a visible difference, especially at later times, between the predictions. This is due to the finite resolution in the metallicity space for the numerical solution. This resolution effect is significant especially at the singular part of the distribution, which we are interested in. We found that as the resoultion increases, the agreement between the analytical result and the numerical result impoves.

The effect of $Z = 0$ infall can be included by adding to eq (2.2) a term $(1 - P)/\tau_{in}$ where $\tau_{in} = M_{gas}/$infall rate is the infall timescale, as can be derived from the infall term in eq (1.38). An example where the infall rate is set equal to the SFR is shown in Fig. 2.2. In this case, infall does not affect the evolution of the primodial fraction during the initial delay time but could maintain a low (but significant) steady-state primordial fraction at larger time when the erasure of primordial gas by mixing is balanced by fresh primodial gas from infall. However, to allow intermediate values of $P(t)$ for a longer time, the infall timescale has to be close to τ_{mix}, implying a huge infall rate. Therefore it is unlikely that infall changes the time at which the primordial fraction arrives at an intermediate value in the turbulent mixing model.

As discussed in §1.3.3, galactic winds do not affect the metallicity pdf if the winds sample the full pdf of metallicity in the ISM. In that case, large wind rates, probably existent in the LBGs (Erb06 et al. 2006), have no effect on the predicted primordial fraction.

From Fig. 2.2, if the galaxies have undergone SF with a star formation age as large as ~ 1 Gyr, the turbulent model predicts negligible primordial gas and thus cannot explain the intermediate primordial fractions claimed by JH. We point out that if SF events in LBGs consist of a number of SF bursts, we only need to replace the star formation age by accumuated SF burst durations if the ISM turbulence

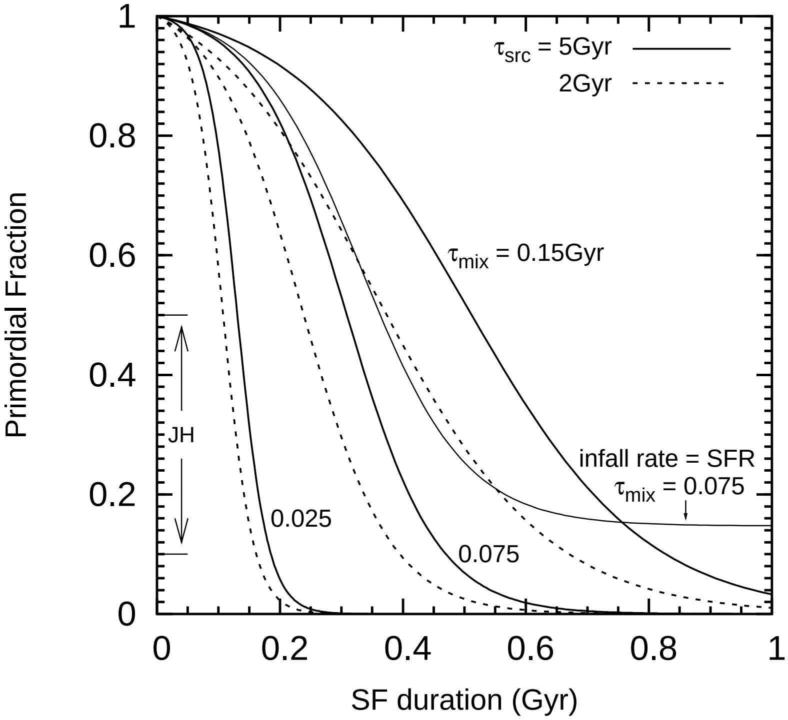

Figure 2.2 Primordial fraction as a function of SF duration

Evolution of primordial fraction for combinations of the mixing timescale τ_{mix} and the source timescale τ_{src}. The empirical value for τ_{src} is about 5 Gyr within a factor of a few for an IMF with $M_l = 0.1$. τ_{src} is independent of M_l if it is smaller than the mass limit for SNe. For a VMS IMF, τ_{src} is much larger but does not affect the result significantly, as discussed in the text. The range suggested for $z \sim 3$ LBGs(JH) is indicated by the arrow. Also shown is an infall model with infall rate equal to the SFR.

is driven by SF. Between the bursts, the chemical state of the interstellar gas is unchanged since the turbulence, thus mixing, is probably turned off and no new metal source are added. This is not true if the ISM tubulence is driven by galaxy interactions or mergers, or magneto-rotational instability etc. In that case, it is more appropriate to take the time since the first star formtaion event as the star formation age.

2.3.2 The SN Sweepup Model

The equation of the primordial fraction for the SN sweepup model was given in §1.4. Neglecting the infall term in eq (1.41), the primordial fraction decreases exponentially with a timescale $\tau_{sw} = M_{gas}/(\nu_{SN} M_{sw})$, the time for SNe to sweep up all the primordial ISM gas. The SN rate $\nu_{SN} = \epsilon B/\langle M_* \rangle$ and the sweepup mass $M_{sw} \sim 2 \times 10^4\ M_\odot$ by isolated SNe for $Z = 0$ gas (Thornton et al. 1998, Hanayama and Tomisaka 2006), twice larger than the sweepup mass in an enriched ISM with $Z \gtrsim 0.01 Z_\odot$. According to the calculation in Appendix C for the effective sweepup mass in the enriched ISM per SN in SBs, we expect that the average sweepup mass in the LBGs primarily with primordial gas by SBs is also mainly determined by the scale height of galaxies; therefore assuming a scale height similar to that of our Galaxy, the presence of SBs does not give an effective sweepup mass per SN very different from $2 \times 10^4 M_\odot$, the value estimated for isolated SNe. For a Salpeter IMF with mass range (0.1, 100) $M_\odot$ the number fraction ϵ of stars that become SNe is 0.004 and the average stellar mass $\langle M_* \rangle = 0.6$, so $\nu_{SN} = 0.7$/yr and $\tau_{sw} = 3 \times 10^6$ yr. A similar result is also obtained for a (-0.4, -1.7) IMF. Equivalently, the accumulated volume filling factor $NQ = t/\tau_{sw}$ (Oey 2000), so $P = exp(-t/\tau_{sw}) = exp(-NQ)$ and it is impossible to preserve primordial gas in LBGs for longer than $\sim 1\%$ of the observed SF ages $\sim 3 \times 10^8$ yr, unless the mixing efficiency is artificially tuned to 1%. In that case, the model predicts too large a present-day scatter in metallicity compared to observations (see Chapter 3). From eq (1.41), infalling $Z = 0$ gas can give a significant primordial gas only if the infall rate is larger than the SFR by a factor of 100, which is unlikey considering the already very large SF rates in LBGs.

Again we evaluate the effect of a VMS IMF. The SN rate ν_{SN} decreases by a factor of 100 due to the much smaller SFR in mass and the even smaller mumber rate of stars. However, this decrease is compensated by the increase of M_{sw} by a factor of ~ 50 due to the large explosion energy of pair instability SNe up to 10^{53} erg (see Woosley et al. 2002). Therefore τ_{sw} for a VMS IMF is nearly unchanged, which was unexpected. Thus our conclusion that SN or SB sweep-up mixing is too fast to have any zero primordial gas preserved in LBGs is virtually independent of the IMF. The mixing would be 100 times faster using the mixed mass per event adopted by Tumlinson (2006)[2].

Finally we point out that we just need to choose the SF age to be the accumulated SF formation duration if the SF history is a series of SF bursts because the metal sources and sweepup mixing are by definition turned off between the bursts.

2.3.3 Other Catalyzing Velocity Fields

Tenorio-Tagle (1996) gave a mixing model for the ISM where unmixed pockets of metals in SBs blast out of a galactic disk, later showering the disk with "droplets" of pure metals, diffusively mixing with the disk gas once they land in the disk. In this model, the primordial fraction is determined by the number of droplets, or equivalently the mixed mass, per SN. A fine tuning of the parameter is required to give the desired timescale that results in the primordial fraction otained by JH. However, since the paremater is unspecified by the model, we cannot draw a conclusion whether this mixing mechanism is a viable one to explain the JH result.

Differential rotation could stretch the products of nucleosynthesis deposited in a ~ 100 pc SN blob, into long thin annuli until the scale of diffusivity is reached. The shear rate in LBGs, or whether they differentially rotate, is unknown. Using the rate ~ 10 km/sec/kpc in our Galaxy as an illustration, we found that the timescale to reach the diffusive scale derived in §1.3.2.1, is about 8 Gyr, which is too slow.

2.4 Discussion

We examined the erasure of primordial gas in high redshift LBGs by various mixing mechanisms. We find that the turbulence-enhanced diffusivity model preserves primordial gas from rapid mixing for a few times the mixing time. This preservation

---

[2] The recent estimate by Tumlinson (2006) of the primordial fraction at high redshift using the SN sweepup mixing model apparently took a shell mass much larger than found in analytical and numerical calculations of supernova remnant evolution (see Thornton et al. 1998, Hanayama and Tomisaka 2006)

time coincides with the SF age $\sim 1-3\times10^8$ yr in LBGs, predicting an intermediate primordial fraction in these galaxies in agreement with a recent interpretation by JH. The preservation time only has very week, logarithmic, dependence on parameters such as the IMF through the source timescale and the averaged diffusivity in the ISM through the mixing timescale. Other mixing processes we considered predict a primordial fraction that is either unity or zero at $z \sim 3$ because they mix on a timescale that is much larger or smaller than the empirical SF ages. The primordial fraction should be zero in almost all galaxies if SN shells from stellar explosions mix as efficiently as assumed in sequential enrichment models (or much more efficiently, Tumlinson 2006). Future systematic investigations of the spectrophotometric signatures of primordial gas in high-redshift galaxies could distinguish these possibilities.

Chapter 3

Metallicity scatter as a constraint on chemical evolution models

Chapter Synopsis: Empirical upper limits to the metallicity dispersion at a give age in the Galaxy are less than ~ 0.05 dex at present, and probably not much larger in the past. We ask how the Galaxy could remain so homogeneous in the face of continuing localized sources of new metals and, if present, infall of low-metallicity gas. Using the physical mixing model in the turbulent interstellar medium and solving the kinetic equation from the metallicity probability distribution, developed in Chapter 1, we calculate the evolution of the metallicity scatter in the ISM. We find that, for chemical evolution models with infall, the finite time to mix accreted gas with disk gas gives metallicity scatter at least 5 times larger than the observed upper limits, while models without infall are consistent with observations. To reduce the mixing time, we added efficient mixing within SNR and superbubble shells formulated in §1.4, considered pre-enriched infall and episodic infall, and pushed all parameters to their limits, but the results still require a mixing timescale smaller by a factor of 20. The discrepancy can be removed if the infall is primarily in the form of clouds of size ~ 5 pc, small enough to mix with the disk in less than a few million years.

3.1 Introduction

Tinsley (1976) recognized the significance of the dispersion in metal abundances at a given age for studies of Galactic chemical evolution, but also that the apparent scatter could be due to observational uncertainties. Estimates of the dispersion δ in logarithmic metallicity log Z (we use log Z and metallicity indiscriminantly unless otherwise warranted) based on field stars and isochrone ages (e.g. Edvardsson et al. 2003, Feltzing et al. 2001, Nordstrom et al. 2004) were large, δ ~0.2-0.3 dex, giving rise to a number of proposals for retaining large scatter in the face of mixing (see van den Hoek & de Jong 1997, Scalo & Elmegreen 2004 for reviews). However there is compelling recent evidence that δ is much smaller, and that the earlier large values were due to a combination of uncertainties in ages (Pont & Eyer 2004), contamination by thick disk stars, and radial orbital diffusion. In particular, accurate abundances for several elements using UV absorption lines along many lines of sight sampling a large range in distances by FUSE and HST give an estimated upper limit of 0.04 dex (10%; see Cartledge et al. 2006). Studies of δ in several open clusters (Friel & Boesgaard 1992, King et al. 2000, Wilden et al. 2002, Quillen et al. 2002, Paulsen et al. 2002, Shen et al. 2005; DeSilva et al. 2006) give similar upper limits of 0.02 to 0.06 dex (5-12%) for the current epoch, and at ∼ 4-5 Gyr ago if the M67 sample is included (Randich et al. 2006). The scatter in abundance ratios of elements that should be produced in different nucleosynthetic sources for thin disk (Reddy et al. 2003) and thick disk (Reddy et al. 2006) field stars of given iron abundance imply upper limits of less than 0.1 dex for δ covering ages 1-10 Gyr, a result already apparent in the small [α/Fe] scatter of Edvardsson et al. (1993). Even smaller δ was inferred for the early solar system environment by Nittler (2005) based on meteoritic abundances.

This chapter addresses the question why the Galaxy has been very homogeneous during most of its history. We calculate the scatter in metallicity as a function of age for chemical evolution models with and without low-metallicity infall gas using the turbulent mixing model established in Chapter 1. The model has a finite and realistic time for mixing of the metal sources with the disk gas and the accreting gas (if present), which is assumed to be zero in mean field homogeneous chemical evolution models. We compute the evolution of the probability density function (pdf) of metallicity in the presence of sources, infall, and mixing by solving the kinetic equation given in §1.3. The scatter, i.e., the standard deviation in the logarithmic abundance of oxygen, is then obtained from the pdf. Our calculations include a sample of different yields and ejected masses, choices of IMFs, infall metallicities, and proposed infall rates as a function of time.

In §1.3.2, we present our calculations and results for the predicted metallicity scatter for various chemical evolution models from turbulent mixing in the ISM. We find that models without infall give a scatter consistent with observations while the infall models result in a scatter at least 5 times larger than the observed upper limit. In an attempt to solve this discrepancy for infall models, we include the SN sweepup mixing, whose existence remains to be examined, consider episodic infall and the possibility of faster mixing between the infall gas and the disk gas §1.3.3. The results are discussed in §1.3.4.

3.2 Mixing in ISM Turbulence

We compute the metallicity scatter using the turbulent mixing model and the kinetic equation for the metallicicty pdf given in §1.3. In this chapter we primarily consider the scatter in the oxygen abundance, which, as discussed in the introduction, is constrained by UV absorption line observations over many lines of signt in the ISM. The source term for oxygen, including core-collase SN sources (throughout this chapter we will use "SN" to denote only core collapse supernovae excluding thermonuclear SNe) and infall (if present), is given by eq. (1.37). We neglect the large scale abundance gradient, whose effect will be discussed later. Assuming statistical homogeneity, the advection term in eq. (1.2) vanishes and the equation for the oxygen abundance pdf is given by,

$$\begin{aligned}\frac{\partial f(Z)}{\partial t} = \; & \frac{1}{\tau_{mix}}\left(\int\limits_{0}^{Z} dZ_1 f(Z_1) \int\limits_{Z}^{Z_s} dZ_2 \frac{2}{Z_2 - Z_1} f(Z_2) - f(Z)\right) \\ & - \frac{\nu_{SN} M_{ej}}{M_g} f(Z,t) + \frac{\nu_{SN} M_{ej}}{M_g} \delta(Z - Z_s) \\ & - \frac{I}{M_g} f(Z,t) + \frac{I}{M_g} \delta(Z - Z_i)\end{aligned} \tag{3.1}$$

where the SN sources are assumed to be identical, each producing the same amount of ejecta, M_{ej}, and oxygen, M_Z. We set M_{ej} and M_Z to be the average ejecta mass and oxygen yield over the IMF. They are calculated using different IMFs and different nucleosynthesis results for the ejecta mass and the oxygen yield as a function of the progenitor mass in order to estimate the uncertainties. The nucleosynthesis results adopted here are from Woosley and Weaver (1995), Meynet and Mader (2002), and Nomoto et al. (2006). We experiment with different IMF slopes at high stellar mass around a fiducial IMF that is a -2.7 power law above 1 $M_\odot$ and a -1.4 power law below 1 $M_\odot$ (we refer to such an IMF as (-1.4, -2.7) for brevity). We find that the resulting average ejecta mass and oxygen yield have little variations from different nucleosynthesis works and different slopes for the IMF, $\langle M_{ej} \rangle \sim 13 - 16$ $M_\odot$ and $\langle M_Z \rangle \sim 0.8 - 1.3 M_\odot$. Therefore $Z_s \simeq M_Z/M_{ej} \sim 0.06 - 0.1$. Note that using a delta function in the SN source term at M_Z/M_{ej} assumes that new metals in the ejecta are well mixed (see Chapter 1 for the justification). We take $\langle M_{ej} \rangle = 15$ $M_\odot$ and $\langle Z_s \rangle = 0.08$ in the calculations. The effect of SN source variations due to the progenitor mass distribution will be dicussed in §3.2.3.

The core-collpase SN rate ν_{SN} (denoted as ν_{cc} in Chapter 1), the infall rate $I(t)$ (if present) and the gas mass M_g in eq. (3.1) will be taken from two types of chemical evolution models: closed-box models and infall models. For closed-box models, several different star formation laws are used to calculate the gas mass and the star formation rate as a function of time. In all the cases, the parameters in the SF law are chosen to result in a SFH that gives a current gas fraction of about 15%. For models with infall, we use three different infall rates $I(t)$: the local (solar annulus) and global infall rates of Naab and Ostriker (2006), and the infall model of Chiappini et al. (1997, 2001), calculating the gas mass and the star formation rates from the differential equation for the gas mass and the assumed SF law exactly the same as in those papers. These infall rates range from increasing with time (Naab and Ostriker, local) to slowly decreasing (Chiappini et al). For the infall metallicities Z_i in eq. (3.1), we consider three cases: $Z_i = 0$ and $Z_i = 0.1Z_\odot$ constant in time, and a time-dependent infall metallicity $Z_i(t)$ increasing from 0 to 0.3 $Z_\odot$ today. In all the models, the SN rate is obtained by converting from the star formation rate using the fiducial (-0.7, -1.4) IMF and $8M_\odot$ for the lower mass limit for core-collapse SN progenitors.

The mixing timescale τ_{mix} has been estimated to be about 75 Myr in §1.3.3, with an uncertainty factor of 3. For SN sources, a rigid lower limit for the mixing timescale is 25 Myr. In our calculations, we set the mixing timescale in the range of $25 - 75$ Myr. Note that the mixing timescale could be larger than this range if the source size is considerably larger than 100 pc (see §1.3.3). In eq (3.1), the infall gas is assumed to have the same mixing timescale as the SN sources. The possibility of a smaller timescale for the infall gas will be dicussed in §3.3.3.

3.2.1 Predicted scatters

We use the numerical scheme outlined in §1.3.4 to solve the pdf equation (3.1). From the solution we calculate the scatter in the oxygen abundance, defined as $\int (log(Z) - \langle log(Z) \rangle)^2 f(Z,t) dZ$, as a function of time. The results are shown in Fig. 3.1. The bottom medium-grey band is the predicted scatter for a closed-box model without infall. In the model, the star formation rate (SFR) per unit mass is taken to be constant (equivalent to a linear star formation law and thus an exponentially decreasing SF rate) with a timescale $M_g/\mathrm{SFR} = 5$ Gyr to satisfy the current gas fraction of $\sim 15\%$. The width of the band corresponds to the range of the turbulent mixing timescale, $25 - 75$ Myr. Comparison with the observed upper limits for abundance scatters in the ISM and open clusters (thin bar and arrow in the figure) and scatters in abundance ratios in the field stars (thick bar and arrow) shows that this model without infall gives a scatter consistent with the observations without any parameter fine-tuning.

We have also carried out calculations for other closed-box models with different star formation histories. We find that a constant star formation rate results in a scatter about 50% percent larger while a star formation law with the SF rate proportional to the square of the gas mass gives a scatter 30-40% smaller at all times in the Galactic history. (In the latter case, the SFR rate declines faster than exponentially and a relatively flat age-metallicity relation can be obtained.) Therefore we have a general conclusion that, with turbulent mixing in the ISM, closed-box models give metallicity scatters in agreement with the observations.

In contrast, all the chemical evolution models with infall we considered predict scatters in severe discrepancy with the observed upper limits. In Fig. 3.1, the top three bands correspond to infall models with three different turbulent mixing timescales, 10 Myr, 25 Myr and 70 Myr. The light-grey band, corresponding to an extremly small mixing timescale, is primarily for illustration because τ_{mix} probably has a strict lower limit of 25 Myr (see Chapter 1 and §3.2.1; see, however, §3.3.3 for a possible exception that the mixing timescale for the infall clouds with the disk gas can be smaller). Each band encloses the results predicted by the three different infall models: Chiappini et al. (1997) local infall rate (bottom), Naab and Ostriker (2006) local infall rate (middle) and global infall rate (upper). In our numerical solutions, we could only resolve to 0.01 $Z_\odot$ in the abundance space. Therefore the lowest infall metallicity that can be accounted for in our solution is 0.01 $Z_\odot$. A calculation for completely primordial infall was impossible due to the finite resolution. The results shown in Fig 3.1 from calculations, intended for primordial infall, all correspond to an effective infall metallicity of 0.01 $Z_\odot$. This applies to all the later results from numerical calculations for primordial infall. The effect of the infall metallicity on the predicted scatter for various models is given in Table 3.1 and will be discussed below. The present-day scatter for the infall models is ~ 0.2 dex using our turbulent mixing model with $\tau_{mix} = 25$ Myr, 5 times larger than the observed upper limits. Even for the extreme case with $\tau_{mix} = 10$ Myr, the infall models overpredict the present-day scatter and the scatter in the thick disk stars by a factor of 2-3. As seen from the three bands, the predicted scatter scales with the mixing timescale as $\sim \tau_{mix}^{1/2}$.

Since the closed-box models agree with the observed metallicity scatter, we will primarily concentrate on the infall models in the following sections, with partic-

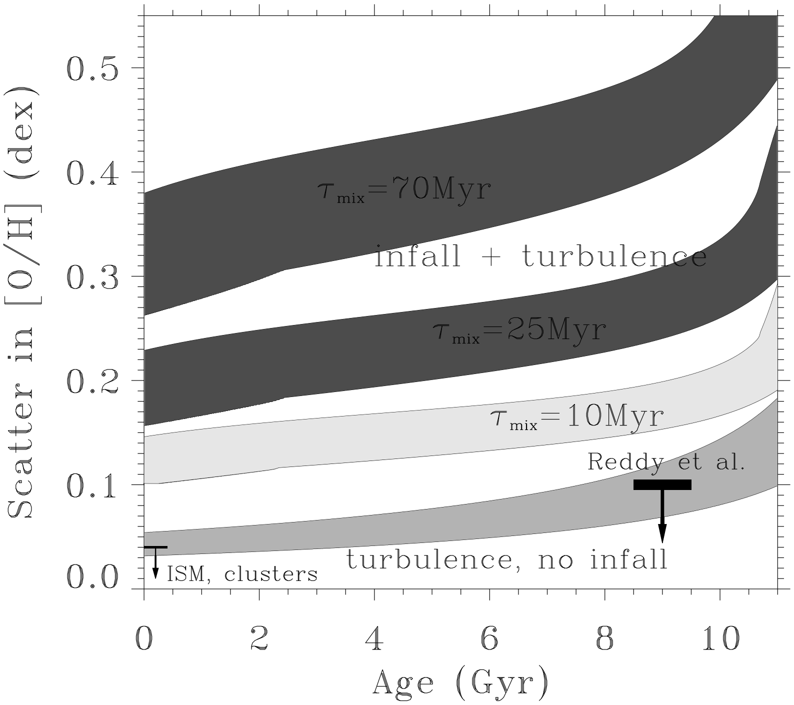

Figure 3.1 Scatter in [O/H] from the turbulent mixing model.

Scatter in [O/H] as a function of time predicted by the turbulent mixing model. The upper three bands are for the infall models with mixing timescales of 70 Myr, 25 Myr and 10 Myr, respectively. The width of each band encloses the scatter predicted by the three infall models. The light grayscale for the 10 Myr band indicates that this timescale is unrealistically small and is just for illustration. The bottom band is for the non-infall model and the width corresponds to the range of the mixing timescale (25-70) Myr. Thin bar and arrow: Observed upper limit in the ISM by Cartledge et al. (2006) and in open clusters; thick bar and arrow: Scatter of abundance ratios in thick disk stars by Reddy et al. (2006).

ular attention to whether and how the discrepancy with observations can be solved in these models.

3.2.2 Mixing timescale and infall metallicity dependence

We derive the scaling behavior of the predicted scatter with the mixing timescale and the infall metallicity from a simple physical consideration in the metallicity space. The contribution to the metallicity inhomogeneity in the ISM at a given time is mainly from recent infall gas and SN sources since the old sources have already been well mixed. Only infall gas and SN sources that occurred within a mixing timescale significantly contribute to the metallicity variations in the ISM. As shown in Fig. 1.2, continuous infall and SN sources force two spikes at small and large values in the metallicity space. The heights of the two spikes are determined by the competition between the forcing rate by sources and the erasure rate by turbulence-enhanced mixing. There is a simple way to estimate the probability contained around the infall and SN source spikes. At a given time t, the mass of the infall gas that has not been mixed is about $I(t)\tau_{mix}$ where we have used the fact that the timescale for the infall rate evolution is much larger than τ_{mix}. This mass of unmixed infall gas corresponds to a fraction, $\tau_{mix}I(t)/M_g$, of the total gas mass, M_g. Therefore the probability in the infall spike is $\tau_{mix}I(t)/M_g$. Similarly the probability contained in the source spike is given by $\tau_{mix}\nu_{SN}M_{ej}/M_g$. Since the returned fraction from the SN ejecta is ~ 0.1, i.e., $\nu_{SN}M_{ej} \sim 0.1$ SFR, and the infall rate $I(t)$ in most chemical evolution models nearly balances the SFR, we have $I(t) \gg \nu_{SN}M_{ej}$. This means that the infall spike is much higher and gives a much larger contribution to the metallicity scatter than the SN source spike. The contribution from the infall spike to the variance of $log(Z)$ is given by the product of the probability in the infall spike and the square of the distance (in logarithmic scale) from the source spike to the mean metallicity, i.e., $\tau_{mix}I(t)/M_g(log(Z_I/\langle Z\rangle))^2$. Neglecting the contribution from the source spike and that from the central region where $log(Z/\langle Z\rangle)$ is small, the scatter δ, defined as the square root of the variance of $log(Z)$, is approximately given by

$$\delta \simeq (\tau_{mix}I(t)/M_g)^{1/2}log_{10}(\langle Z\rangle/Z_I). \tag{3.2}$$

This formula more than just explains the scaling behavior of the predicted scatter on the mixing timescale and on the infall metallicity seen in Fig 3.1 and in Table 3.1;

it almost gives the same exact results as from numerical solutions. For example, in the three infall models we used, the infall timescale, defined as $M_g/I(t)$, is about 2.5 Gyr and the average present-day metallicity is about $Z_\odot$. If the mixing timescale $\tau_{mix} = 25$ Myr and the infall metallicity $Z_i = 10^{-2} Z_\odot$ (which is the effective infall metallicity in our numerical solutions for Z_i smaller than 0.01 solar due to the limited resolution), we get a scatter of 0.2 dex from eq. (3.2), the same as the result shown in Fig. 3.1. For infall metallicity of 0.1 $Z_\odot$, eq. (3.2) gives a scatter of 0.1 dex, consistent with the corresponding result in Table 3.1.

Eq. (3.2) shows that the scatter has a quite weak dependence on the mixing timescale and the infall metallicity. Therefore a decrease in the scatter requires a significant reduction in the mixing timescale. We discuss the possibility of a much smaller timescale to mix the infall gas in §3.3.3. Due to the logarithmic dependence, pre-enrichment in the infall gas almost certainly cannot help reduce the predicted scatter. Note that for primordial infall $Z_I = 0$ (unrealizable in our numerical solutions), the predicted scatter by eq. (3.2) is infinite.

We find in our numerical solutions that the scaling $\delta \propto \tau_{mix}^{1/2}$ applies to models without infall. In these models the primary contribution to the scatter is from the spread in the central region of the metallicity distribution instead of from a spike (in this case the source spike is the only one). To estimate the spread around the central region, a different approach is used: the mean metallicity $\langle Z \rangle$ equation and the variance $\langle z^2 \rangle$ equation (where z is the fluctuating part of the metallicity field) are derived from the pdf equation (3.1). We then evaluate the ratio $\langle z^2 \rangle^{1/2}/\langle Z \rangle$, which gives a measure of the metallicity dispersion around the mean. The two moment equations can be solved analytically and we find that the ratio $\langle z^2 \rangle^{1/2}/\langle Z \rangle \propto \tau_{mix}^{1/2}$. It can be shown that this ratio goes linearly with δ for $\delta \ll 1$, which is the case for closed-box models. Therefore this analytical derivation confirms the numerically found scaling for models without infall.

3.2.3 Source variations

In eq. 3.1, we assume that all the SN sources are identical, i.e., each SN source produces the same amount of ejecta M_{ej} and oxygen M_Z. In reality, M_{ej} and M_Z vary from source to source because they depend on the source progenitor mass m and thus has a distribution determined by the initial mass function $\phi(m)$. Clearly, the source variations give additional contribution to the metallicity scatter obtained from calculations neglecting the distribution of Z_s. From eq. (1.37), the real source term is an integral, from which we define the source metallicity pdf $P_s(Z) = \int M_{ej}(m)\delta(Z - M_Z(m)/M_{ej}(m))\phi(m)dm / \int M_{ej}(m)\phi(m)dm$. With this definition, the source term becomes $\nu_{SN} M_{ej} P_s(Z)/M_g$. The source pdf is calculated from the IMF and the ejecta mass and oxygen yield as a function of m. Again, we take nucleosythesis results from three sources: Woosley and Weaver (1995), Mayer and Meynet (2002) and Nomoto et al. (2006) and use IMFs that have different slopes at high masses in a range from -1.4 to -1.9. We carried out example calculations where we exactly use the real source distributions $P_s(Z)$ instead of the delta function in eq (3.1) in order to see the source variation effect on the predicted metallicity scatter.

We numerically integrate the pdf equation with the source delta function in eq (3.1) replaced by $P_s(Z)$. For models with infall, the local infall rate by Naab and Ostriker (2006) and a mixing timescale of $\tau_{mix} = 25$ Myr is used as an example. We find that, for all the nucleosynthesis results and IMFs with which we experimented, the resulting scatter is larger only by $\lesssim 0.01$ dex when source variations are included: the scatter increases from 0.185 dex to about 0.193 dex for primordial infall, from 0.13 dex to 0.138 dex for preenriched infall with metallicity of 0.1 solar and from 0.10 dex to about 0.105 dex for infall metallicity increasing from 0 to 0.3 solar today used by Naab and Ostriker. This result is explained by the fact that the scatter in infall models is primarily from the low-metallicity infall spike, which is barely affected by the spread around the source spike due to source variations at the other end in the metallicity space.

For models without infall, we used the model with a constant SF timescale and $\tau_{mix} = 25$ Myr for example. Depending on the nucleosynthesis models and the IMFs adopted, the resulting scatter is about 20-40% larger, e.g., taking the average increase of 30%, the scatter changes from 0.035 dex to around ~ 0.046 dex. This result can be interpretated from the same moment equation technique used to derive the scaling of the scatter with the mixing timescale for closed-box models in §3.2. We find that the source variations increase the rms to mean ratio $\langle z^2 \rangle^{1/2}/\langle Z \rangle$ by $\sigma_{Zs}/\langle Z_s \rangle$ where σ_{Zs} and $\langle Z_s \rangle$ are the rms and the mean of the source distribution $P_s(Z)$ respectively. The adopted nucleosynthesis models and IMFs give $\sigma_{Zs}/\langle Z_s \rangle \simeq 0.2 - 0.4$, implying that the rms to mean ratio of the metallicity field

Z increases by 20%-40%. Again since the scatter δ in unit of dex is proportional to the rms to mean ratio of Z for small δ, this calulcation suggests that the increase factor in δ is equal to the rms to mean ratio of the source metallicity pdf.

In summary, the SN source variations only increase the predicted scatter by a negligible amount for infall models and by about 30% for noninfall models. This does not change our conclusion that models without infall give abundance scatters in general agreement with observations while a severe dicrepancy with the observed scatter exists for the infall models.

3.3 Can Infall Models Be Reconciled with Observed Metallicity Scatters?

We seek possible solutions to the discrepancy of the predicted abundance scatter with observations in chemical evolution models with infall. In order to reduce the scatter, we include an additional mixing process, efficient mixing in SN shells, in §3.3.1. As discussed in Chapter 1, this mixing mechanism, assumed in most previous inhomogeneous chemical evolution models, probably does not occur in reality and is thus primarily to illustrate the severity of the scatter problem for infall models. We will show that including this mixing mechanism does not sufficiently reduce the scatter in the infall models. A possible solution is that infall is episodic and the current time is between two infall bursts. The infall gas from the last burst might have already been mixed and thus does not give significant contribution to current scatter in the ISM. In §3.3.2, we calculate how long it has to be since the last infall event so that the predicted present-day scatter is consistent with observations. Finally, there is the possibility of a small mixing timescale for the infall gas with the gas in the disk. This timescale depends on the form of the infall gas and can be much smaller than our fiducial value if the infall gas mainly consists of small clouds. We estimate the size of the infall clouds needed to solve the discrepancy in §3.3.3.

3.3.1 An additional mixing process: SN sweep up mixing

The metallicity pdf equation has been developed for the SN sweepup mixing model in §1.4, i.e., eq. (1.39),

$$\begin{aligned}\frac{\partial f(Z,t)}{\partial t} = \quad & -\frac{\nu_{SN} M_{sw}}{M_g} f(Z,t) + \frac{\nu_{SN} M_{sw}}{M_g} f(Z - \frac{M_Z}{M_{sw}}, t) \\ & -\frac{I}{M_g} f(Z,t) + \frac{I}{M_g}\delta(Z - Z_i)\end{aligned} \tag{3.3}$$

where we have again assumed identical sources using the average oxygen yield (see §3.2). Also the sweepup mass is assumed to be single valued using the average $\langle M_{sw} \rangle$ over different soures (see Appendix C for a dicussion of fluctuations in the sweepup mass and a method to account for the effect). We take $M_Z = 1\ M_\odot$ (§3.2) and a range of 6000-16000 $M_\odot$ for M_{sw} to allow for the uncertainty in the estimation (Appendix C).

We find from our calculations that this equation is equivalent to the models using the overlap argument (Edmunds 1975, Roy and Kunth 1995, Oey 2000). We will refer to this equation as the sweepup shift model since mixing in this model (see SN shell mixing in §1.4) effectively shifts up the metallicity in the gas swept up into a shell by M_Z/M_{sw}. The faster mixing efficiency that turns the distribution in the shell into a delta function discussed in §1.4 will also be considered. We will call it the hyper sweepup mixing. In chapter 1, we pointed out that the shift model already represents the fastest possible mixing rate in SN shells and the hyper sweepup model is a huge overestimate of the mixing efficiency. The results here for the hyper mixing model are just for illustration.

Before combining the sweepup mixing with the turbulent mixing studied in §3.2, we first show the results of the predicted scatter with sweepup mixing only. This would give us a better understanding of the results from the two mixing processes combined. We adopt the same chemical evolution models as used in Fig. 3.1 for the turbulent mixing model. The results are shown in Fig. 3.2.

Interestingly, for models without infall, the SN sweep-up shift mixing alone produces scatter (the upper light grey band) consistent with the observed small metallicity scatter in the ISM (Cartledge et al. 2006) and in stars in open clusters (indicated by the thin bar and arrow in the figure), and with the scatter in abundance ratios for the thick disk stars by Reddy et al. (2006) (the thick bar and arrow) and the thin disk stars of intermediate ages. Similar to the turbulent mixing case, using

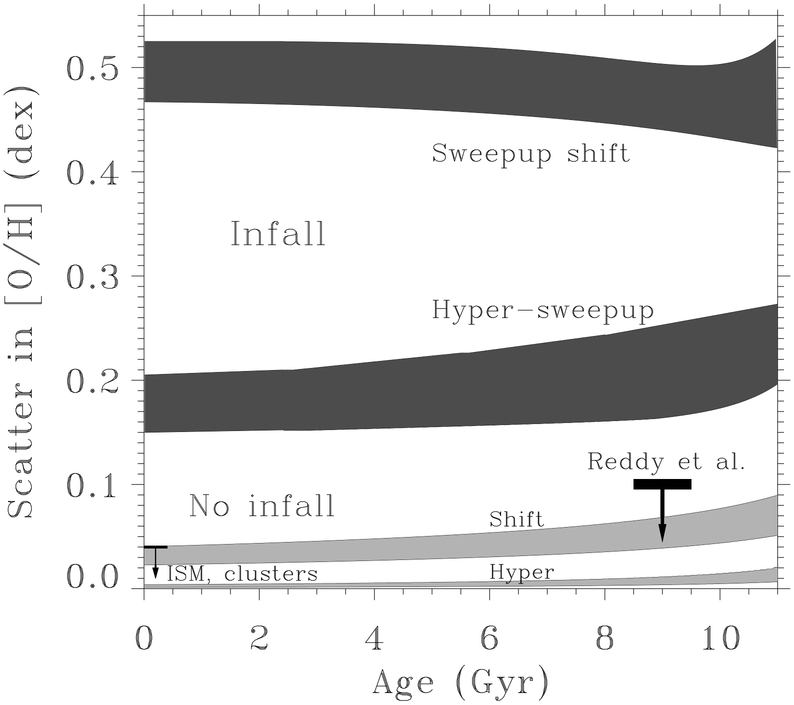

Figure 3.2 Scatter in [O/H] for the SN sweepup model.

Scatter in [O/H] as a function of time predicted by the SN sweepup model. The dark and the light grey bands are for the infall models and the non-infall models respectively. The dark bands enclose the results from the three infall models with the sweep- up mass in the range $(6000-16000)M_{\odot}$. The upper and lower dark bands correspond to the shift model and the hyper sweepup model, respectively. The width of the gray bands corresponds to the range for the sweep- up mass. Again the two light gray bands are for the shift model (upper) and the hyper sweepup model (lower), respectively. The plot for the hyper sweepup mixing, which probably does not exist, is just for illustration and comparison. Bars and arrows are the same as Fig. 3.1

different SFHs that satisfy the current gas fraction does not change this conclusion. We also studied the effect of the source variations, which increase the scatter by up to 100%, pushing the predicted scatter a little over the observed limits. However, the resulting scatter is still generally consistent with observations especially for large values in the adopted range for the sweepup mass. Note that the hyper sweepup mixing gives an undetectably tiny scatter.

The chemical evolution models with primordial infall gas using the SN sweepup shift mixing give an almost constant $\delta \sim 0.5$ dex, far too large compared to all observational estimates, as shown by the top dark grey band in Fig. 3.2, whose width corresponds to the M_{sw} range from 6000 to $16000 M_{\odot}$ and the three infall models. This large scatter agrees with the result of a a similar model by White and Audouze (1983). The analytical pdf they derived corresponds to a scatter of 0.55 dex. In order to reduce the discrepancy, White and Audouze introduced a free parameter to represent an additional unknown mixing process that instantaneously dilutes the infalling gas. However, we know of no physical process that would give such a rapid dilution effect. Motivated by the large stellar scatter believed at that time, van den Hoek and de Jong (1997) obtained a similar result for models with infall. However it is now clear that the scatter is much smaller than found in the work that motivated their studies; even in that work (Edvardsson et al. 1993), δ was only 0.2 dex. The hyper sweepup mixing gives a current-day scatter of about 0.2 dex for infall models, in excess of the observed limits by a factor of 4-5, which is similar to the result for the turbulent mixing model.

We finally consider the model with combined action of the sweepup mixing and the turbulent mixing, which will refer to as a dual mixing model. The pdf equation with both turbulent mixing and SN sweepup shift mixing is,

$$\begin{aligned} \frac{\partial f(Z)}{\partial t} = \; & \frac{1}{\tau_{mix}} \Big(\int_0^Z dZ_1 f(Z_1) \int_Z^{Z_s} dZ_2 \frac{2}{Z_2 - Z_1} f(Z_2) - f(Z) \Big) \\ & - \frac{\nu_{SN} M_{sw}}{M_g} f(Z,t) + \frac{\nu_{SN} M_{sw}}{M_g} f\Big(Z - \frac{M_Z}{M_{sw}}, t\Big) \\ & - \frac{I}{M_g} f(Z,t) + \frac{I}{M_g} \delta(Z - Z_i) \end{aligned} \tag{3.4}$$

which is obtained by replacing the SN source term (the delta function) in eq (3.1) by the SN sweepup shift term in eq (3.3). In effect, this shift term corresponds to the preconditioning of the sweepup gas by mixing in shells before the ISM turbulence stretches the shells and mix them with the ambient ISM gas.

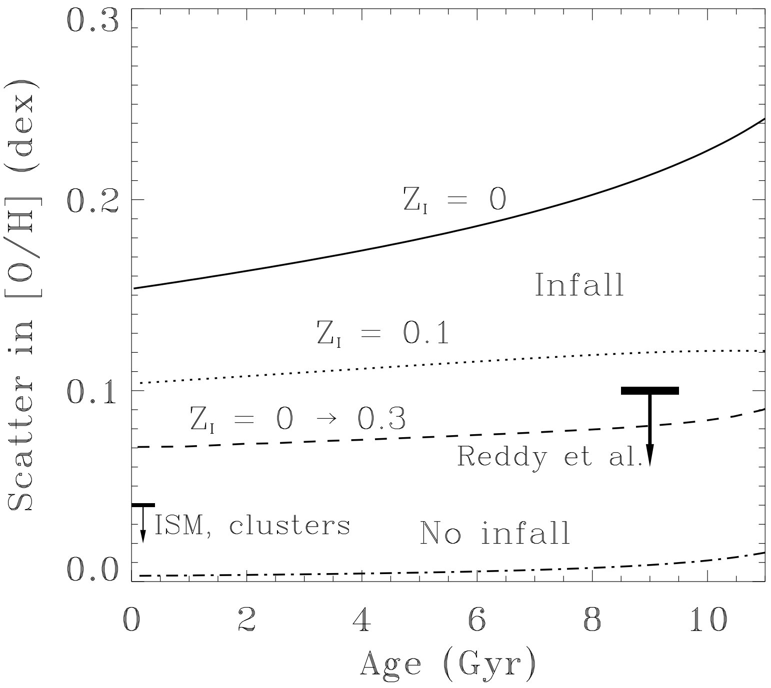

Figure 3.3 Scatter predicted by combined shift mixing and turbulent mixing.

Scatter as a function of time from dual mixing. The upper three curves are for local infall model by Naab and Ostriker (2006) with three different infall metallicities as labelled while the bottom curve is for the non-infall model. The mixing timescale is 25 Myr and the sweepup mass is $10^4 M_\odot$. Even with a current infall metallicity of 0.3 $Z_\odot$, this dual mixing gives a current scatter beyond the observed limits for the infall model. Bars and arrows are the same as Fig. 3.1.

Table 3.1 Scatter (in dex) in models with differing infall, infall preenrichment, and mixing processes.

Infall Z ($Z_\odot$)	Turbulence [a]	Shift[b]	Dual (shift) [c]	Hyper*	Dual (hyper) [c] *
0 [d]	0.19	0.48	0.15	0.16	0.11
0.1	0.13	0.36	0.10	0.077	0.057
$0 \rightarrow 0.3$ [e]	0.10	0.27	0.070	0.045	0.035
noninfall	0.035	0.030	0.003	0.003	0.002

.

---

[a] τ_{mix} = 25 Myr, which is chosen such that the variance decay timescale is given by the stretch timescale eq (1.8), in agreement with de Avillez and Mac low (2002).

[b] The sweepup shift mixing model. The sweepup mass $M_{sw} = 10^4 M_\odot$, assumed independent of the progenitor mass; see Fig. 3.1 for variation in scatter due to (constant) M_{sw} between 6000 and 16000 $M_\odot$

[c] A dual model refers to a model in which turbulence acts on the products of the sweepup mixing models (the shift and the hyper models), i.e., it combines the turbulent and the sweepup mixing.

[d] Our numerical resolution in metallicity space is $0.01 Z_\odot$.

[e] Time-dependent infall metallicity used by Naab and Ostriker (2006), which increases from initially primordial $Z = 0$ to a present-day value of 0.3 $Z_\odot$.

[*] Hyper-sweepup models and dual models with hyper-sweepup and turbulent mixing are only meant as illustrative, since they assume perfect mixing by every SN and SB with all the ISM gas encountered.

Note. — Adopted infall rates and star formation rates are from Naab and Ostriker (2006). See Fig. 3.2 for scatter using the infall model by Chiappini et al. (1997). Noninfall models are standard closed-box chemical evolution models.

Since the sweepup shift mixing by itself results in a very broad distribution with a scatter of 0.5 dex, it is expected that the preconditioning by this mixing mechanism is not efficient and that combining it with turbulent mixing in the ISM would probably not reduce the predicted scatter for infall models significantly. Our calculations confirm that this is the case. We give results for the local infall model by Naab and Ostriker and a closed-box model using the dual mixing in Fig. 3.3 where τ_{mix} and M_{sw} are set to be 25 Myr and 10000 $M_{\odot}$, respectively. In order to push all the parameters to their limits and obtain the lowest possible scatter predicted for infall models, results for different levels of pre-enrichment in the infall gas are also shown. Comparing the $Z_i = 0$ curve here with the band for $\tau_{mix} = 25$ Myr in Fig. 3.1 indicates that including the sweepup shift mixing only decreases the scatter by about 0.03 dex. The predicted scatter is still much larger than observed. The scatter decreases for larger infall metallicity. However, even with a current infall metallicity of 0.3 solar, the present-day scatter is 0.07 dex (the dashed curve in Fig 3.3), still beyond the observed limits. Note that the dual mixing gives a tiny scatter for the non-infall model.

The hyper sweepup mixing alone, which gives a current scatter of 0.2 dex, is almost as efficient as the turbulent mixing for the infall models. Therefore it is possible that a combination of the turbulent mixing and the hyper sweepup mixing produces a small enough scatter. The result for this case is shown in Table 3.1, which lists complete results for all the possible combinations of mixing processes and infall metallicities for the Naab and Ostriker local infall model and the non-infall model with constant SF timescale using $\tau_{mix} = 25$ Myr and $M_{sw} = 10000$ $M_{\odot}$. We see that combining the turbulent mixing and the hyper mixing gives a scatter below the observed limits if the infall metallicity is larger than 0.1 $Z_{\odot}$. Also note that the hyper sweepup mixing alone can produce a scatter of 0.045 dex if the current infall metallicity is 0.3 $Z_{\odot}$. However, we emphasize that the existence of the hyper mixing is extremely unlikely, if not impossible, and the results for this model are only meant as illustrative.

So far we have shown that excluding the unrealistic hyper mixing in SN shells infall models can not be reconciled with the small scatter observed even if all the parameters are pushed as far as possible toward giving a small scatter.

3.3.2 Episodic Infall

One possibility to reconcile the infall models with the observed scatter is that the infall is episodic and we are presently in a lull between infall bursts. In this case, infall gas from last burst might have already been mixed and a large present-day scatter may be avoided. We examine this possibility by calculating the current-day scatter assuming the last infall burst ended at different times and evaluating the minimum noninfall duration needed to produce a small enough scatter since the last infall event. Again we use the local infall model by Naab and Ostriker for example and other infall models give similar results. We assume that infall was continuous before switching off at some time. Prior to that time, we use the same local infall and star formation history as Naab and Ostriker (2006). After that, we set the infall rate to be zero and the Galaxy starts a closed-box phase. The SF formation rate in this phase is assumed to follow the same SF law as before the infall ends. Our results for different switching times are plotted in Fig 3.4 where the mixing timescale is set to be 25 Myr. Right after the infall stops, there is a rapid decrease in the metallicity scatter due to the erasure of low-metallicity infall gas in a turbulent mixing timescale. Then the scatter decreases in the same way as a model without infall. We find that, to avoid a current scatter larger than observed, the infall has to be switched off more than 5 Gyr ago. This result is not surprising if we recognize that it takes a Hubble time for the scatter to decrease below the observed upper limits in a model without infall at all. Lack of infall for the recent 5 Gyr would invalidate the most important motivation for infall models: as a solution to the G-dwarf problem (see Chapter 4), infall models need to have an almost constant infall rate that extends to the current epoch.

In summary, to reconcile with the observational constraint on the metallicity scatter, infall has to be switched off too early to explain the G-dwarf problem and in that case infall models lose their strong motivation. In Chapter 4, we further show that incomplete mixing in the ISM, especially between the infall gas and the gas in the disk due to a finite mixing time, results in a stellar metallicity distribution with low metallicity stars in excess of observed, unless mixing of the infall gas with the disk gas has a very short timescale. We consider the possibility of a much smaller mixing timescale for infall in next subsection.

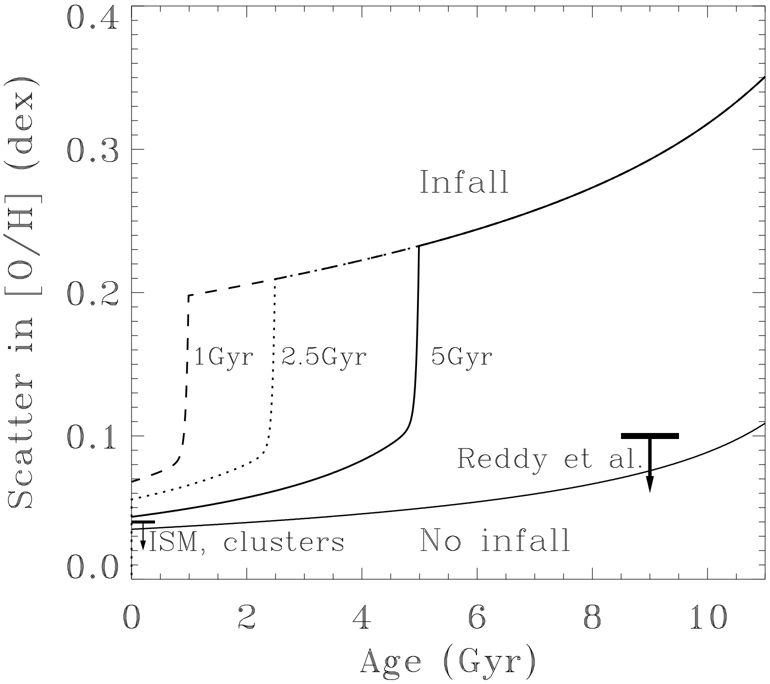

Figure 3.4 Scatter in [O/H] for models with infall switched off.

Scatter as a function of time for a model where the infall is switched off at different times. Before switching off, the infall (primordial) rate follows the local infall model by Naab and Ostriker (2006). After that, a closed-box phase starts. The upper three curves correspond to infall switched off at 5, 2.5 and 1 Gyr ago respectively. The last infall event must have been turned off at least 5 Gyr ago in order to avoid a scatter larger than the observed upper limit for the present-day scatter. The mixing timescale is set to be 25 Myr. Bars and arrows are the same as Fig. 3.1.

3.3.3 Small infall clouds?

As shown in §3.2.2, the predicted scatter decreases with the mixing timescale. A natural question would be how small the mixing timescale has to be to solve the metallicity scatter problem in the infall models and whether that is achievable. Since the scatter $\sigma \propto \tau_{mix}^{1/2}$, the mixing timescale needs to be 16 times smaller than 25 Myr in order to reduce the predicted scatter from 0.2 dex to about 0.5 dex, i.e., the required mixing timescale is $\lesssim 2 Myr$. As discussed in §1.3.3.1 and §1.3.3.2, the mixing timescale τ_{mix} for SN sources is $\gtrsim$ 75 Myr with an uncertainty factor of 3 depending on the interpretation of the stretching timescale (eq. 1.8). Therefore τ_{mix} for SN sources has a minimum of 25 Myr. This seems to imply that it is impossible to get a smaller scatter without artificially adopting an unreasonably small mixing timescale. However, recalling that the large scatter in the infall models is dominated by the infall spike (§1.3.2.2) in the metallicity pdf and that the mixing timescale for infall clouds with the disk gas could be different from that to mix SN remnants (§1.3.2.1), a smaller scatter may be obtained if the mixing timescale for infall clouds is much smaller than that for SN remnants. This is possible if the size of infall clouds is much smaller than the stall radii of SNRs. Since the stretching timescale and hence the mixing time scale goes linearly with the source size, the size of infall clouds is required to be 16 times smaller than 100 pc, which was used to calculate our fiducial τ_{mix}.

Therefore our model predicts that, to avoid the discrepancy with the observed abundance scatter, the infall gas assumed in chemical evolution models must consist of clouds of size smaller than $5 - 6$ pc. This is beyond current detection limits and is much smaller than the size of observed high velocity clouds (HVCs), which are the most studied candidate for infall gas. It is also smaller than the predicted size for cold clouds in galaxy halos formed from thermal instability (Maller and Bullock 2004). The similarity between the predicted properties of these clouds and of the observed HVCs lead Maller and Bullock to propose that the HVCs are the residual halo clouds formed from thermal instability. However, our prediction is consistent with the current consensus that the infall rate inferred from observed HVCs of sizes from 100 pc to 10 kpc is not sufficient to fuel the ongoing star formation rate in the Galaxy (Putman 2006). The small clouds contemplated here, if they exist, may provide an extra infall rate to balance the SFR. The balance between the infall rate and the SFR is assumed in most chemical evolution models with infall. It is also consistent with the argument that small halo clouds are subject to the Kelvin-Helmholtz instability (Maller and Bullock 2004) and may be shred into structures small enough to avoid the discrepancy before landing onto the disk.

3.4 Discussion

Physically realistic mixing in the ISM turbulence with a finite mixing timescale gives metallicity scatter far in excess of observations for chemical evolution models with low metallicity infall at a significant rate. We examined several possibilities for removing this discrepancy.

Pre-enriched infall has a metallicity closer to the mean disk metallicity than primordial infall and thus provides a smaller source of variations. As shown in Table 3.1, we found that infall metallicity up to $Z_i \sim 0.1 Z_{\odot}$ is insufficient to decrease the scatter, giving a present day scatter of 0.13 dex for a mixing timescale of $25 Myr$. Even a time-dependent infall metallicity with current $Z_i = 0.3 Z_{\odot}$ as used by Naab and Ostriker (2006) results in a current scatter of 0.1 dex, at least 2 times the upper limit from observations.

The most efficient mixing we can obtain is to combine two mixing processes, the sweepup shift (pre)mixing in SN shells and the turbulent mixing in the ISM. The results are shown in Fig 3. 3 for the Naab and Ostriker (2006) local infall model with 3 different infall metallicities and for a non-infall model. The former gives a current scatter of 0.07 dex even for preenriched infall with a current metallicity of 0.3 solar, still larger than observed, while the latter gives an undetectably small scatter. We exclude the existence of the unrealistically efficient mixing in SN shells that turns all the sweepup gas into a single metallicity.

We examined the possibility that we are presently in a lull between episodic infall bursts. The infall gas from the last infall burst may have been mixed and does not contribute to the scatter today. However, our calculations show that the present-day scatter constraint requires that infall must have essentially subsided several SF timescales ($\gtrsim$5Gyr) ago. Moreover, if we impose the constraint by Reddy et al. (2003, 2006), the infall must have been negligible for more than 5-9 Gyr. Without significant infall rate that extends to the current epoch, infall models cannot explain the observed metallicity distribution function of G- and K-dwarf stars, the main motivation of infall.

The only possibility to reconcile the small observed metallicity scatter with the infall models is that the infall clouds are in the form of clouds of size $5-6$ pc, which can be stretched by the ISM turbulence and mixed with the disk gas in a very short time. This results in a much less pronounced spike at the infall metallicity and removes the scatter problem for the infall models.

In conclusion, our calculations show that only two possibilities exist to avoid metallicity scatters much larger than observed. First the infall has not been significant during most of the Galaxy history. This result supports suggestions by Larson (1998) and Haywood (2006). It is consistent with the decline in the empirical cosmic SFR by a factor of about ten over the past $\sim$8 Gyr (see Hopkins 2004), and resembles several cosmological disk formation simulations, the extreme case being the rapidly-declining cold mode accretion that dominates lower-mass galaxies in simulations by Keres et al. (2005). Cattaneo et al. (2006) have shown that models with continuing hot mode accretion at rates as large as found in some semi- analytic models and simulations predicts a large population of non-existent massive blue galaxies, and baryonic galaxy masses that are too large; they suggest that accretion must be truncated by satellite galaxies and an additional process, like AGN feedback.

Second, the infall gas could consist primarily of small clouds of size $5-6$ pc, currently beyond detection limits. However, this suggestion is consistent with the current consensus that the infall rate estimated from the observed HVCs is too low to fuel the star formation rate today in the Galaxy (Putman 2006). The predicted clouds, if they exist, can supplement more infall gas to balance the current SFR, as needed in most chemical evolution models. The small infall clouds might form out of cold halo clouds shredded by the Kelvin-Helmholtz instability.

Chapter 4

The effect of finite-time mixing on predicted stellar metallicity distribution functions from chemical evolution models with infall

Chapter Synopsis: A finite mixing time for the infall gas accreting onto the Galactic thin disk with the gas in the disk produces a fraction of stars with metallicity close to the infall metallicity that directly form out of the infall gas that has not been mixed. If the infall metallicity is much smaller than 0.1 solar, the typical minimum metallicity in the observed thin-disk stars, the infall gas is required to be in the form of clouds of size smaller than 10 pc, which can be mixed with the disk gas in a few million years. Slower mixing gives rise to a tail of low-metallicity stars, contradicting the observed stellar metallicity distribution function (MDF) and recreating the G-dwarf problem which infall models are designed to solve. This constraint is consistent with that from the observed metallicity scatter considered in Chapter 3. Infall gas with metallicity close to or larger than 0.1 solar gives a contribution of about 1% to the MDF around the corresponding metallicity. A difference of 1% in the MDF is probably beyond the observational accuracy and no apparent discrepancy exists between the predicted MDF and the observed if the mixing timescale is close to our fiducial value of 25 Myr, corresponding to a source size of 100 pc. In this case, the observed MDF does not give a strong constraint on the form of the infall gas.

4.1 Introduction

The metallicity distribution function (MDF) of low-mass stars, such as G and K stars, that sample the metallicity status in the ISM during most of the history of the Galactic disk, provides a strong constraint on models for Galaxy formation and evolution. The deficiency of low-metallicity stars relative to those predicted from a standard closed-box model, the so-called G-dwarf problem, has led to various solution scenarios (see Pagel 1997). Among the solutions, infall models with significant accretion of low-metallicity gas that extends to the current epoch, are dominant and have been extensively studied. The infall gas provides fuel for star formation at late times and thus maintains a significant star formation rate when the *average* metallicity in the ISM is large. It also gives a flat age-(*mean*) metallicity relation, which implies a small metallicity spread in most stars. Taking the metallicity of stars formed at a given time to be the mean metallicity in the ISM, the former would result in a significantly reduced fraction of low-metallicity stars and the latter would give a narrow stellar metallicity distribution, providing an excellent agreement with observations.

However, using the average metallicity in the ISM, which we will call a mean-field calculation, is equivalent to assuming an instantaneous mixing of metal sources and low-metallicity infall with the gas in the Galactic disk. As discussed in the previous chapters, any physical mixing process has a finite mixing timescale, which, in the presence of continuous sources of metallicity variations, always gives chemical inhomogeneity to some degree. The inhomogeneity, in contrast to the assumed perfect mixing in mean-field calculations, may affect the infall model as a successful solution to explain the observed MDF.

First, a finite timescale allows, at any time, the existence of a fraction of low metallicity infall gas that has not been mixed with the disk gas. Stars forming out of this fraction of gas would contribute to the low-metallicity tail of the stellar MDF. It is important to examine whether low-metallicity stars forming out of the unmixed infall gas recreate the G-dwarf problem if realistic mixing with finite timescales is accounted for.

Second, chemical inhomogeneity in the ISM is expected to be imprinted in stars and to make the stellar MDF broader than predicted from mean-field calculations. In Chapter 3, using our metallicity pdf approach, we found that models with continuous low-metallicity infall give large scatter in the oxygen abundance in the ISM with a fiducial mixing timescale derived from the size of SN sources. A similar scatter is obtained for the iron abundance for the infall models (§4.2). We then check whether the large iron abundance scatter gives an MDF broader with observed. Note that the breadth of the MDF can be a separate constraint from the fraction of low-metallicity stars.

In this chapter we study the effect of physically realistic mixing processes with finite timescales on the infall models as a solution to explain the observed MDF. The purpose here is to investigate whether discrepancy arises between the observed MDF and the predicted MDF when finite-time mixing for the infall gas is considered and, if yes, whether and how the discrepancy can be removed. In §4.2, we solve the evolution equation for the distribution function of the iron abundance, from which the MDF is calculated. Our conclusion is given in §4.3.

4.2 Calculations and Results

We consider the iron abundance probability distribution function in the ISM since the stellar metallicity distribution function is traditionally expressed in terms of the iron abundance. The abundance pdf equation for iron differs from that for oxygen in the source term because iron is thought to be primarily produced by Type Ia SNe. Using our turbulent mixing model, the equation is give by,

$$\begin{aligned} \frac{\partial f(Z)}{\partial t} = & \frac{1}{\tau_{mix}}\Big(\int_0^Z dZ_1 f(Z_1) \int_Z^{Z_s} dZ_2 \frac{2}{Z_2 - Z_1} f(Z_2) - f(Z)\Big) \\ & + \frac{\nu_{Ia} M_{ejIa}}{M_g}(\delta(Z - Z_{sIa}) - f(Z,t) \\ & + \frac{\nu_{cc} M_{ejcc}}{M_g}(\delta(Z - Z_{scc}) - f(Z,t)) \\ & + \frac{I}{M_g}(\delta(Z - Z_i) - f(Z,t)) \end{aligned} \tag{4.1}$$

where $Z_{sIa} = M_{ZIa}/M_{ejIa}$ is the source metallicity for SNe Ia. We use the nucleosythesis result by Theileman et al. (1993) that each Type Ia SN produces about 0.6 $M_\odot$ iron, i.e., $M_{ZIa} = 0.6\ M_\odot$. We take the ejecta mass M_{ejIa} of SNe Ia to be several solar masses (which does not affect our conclusion; see below). The small contribution for core-collapse SNe is also included and the iron yields from core-collapse SNe are taken from Nomoto et al. (2007). The source term for the core-collapse SNe has an identical form as the for oxygen and is evaluated with the same method as described in Chapter 3. The integral limit Z_s in the mixing kernel is set to be Z_{sIa}, which is much larger than Z_{scc}. We need a prescription for the SN Ia progenitors, most likely accreting white dwarfs in close binaries, to evaluate the SN Ia rate ν_{Ia} as a function of time.

We use the SN Ia progenitor model by Kobayashi et al. (2000) (see also Kobayashi and Nomoto 2008), which specifies two types of progenitors based on the evolution stage of the companion star when the explosion occurs: white dwarf + main sequence systems and white dwarf + red giant systems. The mass ranges for main-sequence stars and red giants in the two types of systems are taken to be $0.9 - 1.5\ M_\odot$ and $1.8 - 2.6\ M_\odot$, respectively. A -0.35 mass function is assumed for the companion stars in both systems. The delay time from the formation of a binary system to the explosion is determined by the the lifetime of the companion star. We use the fitting formula for the stellar lifetime as a function of the stellar mass and metallicity by Hurley (1999). The white dwarfs are assumed to have main-sequence masses in the range of $3 - 8\ M_\odot$. The number rate of stars with mass in this range is converted from an IMF with slopes of -0.4 and -1.7 below and above 1 $M_\odot$, respectively. The number fraction of main-sequence stars in this mass range that end up as either of the two types of SN Ia progenitors is a parameter to be fixed by comparison with observations. Generally the fraction for WD+MS systems is around 0.04-0.055 and that for WD+RG systems is about 0.01-0.04 (Kobayashi et al. 2000). In our calculations we adjust these two parameters so that the MDF obtained from a mean-field calculation best fits the observed MDF. With this prescription, the rate of SNe Ia in the iron source term in eq (4.1) can be determined from the star formation history in the adopted chemical evolution model. We again consider the same infall models (Chiappini et al. 1997, Naab & Ostriker 2006) used in our study on the metallicity scatter (Chapter 3). Note that our result in this chapter, which will be primarily concerned with the low-metallicity stars due to the infall gas, does not depend on the detailed model and assumptions for SN Ia sources (similar to the result in Chapter 3 that the abundance scatter in infall models is insensitive to the SN sources).

The pdf equation is then numerically solved to obtain the iron abundance pdf in the ISM at any given time. From the pdf solution, we find that the iron abundance scatter as a function of time is similar to that of oxygen, with a current scatter of 0.2 dex in the ISM today. This is because the scatter is dominated by the low-metallicity spike from the infall and, for a given infall model, the infall spike in the iron abundance pdf is similar to that in the oxygen pdf.

Assuming the metallicity of stars formed at a given time completely samples the metallicity distribution in the ISM, we calculate the metallicity distribution function of all the long-lived stars formed during the history of the Galactic thin disk by integrating over time the distribution $f(Z,t)$ weighted by the star formation rate $B(t)$, i.e., $\int f(Z,t)B(t)dt / \int B(t)dt$.

The result for the local infall model by Naab and Ostriker (2006) using our turbulent mixing model is given in Fig 4.1. The histogram is the observed MDF taken from Jorgenson (2004). The dashed curve is the predicted MDF from the mean-field calculation, assuming perfect mixing at any time. This mean-field MDF, by design, matches the observation very well. The dotted line corresponds to a mixing timescale of 25 Myr (our fiducial mixing timescale for source size of 100 pc, see Chapters 1 and 3) and primordial infall (again due to the limited resolution, the infall gas in the numerical solution has an effective metallicity of 0.01 solar, see Chapter 3). We find that with the finite mixing timescale adopted here the predicted MDF has an excessive number of stars in the low-metallicity tail. As discussed earlier, these stars form out of the infall gas that has not been mixed with the disk gas and thus have metallicities close to the infall metallicity. From the numerical solution, the number of stars with metallicity below -1 dex is about 1% of the total stars. This contradicts, by at least a factor of 10, the observational result of Nordstrom et al. (2004) who find that only about 10 out of a total of 14000 F and G stars have metallicity smaller than 0.1 solar. The fraction of stars that form out of the unmixed infall gas can be estimated by the same argument used to derive the scaling behavior of the predicted metallicity scatter with the mixing timescale in Chapter 3. There, we showed that, at a given time, the infall gas that has not been mixed occupies a mass fraction, $\simeq I(t)\tau_{mix}/M_g$, of the total gas in the disk. This fraction is about 0.01 for the infall models we adopted, which explains the fraction (1%) of low-metallicity stars in the MDF obtained in our numerical solution. The very infall spike, which gives severe discrepancy with the observed scatter, also causes the problem of an excessive number of low metallicity stars in the MDF. Clearly, a solution for the discrepancy is a smaller mixing timescale for the infall gas, similar to the solution for the metallicity scatter problem in Chapter 3. Since the predicted fraction of low-metallicity stars is 10 times larger than observed and the predicted fraction goes linearly with the mixing timescale, the timescale needs to be 10 times smaller than adopted in our calculation. This is possible only if the source size is 10 times smaller. Therefore the size of the infall clouds is required to be smaller than $\sim$ 10 pc, supporting our conclusion in Chapter 3. Note that the predicted MDF with the adopted mixing timescale is only a little broader than, but not in contradiction with, the observation. This is because the central part of the metallicity distribution in the ISM is not broad.

We also compute the MDF for the infall model by Chiappini et al. (1997) using the sweepup shift mixing model. The result for a sweepup mass of 10000 $M_\odot$ is given in Fig.4.2. The histogram is the observed MDF taken from Racho-Pinto and Maciel (1996). Again, a mean-field calculation gives a MDF in agreement with the observed histogram. Clearly, the predicted MDF (the dashed curve) from the sweepup mixing model not only overpredicts the low-metallicity stars but is also much broader than the observed MDF. In fact, the predicted MDF here is very close to that from a closed-box model. White and Audouze (1983) show that the predicted MDF for infall models using a similar model to the sweepup mixing model is the same as the MDF derived for closed-box models (from a mean-field calculation) and the result is independent of the sweepup mass. Our numerical solution confirms this result. Note that White and Audouze introduced an unphysical dilution factor for the infall gas in order to reduce the predicted large scatter for infall models. We know of no physical basis for the dilution and thus do not adopt their assumption. The broad MDF is due to the broad abundance pdf in the ISM for the infall models with the sweepup shift mixing. In Chapter 3, we found a broad pdf for the oxygen abundance with a scatter of 0.5 dex for the same model. This is also true for the iron abundance pdf in the ISM, which gives a broad stellar MDF. Therefore, similar to the situation in Chapter 3, the sweepup shift mixing alone gives a much more severe discrepancy with the observed MDF.

In order to examine possibilities to reduce the discrepancy, we also run calculations where the two mixing mechanisms are combined, called dual mixing models in Chapter 3. However, we find that, similar to the scatter problem for infall models, the dual mixing models are not able to remove the low-metallicity tail although it makes the central part of the MDF a little narrower. Even for the dual model combining hyper sweepup mixing and turbulent mixing, the low-metallicity tail still exists and contains about 1% of all stars.

Finally we consider preenriched infall. If the infall metallicity is much smaller than 0.1 solar, there always exists a low-metallicity tail below -1 dex containing more stars than observed (see the observed MDFs in Fig. 4.1 and 4.2) unless the infall gas primarily consists of small clouds and can mix with the disk gas in less than several million years. On the other hand, if the infall metallicity is close to or larger than 0.1 solar, no low-metallicity tail below -1 dex is produced and there would be no excessive stars with metallicity much lower than the smallest metallicity (which is -1 dex, as seen from the histograms in Figs. 4.1 and 4.2) in the observed thin-disk stars. The stars forming out of the unmixed infall gas would have a contribution of 1% to the MDF at about 0.1 solar or larger. If the infall metallicity is fixed at -1 dex, the predicted MDF would have a spike at -1 dex, which is not observed. However, this spike is probably not observable since it would be spread out by observational uncertainties. Also, a difference of 1% in the MDF is probably beyond the observational accuracy. Even if the observational sensitivity could measure a difference of 1%, changing parameters in the infall model can easily give a change of 1% in the predicted MDF around -1 dex. In that case, no apparent contradiction with the observed MDF exists and the observed MDF does not require a much smaller mixing timescale for the infall gas than the adopted fiducial value. This also applies to the time-dependent infall metallicity if the infall metallicity is close to or above -1 dex during most time in the history of the Galactic thin disk.

4.3 Conclusion

We find that, with our fiducial mixing time, the chemical evolution models with infall give rise to a number of low-metallicity stars in excess of the observed fraction if the infall metallicity is much lower than 0.1 solar. Since the predicted fraction of low-metallicity stars is $\propto \tau_{mix}$ (see §4.2), a solution to remove the discrepancy is similar to that for the scatter problem in Chapter 3, i.e., a smaller timescale for the infall gas to mix with the disk gas. Because the predicted fraction of low-metallicity stars is 10 times larger than observed, the mixing timescale needs to be 10 times smaller than the fiducial mixing timescale. This means that the size of infall clouds is required to be $\sim$ 10 pc (see Chapter 3), 10 times smaller than the source size, 100 pc, used to derive the fiducial mixing timescale. This result is consistent with and supports the conclusion in Chapter 3 that the observed scatter requires that the infall gas primarily consists of clouds of size smaller than $\sim$ 5 pc.

If the infall metallicity is close to or larger than 0.1 solar, no low-metallicity tail below 0.1 solar appears and no apparent discrepancy between the observed MDF and the predicted for infall models exists if the mixing timescale is close to our fiducial value of 25 Myr. No smaller mixing timescale for the infall gas is required. In this case, the observed metallicity scatter discussed in last chapter is a much stronger constraint for the mixing efficiency of the infall clouds with the disk gas than the observed MDF.

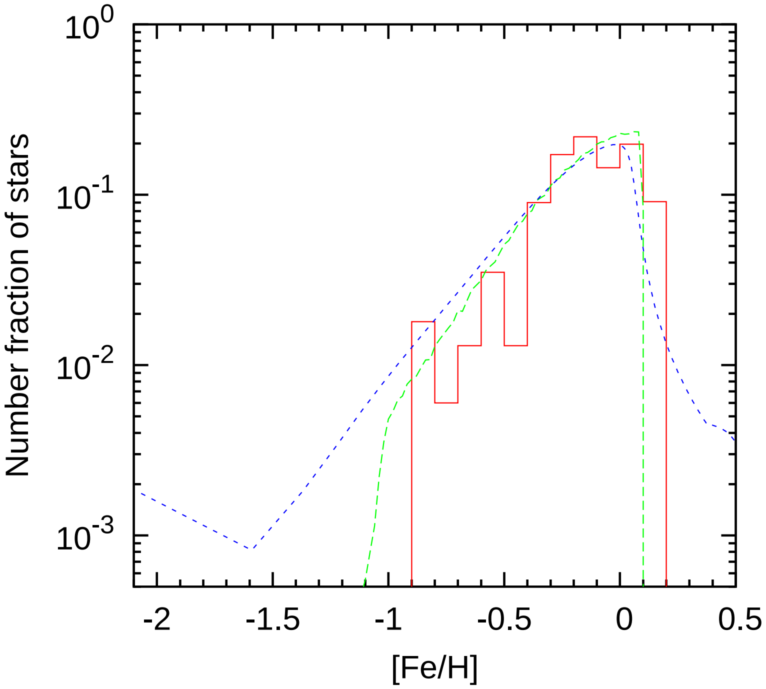

Figure 4.1 Predicted metallicity distribution function with turbulent mixing. Predicted metallicity distribution function (the short-dashed line) for the infall model by Naab and Ostriker (2006) using the turbulent mixing model given in §3 with a mixing time scale of 25 Myr. The histogram is the observed metallicity distribution function taken from Jorgensen (2000). The realistic finite mixing timescale in our turbulent mixing model gives rise to a low-metallicity tail in excess to the observed MDF. This tail represents stars formed out of infall gas before it is mixed with the disk gas. Removing the discrepancy requires the infall gas in the form of small clouds of size 10 pc. The calculation was intended for primordial infall, however, the limited resolution gives rise to an effective infall metallicity of -2 dex in our numerical calculation. An infall metallicity larger than -1 dex would contribute about 1% to the MDF at that metallicity. In that case, no apparent contradiction exists and the MDF does not give a constraint on the mixing timescale of infall clouds (see §4.2). The long-dashed curve is the MDF calculated for the Naab and Ostriker model under the assumption of unphysical instantaneous mixing in the ISM, i.e., assuming the metallicity of all stars formed at a given time is equal to the average interstellar abundance at that time.

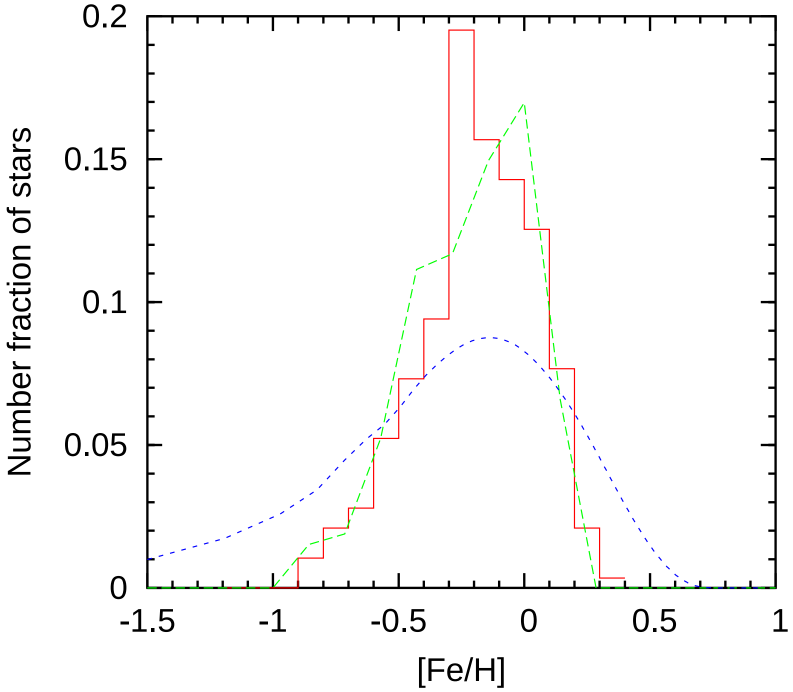

Figure 4.2 Predicted metallicity distribution function with SN sweepup mixing.

Predicted metallicity distribution function (the short-dashed line) for the infall model of Chiappini et al (1997) using the SN sweepup shift mixing model given in §4. The histogram is the observed metallicity distribution function taken from Racho-Pinto and Maciel (1996). The SN sweep mixing alone is very inefficient in homogenizing the low metallicity infall with gas in the disk. As shown by White and Audouze (1983), the MDF calculated from this mixing for infall models is as broad as that predicted from a closed-box model. Therefore for infall models to successfully solve the G-dwarf problem, a faster mechanism for mixing the infall gas with the disk gas is required. As discussed in the text (also in Fig 4.1), if the infall gas is in the form of small clouds of size smaller than 10 pc or the infall metallicity is larger than 0.1 solar, turbulent mixing can remove the discrepancy. The long-dashed curve is the MDF calculated from the Chiappini model assuming instantaneous mixing (unphysical) in the ISM.

Chapter 5

Secular Increase and Inhomogeneity of C/O in the Galaxy: Implications for Liquid Water Habitability

Chapter Synopsis: We investigate fluctuations in abundance ratios of elements produced in different localized nucleosynthesis sources with particular attention to carbon and oxygen, whose primary sources are probably low-mass stars and massive stars, respectively. Fluctuations in the carbon to oxygen ratio in the interstellar medium are of special astrobiological interest: planetary systems that form in regions with C/O>1 would be devoid of water. We give a general procedure for calculating the fluctuations in abundance ratios, which does not require a detailed calculation of mixing in the presence of continuous localized sources, by adopting probability distribution functions of the individual abundances. The results are insensitive to the assumed functional form of these distributions, but do depend on the assumed variance of the abundances, which is taken from observations. We find the fraction of the ISM with C/O>1 at the solar circle today is between 10^{-3} and 10^{-1}, depending on the correlation between sources and assumed cosmic scatter in C and O, if the average present C/O is 0.8. The fraction of long-lived stars that should have C/O>1 is found to be one to two orders of magnitude smaller, with a larger uncertainty because the result depends on the assumed star formation rate history. Combining the radial gradient in C/O found using HII regions and predicted by chemical evolution models, and the time-dependence given by the solar and present C/O ratios, dehydration of the inner disk is already nearly complete. Using this set of parameters, a dehydration front is currently located at about 6 kpc from the Galactic center and should reach the solar galactocentric distance in about 3 Gyr.

5.1 Introduction

Our Galaxy is bound to be chemically patchy at some level simply because elements are repeatedly produced in discrete and localized events, and the mixing of these elements can never be complete. We are particularly interested in fluctuations in significant abundance ratios of elements produced in different nucleosynthesis sources. For example the iron to silicon ratio Fe/Si is expected to play an important role in the effectiveness of plate tectonics, and the carbon to oxygen ratio (C/O ratio) at a location where planet formation is commencing must play an important role in controlling the amount of free oxygen that is available to form ices which later become liquid water. For each of these ratios it is believed that the stellar source is from a different mass range, and hence stellar lifetime, for each element. More importantly, the small average lifetime of open clusters subjected to tidal forces and other dynamical disruptive forces means that elements produced in a massive star (Si and O in the two examples above) will be deposited in the parent cluster, while elements released at the end of the life of a low-to-intermediate mass star, such as carbon detonation supernova explosions of white dwarfs (that produce most of the iron) or strong stellar winds from AGB stars (that contribute significantly to carbon production) will be deposited in the field.

Although there is still some controversy concerning the models for carbon yields, observations of field stars and HII regions seem to have converged in the conclusion that, while triple-alpha carbon from high mass stars may have contributed to carbon production when the Galaxy was young, the carbon enrichment at disk metallicities is primarily due to mixing between the core and interior, and subsequent expulsion in a stellar wind, in low- and intermediate-mass stars (see especially Carigi et al. 2005, Bensby and Feltzing 2006, and references therein). We will show that this situation has two consequences: a significant fraction of the Galactic gas has C/O>1 even when the average ratio is smaller than unity and the fraction increases with time.

Gaidos (2000) was the first to point out the likelihood and the consequences of regions of the Galaxy with enhanced C/O ratios. The nature of condensates that form in protoplanetary disks is extremely sensitive to the C/O ratio, in a way that is well-known from older calculations for red giant spectral type M, S, and carbon stars. The most obvious and severe case is C/O>1, in which case CO (at disk pressures) or CO_2 (at planetary atmosphere pressures) will lock up essentially all the oxygen, leaving only free carbon. Planets formed under such conditions would have no water, whether endogenously produced or delivered by asteroids or comets. Their mantles should be composed of graphite-like material or metal carbides rather than silicates (SiC and TiC are likely candidates; see Kuchner and Seager 2006 for a recent discussion [1]). This is entirely analogous to the shift in molecular and condensation properties known to occur in S stars (C/O just smaller than unity, see Scalo and Ross 1976) and carbon stars (see Gilman 1969 for an early discussion of the solid condensation equilibria; Gail et al. 2004 for a recent model). Further chemical

---

[1] Kuchner and Seager (2006) discussed some of the possible characteristics of planets formed in a disk, or part of a disk, with C/O>1, and pointed out, following Lodders (2004), the possibility of C/O variations within a protoplanetary disk with average C/O<1. We do not consider the internal disk fluctuations here, but concentrate on the Galactic-scale fluctuations.

evolution studies for variable C/O can be found in Sharp (1990), and Lattimer et al. (1978) in the context of supernova explosions. Even at C/O<1, the chemical equilibrium can be severely shifted. Gaidos (2000) suggested important effects for C/O greater than 0.8-0.9, and similar sensitivity in the molecular abundances can be seen in the red giant atmospheric calculations of Scalo (1973). However the absence of water when C/O>1 is the focus here.

Liquid water is widely considered as a prerequisite for life (see Stillinger 1980, Wiggins 1990, Chaplain 2004, Brack 2006, and the comprehensive reviews by Eisenberg and Karuzman 2005, and Ball 2008 for discussions). For a more technical discussion emphasizing the lack of a quantitative theory of water that can explain its unusual properties, see the authoritative review by Dill et al. (2005). Although it is well-known that water also presents obstacles for life, for example hydrolysis of condensation biopolymers, e.g. Benner et al. (2004), the tentative consensus that water is indispensable for life, rather than life having adapted to take advantage of water's unique properties, has apparently only grown stronger with time. An example is the growing recognition that water, by virtue of its network structure with long-range correlations, plays an active role in many types of molecular recognition, a property that may be necessary even in the most primitive organisms (Fuxreiter et al. 2005, Garczarek et al. 2005; see Scalo et al. 2007, sec. 1.8A for a brief review). Bowron (2004) used orientational correlation functions of simulations of a number of interactions in acqueous environments to show the versatility of water in accomodating key structural motifs while maintaining its classical first-neighbor motif. However, the existence of abundant water is crucially dependent on the existence of free oxygen in excess of the mass of oxygen tied up in easily formed and abundant molecules CO and (at higher pressures) CO_2.

The probability of the existence of regions with excessive oxygen depends not only on the average carbon to oxygen ratio, but also on the fluctuations. The observed cosmic scatter in the oxygen abundance of the interstellar medium is known to be small, less than about 10-15% (Cartledge et al. 2005), while that of carbon is less certain. However, even at this level of fluctuations, the Galactic gas from which stars and planets form will have a patchy distribution of C/O, and planets will form from gas with a variety of C/O ratios depending on their time and place of birth. In particular, there will be patches with C/O > 1, especially if the average C/O in our Galaxy has been increasing with time. Here we argue that this is the case, and that, because of the negative radial gradient in C/O, much of the inner portion of our Galaxy is nearly filled with carbon-rich gas from which planets with significant water cannot form, and that this inner region is growing outward in a wave of dehydration.

A model for the expected spatial inhomogeneity in the C/O ratio needs to capture the following physical picture. Carbon and oxygen produced locally in explosions and winds are transported throughout the galaxy by interstellar turbulence, which also produces steep gradients that allow microscopic diffusion to homogenize the gas at very small scales. The balance between the variations generated by spotty sources and mixing due to diffusivity enhanced by gradient production controls the degree of fluctuations in carbon and oxygen abundances, and thus in the C/O ratio. Eventually gas with some C/O ratio will become incorporated into newly formed stars and planetary systems, and so the resulting stars and their associated planets will exhibit some probability distribution of the C/O ratio.

The situation is illustrated in Fig. 5.1, which shows initially circular disks of size L containing two different elements (or any passive scalar property) released into a synthetic stochastic velocity field with a Kolmogorov energy spectrum $E(k) \sim k^{-5/3}$ to mimic a realistic turbulent flow. The synthetic velocity field is purely incompressible; effects of compressibility are discussed Chapter 1. The velocity field (not shown) structure on scales larger than L primarily translates and rotates the blobs. At the same time, the velocity structure on scales smaller than L advects the material within the initial uniform-abundance disks into distorted forms that progressively reflect the velocity gradient structure on smaller and smaller scales. With no initial internal gradients, this abundance gradient structure takes the form of boundary distortions, tongues and tendrils, which spread away from the initial disks. With time, some substructures from different source disks come close to each other. The molecular diffusivity can then mix these small-scale substructures quickly because of the large gradients (note that, if there were no diffusivity, these substructures will just become hyperfinely intertwined, in principle to the scale of the mean free path, without interpenetration or true mixing). However, it is clear that there always exist regions in which the two elements are completely disjoint and have not mixed at all, giving an intrinsic feature of inhomogeneity in the abundance ratio.

We have developed a method to solve this problem for a particular element

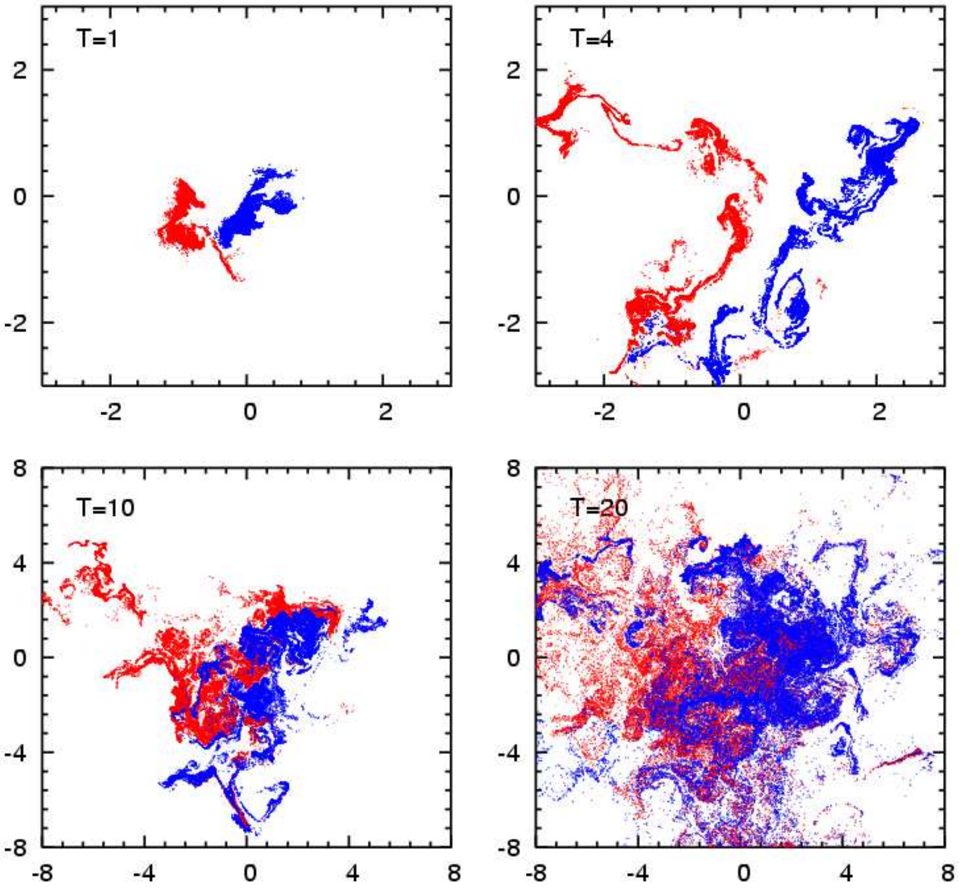

Figure 5.1 Illustration of turbulent transport of two elements.

Turbulent transport of two elements primarily produced in different nucleosynthesis sites in the ISM. Two parcels (circular disks) of particles, representing two different elements, say carbon and oxygen, are released at (-0.5, 0) and (0.5, 0) at time 0 into a synthetic stochastic velocity field. To mimic a realistic turbulent flow, the velocity field was designed to have a Kolmogorov energy spectrum. The four panels are snapshots of particle distributions at 1, 4, 10 and 20 times the flow correlation time. As the parcels are spread out by the large-scale flow, the strain field at smaller scales stretches the parcels and generates small scale structures that are washed out by microscopic diffusivity. The figure shows that, in a turbulent medium, small-scale fluctuations are a generic feature of the spatial distribution of elemental abundances and abundance ratios of elements produced in different nucleosynthesis sites.

by evolving the abundance probability distribution using a kinetic equation that self-consistently models the interaction between the stretching of fluid elements by advection and mixing by microscopic diffusion (Chapter 1, 2 and 3). The method can be generalized to describe the abundance probability distributions of any number of elements. Although we take a simpler approach here, we still deal directly only with the probability density function (pdf) of a concentration or ratio of concentrations. For the present purposes, this pdf can be regarded as a function $p(A)$ giving the fractional volume of the disk, or some large portion of the disk, in which the concentration (or the concentration ratio) of interest falls in a range dA about each possible value of A, irrespective of how this fractional volume is distributed in space. This is the one-point pdf; information about spatial correlations are contained in higher-point pdfs or their low-order moments (e.g. the correlation function). Our goal is to derive, from some information about the one-point pdfs of the abundances of C and O, the cumulative distribution function $P_c(\mathrm{C}>\mathrm{O})$ that gives the fractional volume occupied by regions with C/O>1. Specifically, we assume forms for the probability distributions of the individual elements and take their standard deviations from observations. We show how the pdf of the ratio depends on the ratio of the mean abundances, which, in the case of C/O, is a chronometer. Fortunately it turns out that our results depend only weakly on the assumed form of the underlying pdf of the individual elements, but is sensitive to their standard deviations. This method can be applied to any ratio of elemental abundances.

In §5.2, we briefly review the properties of the chemical evolution of C/O whose implications we explore in later sections. Some of our calculations and conclusions have a fairly strong dependence on these adopted properties. §5.3 develops a fairly general method for calculating the abundance correlation of two elements, which plays a crucial role in determining the ratio probability distribution and hence the filling fraction of carbon-rich regions. We show that the two abundance fields are uncorrelated if their sources are assumed to be independent, an unexpected result given that the transport process could create correlated structures for a single element. The calculations presented here are general, and make no reference to any particular transport or mixing process. Under this assumption, the difficulty of the problem is reduced greatly. In §5.4, we calculate how the filling fraction of carbon-rich regions in the Galaxy increases with the average value of C/O in some annulus in the Galaxy, and whether the results are sensitive to the assumed properties of the underlying pdfs of C and O individually. The prediction of carbon-rich stars is compared with observations in §5.5. In §5.6, we use a rough linear approximation to the time dependence of C/O in the models that were found to best match the CNO gradients by Carigi et al. (2005) in order to estimate the filling fraction of carbon-rich gas as a function of galactocentric radius and time. Our conclusions are given in §5.7.

5.2 Assumed C/O Behaviors and Evidence

We begin by considering the case in which C and O have completely different stellar sources. This assumption implies a patchy C/O distribution and a large variety of C/O ratios in gas clouds, from which planetary systems form. Although there is little doubt that nearly all oxygen is produced in high-mass stars, the fraction of carbon produced in stars of different masses has been uncertain for a number of reasons (see Carigi 2000, Henry, Edmunds, and Koppen 2000, Liang et al. 2001, and Prantzos 2004, Carigi et al. 2005, Favilan, Buell and Molla 2005). In particular, it is difficult to distinguish between models in which carbon production occurs primarily in massive stars with metallicity-dependent wind mass loss, or in low-to-intermediate mass asymptotic giant branch (AGB) stars. Most recent comparison of yield choices with observations now favor low-mass stars as the dominant production site, with carbon probably mixed from the interior and ejected in winds from asymptotic giant branch stars. The recent high spectral resolution study of Bensby et al. (2006) makes an especially strong case for this division of mass ranges for production of C and O. Our calculations that estimate the C/O fluctuations for a given mean $\langle C\rangle/\langle O\rangle$ depend on this separation of production sites. We examine the effect of correlation of production sites for C and O, due to the likelihood that a significant fraction of the C is produced in the massive stars that dominate the O production, in terms of a correlation coefficient in §5.3.2. We do not examine cases in which the relative contributions vary with time, even though this probably occurs, because our calculations are meant to illustrate effects, not produce a detailed chemical evolution models for the C/O ratio.

Although our results for the fraction of the ISM containing C>O gas at a given average C/O is not affected, in §5.4 and 5.6 we will explore the implications of an average C/O ratio that increases with time at a given galactocentric radius.

This behavior is expected as a consequence of the production of carbon primarily in low-mass stars, and is supported by several lines of evidence, including the increase with time of the average C/O ratio in many Galactic chemical evolution models (see Prantzos et al. 1994, Gustafsson et al. 1997, Portinari et al. 1998, Carigi 2000, Henry, Edmunds, and Koppen 2000, Liang et al. 2001, DeDonder & Vanbeveren 2004; Chiappini et al. 2003). In most models the increase in C/O only occurs after a time lag; Chiappini et al. (2003) pointed out that if C is made in low-to-intermediate mass stars, [C/O] should be flat with [O/H], which can be treated as a chronometer, until some threshold [O/H] that corresponds to the time for low-to-intermediate mass stars to leave the main sequence and reach the AGB phase. This is exactly what is seen in the thin disk sample of Bensby and Feltzing (2006) with the threshold occurring at [O/H] ~ -1. However a similar feature could occur due to metallicity-dependent winds in massive stars (see Carigi et al. 2006); but even in the model of Carigi et al., about half the carbon is produced in AGB stars after an age of about 3-4 Gyr.

There is also direct observational evidence for an increase of C/O with O/H and the existence of thin disk nearby solar type stars with C/O close to unity (e.g. Gustafsson et al. 1999, Fig. 7, Nissen 2002, Fig. 4; Bensby and Feltzing 2006, Fig. 12). Earlier results (e.g. Tomkin et al. 1995) that found no such trend are difficult to interpret because of the uncertain admixture of thick disk stars, for which Bensby and Feltzing find no increase in C/O with O/H.

Especially convincing are the results Bensby and Feltzing (2006) because of the careful kinematical separation of thick and thin disk stars and analysis of very high-resolution spectra. They find a clear correlation of [C/O] with [O/H] for thin disk field stars of F-G spectral type for stars having [O/H], with 7 out of 31 thin disk stars having [C/O]>0.1 dex relative to the Sun; the estimated total uncertainty in [C/O] due to errors in atmospheric parameters is estimated to be 0.03 to 0.07 dex for three stars. The ages of the Bensby and Feltzing stars are not known individually, but the most reasonable assumption is that they are uniformly distributed in age, with a mean age of at least 3-5 Gyr, making it reasonable that the average [C/O] in their sample is consistent with the solar ratio. The largest C/O in the sample has C/O = 0.87 if C/O is taken as C/O=0.5 for the Sun, and the next largest 0.69. These are consistent with what Esteban et al. (2005) claim should be the present-day C/O ratio in the solar neighborhood based on a small sample of HII regions distributed in galactocentric radius, as described below, and the rate of increase in C/O that we will adopt in §5.4 and 5.6 based simply on a linear increase from the solar C/O to a present-day C/O of 0.8.

A definite and strong increase in C/O ratio with O/H ratio (considered a proxy for the degree to which the galaxy has evolved) is also observed in Galactic and extragalactic HII regions in disk and irregular galaxies (e.g. Kobulnicky and Skillman 1998, Garnett et al. 1999, Henry et al. 2000).

The increase of C/O with time should manifest itself in finding the largest C/O ratios in the youngest objects. Two young classes of objects that have been studied are the OB stars (see Cunha and Daflon 2005 for a summary) and the Cepheid variables (see Luck, Kovtyukh, and Andrievsky 2006 and references given there). In none of the lists of subsamples of these objects that included C and O could an enhancement in the mean C/O be seen. For example the C/O values given in Luck et al. (2006) is rather uniformly distributed between about 0.2 and 0.6. A similar result is found for the lists of C and O abundances for OB stars in different ranges of galactocentric distances by Cunha and Daflon (2005 and references therein).

There now seems to be little doubt that the carbon production rate has increased faster with time than that of oxygen. The unexplained exceptions are the young OB and Cepheid variables for which available abundance determinations give C/O smaller than solar in most cases. Given the number of field stars and extragalactic HII regions that appear to have C/O close to unity, we assume that a successful chemical evolution model must be able to account for a C/O ratio that increases with time. This will lead to the result that the filling fraction of regions with C/O>1 increases with time.

The actual form of the increase of the average C/O ratio with time in either models or observations is very uncertain. In particular, whether or not the annulus-averaged C/O ratio at any galactocentric radius ever does exceed unity depends on whether significant carbon production takes place in low-to-intermediate mass AGB stars and whether the differential in production rate between C and O saturates at some value after a time that is roughly the difference between the lifetime of a massive star and the lifetime of the lowest-mass star that becomes an AGB carbon-producer. Presently the degree to which mixing of fresh carbon occurs in the lower-mass AGB stars remains very uncertain, and so it is not known how much of the distribution of yield of C versus initial mass comes from very long-lived stars. The helium-and-carbon-rich intershell convection during shell helium flashes has been found to invade the hydrogen-rich layers above only for very metal-poor models, but the problem is one of turbulent mixing and will not be solved except with very high-resolution multidimensional hydrodynamic simulations. The progress in this area has been rapid (see Herwig et al. 2007 for a review). If such mixing does occur in $1-1.5M_{\odot}$ stars, then saturation at larger values of C/O is likely. We will simply assume a linear increase that fits the available results, so the timescales in our calculations must be regarded only as illustrative.

Finally, in studying the difference in C/O change with galactocentric distance R_G, we will examine the implications of a negative radial C/O gradient in our Galaxy. Such a gradient was found in the HII region analysis of Esteban et al. (2005), is seen in HII regions in other spiral galaxies consistently since Garnett et al. (1999; see Prantzos 2004), and is predicted by some chemical evolution models (see e.g. Carigi et al. 2005). However just as with the predicted increase in C/O, we find little evidence for a radial gradient in C/O from abundance analyses of Cepheids and OB stars, although we note that in Daflon and Cunha (2005), the combined data from three recent studies including their own gives a C gradient fit that is definitely steeper than that of O, and the combined sample in their Table 2 gives a gradient in C/O of -0.023 dex kpc^{-1}. This is still considerably smaller than adopted here (-0.058 dex kpc^{-1}).

Therefore, while we recognize the uncertainty in the gradient adopted, we use it as an illustration of the consequences, which are that a negative C/O radial gradient, combined with the adopted increase of C/O with time, for which we think there is strong support, gives rise to an outward-propagating dehydration wave that is approaching the solar galactocentric radius. The effect of reducing or removing the gradient is simple to understand; for example, with no gradient in C/O, all parts of the disk would exceed a mean C/O=1 at the same time, and the Galaxy would become uniformly dehydrated with a filling factor whose timescale to fill the Galaxy depends on the variance in the C and O abundances, as we show below.

5.3 Abundance Correlation of Two Elements

The abundance correlation between two elements is a crucial quantity for determining the probability distribution function of the abundance ratio. In this section we give a general approach to compute the correlation between any two elements transported and mixed in the ISM turbulence. We show that abundances of two elements are uncorrelated if their sources are independent. This result greatly simplifies our calculations for fluctuations in the C/O ratio.

We start with advection-diffusion equations that describe turbulent transport and mixing of two elements in the ISM,

$$\frac{\partial A}{\partial t} + \mathbf{v} \cdot \nabla A = \frac{1}{\rho} \nabla \cdot (\rho \kappa_A \nabla A) + S_A \tag{5.1}$$

and

$$\frac{\partial B}{\partial t} + \mathbf{v} \cdot \nabla B = \frac{1}{\rho} \nabla \cdot (\rho \kappa_B \nabla B) + S_B \tag{5.2}$$

where A and B denote the concentration fields of the two elements and $\mathbf{v}$ is the turbulent velocity field in the ISM, in general a complicated function of position and time. Equations (5.1) and (5.2) are exact, and make no assumptions about compressibility, or homogeneity, omitting only cross terms that would arise if, for example, A and B could chemically react. The molecular diffusivities κ_A and κ_B can be estimated for a mostly neutral gas by $v_{th}/(n\sigma)$ where v_{th}, n and σ are the thermal velocity, the number density of the interstellar gas and the particle cross section, respectively. For a mostly neutral gas the diffusivity is inversely proportional to ρ, so we take $\rho\kappa$ to be constant, neglecting its temperature dependence, and it can be taken outside the gradient, The diffusivity terms then become $\kappa_A \nabla^2 A$ and $\kappa_B \nabla^2 B$. The source terms S_A and S_B correspond to release of fresh metals from SN explosions and stellar winds into the ISM. Additional terms to account for infall, inflow, or other effects could be easily included.

From eqs. (5.1) and (5.2), we derive an equation for the correlation of A and B, defined as $\langle A(\mathbf{x})B(\mathbf{x})\rangle$ at some point $\mathbf{x}$ with $\langle ... \rangle$ denoting the ensemble average,

$$\begin{gathered} \partial\langle AB\rangle/\partial t + \langle \mathbf{v} \cdot \nabla AB\rangle = \kappa_A \nabla \cdot \langle B\nabla A\rangle + \kappa_B \nabla \cdot \langle A\nabla B\rangle \\ -(\kappa_A + \kappa_B)\langle \nabla A \cdot \nabla B\rangle + \langle S_A B\rangle + \langle S_B A\rangle \end{gathered} \tag{5.3}$$

To solve this equation one needs to specify the advection term (a triple correlation), the diffusivity terms, and the source terms or relate them to the variable $\langle AB \rangle$ to be solved.

However, this is practically impossible without making severe assumptions. Consider the advection term as an example. In principle one can derive an equation for it from the momentum equation for the velocity field and eqs. (5.1) and (5.2). Unfortunately the derivation gives rise to 4th order correlations, and again a derivation of the 4th order correlation equations generates 5th order moments and so on. An assumption has to be made to truncate this hierarchy of moment equations to get a closed set. This is the so-called closure problem. A similar problem arises for the diffusivity terms, which are strongly coupled to the velocity field because of the rate of diffusion depends on the scale of gradients created by self-advection of the velocity field.

The essence of the intrinsic difficulty can be seen better using an idealized situation for illustration, in which all the fluctuations can be assumed to be statistically homogeneous. In this case, The closure problem for the advection term does not exist in an incompressible flow: $\langle \mathbf{v} \cdot \nabla AB \rangle = \nabla \cdot \langle \mathbf{v} AB \rangle$ vanishes because the correlation is spatially invariant under the assumption of statistical homogeneity. This does not mean the velocity field has no effect on the correlation (see below). Similarly the first two diffusivity terms on the RHS also vanish from the homogeneity assumption. However, the third diffusivity term $-(\kappa_A + \kappa_B)\langle \nabla A \cdot \nabla B \rangle$, a correlation between gradients of A and B that corresponds to homogenization by turbulence-enhanced mixing, does not vanish even in the idealized situation and always has a closure problem.

In order to evaluate the gradient correlation of A and B, we write it as $\langle \nabla_x A(\mathbf{x}) \cdot \nabla_{x'} B(\mathbf{x}') \rangle$ in the limit $\mathbf{x}' \to \mathbf{x}$. Taking the gradients out of the ensemble average, we have the gradient correlation equal to $\nabla_x \cdot \nabla_{x'} \langle A(\mathbf{x}) B(\mathbf{x}') \rangle$. Assuming statistical homogeneity, the 2-point cross correlation function $\langle A(\mathbf{x}) B(\mathbf{x}') \rangle$ is a function of the spatial lag $\mathbf{r} = \mathbf{x} - \mathbf{x}'$ only, i.e., $\langle A(\mathbf{x}) B(\mathbf{x}') \rangle = R_{AB}(\mathbf{r})$. Therefore the gradient correlation can be written as $-\nabla_r^2 R_{AB}(\mathbf{r})$ in the limit $\mathbf{r} \to 0$. Clearly the gradient correlation depends on the 2-point correlation function of A and B. One is then motivated to derive an equation for the correlation function from eqs (5.1) and (5.2),

$$\partial\langle A(\mathbf{x})B(\mathbf{x}')\rangle/\partial t + \langle \mathbf{v}(\mathbf{x})\cdot\nabla_x A(\mathbf{x})B(\mathbf{x}')\rangle + \langle \mathbf{v}(\mathbf{x}')\cdot\nabla_{x'} A(\mathbf{x})B(\mathbf{x}')\rangle = \kappa_A \nabla_x^2 \langle A(\mathbf{x})B(\mathbf{x}')\rangle \\ +\kappa_B \nabla_{x'}^2 \langle A(\mathbf{x})B(\mathbf{x}')\rangle + \langle S_A(\mathbf{x})B(\mathbf{x}')\rangle + \langle S_B(\mathbf{x}')A(\mathbf{x})\rangle. \tag{5.4}$$

Note that eq. (5.3) is a contraction of this equation in the limit $\mathbf{x}' \to \mathbf{x}$. The correlation $\langle AB\rangle$ can be obtained by solving eq. (5.4) for the correlation function and take the zero separation limit. We find that the diffusivity terms in eq. (5.4) are in a closed form from the statistical homogeneity assumption: $\nabla_x^2\langle A(\mathbf{x})B(\mathbf{x}')\rangle = \nabla_{x'}^2\langle A(\mathbf{x})B(\mathbf{x}')\rangle = \nabla_r^2 R_{AB}(\mathbf{r})$ has an explicit dependence on the correlation function to be solved. However, the advection terms here, 2-point 3rd order correlation functions, are not closed. Similar to the advection term in eq. (5.3), derivation of an equation for this correlation function brings up 2-point 4th order correlation functions, and so on. Note that, different from the case of eq (5.3), the advection terms here do not vanish from the incompressibility and the statistical homogeneity assumptions. In fact, they represent generation of small-scale structures by turbulent stretching. Transforming eq. (5.4) into Fourier space, the advection terms become the transfer function for the cross power spectrum of A and B and are thus responsible for transfer of fluctuations to small scales (see Fig. 5.1), where diffusivity can operate fast. In this way, the turbulent velocity field gives important effects on the abundance correlation of two elements. To close the advection terms in eq. (5.4), one could apply closure approximations, e.g, EDQNM (Lesieur 1990), or use simplifying assumptions for the velocity field that lead to a solvable equation, e.g., a temporally decorrelated velocity field proposed by Kraichnan (1968).

Here we do not use such methods to derive the cross correlation function for A and B. Instead, we give a formal solution for the correlation function, then by an analogy to a single passive scalar, we argue that the phenomenological theories for a single scalar field can also be applied to the two scalar case. This can already be seen in eq. (5.4), which is very similar to the equation for the correlation function of a single scalar.

Since the advection eqs. (5.1) and (5.2) are linear in concentration fields A and B, we can use the method of Green functions. We denote the Green functions of eqs. (5.1) and (5.2) as $G_A(\mathbf{x}, t|\mathbf{x}', t')$ and $G_B(\mathbf{x}, t|\mathbf{x}', t')$, respectively. Note that G_A and G_B only depend on the turbulent velocity field $\mathbf{v}$ and the diffusivities κ_A and

κ_B. Thus we have $G_A = G_B$ if $\kappa_A = \kappa_B$, which is approximately true for elements with similar masses, e.g., C and O. The solutions for A and B can be formally expressed as,

$$A(\mathbf{x}, t) = \int G_A(\mathbf{x}, t|\mathbf{x}', t')S_A(\mathbf{x}', t')d\mathbf{x}'dt' \tag{5.5}$$

and

$$B(\mathbf{x}, t) = \int G_B(\mathbf{x}, t|\mathbf{x}', t')S_B(\mathbf{x}', t')d\mathbf{x}'dt' \tag{5.6}$$

Here we make another assumption: the source terms are independent from the velocity field. This is not true near the sources, assuming the interstellar turbulence is driven by SN explosions. However, the assumption is justified by the fact that most of the mixing occurs far from sources, where the velocity field reflects a large number of sources or other effects. From this assumption, it follows immediately that S_A and S_B are independent of the Green functions G_A and G_B. Thus the correlation function between A and B can be calculated from,

$$\langle A(\mathbf{x}, t)B(\mathbf{x}', t)\rangle = \int \langle G_A(\mathbf{x}, t|\mathbf{x}_1, t_1)G_B(\mathbf{x}', t|\mathbf{x}_2, t_2)\rangle\langle S_A(\mathbf{x}_1, t_1)S_B(\mathbf{x}_2, t_2)\rangle d\mathbf{x}_1dt_1d\mathbf{x}_2dt_2. \tag{5.7}$$

This formal solution shows that the Green function for the cross correlation function is given by $\langle G_A(\mathbf{x}, t|\mathbf{x}_1, t_1)G_B(\mathbf{x}', t|\mathbf{x}_2, t_2)\rangle$.

Similarly, from its formal solution, the Green function for the correlation function of a single scalar A (say) is $\langle G_A(\mathbf{x}, t|\mathbf{x}_1, t_1)G_A(\mathbf{x}', t|\mathbf{x}_2, t_2)\rangle$. In the case of equal κ_A and κ_B, the Green function for the cross correlation function is the same as that for the one scalar correlation function because $G_A = G_B$. Therefore we can apply phenomenological theories for a single scalar to the case of two scalars.

For example, the conventional picture for turbulent advection of a single scalar is a cascade of fluctuations from the injection scale to small scales. The cascade predicts a $-5/3$ scalar power spectrum at convective-inertial scales, with a timescale mainly determined by the timescale of large-scale eddies. We can reach similar results for the two-scalar case. A cascade in the cross spectrum to dissipative scales is expected. In particular, the method used to derive the variance evolution from the cascade picture for a single scalar can be translated to calculate the two scalar correlation of interest here. We just need to replace the source spectrum of a single scalar by the cross-source spectrum of the two elements. Similarly, we can also generalize the new "short-circuit" picture for turbulent mixing, which is dominated by a single-step exponential stretching from the source size to the diffusion scale, favored by recent experiments and numerical simulations (see Chapter 3 for a review and the references therein), to the correlation of two scalars. In the two-scalar case, the source size would probably be replaced by the correlation length scale of the two sources. In the present study, we do not use these models to estimate the correlation between two elements because, as shown below, the two concentration fields of special interest here, are likely to be independent. An estimate of the correlation is thus unnecessary and the calculation is greatly simplified. We will investigate the potential correlation effect by parametrization using a correlation coefficient in §5.4.2.

A case of special interest here is the one with independent source terms S_A and S_B. The source terms are independent if A and B are produced by stars in very different mass ranges. As discussed in §5.2, oxygen is produced almost entirely in massive stars and there is increasing evidence that carbon is primarily produced in low mass to intermediate mass stars (see Bensby et al. 2006). We assume that *all* O (C) is produced in high (low) mass stars. Although its validity for C is uncertain, this assumption will still produce instructive results. From eq. (5.7), we see that if the source terms are independent, i.e., $\langle S_A(\mathbf{x}, t) S_B(\mathbf{x}', t')\rangle = 0$, the concentration fields A and B are also independent, i.e., $\langle A(\mathbf{x}, t) B(\mathbf{x}', t)\rangle = 0$. This implies that the advecting velocity field does not tend to create correlation between two passively advected concentration fields A and B. The result seems to be counter-intuitive because turbulence does produce coherent structures for a single passive scalar. These structures correspond to finite correlations over distances. Even if the forcing source (say, S_A) is spatially uncorrelated, i.e., $\langle S_A(\mathbf{x}) S_A(\mathbf{x}+\mathbf{r})\rangle = \delta(\mathbf{r})$, coherent structures can be generated because turbulent stretching tends to disperse particle pairs of an infinitesimal separation ($\mathbf{r} \to 0$) to a finite distance. However, the situation for the cross correlation is completely different. If the sources for A and B are independent, then source cross correlation $\langle S_A(\mathbf{x}) S_B(\mathbf{x}+\mathbf{r})\rangle$ is not a delta function, instead it is exactly zero. Therefore, although turbulence can create coherent structures for both fields, structures in one field are always independent of those in the other field because their sources are deposited in a complete random way. This result significantly simplifies our calculations.

5.4 Cumulative Probability for C $>$ O

The probability distribution of the abundance ratio of two elements A and B can be derived from the joint probability distribution of the abundances of the two elements. A general method to calculate the pdf of ratios of any two random variables is outlined in Appendix A. As shown in the last section, the concentration fields of two elements are independent from each other if their sources are independent, as assumed for carbon and oxygen. In this case, the joint probability distribution is given by the product of the individual abundance probability distributions of the two elements. Unfortunately, the probability distributions of abundances in the ISM are currently beyond precise observational measurements and theoretical predictions are model-dependent (see Chapter 1 which investigates the metallicity probability distribution with a model that self-consistently accounts for various effects in the ISM, especially the physics of mixing in turbulence). Therefore it is necessary to use various trial forms for the one-point pdfs of individual forms and investigate how the results depend on the choice of form.

5.4.1 Independent sources

Since observations traditionally give abundances in unit of dex, we will assume the distribution functions for the logarithm of concentrations, $a = log(A)$ and $b = log(B)$ instead of the distributions of A and B in linear scale. The calculation is easier in the logarithmic scale than that in the linear scale, given in Appendix A, because in units of dex the ratio r of two abundances, $r = log(A/B)$, becomes the difference of two variables a and b, i.e., $r = a - b$. We will use brackets to denote the logarithm of average abundance ratios, e.g., [C/O] means the average ratio of C and O in unit of dex. Note that usually [X/Y] is used for the logarithm of an abundance ratio relative to the solar abundance. In our notation, it denotes the logarithm of the absolute value of the mean abundance ratio and has no reference to solar abundances or abundance ratios.

The distribution of $r = a - b$ can be calculated from the distribution functions of a and b,

$$\begin{aligned} P(r) &= \int_{-\infty}^{+\infty}\int_{-\infty}^{+\infty} \delta(r-a+b)P_a(a)P_b(b)dadb \\ &= \int_{-\infty}^{+\infty} P_a(r+x)P_b(x)dx \end{aligned} \tag{5.8}$$

where P_a and P_a are probability functions of a and b respectively. In the second equality we integrated the variable a and changed the integral variable b to x. We assume P_a and P_b have the same shape but different means and standard deviations. They can be written as

$$P_a(a) = \frac{1}{\sigma_a} f(\frac{a-\langle a\rangle}{\sigma_a}) \tag{5.9}$$

and

$$P_b(b) = \frac{1}{\sigma_b} f(\frac{b-\langle b\rangle}{\sigma_b}) \tag{5.10}$$

where $\langle a\rangle$ and $\langle b\rangle$ denote the averages of a and b and σ_a and σ_b are their standard deviations, respectively. The function $f(x)$ represents the shape of the distribution of a and b and is normalized to have zero mean and unit standard deviation. The assumption of an identical shape for pdfs of a and b is justified by the fact that both A and B are released from similar sources, i.e., discrete stochastic events such as SNe, SBs, or AGB winds, and transported and mixed by the same ISM turbulence.

Inserting eqs. (5.9) and (10) in eq (5.8) and changing integral variables gives

$$P(r) = \int_{-\infty}^{+\infty} \frac{1}{\sigma_a} f(\frac{r+\sigma_b y - \langle a\rangle + \langle b\rangle}{\sigma_a}) f(y)dy \tag{5.11}$$

The quantity of interest here is the cumulative probability P_c that the abundance of the element A is larger than that of B, i.e., $A > B$, or equivalently $r = log(A/B) > 0$. Clearly $P_c = \int_0^{+\infty} P(r)dr$. Using eq (5.11) and changing integral variables, we get,

$$P_c = \int_{-\infty}^{+\infty} dy f(y) \int_{\frac{\langle b\rangle - \langle a\rangle}{\sigma_a}}^{+\infty} dx f(\tfrac{\sigma_b}{\sigma_a} y + x) \tag{5.12}$$

The cumulative probability P_c depends on the mean difference $\langle b\rangle - \langle a\rangle$ of a and b (corresponding to the ratio of average abundances of A and B) and their standard deviations. The probability P_c as a function of the mean difference and the standard deviations is calculated using three different assumed forms for $f(x)$.

1. Gaussian distribution

If a and b are Gaussian, then r, a difference of two Gaussian variables, is also normally distributed with a mean equal to the mean difference of a and b (i.e., $\langle b\rangle - \langle a\rangle$) and a variance equal to the sum of the individual variances (i.e., $\sigma_a^2 + \sigma_b^2$). This can be shown by explicitly integrating eq (11). The cumulative possibility P_c is then given by an error function,

$$P_c = \int\limits_{\frac{\langle b\rangle - \langle a\rangle}{\sqrt{\sigma_a^2+\sigma_b^2}}}^{+\infty} \frac{1}{\sqrt{2\pi}} exp(-x^2/2)dx \tag{5.13}$$

2. Exponential distribution

We next consider an exponential form for $f(x)$,

$$f(x) = \frac{1}{\sqrt{2}} exp(-\sqrt{2}|x|) \tag{5.14}$$

where $\sqrt{2}$ is chosen so that $f(x)$ has unit standard deviation. Inserting eq. (5.14) into eq. (5.12), we find,

$$P_c = \frac{1}{2}(1+sgn(\langle a\rangle - \langle b\rangle)(1-\frac{1}{\sigma_a^2-\sigma_b^2}(\sigma_a^2 exp(-\sqrt{2}\frac{|\langle a\rangle - \langle b\rangle|}{\sigma_a})-\sigma_b^2 exp(-\sqrt{2}\frac{|\langle a\rangle - \langle b\rangle|}{\sigma_b})) \tag{5.15}$$

where $sgn(x)$ is equal to 1 for positive x and -1 for negative x.

For the special case with $\sigma_a = \sigma_b = \sigma$, both the denominator and numerator of the last term in eq. (5.15) vanish. The term is evaluated using L'Hospital's rule,

$$P_c = \frac{1}{2}(1 + sgn(\langle a\rangle - \langle b\rangle)(1 - (1 + \frac{\sqrt{2}(|\langle a\rangle - \langle b\rangle|}{2\sigma})exp(-\sqrt{2}\frac{|\langle a\rangle - \langle b\rangle|}{\sigma}))) \tag{5.16}$$

3. Uniform distribution

Finally we use a uniform distribution

$$\begin{aligned} f(x) &= 0 && x < -\sqrt{3} \;\; or \;\; x > \sqrt{3} \\ &= \tfrac{1}{2\sqrt{3}} && -\sqrt{3} < x < \sqrt{3} \end{aligned} \tag{5.17}$$

where $\sqrt{3}$ is again chosen so that $f(x)$ has unit variance. After a straightforward but somewhat tedious calculation, we find,

$$\begin{array}{lll} P_c & = 0 & \langle b\rangle - \langle a\rangle > \sqrt{3}(\sigma_a + \sigma_b) \\ & = \frac{1}{24\sigma_a\sigma_b}(\sqrt{3}\sigma_a + \sqrt{3}\sigma_b - (\langle b\rangle - \langle a\rangle))^2 & \sqrt{3}|\sigma_a - \sigma_b| < \langle b\rangle - \langle a\rangle < \sqrt{3}(\sigma_a + \sigma_b) \\ & = \frac{1}{2} - \frac{\langle b\rangle - \langle a\rangle}{2\sqrt{3}Max(\sigma_a,\sigma_b)} & -\sqrt{3}|\sigma_a - \sigma_b| < \langle b\rangle - \langle a\rangle < \sqrt{3}|\sigma_a - \sigma_b| \\ & = 1 - \frac{1}{24\sigma_a\sigma_b}(\sqrt{3}\sigma_a + \sqrt{3}\sigma_b + (\langle b\rangle - \langle a\rangle))^2 & -\sqrt{3}(\sigma_a + \sigma_b) < \langle b\rangle - \langle a\rangle < -\sqrt{3}|\sigma_a - \sigma_b| \\ & = 1 & \langle b\rangle - \langle a\rangle < -\sqrt{3}(\sigma_a + \sigma_b) \end{array} \tag{5.18}$$

The results for the cumulative probability representing the fraction of volume occupied by regions with C>O as a function of the logarithmic mean ratio ⟨C⟩/⟨O⟩ (denoted as [C/O] in the figure) for different distributions, assumed to have an identical form for C and O, are shown in Fig. 5.2, where we adopted a cosmic scatter of $\sigma_a = \sigma_b = 0.05$ dex according to recent observational results on the chemical homogeneity in various objects (see Chapter 3). An upper limit of 0.05 dex for the metallicity scatter in the present-day ISM is found (Cartledge et al 2006). As seen in Fig. 5.2, the dependence of cumulative probability P(C>O) on [C/O] turns out to be insensitive to the shape $f(x)$ of the underlying pdf, allowing us the luxury of obtaining indicative results without solving the entire kinetic equation for the pdf (Chapter 1), whose form would depend on the assumed chemical evolution model and other parameters. We also tried power-law forms for $f(x)$ and found that P(C>O) as a function of [C/O] is not qualitatively different from the three forms we show here.

Fig. 5.3 shows the filling fraction of carbon-rich regions as a function of the average C/O ratio for Gaussian distributions of C and O logarithmic abundances, but with different standard deviations, σ. The variation with σ is significant, although the forms and the general conclusions are not altered. We take $\sigma_a = \sigma_b = 0.05$ dex as our fiducial cosmic scatter, since it is representative of upper limits estimated for a number of elements from a variety of methods reviewed in Chapter 3. However we point out that abundance scatter predicted by the models decreases with time, thus a more realistic calculation needs to include the time dependence of the scatter.

The results show that at the solar [C/O]=-0.27 dex (Aspund et al. 2006), or equivalently $\langle \mathrm{C}\rangle/\langle \mathrm{O}\rangle = 0.54$, the fraction of the ISM gas with C>O is $\sim 10^{-4}$,

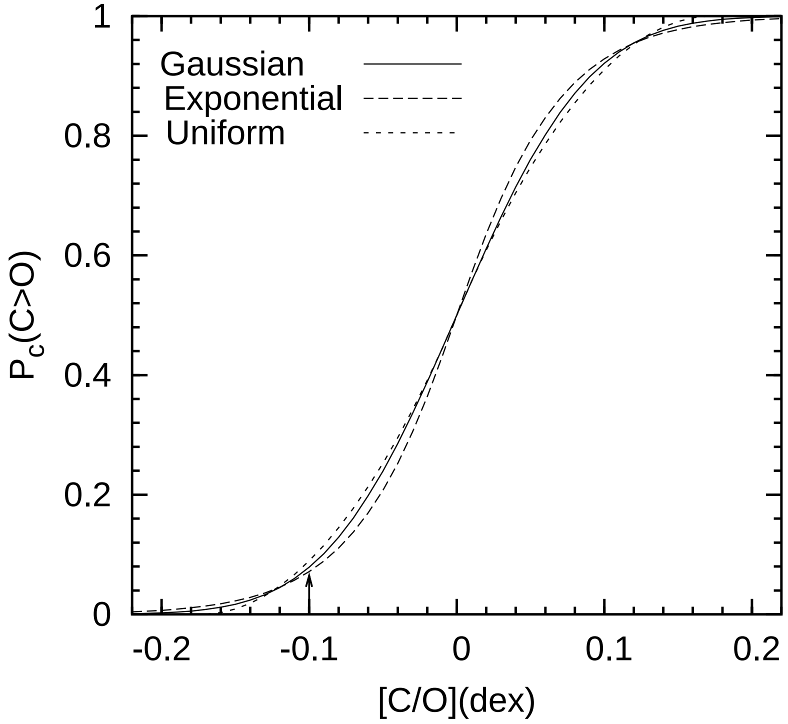

Figure 5.2 Predicted filling fraction of carbon-rich gas from different pdfs.

Fraction of carbon-rich gas, P_c(C>O), as a function of the mean ratio of C and O abundances in logarithmic units, [C/O], predicted by three different pdfs for C and O abundances with a scatter of 0.05 dex. Although [X/Y] traditionally denotes abundances or abundance ratios relative to the solar value, here and in Figs. 5.3, 5.4, 5.5 and 5.6, we use [C/O] to just represent the logarithm of the average ratio, with no reference to the Sun. The solid, dashed and dotted lines correspond to Gaussian, exponential and uniform distributions for $f(x)$. The plot shows that the relation is insensitive to the form of the individual abundance distributions. The vertical arrow at -0.1 dex (C/O=0.79) indicates the adopted mean C/O ratio, based on Esteban et al. (2005) and the maximum C/O ratio in thin disk sample of Bensby and Feltzing (2006) with unknown uncertainty.

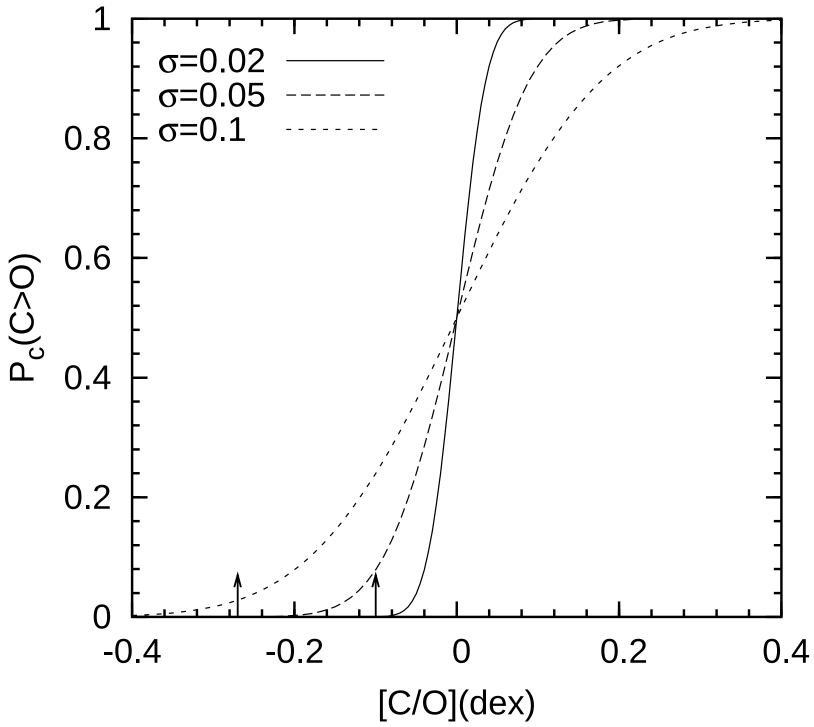

Figure 5.3 Predicted filling fraction of carbon-rich gas for different scatters. The filling fraction of carbon-rich regions, P_c(C>O), as a function of the mean C to O abundance ratio, [C/O], assuming Gaussian distributions for C and O abundances in logarithmic scale. The nucleosynthesis sources of C and O are assumed to be independent. The solid, dashed and dotted lines correspond to $\sigma_a = \sigma_b = 0.02$ dex, 0.05 dex and 0.1 dex respectively. The left arrow at -0.27 dex (C/O=0.54) indicates the observed C to O ratio in the Sun from Asplund et al. (2005) with an uncertainty of ± 0.05 dex. The right arrow is the adopted mean C/O ratio at present time as in Fig. 5.2.

for $\sigma = 0.05$ dex. Presumably the filling fraction of carbon-rich gas was negligible around the solar circle about 4-5 Gyr ago when the Sun was formed. According to Esteban et al. (2005) and other evidence summarized in §5.2, the current interstellar C/O ratio is about 0.79. This corresponds to 8% carbon-rich gas in the ISM today for $\sigma = 0.05$ dex. We will give the implications of this result by comparing with observations below.

As the mean ratio [C/O] approaches zero, as may be the case at the present time at a galactocentric distance of about 6 kpc using the C/O radial gradient found by Esteban et al. (2005; see §5.6 below), the fraction of gas with C/O>1 is about 0.5, independent of the dispersion and the form of the distribution $f(x)$. With increasing [C/O] the carbon-rich regions percolate to nearly fill the galaxy, a mirror image of the oxygen-rich case.

5.4.2 The correlation effect

We study the effect of correlation between sources of two element on the cumulative probability. The correlation between sources of two elements can be understood as meaning that they are both significantly produced in stars in a common narrow mass range so that the production sites of the two elements tend to be spatially correlated.

In §5.2, we showed that abundances of two elements are correlated if their sources are spatially correlated and how the correlation can be calculated using phenomenological theories originally proposed for a single scalar. If two elemental abundances are correlated, we need their joint pdf to derive the distribution of the ratio. The joint pdf can be determined from the individual pdfs and the correlation. The correlation of two abundances depends on their source correlation, which is difficult to quantify. Here we do not try to compute the correlation from a theoretical model, instead we parametrize it using a correlation coefficient,

$$R = \frac{\langle (a - \langle a \rangle)(b - \langle b \rangle) \rangle}{\sigma_a \sigma_b}. \tag{5.19}$$

Clearly, $R = 0$ corresponds to the independent case and $R = 1$ represents a complete correlation.

With the correlation coefficient we calculate the pdf of $r = a - b$ assuming individual distribution functions of a and b. If a and b are Gaussian, the joint pdf is given by,

$$\begin{array}{rcl} P(a,b) & = & (4\pi^2\sigma_a^2\sigma_b^2(1-R^2))^{-1/2} \\ & & \times exp(-\frac{1}{2(1-R^2)}(\frac{(a-\langle a\rangle)^2}{\sigma_a^2} - \frac{2R(a-\langle a\rangle)(b-\langle b\rangle)}{\sigma_a\sigma_b} + \frac{(b-\langle b\rangle)^2}{\sigma_b})) \end{array} \tag{5.20}$$

For arbitrary pdfs of a and b, there is no simple explicit form for the joint pdf. In that case, one can use variable changes to map a and b to Gaussian variables. The joint probability function of the new variables then has the form of eq. (5.20). Then the distribution of r, as a function of the new variables, can be determined from the joint pdf. The calculation is complicated and we will restrict our analysis to the Gaussian case for an illustration of the correlation effect on the cumulative probability.

The distribution of r can be derived in a similar way as in eq. (5.8),

$$P(r) = \int_{-\infty}^{+\infty} P(r+x,x)dx \tag{5.21}$$

Inserting eq. (5.20), we get,

$$P(r) = \frac{1}{(2\pi(\sigma_a^2 - 2R\sigma_a\sigma_b + \sigma_b^2))^{1/2}} exp(-\frac{(r+\langle b\rangle - \langle a\rangle)^2}{2(\sigma_a^2 - 2R\sigma_a\sigma_b + \sigma_b^2)}). \tag{5.22}$$

We see the distribution of r is Gaussian with variance $\sigma_a^2 - 2R\sigma_a\sigma_b + \sigma_b^2$, which reduces to the independent case if $R = 0$. The cumulative probability for $r > 0$ is again given by an error function,

$$P_c = \int_{\frac{\langle b\rangle - \langle a\rangle}{\sqrt{\sigma_a^2 - 2R\sigma_a\sigma_b + \sigma_b^2}}}^{+\infty} \frac{1}{\sqrt{2\pi}} exp(-x^2/2)dx. \tag{5.23}$$

Note that eq. (5.13) for independent A and B is a special case of this equation with $R = 0$.

The result is given in Fig. 5.4, which shows the effect of correlation on the cumulative probability as a function of the mean ratio. The solid, dashed and dotted lines correspond to the correlation coefficient $R = 0$ (independent), $R = 0.3$ and $R = 0.5$, respectively, for the case of a Gaussian pdf with a standard deviation of 0.05 dex for both C and O. For correlated sources, the fraction of carbon-rich regions is larger when [C/O]>0 and smaller when [C/O]<0. Obviously a strong source correlation means the C and O are deposited in the same regions of the ISM, and so mix more quickly, with little chance of finding a region, even near a source, that is extremely inhomogeneous.

The effect on the present-day local ISM prediction is that the fraction of regions with C/O>1 decreases from about 8% to about 2% as we go from the independent case to a correlation coefficient $R = 0.5$. Of course if the correlation were even larger, the fraction of carbon-rich regions would be even smaller, and we find that by $R = 0.9$ the fraction is completely negligible ($\lesssim 10^{-5}$). Given available evidence on the fraction of C and O produced in progenitor stars with various masses, we think a correlation coefficient of 0.5 is probably an upper limit. However the example does illustrate the sensitivity of the results to correlations in the sources, so that investigations of the statistics of elemental abundance ratios do need to carefully examine the uncertainty in the mass-dependent yields adopted for each element.

5.4.3 Fraction of C>O stars

We have developed a method for calculating the filling fraction of the ISM gas with C>O given the average mean ratio. To compare with observations of C and O abundances in stars, we assume that the probability distribution of the C/O ratio in stars formed at a given time samples the C/O distribution in the ISM. Under this assumption, the predicted fraction of carbon-rich stars formed at any time can be found from Fig. 5.3 and Fig. 5.4, given the average C/O ratio, the abundance scatter and the correlation coefficient. In order to explicitly see the sensitive dependence of the fraction on the abundance scatter, we plot in Fig. 5.5 the predicted fraction of carbon-rich stars as a function of the assumed scatter for two choices of the correlation coefficient: $R = 0$, and $R = 0.5$ at current time and at the Sun's formation. Again we adopt 0.79 for the current average C/O ratio and the solar value 0.54 for the average ratio at the Sun's formation. Same as the results given earlier for the current filling fraction of cabon-rich gas, the fraction of young stars with C>O is expected to be 8% for the fiducial scatter of 0.05 dex and a correlation coefficient of 0.5 reduces it to 2%. The fraction of carbon-rich

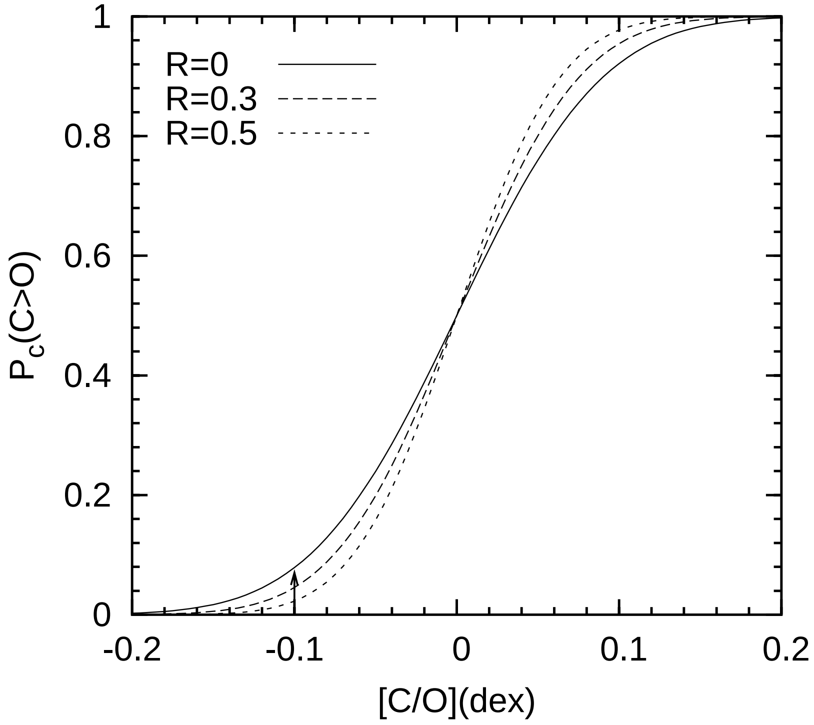

Figure 5.4 Filling fraction of carbon-rich gas for different correlation coefficients

The filling fraction of P_c(C>O) regions as a function of the mean ratio [C/O] for different choices of correlation coefficients (see the text for definition). The probability distributions of logarithmic C and O abundances are assumed Gaussian with a standard deviation of 0.05 dex. The solid, dashed, and dotted lines correspond to the correlation coefficient $R = 0$, 0.3, 0.5, respectively. The vertical arrow at -0.1 dex is the adopted mean C/O ratio (0.79) at present time as in Fig. 5.2.

stars has a strong dependence on the assumed abundance scatter for $\sigma < 0.1$ dex. If $\sigma \sim 0.1 - 0.2$ dex, the carbon-rich fraction is 10-20%. This fraction, if true, could have already been detected (see §5.5). Lack of observed carbon-rich young stars therefore rules out a large abundance scatter in the current ISM. This is consistent with the observed small metallicty scatter in the present-day ISM. At the Sun's mean C/O ratio, the fraction of carbon-rich stars is much smaller, 10^{-4}. The fraction increases rapidly with the mean ratio, reaching the maximum today.

In order to compare with observations of low-mass stars, we also calculate the fraction of long-lived stars with C>O formed in the Galactic history as a function of the assumed abundance C and O scatter. The fraction is calculated by $\int B(t) P_c(\langle \mathrm{C} \rangle / \langle \mathrm{O} \rangle (t)) dt / \int B(t) dt$ where $B(t)$ is the star formation rate and the mean ratio $\langle \mathrm{C} \rangle / \langle \mathrm{O} \rangle$ is assumed to increase linearly with time. The increase rate is chosen such that the mean ratio is equal to the solar value at 4.6 Gyr ago and equal to 0.79 at the current epoch. We assume normal distributions for C and O logarithmic abundances. Two different SFHs are used, a constant star formation rate and an SFR exponentially declining with a timescale of 5 Gyr, for illustration. The results are shown in Fig. 5.6. For $\sigma = 0.05$ dex, the fraction is 0.5% for the case with constant SFR and is 0.06% for the exponential SFR. Also shown are the results for the correlation coefficient of R=0.5. This correlation reduces the fraction from 0.5% to 0.1% for the constant SFR and from 0.06% to 10^{-4} for the exponential SFR.

5.5 Observational Tests of Carbon Rich Stars

In this section we consider observational tests on our predictions.

Main sequence, or at least dwarf, carbon stars are known to exist since the discovery of the first dwarf carbon (dC) star, G77-61, by Dahn et al. (1977). The lack of another explanation for how a low-mass main sequence star could produce excess carbon led Dahn et al. to propose that it was a product of mass transfer from a secondary that had already passed through its asymptotic giant branch (AGB) phase with excess carbon mixed from its interior, transferred some of the material onto the lower-mass main sequence star, and presently is cooling as a white dwarf. This idea was supported by discovery of white dwarf companions and radial velocity variations in several dC stars (see Green 2000 for a review), the fact that

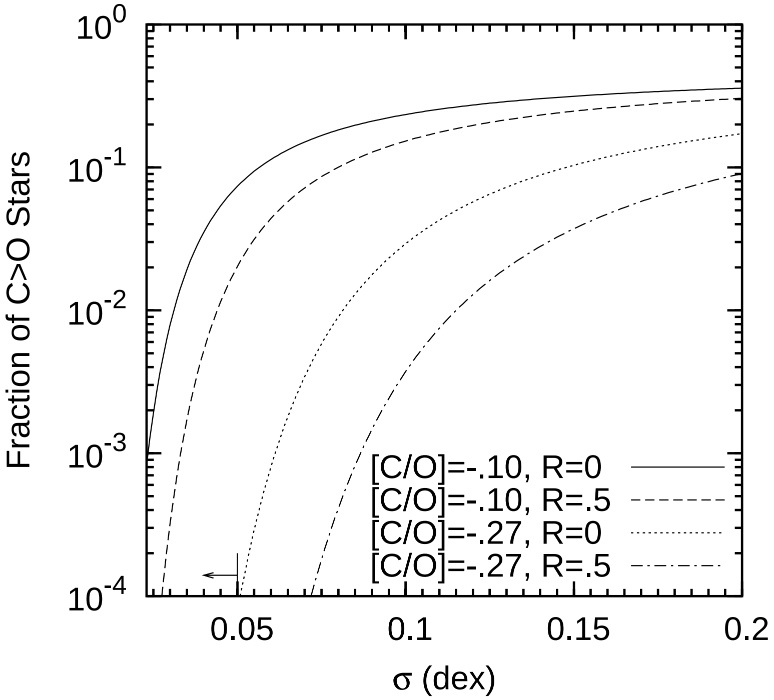

Figure 5.5 Fraction of carbon-rich stars at Sun's formation and today

Fraction of carbon-rich stars that formed 4.5 Gyr ago and that are forming today as a function of the assumed abundance scatter for C and O. We take the solar value, [C/O]=-0.27 dex (C/O=0.54), for the average C/O ratio at 4.5 Gyr ago and -0.1 dex (C/O=0.79) mean C/O ratio in the current ISM. For each case, two correlation coefficients $R = 0$ and $R = 0.5$ are shown. The probability distributions of logarithmic C and O abundances are assumed Gaussian. The fraction of carbon-rich stars has a very sensitive dependence on the scatter σ in C and O abunances at $\sigma \lesssim 0.1$ dex. It also has a strong dependence on the average C/O ratio and hence on time. At the Sun's formation, the fraction of C/O gas in the local ISM and thus stars formed then is $< 10^{-4}$ while the current fraction is 8% for $\sigma = 0.05$ dex and independent sources. The latter is probably an overestimate, a correlation coefficient of 0.5 reduces it to about 2% (see the text). The vertical bar and the arrow at 0.05 dex indicate the observed upper limit for abundance scatters in various objects (Chapter 3).

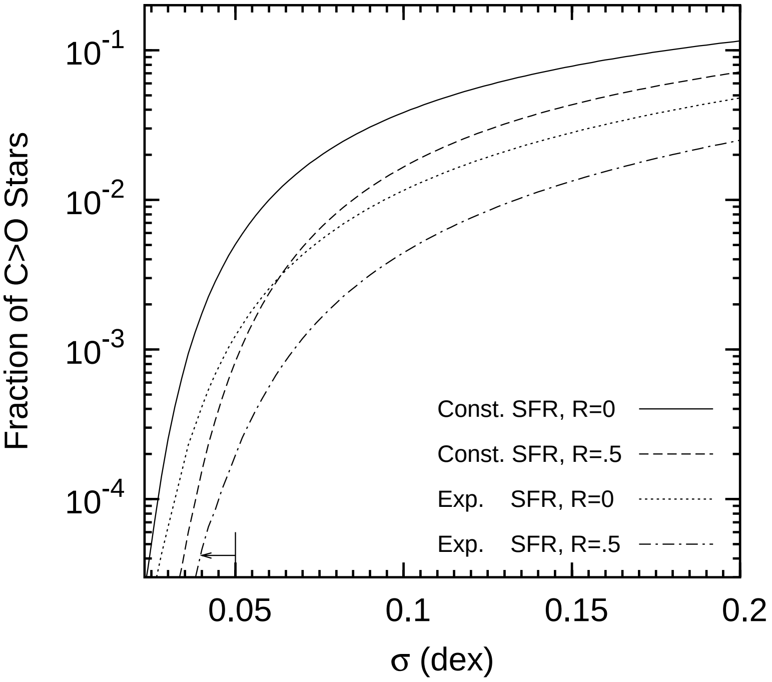

Figure 5.6 Fraction of long-lived stars with C>O.

Fraction of long-lived stars with C>O formed in the Galactic history as a function of the assumed abundance scatter for C and O. For illustration, the mean C to O ratio is assumed to increase linearly with time. The increase rate is chosen such that the mean ratio is equal to the solar value at 4.6 Gyr ago and is 0.79 at the current epoch. Two SFHs are used: a star formation rate (SFR) constant in time and an exponentially declining SFR. For each case we also show two choices of the correlation coefficient, $R = 0$ and $R = 0.5$. The probability distributions of logarithmic C and O abundances are assumed Gaussian. The fraction of carbon rich stars has a very sensitive dependence on the scatter σ in C and O abundances at $\sigma \lesssim 0.1$ dex. Depending on the abundance scatter, the SFH, and the correlation coefficient, the predicted fraction of carbon-rich stars varies from $10^{-4} - 10^{-2}$. Note that at the fiducial scatter of 0.05 dex, the constant SFR and $R = 0$ gives a fraction of 0.5%. A correlation coefficient of 0.5 reduces the fraction to 0.1%. A declining SFR gives a carbon-rich fraction below 10^{-3}. As in Fig. 5.5, the vertical bar and the arrow at 0.05 dex show the observed upper limit for abundance scatters in various objects.

essentially all higher-luminosity CH stars belong to systems with unseen companions (see McClure and Woodsworth 1990), and the establishment of enhanced s-process element abundances in a significant fraction of about 20 carbon-enhanced metal-poor (CEMP) stars studied (see Aoki et al. 2007).

A class of dC stars without s-process enhancements (the CEMP-no s stars) is also known to exist (see Aoki et al. 2002, Ryan et al. 2005), which might be thought to be candidates for the process discussed here, in which some fraction of stars are carbon-rich from birth. A binary mass-transfer scenario is also favored for carbon-enhanced extremely metal-poor (CEMP) stars (only some of them are dC stars; see Komiya et al. 2007 for a thorough review). We note that Karlsson (2006) suggested a local pollution scenario for extremely metal-poor carbon-enhanced stars, using a population of very massive rotating stars that end up as black holes while ejecting only their carbon-rich envelopes, an idea similar in kind to the idea developed here.

The Sloan Digital Sky Survey produced a major increase in the number of known dC stars, with Downes et al. (2004) finding about half of the 250 high-latitude carbon stars to be relatively nearby dC stars, confirming the earlier SDSS study by Margon et al. (2002). These numbers give information about the number of dC stars in a certain apparent magnitude interval by comparing with red giant carbon stars. However, it is not easy to obtain a space density, especially for the disk dC stars, because the red giant carbon stars do not have a well-established space density, and most of the giants detected are distant halo objects. Greene (2000) quotes a space density estimate of order 10^{-6} pc^{-3} for disk dC stars, but the uncertainty is great, and indeed it is not certain that there exist any disk population dC stars. Candidate C stars can also be found by color criteria, and then spectroscopic follow-up to find whether they are dwarfs. Lowrance et al. (2003) used this procedure on a sample of over 36,000 NLTT catalog objects cross referenced against 2MASS, and found two new dC stars. One of these (LSR 2105+2514) also showed up in a search for nearby cool dwarfs by Reid (2003).

However, the observations of most dC stars cannot be used to constrain our calculations for a number of reasons. Nearly all the dwarf carbon stars that have been studied are metal-deficient to various degrees (to an extreme degree for the halo dC stars), and are believed to be members of the halo or thick disk population. At the time of formation of such old stars, our calculations would predict a miniscule fraction of carbon-enhanced stars (see Fig. 5.3), too small to be detected even in the largest SDSS samples. Furthermore, the models presented here may not be applicable to old populations because of different contributions of different masses to carbon production than adopted in the present work. However we think color-based searches like that by Lowrance et al. (2003) and Reid (2003, which were not searching for dC stars) would provide a constraint if metallicities were estimated. We are unaware of an estimate of the metallicity of either of the two stars discovered by Lowrance et al.; if they are neither metal poor nor produced by mass transfer, then they provide a constraint on the carbon-rich fraction calculated here, although the selection effects inherent in the selection procedure would have to be accounted for. However, even with disk metallicities, the ages of such objects cannot be constrained, so it would not be possible to identify these objects with a mean C/O ratio (which is assumed to vary linearly with age in our model); depending on the mean ratio, the predicted fraction with C/O>1 could differ by orders of magnitude (Fig. 5.3).

The best chance of testing the present results lies in searches for carbon-rich dwarfs among young stars. The predicted fraction for young stars is largest for any given set of parameters. Carbon stars can be distinguished from other late-type stars unambiguously with even low-resolution spectroscopy. The ease of identification is due to the prominence of CN and C2 bands and absence of metal oxide bands in the visible region, or water vapor bands in the near-infrared for some brown dwarfs, for example. For this reason one possibility that only involves homogeneous samples of young stars is contained in the many studies of the low-mass stellar and brown dwarf populations in local clusters and groups. When not purely photometrically-based studies of the IMF, these surveys obtain spectra for between 50 and 500 stars for each region studied (see Hillenbrand 1997, Luhman et al. 2003, Slesnick et al. 2006, Levine et al. 2006, Luhman 2007, and references therein). Among the several thousand stars contained in these studies, we are not aware of a single carbon-rich star being identified. This result suggests that the fraction of C/O $>$ 1 stars is smaller than about 10^{-3} to 10^{-4}. This suggests that the abundance distribution in the regions out of which the clusters form is very homogeneous, smaller than about 0.02 dex. This would probably rule out the possibility of a large metallicity in the ISM, as discussed above. The carbon star found among several new low-mass stars in a survey of the young sparse cluster eta Cha by Luhman (2004) apparently turned out to be a field star, since it does not appear in subsequent lists of members for this group. Otherwise, the discovery of such an object could be interpreted as providing a limit on the current frequency of stars that are carbon-rich due to ISM chemical inhomogeneity.

Finally, we note that although the debris disk orbiting beta Pic has been found to be surprisingly carbon-rich (Roberge et al. 2006), the central star exhibits normal abundances, although the status of the C/O ratio is not clear. Holweger et al. (1997) found a solar carbon abundance using CI lines. Kamp, Hempel and Holweger (2002) determined oxygen and other abundances in A stars with debris disks, but the abundance determination depends sensitively on the well-known uncertainty in the NLTE correction for the oxygen 7774 triplet, a correction that averaged 0.5 dex for that sample. Since the carbon abundance may have an uncertainty of 0.2 to 0.4 dex, it is difficult to say whether C/O is less than unity, but it is certainly not as huge as the carbon enhancement found for the disk by Roberge et al., so it may be that segregation processes within the disk have altered the C/O ratio, not a low-probability birthplace. We are hopeful that a renewed analysis of C and O in beta Pic will result in a definitive answer to the normalcy of the C/O ratio.

A future search for carbon-rich stars would be greatly aided by some knowledge of the expected spatial scales on which the carbon enhancements should be occurring in today's solar neighborhood. The probability calculations presented here only deal with the one-point pdf of C/O ratios, and give no guidance on the expected spatial distribution of regions with carbon excesses. Fig. 5.1 indicates how a (synthetic) turbulent velocity field can produce structure on smaller and larger scales than the initial size of the sources, presumably supernova remnants. Most of the material that remains enhanced in one or the other element becomes striated on increasingly small scales. The size of the smallest structure is limited by microscopic diffusion which will smooth out abundance variations on scales $\sim$ 0.01-1 pc, depending on the interstellar environment. Stars that formed from molecular clouds much larger than this scale would have sampled and averaged over a range in C/O ratios, so it is possible that finding a trace of the phenomenon will be quite difficult, unless a region predicted to be mostly carbon stars could be studied for C/O ratios. Unfortunately only fairly massive stars are bright enough to be studied at such distances, and the abundance analyses difficult. The same remark applies to HII regions, for which only a small number of objects are available. If a large scale radial gradient, which we consider in next section, exists, the probablity of finding carbon-rich stars would be larger toward the direction of the gradient.

5.6 Propagation of the Dehydration Front

So far we have shown that the complex problem of turbulent transport and mixing of two elements produced in two different discrete and localized stellar sources can be reduced to a much simpler problem of probability transformations if we assume that the spatial distribution of sources is random. We justify this assumption in the C/O case by the continuing evidence (Bensby et al. 2006) that the primary source of carbon is low-mass stars, which wander far from their birthplace before the red giant phase during which mass is returned to the ISM, while it is generally accepted that oxygen is nearly all produced in core collapse supernovae associated with massive stars. Given our solution for the cumulative probability P_c(C/O>1) as a function of the mean ratio $\langle \mathrm{C} \rangle / \langle \mathrm{O} \rangle$ for a given standard deviation of the C and O abundances, in this section we show the radial gradient in C/O found by Esteban et al. (2005) from HII regions and predicted by some chemical evolution models should result in a transition to a large filling factor of C/O>1 ISM inside a certain critical galactocentric radius, and that the critical galactocentric radius moves outward with time at about 0.5 kpc/Gyr. We refer to this outward-moving transition annulus as a dehydration front.

The spatio-temporal evolution of C/O in our Galaxy can be estimated approximately by assuming that the ratio increases linearly with time, at a rate $\lambda_{(\mathrm{C/O})} = \mathrm{d(C/O)(R_G,t)/dt}$, and a present-day radial logarithmic C/O gradient $\Delta = \mathrm{d}\mathit{log}\mathrm{(C/O)/dR_G}$ dex/kpc is independent of galactocentric radius. These are severe assumptions, but the former is commonly made for elemental radial gradients (but see Maciel et al. 2006); the linear increase does not agree with several models that assume the C production cuts off below 3-4 $M_\odot$, but may be a better approximation if the C yields are allowed to increase down to 1 $M_\odot$, as is indicated by observations. Thus the results should only be interpreted as illustrating the expected behavior.

With these assumptions $\mathrm{d(C/O)(R_G,t)/dt} = \lambda_{(\mathrm{C/O})}$ gives

$$\mathrm{C/O(R_G,\ t)} = \mathrm{C/O(R_G,\ t_0)} + \lambda_{(\mathrm{C/O})}\mathrm{t} = \mathrm{(C/O)_0}\ \mathit{exp}(-2.3\Delta\mathrm{R}) + \lambda_{(\mathrm{C/O})}\mathrm{t} \quad (5.24)$$

where $\mathrm{t_0}$=0 refers to the present time, and the first term on the right follows from a linear fit to the present radial distribution *log* (C/O) $(\mathrm{R_G},\ \mathrm{t_0}) = \mathrm{A} + \Delta\ \mathrm{R_G}$, with $\mathrm{R_0}$ the Sun's galactocentric distance. We adopt the results of Esteban et al. (2005) for a fit to the HII region results and the best-fitting chemical evolution models, in which case $\Delta = -0.058$ dex/kpc, A = 0.36 (so the current average C/O ratio at the sun's position is 0.79), and

$$\mathrm{C/O(R_G,\ t_0)} = 2.29\ exp(-\mathrm{R}/7.46\ \ \mathrm{kpc}). \qquad (5.25)$$

Using $(\mathrm{C/O})_\odot = 0.54$ (Asplund et al. 2005) at 4.6 Gyr ago and C/O =0.79 for the present value at 8 kpc (Esteban et al. 2005) gives $\lambda_{(\mathrm{C/O})} = 0.052\ \mathrm{Gyr}^{-1}$. According to this rate of increase, the C/O ratio will reach unity at the Sun's galactocentric distance in 4.2 Gyr. However the models that agree best with the HII region data give a larger rate of increase, $\lambda_{(\mathrm{C/O})} = 0.087\ \mathrm{Gyr}^{-1}$. For this illustration we adopt an intermediate value $\lambda_{(\mathrm{C/O})} = 0.07\ \mathrm{Gyr}^{-1}$, so the solar galactocentric distance will exceed C/O = 1 in about 3 Gyr, and

$$\mathrm{C/O(R_G,\ t)} = 2.29\ exp(-\mathrm{R}/7.46\,\mathrm{kpc}) + 0.07(\mathrm{t}/1\ \mathrm{Gyr}). \qquad (5.26)$$

Galactocentric distances inward of R (C/O=1) = 6.18 − 7.46 *ln* (1 - 0.07 t/Gyr) ∼ 6.2 + 0.52 (t/Gyr) kpc have C/O > 1 and represent a dehydration front moving outward at an approximate rate 0.5 kpc/Gyr.

Using the mean C/O at each galactocentric radius R as a function of time, we calculate from eq. (5.13) the volume filling factor of pockets of C/O>1 gas as a function of $\mathrm{R_G}$ and time, P_c(C/O>1; R, t). We show the filling factor as a function of R for a Gaussian distribution of C and O abundances (the result is not sensitive to the assumed pdf) in Fig. 5.7 for several times and for the assumed standard deviation, 0.1 dex, of C and O. The transition at $\langle \mathrm{C} \rangle / \langle \mathrm{O} \rangle \sim 1$ is the dehydration front whose thickness depends on the assumed scatter σ of the C and O abundances and the mean radial gradient of the C/O ratio. The filling fraction as a function of $\mathrm{R_G}$ is basically a translation of the $P_c -$ [C/O] curve from the mean ratio [C/O] as a function of $\mathrm{R_G}$. Therefore, the P_c profile in Fig. 5.7 corresponds to the transition in Fig. 5.3 from small filling fraction to P_c close to unity. The change in the mean ratio across the front is then expected to be approximately equal to that over which the transition occurs in the $P_c -$ [C/O] curve in Fig. 5.3. For a scatter of 0.1 dex in C and O, typical of most observational determinations (Chapter 3), the transition occurs over a change of ∼ 0.3 dex in [C/O] (Fig 5.3). In this case, the front thickness can be estimated as 0.3 dex divided by the [C/O] radial gradient. For the gradient of -0.06 ± 0.02 dex kpc^{-1}, we get a front thickness of ∼ 5 kpc. This explains the very broad front shown in Fig. 5.7. The large front thickness is mainly due to the small mean [C/O] gradient. If the scatter in C and O abundances is 0.05 dex, a similar estimate gives a front thickness twice smaller, i.e., ~ 2.5 kpc.

If water is a requirement for life (see §5.7 for alternatives), then the filling of the Galaxy with carbon-rich regions spells a reduction and finally halt in the rate of production of life-bearing planets because it is unlikely that a nonequilibrium chemical process would allow substantial water or ice production at places with carbon abundance in excess of that of oxygen. The outward-moving dehydration wave marks the termination of new life-bearing planets for galactocentric distances inside of the front. The Galactic annulus extending from just interior to the solar circle to a galactocentric radius of 4-6 kpc has been suggested as the region most likely to form habitable planets, at least over some time intervals, because of the slightly higher metallicity and the correlation of incidence of giant planets and metallicity (see Gonzales et al. 2001, Ward and Brownlee 2002, Lineweaver, Fenner, and Gibson 2004). Instead, if biochemistry requires liquid water, then the current radial gradient and increase with time of C/O makes this inner disk region the least hospitable of environments, far outweighing relatively small changes in metallicity, supernova rates, etc., but only for times more recent than about 2-3 Gyr ago, and at all times in the future.

Although the dehydration front would effectively terminate new origins for life in our Galaxy, it should have little effect for terrestrial planet searches or SETI searches. One might think that a search directed away from the Galactic Center might yield a higher probability of success than a search toward the inner galaxy. However the targets for such searches are nearby stars (except for gravitational lensing), and, except for possibly the oldest of these stars, the rate of radial orbit migration (Wielen et al. 1996) is small enough that very few have their birthplaces more than a kpc or so away in the radial direction, even though their azimuthal mixing distances should be much larger.

5.7 Conclusions

We summerize results found in previous sections that depend on successively more, and more uncertain, assumptions.

1. The prediction that there must exist localized fluctuations in the C/O ratio

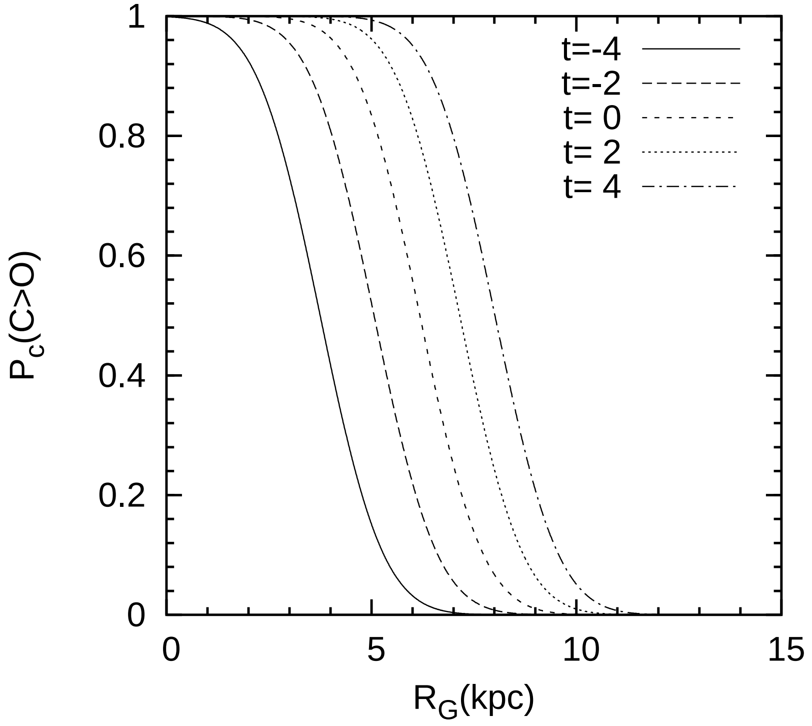

Figure 5.7 Propagation of the dehydration front

The fraction of carbon-rich regions P_c(C>O) as a function of Galactocentric radius and time. We used eq. (5.26) for the mean ratio [C/O] as a function of space and time. The distributions of C and O abundances are assumed to be Gaussian with a standard deviation of 0.05 dex. The $t = 0$ curve (dashed) corresponds to "the dehydration front", which separates carbon-rich from oxygen-region regions in the Galaxy, at the current epoch. The solid and long-dashed curves represent the fronts at 4 and 2 Gyr ago and the dotted and dot-dashed curves are the predicted fronts in 2 and 4 Gyr, respectively. With time the dehydration front propagates outward to larger Galactocentric radius at a rate of $\sim$ 0.5 kpc/Gyr.

that may exceed unity seems inescapable, as long as some of the carbon production takes place in a nucleosynthesis site that is different from the site(s) of oxygen production. Nearly all theoretical models agree that the C and O yields as a function of initial stellar mass are different, with disagreements arising only as a matter of degree. We showed that for a given C/O ratio averaged over an annulus in the disk we can estimate the volume filling fraction of C/O>1 fluctuations, independent of its time or space dependence. This predicted filling factor depends on the assumed metallicity dispersion or scatter, sigma, and the degree of correlation assigned to the carbon and oxygen production sites.

2. If the increase in average C/O continues, there will be a time window during which scattered pockets of C/O>1 gas percolates to nearly fill the disk as the mean C/O passes through unity. This result is independent of the adopted parameters, which only affect the time over which the transition occurs. It is also independent of whether or not a radial C/O gradient exists in the Galaxy; without a radial gradient, the entire disk would undergo the transition at about the same time. After this transition, it is difficult to imagine how there could exist significant water in any form, let alone the liquid water that is often considered necessary for life. A transition to a hydrocarbon-based biochemistry, perhaps involving a primordial oil slick of carbonaceous polymers (Laczano 1971), or the methanogenic protolife envisioned by McKay et al. (2001), Benner et al. (2004), and Trainer et al. (2006), is possible, although whether the unusual, and poorly understood, properties of the dynamic hydrogen-bonded network of liquid water are required for a workable biochemistry is still unknown. The various possibilities for a number of properties of carbon-rich planets were discussed by Kuchner (2003) and Kuchner and Seager (2005), who were more interested in a situation in which C/O>1 might occur locally in protoplanetary disks because of particle migration or certain chemical cycles, and considered chemical consequences of an equilibrium condensation sequence at elevated C/O.

3. A number of observational considerations and theoretical yield estimates indicate that C is preferentially produced in low-to-intermediate mass stars, in which case C/O should increase with time. As reviewed in §5.2, abundance studies of a few small samples of stars (e.g. Gustaffson et al. 1999) directly support this increase with time, a result that is consistent with the rate of increase based on the solar C/O at its known age, and the C/O ratios found for HII regions (Esteban et al.

2005). For the adopted present average C/O value of 0.79, we found this fraction of carbon rich stars to be tantalizingly significant, in the 10^{-1} to 10^{-3} range for young stars forming today and in the 10^{-2} to 10^{-4} range for low-mass stars formed in the Galaxy history with the result depending on the metallicity dispersion or scatter, the degree of correlation between C and O nucleosynthesis sources, and somewhat on the adopted star formation rate history. This prediction needs to be tested against furture observations of carbon-rich stars.

4. If we accept the radial gradient in the mean C/O ratio found by Esteban et al. (2005), bolstered by some theoretical chemical evolution models (e.g. Gavilan et al. 2005) and observations of HII regions in other galaxies, then the transition takes place first in the inner regions of the disk, with a dehydration wave propagating outward as the radial C/O profile is gradually elevated everywhere. This assumes that the rate of increase of C/O is the same at all galactocentric radii, and that the increase is linear with time, which is probably our most severe assumption. However, a nonlinear increase with time, or even one that saturates at some mean C/O>1, will give a qualitatively similar result. However the thickness of the dehydration front, its present position ($R_G \sim 6$ kpc for the adopted parameters), and its rate of propagation all depend on these admittedly simple assumptions. For our purposes, the demonstration that an astrobiologically severe and irreversible phase of Galactic evolution must occur, basically because of the nature of stellar nucleosynthesis yields as a function of mass, is the important point, and precise parameters of the dehydration front, which in reality could be quite complex and need not propagate as a circular region, is of secondary interest, especially since we do not know of a technique to determine C/O ratios in a sufficiently large number of inner disk objects to detect the C/O>1 inner disk directly. As pointed out by Kuchner (2005), gravitational microlensing searches for extrasolar planets should be able to detect planets within this inner Galactic zone, but such detections give no information on composition, and usually the parent star is not accessible for a spectroscopic study.

Chapter 6

The effect of turbulent intermittency on the deglagration to detonation transition in type Ia supernova explosions

Chapter Synopsis: We examine the effects of turbulent intermittency on the deflagration to detonation transition (DDT) in Type Ia supernovae. The Zel'dovich mechanism for DDT requires the formation of a nearly isothermal region of mixed ash and fuel that is larger than a critical size. We primarily consider the hypothesis by Khokhlov et al. and Niemeyer and Woosley that the nearly isothermal, mixed region is produced when the flame makes the transition to the distributed regime. We use two models for the distribution of the turbulent velocity fluctuations to estimate the probability as a function of the density in the exploding white dwarf that a given region of critical size is in the distributed regime due to strong local turbulent stretching of the flame structure. We also estimate lower limits on the number of such regions as a function of density. We find that the distributed regime, and hence perhaps DDT, occurs in a local region of critical size at a density at least a factor of $2-3$ larger than predicted for mean conditions that neglect intermittency. This factor brings the transition density to be much larger than the empirical value from observations in most situations. We also consider the intermittency effect on the more stringent conditions for DDT by Lisewski et al. and Woosley. We find that a turbulent velocity of 10^8 cm/s in a region of size 10^6 cm, required by Lisewski et al., is rare. We expect that intermittency gives a weaker effect on the Woosley model with stronger criterion. The predicted transition density from this criterion remains below 10^7 g/cm^3 after accounting for intermittency using our intermittency models.

6.1 Introduction

A successful model for Type Ia Supernova (SNIa) explosions is required to produce a deflagration to detonation transition (DDT) by observational constraints. A pure deflagration model gives exploding kinetic energy lower than observed (Khokhlov 1991; Gamezo et al. 2003; Röpke & Hillebrandt 2005) and pure detonation leads to overproduction of iron group elements and too little intermediate elements (Branch et al. 1982, 1983). The density ρ_{tr} at which the transition occurs determines the amount of the nickel produced (Höflich 1995; Höflich and Khokhlov 1996; Dominguez, Höflich & Straniero 2001). Therefore a prediction of ρ_{tr}, consistent with the observed nickel production, is essential to a DDT theory for SNe Ia .

The mechanism by which the DDT occurs still remains a mystery. The most studied candidate is the Zel'dovich mechanism, which requires the existence of an almost isothermal region of mixed ash and fuel that is larger than a critical size l_c to drive a supersonic shock that is sufficiently strong to sweep over the entire star (Khokhlov et al. 1997, hereafter KOW; Niemeyer and Woosley 1997, hereafter NW). One hypothesis is that a nearly isothermal region is produced by turbulent preconditioning. KOW argued that, to produce an almost isothermal mixture of ash and fuel, the laminar flame must be quenched by turbulent stretching, at least locally. This might allow the cold fuel to mix with the ash both thermally by electron conduction and chemically by diffusivity without being burned. They assumed that the criterion to quench a flame is that the turbulent velocity at the laminar flame thickness must be larger than the laminar flame speed. NW gave a similar argument based on the distributed flame burning regime in turbulent combustion. The criterion for a distributed flame is expressed in terms of the Gibson scale at which the turbulence velocity equals the laminar flame speed. If the Gibson scale is smaller than the laminar flame thickness, turbulent stretching can generate structures within the flame and the flame is in the distributed regime. NW speculated that in this regime flames can be temporally quenched in some regions, which can host the detonation after being homogenized in temperature and composition by turbulent mixing. The criterion for the distributed regime is equivalent to that for flame quenching used by KOW. Both criteria give the same condition on the turbulence intensity for given laminar flame properties (see §6.2). As the density in the star drops due to the overall expansion, it is easier for turbulence to affect the laminar flame because of the decrease in the flame speed and the increase in flame thickness. With presumed turbulence parameters, the criterion for the turbulence intensity, determined by the robustness of laminar flames disturbed by turbulent motions, translates to a transition density ρ_{tr} for the DDT.

Several uncertainties exist in the simple model given by these two early studies. First, it is not clear whether the criterion used by KOW, equivalent to that for a distributed regime (NW), is sufficient for flame breaking. How, or even if, flames are quenched is still an open question. Second, it is uncertain whether (local) flame quenching is indeed necessary to produce a nearly isothermal region. Finally, later studies by Lisewski, Hillebrandt and Woosley (2000) (hereafter Lisewski et al 2000; see also Lisewski et al. 2000b) and Woosley (2007) find that entering the distributed regime, while probably a necessary condition, is not sufficient for the DDT to occur.

Based on a requirement for turbulent transport to be efficient at producing a shallow temperature and composition gradient around the laminar flame, Lisewski et al. (2000) find that the turbulent velocity at the scale 10^6 cm needed for a detonation is very large, $\sim 10^8$ cm/s. Woosley (2007) claims that the DDT occurs only when the turbulent flame thickness exceeds a critical length scale. We show in §6.2 that the two criteria, although arising from different physical considerations, are basically equivalent. The corresponding condition is more stringent than that assumed by KOW and NW.

In this chapter we examine the effect of turbulent intermittency on the onset of distributed burning that may relate to the DDT. Despite the uncertainties listed above, we will mainly consider the model by KOW and NW and use it to illustrate the potential importance of intermittency in SN Ia explosions. Our calculations can be applied to the criteria by Lisewski et al. (2000) and Woosley (2007) in a straightforward way. A quantitative analysis using their criteria requires data for laminar flame properties and critical length scales at densities below 10^7 g cm^{-3} that are not immediately available (see §6.2). We give a qualitative discussion of the intermittency effect on their DDT models.

Intermittency is an important concept in turbulence theory. It is characterized by intense local events, e.g., strong stretching at small scales, which occur at a frequency much larger than predicted from a Gaussian distribution (see, e.g., Frisch 1995). The physical origin of intermittency in turbulent flows is the spatial inhomogeneity in the energy dissipation rate: most kinetic energy is viscously dissipated in the finest structures, e.g., vortex tubes, which occupy only a small volume fraction. These rare but intense dissipative structures give rise to a spatially inhomogeneous and intermittent distribution for the turbulent intensity and the stretching rate. Intermittency is shown as broad exponential tails in the probability distribution for the stretching rate or the dissipation rate at small scales (see §6.3). The tails get broader at smaller scales, meaning that the probability of finding an extreme turbulent stretching rate or intensity increases with decreasing scales.

According to 1D simulation results by KOW and NW, the critical size, l_c, of the isothermal region required for a DDT via the Zel'dovich mechanism is much smaller, especially at large densities, than the expected integral length scale for the buoyancy-driven turbulence in SN Ia progenitors. This suggests that only a small flame region with a sufficiently strong local turbulence intensity may be needed to trigger a detonation. Turbulent intermittency, which indicates the existence of regions of small sizes where the turbulent stretching is much larger than the average value over the flow, is therefore expected to have important consequences for DDT. The transition could happen earlier at a higher transition density ρ_{tr} than predicted by models using the average turbulent intensity. At higher densities, much larger turbulent intensity is required for the DDT, but the rapid decrease of l_c with increasing density makes an earlier DDT possible for two reasons. First, the probability is larger to find regions of smaller sizes l_c with extreme turbulent stretching rate or intensity. Second, there are more regions of smaller size available as candidates to host the detonation. Clearly, the intermittency effect accounts for the intuitive dependence of ρ_{tr} on l_c: the smaller the critical size, the easier it may be for the transition to happen. To what degree the intermittency effect increases ρ_{tr} is the main question we investigate in this chapter.

In §6.2, we review the criteria for the DDT in models by KOW, NW, Lisewski et al. (2007) and Woosley (2007) and formulate a new criterion taking into account the effect of intermittency. We describe two intermittency models by Oboukhov (1962) and Kolmogorov (1962) and by She and Leveque (1994) in §6.3. Using the intermittency models, we evaluate the transition density from the new criteria in §6.4. Our results are summarized and discussed in §6.5.

6.2 Criteria for the DDT

The criterion used in NW for judging whether a flame is in the distributed regime, which was also assumed to be the condition for the DDT, is to compare the Gibson scale l_G with the laminar flame thickness l_f. The Gibson scale is defined such that $\delta u(l_G) = S_l$ where $\delta u(l)$ is the amplitude of the velocity fluctuations at the scale l (or equivalently the velocity difference over a scale l, i.e., $\delta u(l) = u(l + x) - u(x)$) and S_l is the laminar flame speed [1]. If $l_G \gtrsim l_f$, the turbulence cannot internally disturb the flame and the turbulence in effect wrinkles the flame. This is called the flamelet regime. Only when $l_G \lesssim l_f$, can turbulence stretch the flame efficiently

---

[1] Note that NW, accounting for the cellular stabilization effect against instabilities, e.g., the Landau- Darrieus instability, defined l_G as the scale where the turbulent velocity exceeds the effective cellular flame speed. This does not introduce a significant difference in the estimate of l_G since the effective cellular speed is close to the laminar speed and has a very weak dependence on scale; see their Fig. 1.

to generate structures within the flame and the turbulent combustion enters the distributed regime. The condition $l_G \lesssim l_f$ is equivalent to $\delta u(l_f) \gtrsim \delta u(l_G) = S_l$ since $\delta u(l)$ is an increasing function of the scale l[2]. The latter, which means that the turbulent velocity fluctuation $\delta u(l_f)$ at the scale of the flame thickness l_f is larger than the laminar flame speed, is the criterion used in KOW for flame quenching and the DDT.

Following KOW, we introduce a factor of $K \sim 1$ in the criterion to account for the uncertainty in the flame breaking mechanism, i.e., $\delta u(l_f) \geq K S_l$. We will consider two values for K, i.e., $K = 1$ and $K = 8$ (KOW; For $K = 8$, to quench a flame, the Gibson scale has to be $K^3 = 512$ times smaller than the flame width). This criterion can also be written in terms of timescales. Noting that the turbulent stretching timescale, τ_t, at the flame thickness is $\tau_t(l_f) = l_f/\delta u(l_f)$ and that the nuclear reaction timescale, τ_n, is related to the flame speed $\tau_n = l_f/S_l$, the criterion is equivalent to $\tau_t(l_f) < \tau_n/K$, i.e., to break the flame the stretching timescale at the flame thickness must be smaller than the nuclear burning timescale (see Niemeyer and Kerstein 1997).

To apply this criterion, the Kolmogorov (1941) scaling $\delta u(l) = \bar{\epsilon}^{1/3} l^{1/3}$ is usually used to calculate $\delta u(l_f)$ from the turbulent velocity fluctuations at large scales where $\bar{\epsilon}$ is the average dissipation rate in the flow. From this scaling, the criterion can be written as (KOW, NW),

$$\bar{\epsilon}^{1/3} l_f^{1/3} > K S_l \tag{6.1}$$

or

$$\bar{\epsilon} > K^3 S_l^3 / l_f = K^3 \epsilon_f \tag{6.2}$$

where ϵ_f is defined as S_l^3/l_f. Although we use the convenient criterion (6.2) in terms of the dissipation rate in our calculations, the turbulent stretching is more fundamental and we will use the concept of the flame stretching in our discussions.

The laminar flame speed and thickness depend on the chemical composition

---

[2] This is also equivalent to the diffusivity criterion by Niemeyer and Kerstein (1997) for the onset of distributed regime and flame extinction at Prandtl number larger than unity, which is the case for white dwarfs. Their criterion was motivated by the observation that, at Prandtl number different from unity, two previous criteria proposed for the flamelet breakdown and for the flame quenching, using the ratio of the flow viscous length scale to the flame thickness and the ratio of the viscous timescale to the reaction timescale, respectively, are not equivalent.

and the density (Timmes and Woosley 1992, KOW). In Table 6.1, we list the flame speed, the flame thickness as a function of density for a white dwarf with half carbon and half oxygen, mainly taken from Timmes and Woosley (1992). The laminar speed decreases and the thickness increases quickly with decreasing density ρ, therefore ϵ_f decreases rapidly with decreasing ρ as shown in Table 6.1. The average dissipation rate is estimated to be $\bar{\epsilon} = U^3/L$ where U and L are the characteristic velocity and length scales of the turbulence, normally set by motions on the large, driving scale. At large scales, the turbulence is driven by the Rayleigh-Taylor instability. The length scale L might be expected to be about the size, R_f, of the flame region, $L \simeq R_f \sim 10^8$ cm and the velocity scale to be about the Rayleigh-Taylor velocity at this scale $U \sim 0.5\sqrt{g_{eff}L} \simeq 10^8$ cm/s where the effective gravity is taken to be $\sim g_{eff} = 5 \times 10^8$ cm/s^2 (KOW, NW). Khokhlov (1995), however, showed that motions at scales larger than 10^6 cm freeze out due to the overall expansion of the star. In that case, $L \sim 10^6 - 10^7$ cm and $U \sim 10^7$ cm/s. We will take U and L as parameters. Note that the criterion eq (6.2) depends on U and L through the dissipation rate. Given the dissipation rate $\bar{\epsilon}$, the critical density below which the inequality (eq 6.2) is satisfied can be obtained using ϵ_f as a function of ρ in Table 6.1. For example, if $U \sim 100$ km/s and $L \sim 100$ km, $\bar{\epsilon} \sim 10^{14}$ cm^2/s^3 and we find that, from interpolation in Table 6.1, $\bar{\epsilon}$ is larger than ϵ_f at a density less than $\sim 4 \times 10^7$ g/cm^3. Therefore criterion (6.2) predicts a transition density $\rho_{tr} \simeq 4 \times 10^7$ g/cm^3 for $K = 1$ (see KOW and NW). If $K = 8$, the predicted transition density is smaller, $\rho_{tr} \sim 1.5 \times 10^7$ g/cm^3. In the second line of Table 6.2, we give the predicted ρ_{tr} for different values of the parameters, which decreases with decreasing dissipation rate $\bar{\epsilon}$. The numbers in parenthesis correspond to $K = 8$.

When using the criterion eq (6.2), we need to keep in mind that the spatial fluctuations of ϵ (see §6.3) are completely neglected and the criterion only applies to the overall situation in the combustion flow. We will refer to this criterion as the mean criterion. When the mean criterion is met, the only implication is that the combustion is in the distributed regime in general. Considering the intermittency of turbulence, i.e., the spatially inhomogeneous distribution of the stretching strength, there can be places where the stretching rate is much weaker than the average. These places could still be in the flamelet stage while most other places are in the distributed regime. Or conversely, even if the mean criterion (6.2) is not satisfied, one cannot exclude the possibility of there existing a region that experiences strong

Table 6.1 The laminar flame speed, the flame thickness and the critical length for a white dwarf with half carbon and half oxygen

ρ (10^9 g/cm^3)	S_l (10^5 cm/s)	l_f (cm)	ϵ_f (10^{15} cm^2/s^3)	l_c(cm)
2	75.8	9.35(-5)	4.66(9)	7(1)
0.5	18.1	9.46(-4)	6.27(6)	—
0.1	2.33	2.75 (-2)	4.60(2)	2(2)
0.05	0.599	5.19 (-1)	0.414	1.3(3)[a]
0.03	0.26[b]	1.78[b]	0.98 (-2)	5(3)
0.01	4.72(-2)	4.22	2.59(-5)	2(5)

---

[a] Read from Fig. 6 in KOW.

[b] Read from Fig. 7 in KOW.

Note. — The values of S_l and l_f are mainly taken from Table 3 of Timmes and Woosley 1992. The value of l_c is mainly taken from NW. We also include numbers (marked) from KOW because their results are very similar to *NW* despite the difference of details in the two models. Numbers in parentheses are powers of 10.

stretching and gets into the distributed regime when most of the structure is still in the flamelet regime. This latter fact is important for the deflagration to detonation transition. The fact that the DDT does not require the entire star to be in the distributed regime but instead only needs a region of size much smaller than the white dwarf radius (see below, KOW), coupled with the intrinsic intermittency, suggests that DDT could occur earlier than predicted by eq (6.2) and hence at a larger transition density. The detonation can be triggered locally when a region appears that is larger than the critical size and enters the distributed regime due to a strong *local* stretching. It is important to study the degree to which this intermittency effect increases the transition density, which is constrained by observations. Clearly the answer depends on the critical size, which we consider next.

The question of how large the isothermal region with well-mixed ash and fuel has to be for a detonation was studied by KOW (see also NW). In their model, the DDT occurs via the Zel'dovich mechanism (Zel'dovich et al. 1970) where the mixed region begins spontaneous ignition at the place with the minimum induction time, and the flame propagates with a phase speed equal to the inverse of the spatial gradient of the induction time, which is large for nearly isothermal and well-mixed regions and is not limited by the speed of sound. As the phase speed decreases below the Chapman-Jouget speed, a shock forms just ahead of the flame front. Whether this shock can explode the whole star depends on the strength of the shock when entering the pure fuel, which is determined by the size of the isothermal region. If the isothermal region is small and the shock is weak, the flame front and shock separate with the flame front lagging behind the shock and the shock cannot make the whole star explode. The critical strength of the shock corresponds to a critical size of the isothermal region, over which the shock can be strengthened. Using 1D simulations, KOW and NW obtained the critical size, l_c, which depends on the density and the chemical composition. It is interesting to note that at early time when the density is large, the required size is much smaller than that at later times. We will show this has important consequences. The critical size is much smaller than what current numerical simulations can resolve, therefore the problem of the intermittent stretching at scale l_c cannot be addressed by simulations.

We need a local criterion to check whether a region of a given size l, in particular l_c, is in the distributed regime or not. For that purpose, we use a local average dissipation rate ϵ_l (see eq. 6.8 in §6.3 for a definition) in a region of size l to replace $\bar{\epsilon}$. Following the same argument that leads to equation (6.2), the criterion for a region of size l being in the distributed regime is

$$\epsilon_l > K^3 \epsilon_f \tag{6.3}$$

where we have used the refined similarity hypothesis by Kolmogorov (1962) (see eq. 9 in §6.3). Due to the random nature of turbulent flows, ϵ_l is stochastic, and a statistical approach is necessary. We therefore ask the question: what is the probability that any region of size l is in the distributed regime? This is given by the cumulative probability $P(\epsilon_l > K^3\epsilon_f)$. To answer this question, we need the probability distribution $P(\epsilon_l)$ of ϵ_l. Fortunately, this distribution has been extensively studied in the intermittency models for turbulence, which we describe in §6.3. Although these models were originally proposed for homogeneous and isotropic turbulence, we will assume they apply to SNe Ia where the turbulence is stratified and may not arrive at isotropy even at very small scales. Once the distribution is specified, one can calculate the probability of finding that a region of given size l_c

is in the distributed regime,

$$P(\epsilon_{l_c} > K^3\epsilon_f) = \int_{K^3\epsilon_f}^{\infty} P(\epsilon_{l_c}) d\epsilon_{l_c} \tag{6.4}$$

which depends on the density through l_c and ϵ_f. An immediate examination of eq (6.4) shows that, at larger density, the lower limit of the integral $K^3\epsilon_f$ is larger because of the fast flame speed and the small flame thickness. This tends to decrease the probability. However, at larger density, l_c is smaller and the intermittency of turbulence tells us that the tail of the distribution $P(\epsilon_l)$ is broader for smaller l. This tends to counteract the decrease of the cumulative probability due to the larger lower integral limit at higher densities.

Furthermore, for smaller l_c, there are more regions of size l_c available in the star. This could make the transition occur significantly earlier with a transition density considerably larger than predicted by eq (6.2). We need to multiply the probability that a given region of size l_c is in the distributed regime by the number, N_{l_c}, of regions of size l_c available in order to calculate the number of regions that are both larger than l_c and in the distributed regime at any given density. We assume that the deflagration to detonation transition happens when

$$N_{l_c} \times P(\epsilon_{l_c} > K^3\epsilon_f) = 1. \tag{6.5}$$

Since we are concerned with the flame being stretched into the distributed regime, only locations around the flame front are of interest when calculating N_{l_c}. Therefore, we only count regions in the vicinity of the flame front. N_{l_c} depends on the size, R_f, of the flame region and the flame geometry. A typical value for R_f is 10^8 cm (Khokhlov 1995), which could be smaller at an earlier time. We will set $R_f \simeq L$ in our calculations in order to decrease the number of parameters. Note that $R_f > L$ when the freezeout effect is considered and therefore the number N_{l_c} we use is a lower limit. If the flame region is a 2D spherical front, $N_{l_c} \sim 4\pi R_f^2/l_c^2$. If the flame structure is highly convoluted, it may have a fractal dimension larger than 2. In that case, N_{l_c} is larger. The upper limit for N_{l_c} is $\simeq 4\pi R_f^3/3l_c^3$, which applies if the flame geometry is close to 3D. Again, we take the lower limit $N_{l_c} = 4\pi R_f^2/l_c^2$, thus the transition density we will get is a lower limit.

As discussed in the Introduction, Lisewski et al. (2000) and Woosley (2007) find that entering the distributed regime is not sufficient for the DDT to occur and give criteria stronger than that used in KOW and NW. Lisewski et al. (2000) considered how turbulent transport affects the temperature and composition profile around a laminar flame. They assumed that, at any point, turbulence translates the temperature and composition by a distance l_t, over which turbulence can transport during a local induction time τ_i. The distance l_t is a function of position since τ_i depends on local temperature and composition. It is estimated by the length scale of a turbulent eddy with turnover time equal to τ_i, i.e., $l_t/\delta u(l_t) = \tau_i$. Using the Kolmogorov (1941) scaling, we get $l_t = \bar{\epsilon}^{1/2}\tau_i^{3/2}$. For given turbulence intensity, temperature and composition profiles around a laminar flame front can be calculated from the translation. Clearly, more efficient turbulent transport gives shallower temperature and composition profile, which is needed for detonation. By checking whether the resulting profiles, as initial conditions to solve the 1D hydrodynamic equations, can lead to a detonation, Lisewski et al. (2000), obtained a condition for the DDT on the turbulent intensity. They found that, for a successful detonation, the turbulent velocity has to be $\sim 10^8$ cm/s at the scale 10^6 cm. This condition is stronger than just entering the distributed regime[3]. Since the expected turbulent velocity at scale 10^6 cm is $10^6 - 10^7$ cm/s, Lisewski et al. (2000) concluded that a DDT via the Zel'dovich mechanism in SNe Ia is unlikely. However, considering the spatial inhomogeneity of turbulent intensity, i.e., intermittency, it is possible for regions of size 10^6 cm with large enough turbulent velocity to arise.

The result of Lisewski et al. (2000) motivated Röpke (2007) to study the probability of finding a region of size 10^6 cm with a turbulent rms velocity of $\sim 10^8$ cm/s. Using data from 3D numerical simulations with a turbulent subgrid-scale method, Röpke (2007) analyzed the velocity fluctuations at the grid size (10^6 cm) and obtained a fat exponential tail for large velocity fluctuations that extends up to 10^8 cm/s. The large velocity fluctuations seem likely to be located at the trailing edge of a bubble-like feature (Röpke 2007). This confirms the intermittency in

---

[3] This condition can be converted into a form that can be directly compared with eq. 6.2. Roughly speaking, the physical condition for a detonation in this model is that l_t at the laminar flame front is larger than l_c, i.e., a shallow temperature gradient can be produced over a critical size around the flame front. Requiring $l_t > l_c$, we get the criterion $\bar{\epsilon} > (l_c/l_f)^2(\tau_n/\tau_i)^3\epsilon_f$. Considering that τ_i defined by Lisewski et al. (2000) is smaller than the nuclear timescale τ_n and that $l_c \gg l_f$, this condition is much stronger than the condition of eq. 6.2. Note that this condition is similar to the criterion of Woosley (2007) given below.

the turbulent combustion flow in SNe Ia; there exist grid cells where the turbulent intensity is much stronger than the average. From the probability of finding a grid cell with required turbulent intensity, Röpke concluded that the DDT triggered by a local cell with large velocity fluctuations is possible but probably rare. In our notations, the probability is given by $P(\epsilon_{10^6\,\mathrm{cm}} > 10^{18}\ \mathrm{cm}^2/\mathrm{s}^3)$ where $10^{18}\ \mathrm{cm}^2/\mathrm{s}^3$ corresponds to the dissipation rate in a region of size 10^6 cm with a rms velocity of 10^8 cm/s. We will calculate this probability and consider the availability of such regions using two intermittency models given in §6.3 and compare with the results of Röpke (2007) in §6.4.

Woosley (2007) proposed a new criterion for the DDT based on a calculation of the distributed flame width using an eddy diffusivity approximation. Making an analogy to the estimate of the laminar flame thickness, Woosley (2007) obtained the distributed flame width λ from the equation $\lambda \simeq (D(\lambda)\tau_n)^{1/2}$ where $D(\lambda) = \delta u(\lambda)\lambda$ is the eddy diffusivity at scale λ and τ_n is the nuclear reaction timescale. Using the Kolmogorov (1941) scaling for $\delta u(\lambda)$, the distributed flame width is given by $\lambda = \bar{\epsilon}^{1/2}\tau_n^{3/2}$ (note that this formula for λ is similar to l_t in Lisewski et al. (2000)). Woosley (2007) assumed that the condition for detonation is that the minimum burning timescale in the distributed flame is smaller than the sound crossing time over the distributed flame width λ, or equivalently, $\lambda \gtrsim r_{sonic}^{min}$ where r_{sonic}^{min} is the sound crossing length over the minimum burning timescale in the distributed flame. The minimum sound crossing length is thus the critical size of the distributed flame width for detonation. The criterion $\lambda \gtrsim r_{sonic}^{min}$ is equivalent to $\bar{\epsilon} \gtrsim (r_{sonic}^{min})^2/\tau_n^3$. Noting that $\tau_n = l_f/S_l$, the condition can be written as $\bar{\epsilon} \gtrsim (r_{sonic}^{min}/l_f)^2\epsilon_f$. Since r_{sonic}^{min} given in Table 4 of Woosley (2007) is close to l_c listed in Table 6.1, we will use l_c instead of r_{sonic}^{min} for simplicity, i.e.,

$$\bar{\epsilon} \gtrsim (l_c/l_f)^2\epsilon_f. \tag{6.6}$$

which is much stronger than eq (6.2) because l_c is much larger than the laminar flame thickness l_f. This condition can be used to determine the transition density ρ_{tr} by the same calculation process as in the case of the criterion eq (6.2). Note that, expect a factor of $(\tau_n/\tau_i)^3$, this criterion is basically equivalent to that given in footnote (3) for the requirement by Lisewski et al. (2000). We find that, for the reasonable turbulence parameters listed in Table 6.2, the criterion results in a transition density below 10^7 g cm^{-3} and we cannot specify it due to the lack of data for l_c, S_l and l_f at densities below 10^7 g cm^{-3}.

In his estimate for ρ_{tr}, Woosley (2007) used $U = 10^8$ cm/s at scale $L = 10^6$ cm throughout the calculations, based on the result by Röpke (2007) on the possibility of the existence of regions of size 10^6 cm with a rms velocity of 10^8 cm/s. With these turbulence parameters he derived $\rho_{tr} = 10^7$ g cm^{-3}. Clearly, in Woosley's calculation, the intermittency effect implicitly contributes to the transition density obtained because, as discussed earlier, a turbulent rms velocity of 10^8 cm/s at 10^6 cm can only arise from intermittency.

The intermittency effect for the criterion of Woosley (2007) can be included more consistently in our formulation. Instead of considering a single special scale 10^6 cm, our model specifies intermittency over a continuous range of scales corresponding to critical sizes at different densities. Following the same steps that lead to eq (6.5), we incorporate the intermittency effect in the DDT model of Woosley (2007) and obtain a criterion,

$$N_{l_c} \times P(\epsilon_{l_c} > (l_c/l_f)^2 \epsilon_f) = 1. \tag{6.7}$$

which only differs from eq. 6.5 by the lower limit in the cumulative probability. We will discuss about this criterion in §6.4.

We point out that the eddy diffusivity method used by Woosley (2007) to approximate the combined action of the turbulent advection and the microscopic diffusivity is an oversimplification. This procedure implicitly assumes a smooth structure in the distributed flame and neglects the fluctuations of temperature and concentration, which may be important in determining the effective width of distributed flames.

6.3 Intermittency

Kolmogorov's 1941 theory assumes that the energy transfer in the inertial range is equal to the average dissipation rate $\bar{\epsilon}$ in the flow and is the same throughout the inertial scales down to the viscous scale where the kinetic energy is removed. This assumption, together with the similarity hypothesis, predicts that the statistics of the velocity difference (or the velocity fluctuations) at any inertial scale is completely determined by the average dissipation rate $\bar{\epsilon}$. However, fluctuations in the dissipation rate clearly exist as can be seen from the formula for the local viscous dissipation rate, $\epsilon(\mathbf{x}, t) = \frac{\nu}{2} \sum_{i,j} (\partial_i u_j + \partial_j u_i)^2$, which is a function of the fluctuating velocity field. The spatial fluctuations in ϵ are well-illustrated by the intense dissipation structures at small scales such as vortex tubes. This effect needs to be taken into account for a more accurate prediction of the scaling behavior of the velocity difference (Landau and Lifshitz 1944). The statistics of the velocity difference over a separation l depends on the distribution of the dissipation rate over regions of size l, which is defined as (e.g., Kolmogorov 1962),

$$\epsilon_l(\mathbf{x}, t) = \frac{3}{4\pi l^3} \int\limits_{|\mathbf{x}'|<l} \epsilon(\mathbf{x} + \mathbf{x}', t) d\mathbf{x}'. \tag{6.8}$$

Clearly, the mean of ϵ_l is equal to $\bar{\epsilon}$ and thus is independent of l. This means that the *average* energy flux over all the inertial scales is constant. The ϵ_l distribution is essential to the intermittency models for turbulence. Note that this distribution is exactly what we need in our calculations for the transition of the turbulent combustion to the distributed regime by turbulent stretching and quenching described in §6.2, eqs (6.4) and (6.5).

Intermittency in turbulence is usually expressed in terms of the scaling behavior of the structure functions $\langle \delta u(l)^p \rangle \sim l^{\zeta_p}$ where $\delta u(l) = u(x + l) - u(x)$ is the (longitudinal) velocity difference and ζ_p is the scaling exponent for the pth-order structure function. Kolmogorov's 1941 theory predicts that the exponent ζ_p goes with p as $\zeta_p = p/3$. However experimental data (e.g., Anselmet et al. 1984) have shown departure from this linear relation and ζ_p increases significantly slower than $p/3$ at large p. This "anomalous" scaling is referred to as intermittency. The data indicate broader and broader tails for the distribution of $\delta u(l)$ at smaller and smaller scales, e.g., the kurtosis of the distribution, $\langle \delta u(l)^4 \rangle / \langle \delta u(l)^2 \rangle^2 \propto l^{\zeta_4 - 2\zeta_2}$, increases with decreasing l because $\zeta_4 < 2\zeta_2$. The distribution of $\delta u(l)$ is fatter for smaller l. The anomalous scaling is fundamentally caused by the fluctuations in the dissipation rate ϵ_l. Applying the refined similarity argument for homogeneous and isotropic turbulence (Kolmogorov 1962), the velocity difference over a separation l can be related to the dissipation rate ϵ_l,

$$\delta u(l) \sim \epsilon_l^{1/3} l^{1/3}. \tag{6.9}$$

(note that the Kolmogorov's 1941 theory uses $\bar{\epsilon}$.) The structure functions are then given by,

$$\langle \delta u(l)^p \rangle \propto \langle \epsilon_l^{p/3} \rangle l^{p/3}. \tag{6.10}$$

Clearly, the departure from the linear scaling for the velocity difference comes from the statistics of the dissipation rate. Assuming $\langle \epsilon_l^p \rangle \propto l^{\tau_p}$ (e.g., She and Leveque 1994), we have,

$$\zeta_p = p/3 + \tau_{p/3}. \tag{6.11}$$

Developing a physical model for τ_p that satisfies the experimental result for $\zeta(p)$ has been the main task of intermittency theories. Although we are mainly concerned with the distribution of ϵ_l, discussions of the structure functions are necessary because they are directly measurable in experiments and give important information and constraints on the ϵ_l distribution. We will use two intermittency models in our calculations: the log-normal model (Oboukhov 1962 and Kolmogorov 1962) and the log- Poisson model by She and Leveque (1994).

6.3.1 The log-normal model

Oboukhov (1962) and Kolmogorov (1962) developed the first intermittency model. In this model, the distribution of ϵ_l is assumed to be log-normal (Kolmogorov 1962). A justification for this "natural" distribution for ϵ_l was given by Yaglom (1966). Imagine the cascade progress as successive eddy fragmentations from the integral scale L to the dissipation scale η. The statistics of the energy flux at an inertial scale l (or equivalently the dissipation rate ϵ_l) depends on the fragmentations before the scale is reached. The total number N of steps that lead to the scale l is proportional to $N \sim ln(L/l)$. Defining $\chi_i = \epsilon_i/\epsilon_{i-1}$ as the ratio of the energy transfer rates at two successive fragmentation steps, the energy flux at the scale l can be expressed in the ratios (see e.g., Monin & Yaglom 1975),

$$\epsilon_l = \epsilon_L \chi_1 \chi_2 \cdots \chi_N \tag{6.12}$$

where ϵ_L is the dissipation rate at the integral scale (or the transfer flux at the largest scale), $\epsilon_L \simeq \bar{\epsilon}$. Due to the randomness in the fragmentation process, χ_i's are stochastic variables. Assuming a self- similar fragmentation process, the distributions of χ_i's are similar and $ln(\epsilon_l/\epsilon_L) = \sum_{i=1}^{N} ln(\chi_i)$ is expected to be Gaussian from the central limit theorem,

$$p(\epsilon_l)d\epsilon_l = \frac{1}{\sqrt{2\pi\sigma_l^2}} exp(-\frac{(ln(\epsilon_l/\bar{\epsilon}) + \sigma_l^2/2)^2}{2\sigma_l^2}) dln(\epsilon_l/\bar{\epsilon}) \tag{6.13}$$

where the variance σ_l^2 is proportional to the number of steps $\sigma_l^2 = \mu ln(L/l)$ with μ being a parameter to be determined by experimental data and the $\sigma_l^2/2$ term in the numerator in the exponential is to guarantee the mean $\langle\epsilon_l\rangle$ is equal to the overall average dissipation rate $\bar{\epsilon}$. This distribution will be used later to calculate the probability (eq. 6.4) for a region of a given size being in the distributed regime.

The scaling behavior of ϵ_l can be derived by integrating equation (6.13),

$$\langle\epsilon_l^p\rangle \propto l^{-\frac{1}{2}\mu p(p-1)} \tag{6.14}$$

which gives $\tau_p = -\frac{1}{2}\mu p(p-1)$. From eq (6.11), we have

$$\zeta_p = p/3 - \frac{1}{18}\mu p(p-3) \tag{6.15}$$

Therefore $\mu = 2 - \zeta_6$, which can be obtained from the results of experiments and simulations. It has been found that $\mu \simeq 0.2$ (Frisch 1995, Biskamp 2000). The relation (15) agrees with experiments quite well at small p but starts to exhibit deviation at $p \gtrsim 10$ and gives an unrealistic maximum and turnover at $p > 16$, violating the requirement that the $\zeta(p)$- p curve must be monotonic and concave (Frisch 1995). Simulations by Wang et al. (1996) suggest that this disagreement corresponds to the departure of the distribution for $ln(\epsilon_l/\bar{\epsilon})$ from normal at scales close to the dissipation scale. They find that, at these scales, the distribution of $ln(\epsilon_l/\bar{\epsilon})$ shows a negative skewness, meaning that the log-normal distribution overestimates the probability in the very high ϵ_l tail. However the distribution of ϵ_l agrees with log-normal very well in the inertial range away from the dissipation scale and the agreement is better and better for larger and larger scales (Wang et al. 1996). Fortunately the critical scale we are concerned with is well within the inertial range (see §6.4) and according to Fig. 6 in Wang et al. (1996) the log normal fit is very good at least up to the $4-\sigma$ tail. They also show that the fit gets better as the Reynolds number increases. More recent simulations by Yeung et al. (2006) with resolutions up to 2048^3 obtained similar results. The log normal distribution gives a very good fit to $4-\sigma$ and only deviates by a factor of 2 at the $5-\sigma$ tail. They also find that the negative skewness gets closer to zero with increasing Reynolds number. The Reynolds number in SNe Ia is $Re \sim 10^{14}$ for typical velocity scale 10^7 cm/s, length scale 10^7 cm and viscosity 1 cm^2/s. This is much larger than in all the current simulations. Therefore one may expect that the log-normal distribution probably applies even further out on the tail for the inertial scales of the turbulence in SNe Ia. However, the departure of the predicted $\zeta(p)-p$ curve from the experiments (with high Re) at $p \gtrsim 10$ suggests that, even at huge Reynolds number, the log normal fit eventually breaks down at some large ϵ_l in the tail. Therefore we need to be careful when using the log-normal model. We will give more discussion on this point in the calculations given in §6.4.

Another issue is that the distribution of ϵ_l has a physical cutoff in a realistic system due to the finite viscosity. Since the intermittency is stronger at smaller scales, the cutoff in the distribution of ϵ_l is probably larger for smaller l and obtains a maximum at the dissipation scale, η. For Kolmogorov scaling, the cutoff in the distribution of ϵ_η is is given by $\bar{\epsilon} Re^{1/2}$. Since $Re \sim 10^{14}$ in SNe Ia, this maximum dissipation rate is far beyond that required to break flames at density $\lesssim 10^8$ $\mathrm{g/cm}^3$. Therefore ignoring this maximum cutoff does not affect our result. However, the largest available dissipation rate at an inertial scale l is probably smaller than the cutoff in the distribution of ϵ_η and thus may affect the calculation for the cumulative probability defined in eq (6.4) if the cutoff in the distribution $P(\epsilon_{l_c})$ is close to or even smaller than $K^3\epsilon_f$. Since the log-normal model does not address the cutoff in the distribution of ϵ_l, we will neglect this potential effect in this model.

On the other hand, the log-Poisson model we consider in the next subsection gives a maximum dissipation rate at each inertial scale, corresponding to the strongest dissipative structures at that scale. In that model, a nonzero cumulative probability in eq (6.5) requires the lower limit $K^3\epsilon_f$ in eq (6.4) be smaller than the maximum.

6.3.2 The log-Poisson model

A major success in the intermittency theory is the model by She and Leveque (1994). In this model, She and Leveque studied the hierarchy of dissipation intensity in structures of size l and, by invoking an unknown "hidden symmetry," they related the characteristic dissipation rates in structures of different intensity levels to the strongest dissipative structures. This relation gives a prediction of τ_p as a function of p, which only depends on the proprieties of the most intermittent structures. Assuming that the dissipation rate in regions of size l containing the most intense structures exhibits a scaling $\propto l^{-2/3}$ (see explanation in Appendix E) and the most intermittent structures are filamentary, corresponding to a codimension of 2, She and Leveque obtained a $\zeta(p) - p$ relation, which is in excellent agreement with experimental data. The "hidden symmetry" has been immediately interpreted as a log-Poisson process (Dubrulle 1994, She and Waymire 1995) in a multiplicative cascade model. In this subsection, we adopt the log-Poisson version of the She-Leveque model. The original presentation by She and Leveque (1994) is given in Appendix E.

In a multiplicative model, the dissipative rates at two scales l_2 and l_1 ($l_1 > l_2$) are related by a multiplicative factor $W_{l_1 l_2}$,

$$\epsilon_{l_2} = W_{l_2 l_1} \epsilon_{l_1} \tag{6.16}$$

The average $\langle W_{l_1 l_2} \rangle$ is equal to unity since $\langle \epsilon_{l_1} \rangle = \langle \epsilon_{l_2} \rangle = \bar{\epsilon}$. She and Waymire (1995) speculated that $W_{l_2 l_1}$ consists of two events. First is the amplification of the dissipation rate in the cascade, which tends to produce singular structures with $\epsilon_{l_2} \propto (l_1/l_2)^\gamma$ approaching infinity as l_2 goes to 0. The meaning of γ is discussed below. To ensure $\langle W_{l_1 l_2} \rangle = 1$, a second event is required to reduce $W_{l_1 l_2}$. She and Waymire (1995) called this event the modulation-defects since it modulates the singular structures. The defects were assumed to be a discrete Poisson process. Each of the defects decreases $W_{l_1 l_2}$ by a factor of β, thus

$$W_{l_2 l_1} = (l_1/l_2)^\gamma \beta^n \tag{6.17}$$

if there are n defect events in the cascade. The number n of the events that occur in the cascade from the scale l_1 to l_2 obeys a Poisson distribution,

$$P(n) = exp(-\lambda_{l_1 l_2}) \frac{\lambda_{l_1 l_2}^n}{n!} \tag{6.18}$$

where $\lambda_{l_1 l_2}$ is the mean number of the defect events in the cascade, which is expected to be proportional to the total number of the cascade steps, i.e., $\lambda_{l_1 l_2} \propto ln(l_1/l_2)$. In fact, $\lambda_{l_1 l_2}$ can obtained by taking the average of eq. (6.17) and requiring $\langle W_{l_1 l_2} \rangle = 1$. Using the identity $\sum\limits_{n=0}^{\infty} \frac{\alpha^n}{n!} = exp(\alpha)$, we get $\langle \beta^n \rangle = exp((\beta - 1)\lambda_{l_1 l_2})$ for the Poisson distribution eq (6.18), therefore,

$$\lambda_{l_1 l_2} = \frac{\gamma ln(l_1/l_2)}{1 - \beta} \tag{6.19}$$

In this model, there is a largest dissipation rate at any scale. Clearly the largest dissipation rate is achieved if there is no defect, i.e., $n = 0$, in a cascade from the integral scale L to the scale l of interest, thus the largest dissipation rate is equal to $\epsilon_L (L/l)^\gamma$. This largest dissipation rate corresponds to $\epsilon_l^{(\infty)}$ in Appendix E. Similarly $n = 1$ gives the second strongest dissipative rate at a given scale, and so on.

From eqs (6.16) and (6.17), we have,

$$ln(\epsilon_{l_2}/\bar{\epsilon}) = ln(\epsilon_{l_1}/\bar{\epsilon}) + \gamma ln(l_1/l_2) + n ln(\beta) \tag{6.20}$$

thus, using the Poisson distribution for n, the distribution for the dissipation rate at l_2 can be derived from that at any scale l_1 larger than l_2. In particular, we consider deriving the distribution of ϵ_l at any scale l from the integral scale L. The distribution function of ϵ_L at the integral scale depends on how the energy is injected in the flow, thus is not universal and may vary from flow to flow. Therefore the function form cannot be specified. However, there is a strong constraint for its width. Since $\epsilon_L \simeq \bar{\epsilon}$, the distribution of $ln(\epsilon_L/\bar{\epsilon})$ is expected to be very narrow around $ln(\epsilon_L/\bar{\epsilon}) \simeq 0$ and hence to be approximately a delta function. We denote the distribution of $ln(\epsilon_L/\bar{\epsilon})$ as $P_L(ln(\epsilon_L/\bar{\epsilon}))$. It then follows from eqs (6.18) and (6.20) that

$$P(\epsilon_l) d\epsilon_l = \sum_{n=0}^{\infty} exp(-\lambda) \frac{\lambda^n}{n!} P_L(ln(\epsilon_l/\bar{\epsilon}) - \gamma ln(L/l) - n ln(\beta)) d ln(\epsilon_l/\bar{\epsilon}) \tag{6.21}$$

where $\lambda = \lambda_{Ll} = \gamma ln(L/l)/(1-\beta)$. Each term in eq (6.21) represents the contribution from dissipation structures of different levels, e.g., the $n = 0$ term corresponds to the most intensive structures of size l.

To compare the model with experiments and obtain the parameters, we calculate the moments $\langle \epsilon_l \rangle$ from the distribution eq. (6.21),

$$\begin{array}{rcl} \langle \epsilon_l^p \rangle & \propto & \sum\limits_{n=0}^{\infty} \int exp(-\lambda) \frac{\lambda^n}{n!} exp(px) P_L(x - \gamma ln(L/l) - nln(\beta)) dx \\ & = & (l/L)^{-\gamma p} exp(-\lambda) \sum\limits_{n=0}^{\infty} \frac{(\beta^p \lambda)^n}{n!} \int exp(x') P_L(x') dx' \\ & = & B_p exp(-\lambda(1-\beta^p))(l/L)^{-\gamma p} \\ & = & B_p (l/L)^{-\gamma p + \gamma(1-\beta^p)/(1-\beta)} \end{array} \tag{6.22}$$

where we used a variable change $x' = x - \gamma ln(L/l) - nln(\beta)$ in the second step and the identity $\sum\limits_{n=0}^{\infty} \frac{\alpha^n}{n!} = exp(\alpha)$ in the third step. The coefficients $B_p = \int exp(px') P_L(x') dx'$; $B_0 = B_1 = 1$ from the normalization of P_L and the requirement that $\langle \epsilon_L \rangle = \bar{\epsilon}$ respectively.

The result eq (6.22) gives $\tau_p = -\gamma p + \gamma(1-\beta^p)/(1-\beta)$, which is the same as (A8) in Appendix E, meaning that the "hidden symmetry" described in the appendix is equivalent to a log-Poisson process. The parameters γ and β introduced here are identical to those described in the appendix, and thus have the physical meanings explained there, i.e., γ can be interpreted as the exponent of the dissipation rate scaling in regions containing the most intermittent structures and β is related to the codimension C of the strongest dissipation structures, $\gamma/(1-\beta) = C$ (see Appendix E for details). As discussed in the appendix, She and Leveque argued that $\gamma = 2/3$ and $\beta = 2/3$ for $C = 2$ corresponding to filamentary dissipation structures in incompressible turbulence. This results in ζ_p as a function of p that agrees with the experiments with an accuracy of 1%, implying eq (6.21) provides a good distribution for ϵ_l. The She-Leveque formulation has been extended to supersonic turbulence (Boldyrev et al. 2002) and MHD turbulence (Muller & Biskamp 2000) where the dissipation structures are dissipation sheets and the current sheets, respectively. For these 2 dimensional dissipation structures, the codimension $C = 1$ and $\beta = 1/3$. In next section we use the log-Poisson distribution (eq 6.21) in our calculations for the cumulative probability in eq 6.4. We will take $\gamma = 2/3$ and consider both filaments ($\beta = 2/3$) and sheets ($\beta = 1/3$) as the most intermittent dissipation structures.

6.4 Results

6.4.1 The log-normal model

We are ready to calculate the probability $P(\epsilon_{l_c} > K^3\epsilon_f)$ using the distributions $P(\epsilon_l)$ given in §6.3. The calculation is straightforward for the log-normal distribution eq. (6.13),

$$\begin{aligned} P(\epsilon_{l_c} > K^3\epsilon_f) &= \int\limits_{ln(K^3\epsilon_f/\bar{\epsilon})}^{\infty} \frac{1}{\sqrt{2\pi\sigma_{l_c}^2}} exp(-\frac{(x+\sigma_{l_c}^2/2)^2}{2\sigma_{l_c}^2})dx \\ &= \int\limits_{\frac{ln(K^3\epsilon_f/\bar{\epsilon})+\sigma_{l_c}^2/2}{\sigma_{l_c}}}^{\infty} \frac{1}{\sqrt{2\pi}} exp(-x^2/2)dx \qquad (6.23) \\ &= \frac{1}{2} erfc(\frac{ln(K^3\epsilon_f/\bar{\epsilon})}{\sqrt{2}\sigma_{l_c}} + \frac{\sigma_{l_c}}{2\sqrt{2}}) \end{aligned}$$

where $\bar{\epsilon} \simeq U^3/L$, $\sigma_{l_c}^2 = \mu ln(L/l_c) \simeq 0.2 ln(L/l_c)$ and $erfc(x)$ is the complementary error function. Using ϵ_f and l_c given in Table 6.1, we calculated the probability as a function of the density assuming different values for the characteristic velocity (U) and length (L) scales. For example, if $U = 100$ km/s and $L = 100$ km, the probabilities are 0.5×10^{-10}, 0.042, 0.9 and 1 at $\rho = 10^8$, 5×10^7, 3×10^7 and 10^7 g/cm^3 respectively if $K = 1$. It is interesting to note that, at a density 3×10^7 g/cm^3, 10% of the local regions of the critical size are still in the flamelet regime, although generally the flame has reached the distributed regime according to the mean criterion eq (6.2). With $R_f \simeq L = 100$ km, at the 4 densities above from high to low, the corresponding numbers $N_{lc} = 4\pi R_f^2/l_c^2$ of regions of the critical size that cover the flame front are 3×10^{10}, 7×10^8, 5×10^7 and 3×10^4. Multiplying $P(\epsilon_{l_c} > K^3\epsilon_f)$ with N_{l_c} (eq. 6.5), we see that there is already one region of size l_c in the distributed regime at a density 10^8 g/cm^3. Recalling that, according to the criterion eq (6.2), the DDT does not occur until the density decreases to 4×10^7 g/cm^3, we find that in this case the intermittency effect may increase the transition density by more than a factor of 2.

We point out the cumulative probability calculated from eq (6.23) at density 10^8 g/cm^3 in the example above comes from a little beyond the $6-\sigma$ tail of the distribution for $ln(\epsilon_l/\bar{\epsilon})$ and we need to check whether the log-normal distribution there is a good approximation. As discussed in §6.3.1, numerical simulations have shown that for a scale l in the inertial range, the distribution of ϵ_l is well approximated by log-normal up to the $5-\sigma$ tail (Yeung et al. 2006). Assuming the Kolmogorov scaling, the dissipation scale in Type Ia SNe is $\eta = LRe^{-3/4} \simeq 10^{-3}$ cm for $L \sim 10^7$ cm and the Reynolds number $Re \simeq 10^{14}$. The critical scale $l_c \sim 10^2 - 10^4$ cm of interest here is well between the integral scale and the dissipation scale, thus we expect that the distribution for ϵ_{l_c} is close to log-normal at least up to the $\sim 5-\sigma$ tail. The question is then whether the good fit extends further. Wang et al. (1996) and Yeung et al. (2006) found that the log-normal fit is better for larger Reynolds number, thus it is expected that the log-normal approximation probably applies to higher on the tail than $5-\sigma$. As argued in §6.3.1, the log normal approximation eventually fails somewhere in the extreme tail even at high Reynolds number. To know exactly how far the log-normal fit extends, numerical simulations with much higher resolution are needed. We have to be careful about the validity of the log-normal approximation in the far tail because it overestimates the probability distribution for ϵ_l once it breaks down and in that case eq (6.23) overestimates $P(\epsilon_{l_c} > K^3\epsilon_f)$.

Due to the complication of the validity of the log-normal distribution at the far tail, we consider two extreme cases and give the upper and lower limits for the transition density. First, we ignore the departure from log-normal and evaluate the density at which $N_{l_c} \times P(\epsilon_{l_c} > K^3\epsilon_f) = 1$ using eq (6.23) for $P(\epsilon_{l_c} > K^3\epsilon_f)$ and Table 6.1 for ϵ_f and l_c with different parameters U and L. We will denote this density as ρ_{LN} with the subscript LN standing for log-normal. Interpolation was used to obtain ϵ_f and l_c not tabulated in Table 6.1. If the distribution of ϵ_l is exactly log-normal as given by eq (6.13), then ρ_{LN} is the predicted transition density for the DDT with the intermittency taken into account. On the other hand, if the log-normal distribution overestimates the probability at the high tail, eq (6.23) overestimates the cumulative probability and ρ_{LN} is the upper limit for ρ_{tr}. We give ρ_{LN} for different parameters U and L in the second line of Table 6.2.

In the other extreme, we assume that the log-normal distribution fails to fit the distribution of ϵ_l beyond the $5-\sigma$ tail. This gives a lower limit for the transition density since numerical simulations have shown that the log-normal fit applies at least to $5-\sigma$. In this case, we keep track of the integral limit in the second line of eq (6.23) at ρ_{LN}, which tells us which part of the tail of the distribution gives the main contribution to $P(\epsilon_{l_c} > K^3\epsilon_f)$ at that density. If the integral limit is smaller than 5, the contribution to the cumulative probability is from within $5-\sigma$ and vice versa. We calculate the density at which the integral limit is equal to 5 and denote this density as $\rho_{5\sigma}$. Since the integral limit is a decreasing function of the density, if

$\rho_{LN} < \rho_{5\sigma}$, the contribution to $P(\epsilon_{l_c} > K^3\epsilon_f)$ at density ρ_{LN} is from within $5-\sigma$. In this case, the cumulative probability calculated from eq (6.23) is valid and ρ_{LN} is a good estimate for the transition density. Otherwise if $\rho_{LN} > \rho_{5\sigma}$, the contribution to the probability is from beyond the $5-\sigma$ tail, eq (6.23) overestimates it and thus ρ_{LN} overestimates the transition density ρ_{tr}. In this case, $\rho_{5\sigma}$ gives a lower limit for the transition density because at $\rho_{5\sigma}$, we have $N_{l_c} \times P(\epsilon_{l_c} > K^3\epsilon_f) \gg 1$ using eq. (6.23) which applies for $\rho \leq \rho_{5\sigma}$. Therefore if the log-normal fit fails just beyond $5-\sigma$, we have a lower limit for the transition density, $min(\rho_{LN}, \rho_{5\sigma})$. We give this lower limit in the 3rd line of Table 6.2.

Similar calculations can be done for the $K = 8$ case. The results of the upper and lower limits for the transition density in the $K = 8$ case are given in parenthesis in Table 6.2. Comparing with predictions from the mean criterion eq (6.2) (the first line in Table 6.2), the log-normal model predicts that the intermittency effect increases the transition density by a factor of 2-3 for all the cases we list in Table 6.2.

We evaluate the probability of the existence of a region of size 10^6 cm with a rms velocity 10^8 cm/s, required for the DDT by Lisewski et al. (2000), and compare with the numerical results of Röpke (2007). Using the log-normal distribution for ϵ_l, we find that the requirement $P(\epsilon_{10^6\ \mathrm{cm}} > 10^{18}\ \mathrm{cm}^2/\mathrm{s}^3)$ requires conditions from the extreme tail of the distribution. The likelihood is completely negligible ($\sim 10^{-40}$) if the velocity U at the integral length scale is less than $\sim 10^7$ cm/s. Only if U is larger than 5×10^7 cm/s is the probability appreciably larger so that the required region might be available. For example, if $U = 5 \times 10^7$ cm/s at $L = 10^7$ cm, the probability is $\sim 10^{-11}$. This is still too small to guarantee the existence of a region as required by Lisewski et al. (2000). The number of available candidate regions of size 10^6 cm around the flame front is probably smaller than $10^5 - 10^7$, assuming the flame front radius is $\sim 10^8 - 10^9$ cm. This result agrees with the conclusion of Röpke (2007) that the existence of a region as required by Lisewski et al. (2000) is rare. To ensure such a region, the velocity at the integral scale has to be larger than 10^8 cm/s, which is probably impossible as discussed in §6.2.

We also carry out a calculation for ρ_{tr} based on the criterion of Woosley (2007) taking into account the effect of intermittency. Using the log-normal distribution to calculate the cumulative probability in eq. (6.7), we find that no regions of critical size that meet Woosley's criterion appear at density above 10^7 g/cm^3. We cannot give an exact predicted transition density for this model because we do not have data at densities below 10^7 g/cm^3 for relevant quantities listed in Table 6.1. Note that Woosley (2007) obtained a transition density around 10^7 g/cm^3 under the assumption that a region of size 10^6 cm with rms velocity of 10^8 cm/s is available. From our estimate above and the result in Röpke (2007), the probability that such a region exists is small, therefore it is appropriate to take the transition density predicted in Woosley (2007) as an upper limit for his DDT criterion.

6.4.2 The log-Poisson model

We next consider the log-Poisson model. Using the distribution eq (6.21), we have,

$$\begin{aligned} P(\epsilon_{l_c} > K^3\epsilon_f) &= exp(-\lambda_c)\sum_{n=0}^{\infty}\frac{\lambda_c^n}{n!}\int\limits_{ln(K^3\epsilon_f/\bar{\epsilon})}^{\infty} P_L(x-\gamma ln(L/l_c)-nln(\beta))dx \\ &= exp(-\lambda_c)\sum_{n=0}^{\infty}\frac{\lambda_c^n}{n!}\int\limits_{ln(K^3\epsilon_f/\bar{\epsilon})-\gamma ln(L/l_c)-nln(\beta)}^{\infty} P_L(x)dx \\ &= exp(-\lambda_c)\sum_{n=0}^{\infty}\frac{\lambda_c^n}{n!}F_n \end{aligned} \tag{6.24}$$

where $\lambda_c = \gamma ln(L/l_c)/(1-\beta)$ and the integrals in the second line are denoted as F_n for convenience. Note that the integral lower limit $ln(K^3\epsilon_f/\bar{\epsilon}) - \gamma ln(L/l_c) - nln(\beta)$ increases with n because $\beta < 1$, therefore F_n is a decreasing function of n. An exact calculation for the cumulative probability is impossible because of the unspecified function P_L. We will neglect all the $n \geq 1$ terms and only keep the $n = 0$ term in our calculation, i.e., we only include the contribution of the most intensive structures at scale l_c. Obviously, this approximation gives a lower limit for the probability and the transition density we obtain will also be a lower limit. We will show that the criterion for DDT obtained from this approximation is exact if P_L is a delta function.

The contribution from $n = 0$ is $exp(-\lambda_c) = (\frac{l_c}{L})^{\gamma/(1-\beta)}F_0$. For $\gamma = 2/3$ and $\beta = 2/3$, it is equal to $(l_c/L)^2F_0$ and $N_{l_c} \times P(\epsilon_{l_c} > K^3\epsilon_f) \geq 4\pi(R_f/l_c)^2(l_c/L)^2F_0 = 4\pi(R_f/L)^2F_0$. Since the size of the flame region $R_f \geq L$, it means that the number of regions which are larger than the critical size and in the distributed regime is $\simeq 4\pi F_0$. Since the distribution $P_L(x)$ is probably strongly concentrated at $x = 0$, the sufficient and almost necessary condition for $F_0 \simeq 1$ is that the integral limit

$ln(K^3\epsilon_f/\bar{\epsilon}) - \gamma ln(L/l_c) \leq 0$, or equivalently,

$$\bar{\epsilon} > (l_c/L)^{2/3} K^3 \epsilon_f \tag{6.25}$$

which is a convenient criterion for the DDT in the log-Poisson model. Note this criterion is much weaker than the mean criterion eq (6.2). Once the condition is satisfied, at least one region of critical size that covers the flame enters the distributed regime due to the most intense stretching strength available at scale l_c.

As mentioned in §6.3.2, if the dissipation structures are 2-dimensional, $\beta = 1/3$. In that case, the contribution from the $n = 0$ term is $(l_c/L)F_0$ and $N_{l_c} \times P(\epsilon_{l_c} > K^3\epsilon_f) \geq 4\pi(R_f/l_c)(R_f/L)F_0$, which is much larger than 1 if $F_0 \gtrsim 1$. Therefore, the criterion eq (6.25) is a sufficient condition for the case with sheet-like dissipation structures such as in MHD turbulence or highly compressible turbulence.

We have neglected the $n > 1$ terms in eq. (6.24), the contribution of which depends on how rapidly $P_L(x)$ decreases with $x > 0$. We consider the extreme example where P_L is a delta function. In this case, before the condition eq (6.25) is met, $F_n = 0$ for any n thus the cumulative probability is zero. When the condition is just satisfied as the density decreases, only the $n = 0$ term contributes and all the $n > 1$ terms are still zero, i.e., the most intensive ($n = 0$) structures at l_c can stretch a local flame into the distributed regime while all the less intensive structures ($n \geq 1$) still cannot. From the calculation above, we see that in this case once the $n = 0$ term contributes, at least one region around the flame front experiences the largest stretching rate and enters the distributed regime. Therefore, if P_L is a delta function, eq (6.25) is both the necessary and the sufficient condition. This is true for both $\beta = 2/3$ and $\beta = 1/3$. If P_L is not a delta function, the tail of P_L gives rise to the possibility that the distributed regime can emerge in a local region of critical size before the condition eq (6.25) is met. This could lead to an even weaker condition than eq (6.25). Since we expect that ϵ_L can only vary within a factor of a few, the condition can be weaker only by a factor of a few. Because the r.h.s of the condition (6.23), especially ϵ_f, depends on the density very sensitively, this would not increase the predicted ρ_{tr} considerably.

The condition eq (6.25) can be easily applied to calculate the transition density using ϵ_f and l_c in Table 6.1. For example, we get $\rho_{tr} = 8.7 \times 10^7$ g/cm^3 for $U = 100$ km/s and $L = 100$ km if $K = 1$. This result is consistent with that from

Table 6.2 The predicted transition densities ρ_{tr} (in unit of 10^7 g/cm^3) for various models

Cases [a]	A	B	C	D	E
mean criterion	6.9(3.3)	5.5(2.3)	4.1(1.5)	3.0(1.0)	2.0 (—)
log- normal [b]	27(10)	11(4.9)	10(4.4)	9.4 (4.0)	4.3 (—)
log- normal [c]	23(7.6)	9.7(4.9)	8.4(3.9)	7.1 (3.0)	4.3 (—)
log- Poisson	24(8.6)	9.5(4.3)	8.7(3.8)	7.9(3.3)	3.8 (—)

---

[a] A: $U = 10^8$ cm/s, $L = 10^8$ cm, $\bar{\epsilon} = 10^{16}$cm^2/s^3;
B: $U = 10^7$ cm/s, $L = 10^6$ cm, $\bar{\epsilon} = 10^{15}$cm^2/s^3;
C: $U = 10^7$ cm/s, $L = 10^7$ cm, $\bar{\epsilon} = 10^{14}$cm^2/s^3;
D: $U = 10^7$ cm/s, $L = 10^8$ cm, $\bar{\epsilon} = 10^{13}$cm^2/s^3;
E: $U = 10^6$ cm/s, $L = 10^6$ cm, $\bar{\epsilon} = 10^{12}$cm^2/s^3

[b] The predicted transition density assuming a perfect fit of the distribution $P(\epsilon_{l_c})$ by log-normal. This is the upper limit for ρ_{tr} since the log-normal approximation may break down and overestimate the distribution at the far tail.

[c] The lower limit for the transition density assuming the log-normal approximation applies only up to $5 - \sigma$.

Note. — The numbers in parentheses are the results predicted if the Gibson scale has to be 512 times smaller than the flame thickness for the transition to the distributed regime. In case E, (—) indicates that the transition density is smaller than 10^7 g/cm^3, which cannot be well estimated since we only have data to 10^7 g/cm^3 in Table 6.1.

the log-normal model and is also about a factor of 2 larger than the prediction by the mean criterion eq (6.2).

The transition density predicted by the log-Poisson model with different parameters for turbulence is given in the 4th line of Table 6.2. Again the numbers in parenthesis are for $K = 8$. The results are consistent with those from the log-normal model and are at least $2 - 3$ times larger than from the criterion eq (6.2).

Again we consider the possibility that there exists a region of size 10^6 cm with rms turbulent velocity of 10^8 cm/s required for DDT by Lisewski et al. (2000). The probability $P(\epsilon_{10^6 \text{ cm}} > 10^{18} \text{ cm}^2/\text{s}^3)$ depends on P_L, the probability distribution of the dissipation rate at the integral scale L. Since P_L is probably not universal and is flow-dependent, the log-Poisson model cannot give an exact estimate for the probability. Here we assume P_L is a delta function and see under what condition it is possible to find a required region. We find that the necessary and sufficient condition to have such a region is that $U > 10^{22/3}(L/\text{cm})^{1/9}$ cm/s. For $L \simeq 10^7$ cm,

U has to be larger than 10^8 cm/s. This can be understood from the fact that, in the log-Poisson model, the available kinetic energy in the most intermittent structures for dissipation is assumed to be the kinetic energy at the integral scale (see Appendix E). Since $U > 10^8$ cm/s is probably not achievable, it is rare that a region as required by Lisewski et al. (2000) exists, again in agreement with Röpke (2007).

Using the same calculation that leads to eq (6.25), we obtain a criterion for the DDT model by Woosley (2007) accounting for the intermittency effect,

$$\bar{\epsilon} > (l_c/L)^{2/3}(l_c/l_f)^2\epsilon_f. \tag{6.26}$$

This is weaker than the corresponding mean criterion eq (6.6) by a factor of $(l_c/L)^{2/3}$, meaning that intermittency increases the transition density. In comparison with eq (6.25), the condition is stronger and thus gives a smaller transition density than that for the KOW and NW model with intermittency included. At smaller density, the critical length l_c is larger and the factor $(l_c/L)^{2/3}$, representing the intermittency effect, is closer to unity. This implies that intermittency gives a weaker effect on the the transition density for the Woosley (2007) criterion than for that by KOW and NW. Using Table 6.1, we again find that the condition eq (6.26) is not satisfied at densities above 10^7 g/cm^3 for the five cases listed in Table 6.2, i.e., the predicted transition density is still below 10^7 g/cm^3 after including intermittency (see discussion in §6.4.1).

In summary, intermittency can considerably enhance the onset of the distributed flame regime and hence increase the transition density in the DDT model of KOW and NW. Both the intermittency models we consider here predict a transition density $2-3$ times larger than from the criterion using the mean dissipation rate. This factor of $2-3$ brings the transition density to be in disagreement with the observational constraints for turbulent velocity larger than $U = 10^6$ cm/s in the case $K = 1$. We discuss the implications of this result in the next section. We also find that existence of regions of size 10^6 cm with velocity 10^8 cm/s is rare, in agreement with the numerical result of Röpke (2007). The strong DDT criterion given by Woosley (2007) gives a transition density below $\rho_{tr} = 10^7$ g/cm^3 even when intermittency is included. We expect that the intermittency effect is weaker for stronger DDT criteria.

6.5 Conclusion and Discussion

We have studied the effect of intermittency on the transition from the flamelet regime to the distributed regime in Type Ia SNe, and hence on the transition density for the DDT model by KOW and NW. In their model, the detonation occurs via the Zel'dovich mechanism that requires a nearly isothermal region larger than a critical size to drive a sufficiently strong supersonic shock. KOW and NW assumed that the almost isothermal mixture of fuel and ash can be produced once turbulence is strong enough to get the flame into the distributed regime. The DDT is assumed by KOW and NW to occur when the *average* flow gets into the distributed regime. We argue that the sufficient condition for the DDT is that there is *one* region that is larger than the critical size and in the distributed regime.

The intermittency in turbulence, as a result of the spatial inhomogeneity of the dissipation rate, gives rise to regions with strong local turbulent strength that can force the flame into the distributed regime earlier than elsewhere. Therefore the transition from the flamelet regime to the distributed regime is not spatially smooth, but intermittent. At early time when the density in the white dwarf is large, the flame has a large speed and a small width and thus resists being efficiently stretched and broken by the turbulence. At the same time, the critical size is very small. This has two effects that tend to make an early DDT likely. First, the intermittency of turbulence tells us that the probability of finding extremely strong stretching within a smaller critical size is larger. Second, there are more regions of smaller sizes available. Therefore it is possible that the DDT is triggered at a small "spot" when the density is larger than needed for the average flow to enter the distributed regime. As we pointed out in the Introduction, the critical size as a function of the density plays an important role in determining the transition density for the DDT in our calculations.

We used two analytical intermittency models to statistically investigate when the first region appears which is both larger than the critical size and in the distributed region. This is assumed to be the time when the DDT occurs by KOW and NW. We found that, for various parameters for the intensity and length scales, DDT occurs at a transition density at least $2-3$ times larger than the density at which the average flow enters the distributed regime. The transition density has been determined empirically by invoking it as a free parameter in spherically-symmetric models and then computing models that best match the observed multicolor light curve shapes and magnitudes (Höflich & Khokhlov 1996). Recognizing that the spherical models are oversimplified, they do give some guidance to the empirical constraints on the density at which DDT occurs. Höflich (1995) used this procedure to fit observations of the Branch core normal SN 1994D and preferred a value of the transition density of 2×10^7 gm cm^{-3}. Höflich, Khokhlov & Wheeler (1995) explored a range of transition densities in the context of pulsating delayed detonation models and favored densities in the range $0.8 - 2.2 \times 10^7$ gm cm^{-3}. Dominguez, Höflich & Straniero (2001) adopted 2.3×10^7 gm cm^{-3}. Allowing for an uncertainty of a factor of 2, the predicted transition densities by the mean criterion are consistent with 2×10^7 gm cm^{-3} as favored by the observations in all the cases except that with $\bar{\epsilon} = 10^{16}$ cm^2/s^3 and $K = 1$ (Table 6.2). With the intermittency effects we have examined here, the transition density would be a factor of $2 - 3$ higher. If $K = 1$, all the predicted ρ_{tr} are larger than 2×10^7 gm cm^{-3} by at least a factor of 2 except the case with $U = 10^6$ cm/s. The predicted transition density with $K = 8$ is $2 - 3$ times smaller than from $K = 1$. From Table 6.2, the predicted ρ_{tr} for the intermittency models with $K = 8$ agree with the observations within a factor of 2 except the case with a large velocity scale $U = 10^8$ cm/s at the integral length scale. To avoid discrepancy with the observations, our result indicates several possibilities.

1. The large scale motions caused by Rayleigh-Taylor instability freeze out due to the overall expansion of the star (Khokhlov 1995). The freezeout effect has to be efficient enough so that the developed part of the flow has a velocity scale of $\lesssim 10^6$ cm/s (see Table 6.2).

2. The flame is very robust. To break the flame, the local Gibson scale has to be at least $K^3 = 512$ times smaller than the flame thickness. In this case, the predicted transition density is $2 - 3$ times smaller than from $K = 1$.

3. There is not enough time for the buoyancy-driven turbulence to fully develop down to the critical size before the predicted density for the DDT by our intermittency models is attained, thus motions at scales below the critical size are either absent or non-intermittent.

4. The DDT does not occur immediately after a region of the critical size enters the distributed regime. It may take some time for turbulence to help mix the region and make it nearly isothermal. However, the time scale for turbulence to mix a region of the critical size in the distributed regime is very small, $\lesssim 10^{-2}$ s at densities larger than 3×10^7 g/cm^3. It is unlikely that the density drops much in such a short timescale.

5. Having a large enough region entering the distributed regime is not a sufficient condition for detonation. As mentioned in the Introduction, there are several uncertainties in the simple model by KOW and NW assuming flame quenching, entering the distributed regime and the DDT all occur simultaneously.

Our result alludes to the possibility that the criterion by KOW and NW is too weak for the DDT, supporting the claim of Lisewski et al (2000) and Woosley (2007) that just entering the distributed regime is not sufficient for the DDT. We have shown that their criteria for the DDT are much stronger than just entering the distributed regime. We also studied the intermittency effect on their conditions for the DDT. We find that the existence of a region of size 10^6 cm with rms turbulent velocity of 10^8 cm/s required by Lisewski et al (2007) for a DDT is rare, consistent with numerical results of Röpke (2007). We have also examined the intermittency effect on the transition density for the DDT criterion by Woosley (2007). We find that the effect is weaker for the stronger criterion and does not increase ρ_{tr} to above 10^7 g/cm^3. Woosley (2007) obtained ρ_{tr} around 10^7 g/cm^3 because of the assumption of strong turbulence velocity of 10^8 cm/s in a region of size 10^6 cm. Since the existence of such a region is rare, Woosley (2007) may considerably overestimate the transition density. This may imply that the condition for DDT by Lisewski et al. (2000) and Woosley (2007) is too strong and predicts a transition density smaller than that empirically determined from observations.

We have only studied the DDT in white dwarfs with the initial chemical composition of half carbon and half oxygen. In a white dwarf with more carbon, the nuclear timescale is smaller thus a stronger turbulent intensity is needed to break the flame. This results in a smaller transition density using the mean criterion (NW). On the other hand, the critical size for detonation in such a white dwarf is smaller, therefore the intermittency effect could be more efficient in increasing the transition density. We were not able to perform a calculation for the chemical composition with the carbon abundance larger than 0.5 due to the lack of sufficient data for the critical length scale in this case.

We point out that the intermittency models we used were originally proposed for homogeneous and isotropic turbulence. Turbulence in SNe Ia is stratified and may not achieve homogeneity and isotropy at very small scales even if the turbulence is developed at these scales. The effect of the departure from homogeneity and isotropy on the predicted transition density is out of the scope of this study.

Appendix A

The pdf formulation for mixing

In this Appendix, we derive the equation for the coarse-grained density-weighted pdf of the concentration (metallicity) field, which is defined as the concentration probability distribution weighted by the density over an ensemble of independent realizations. In each realization, the velocity field and the sources are drawn from their distributions independently and the concentration field evolves under the advection-diffusion equation (1.1). We derive an equation for the fine-grained density-weighted pdf in a specific realization using eq (1.1) in sec A.1 and averge it over the realizations to obtain the corresponding coarse-grained pdf equation in sec A.2.

A.1 Fine-grained density-weighted pdf equation

We first define a one-point, one-time fine-grained pdf for the concentration field in a given realization, which is a delta function because the concentration field in a given realization is essentially derterministic and thus single-valued at given time and space,

$$g'(C; \mathbf{x}, t) = \delta(C - Z(\mathbf{x}, t)) \tag{A.1}$$

where C is the sample variable and $Z(\mathbf{x}, t)$ is the concentration field in the specified realization. Note that g' is defined as a function of C, $\mathbf{x}$ and t and that $Z(\mathbf{x}, t)$, a function of $\mathbf{x}$ and t, is independent of the sample variable.

For compressible flows with significant density variations, it is appropriate to use a density-weighted pdf, which measures the fraction of mass in an infinitesimal metallicity range. We define a density-weighted fine-grained pdf,

$$f'(C;\mathbf{x},t) = \frac{\rho(\mathbf{x},t)}{\langle\rho\rangle}\delta(C - Z(\mathbf{x},t)) = w_\rho(\mathbf{x},t)g'(C;\mathbf{x},t) \tag{A.2}$$

where $\langle\rho\rangle$ denotes the mean density of the system. For convenience, we have denoted the ratio $\frac{\rho(\mathbf{x},t)}{\langle\rho\rangle}$ as $w_\rho(\mathbf{x},t)$, which satisfies continuity equation since $\langle\rho\rangle$ is constant.

We calculate the time derivative of the density-weighted fine-grained pdf from eq (A2),

$$\frac{\partial}{\partial t}f'(C;\mathbf{x},t) = \frac{\partial w_\rho}{\partial t}g'(C;\mathbf{x},t) + w_\rho\frac{\partial}{\partial t}g'(C;\mathbf{x},t) \tag{A.3}$$

From the definition (A1), $g'(C;\mathbf{x},t)$ depends on t only through the function $C - Z(\mathbf{x},t)$, thus we have

$$\begin{aligned} \frac{\partial g'(C;\mathbf{x},t)}{\partial t} &= \frac{\partial\delta(X)}{\partial X}\frac{\partial X}{\partial t}\Big|_{X=C-Z(\mathbf{x},t)} = \frac{\partial\delta(C-Z(\mathbf{x},t))}{\partial C}\frac{\partial(C-Z(\mathbf{x},t))}{\partial t} \\ &= -\frac{\partial\delta(C-Z(\mathbf{x},t))}{\partial C}\frac{\partial Z(\mathbf{x},t)}{\partial t} = -\frac{\partial g'(C;\mathbf{x},t)}{\partial C}\frac{\partial Z(\mathbf{x},t)}{\partial t} \end{aligned} \tag{A.4}$$

where the chain rule is used in the first step. Inserting (A4) into (A3), we get

$$\frac{\partial f'(C;\mathbf{x},t)}{\partial t} = \frac{\partial w_\rho}{\partial t}g'(C;\mathbf{x},t) - \frac{\partial g'(C;\mathbf{x},t)}{\partial C}w_\rho\frac{\partial Z(\mathbf{x},t)}{\partial t} \tag{A.5}$$

Now using the continuity equation $\partial_t w_\rho = -\nabla\cdot(w_\rho\mathbf{v})$ and the advection-diffusion equation (1.1) for $\partial_t Z$, we get

$$\frac{\partial f'(C;\mathbf{x},t)}{\partial t} + \nabla\cdot(w_\rho\mathbf{v})g'(C;\mathbf{x},t) - \frac{\partial g'(C;\mathbf{x},t)}{\partial C}(w_\rho\mathbf{v}\cdot\nabla Z(\mathbf{x},t)) = -\frac{\partial g'(C;\mathbf{x},t)}{\partial C}w_\rho(\frac{1}{\rho}\nabla\cdot(\rho\kappa\nabla Z) + S) \tag{A.6}$$

The third term $-\frac{\partial g'}{\partial C}(w_\rho\mathbf{v}\cdot\nabla Z)$ is equal to $w_\rho\mathbf{v}\cdot\nabla g'$ using the identity

$$\nabla g'(C;\mathbf{x},t) = \frac{\partial g'(C;\mathbf{x},t)}{\partial C}\nabla(C - Z(\mathbf{x},t)) = -\frac{\partial g'(C;\mathbf{x},t)}{\partial C}\nabla Z(\mathbf{x},t) \tag{A.7}$$

where the calculation is similar to eq (A4). Then the sum of the second term and the third term in eq (A6) can be written as a divergence term $\nabla\cdot(w_\rho\mathbf{v})g' + w_\rho\mathbf{v}\cdot\nabla g' = \nabla\cdot(w_\rho\mathbf{v}g') = \nabla\cdot(f'\mathbf{v})$ and we finanly have the fine-grained density-weighted pdf equation,

$$\frac{\partial}{\partial t}f'(C;\mathbf{x},t)+\nabla\cdot(f'(C;\mathbf{x},t)\mathbf{v})=-\frac{\partial}{\partial C}(f'(C;\mathbf{x},t)(\frac{1}{\rho}\nabla\cdot(\rho\kappa\nabla Z)+S)) \quad \text{(A.8)}$$

where in the last term we used the fact that w_ρ, Z, S etc are functions of only $\mathbf{x}$ and t and independent of C. As expected, this equation is in the form of a Liouville equation which states the conservation of probability in the phase-space $(\mathbf{x}, C)$,

$$\frac{\partial f'}{\partial t}+\nabla\cdot(f'\mathbf{v})+\frac{\partial(f'\dot{C})}{\partial C}=0 \quad \text{(A.9)}$$

where $\dot{C}$ denotes the change rate in the metallicity space. Comparing with eq (A8), $\dot{C}=\frac{1}{\rho}\nabla\cdot(\rho\kappa\nabla Z)+S$ which implies that the change rate in the metallicity space is determined only by the diffusivity term and the source term; the velocity term does not affect the metallicity space directly.

A.2 Coarse-grained density-weighted pdf equation

The coarse-grained pdf is defined as the average of the fine-grained pdf over the ensemble of independent realizations. The coarse-grained volume-weighted pdf and density-weighted pdf are, respectively,

$$g(C;\mathbf{x},t)=\langle g'(C;\mathbf{x},t)\rangle \quad \text{(A.10)}$$

and

$$f(C;\mathbf{x},t)=\langle f'(C;\mathbf{x},t)\rangle \quad \text{(A.11)}$$

where $\langle ... \rangle$ denotes the ensemble average.

We obtain the equation for the coarse-grained density-weighted pdf $f(C;\mathbf{x},t)$ by ensemble averaging the fine-grained pdf equation (A9),

$$\frac{\partial}{\partial t}f(C;\mathbf{x},t)+\nabla\cdot\langle f'(C;\mathbf{x},t)\mathbf{v}\rangle=-\frac{\partial}{\partial C}\langle f'(C;\mathbf{x},t)(\frac{1}{\rho}\nabla\cdot(\rho\kappa\nabla Z)+S)\rangle \quad \text{(A.12)}$$

To evaluate the ensemble average terms, we prove a lemma that for any function $\phi(\mathbf{x},t)$, the ensemble average $\langle g'(C;\mathbf{x},t)\phi(\mathbf{x},t)\rangle$ can be expressed as the product of the coarse-grained pdf $g(C;\mathbf{x},t)$ with the mean of ϕ conditioned on

$Z(\mathbf{x}, t) = C$, i.e., the average of ϕ over only the realizations that have metallicity at $(\mathbf{x}, t)$ equal to C,

$$\begin{aligned} \langle g'(C; \mathbf{x}, t)\phi(\mathbf{x}, t)\rangle &= \textstyle\int\int \phi\delta(C - Z(\mathbf{x}, t))P(\phi, Z; \mathbf{x}, t)d\phi dZ \\ &= \textstyle\int \phi P(\phi, C; \mathbf{x}, t)d\phi \\ &= \textstyle\int \phi P(\phi|Z(\mathbf{x}, t) = C; \mathbf{x}, t)g(C; \mathbf{x}, t)d\phi \\ &= g(C; \mathbf{x}, t)\langle\phi(\mathbf{x}, t)|Z(\mathbf{x}, t) = C\rangle \end{aligned} \tag{A.13}$$

where $P(\phi, Z; \mathbf{x}, t)$ is the joint pdf (in the ensemble sense) of ϕ and Z at $\mathbf{x}$ and t and $\langle...|...\rangle$ denotes the conditional mean. In the first line we used the definition of the fine-grained pdf $g'(C; \mathbf{x}, t)$. In the third line the relation between the joint-pdf and the conditional pdf, i.e., $P(\phi, C; \mathbf{x}, t) = P(\phi|Z = C; \mathbf{x}, t)g(C; \mathbf{x}, t)$, is used. As a direct application, we have

$$f(C; \mathbf{x}, t) = \langle w_\rho g'(C; \mathbf{x}, t)\rangle = g(C; \mathbf{x}, t)\langle w_\rho|Z(\mathbf{x}, t) = C\rangle. \tag{A.14}$$

Using eq (A13), the coarse-grained density-weighted pdf equation (A12) is written as,

$$\frac{\partial f(C; \mathbf{x}, t)}{\partial t} + \nabla \cdot (g\langle w_\rho \mathbf{v}|Z(\mathbf{x}, t) = C\rangle) = -\frac{\partial}{\partial C}(g\langle(\nabla \cdot w_\rho\kappa\nabla Z + w_\rho S)|Z(\mathbf{x}, t) = C\rangle) \tag{A.15}$$

or converting g to f with eq (A14),

$$\frac{\partial f}{\partial t} + \nabla\cdot(f\frac{\langle\rho\mathbf{v}|Z(\mathbf{x}, t) = C\rangle}{\langle\rho|Z(\mathbf{x}, t) = C\rangle}) = -\frac{\partial}{\partial C}(f\frac{\langle\nabla \cdot (\rho\kappa\nabla Z)|Z(\mathbf{x}, t) = C\rangle + \langle\rho S|Z(\mathbf{x}, t) = C\rangle}{\langle\rho|Z(\mathbf{x}, t) = C\rangle}) \tag{A.16}$$

where w_ρ is eliminated using $w_\rho = \rho/\langle\rho\rangle$.

Each term in eq (A16) is a function of C, $\mathbf{x}$ and t. To make the equation more compact, we replace the the variable C with a new sampling variable Z. It should be kept in mind that the new sampling variable Z is different from the concentration field, $Z(\mathbf{x}, t)$. After this variable change, terms in equation (A16) are functions of Z , $\mathbf{x}$ and t and the conditional means become $\langle...|Z(\mathbf{x}, t) = Z\rangle$. Replacing $\langle...|Z(\mathbf{x}, t) = Z\rangle$ by $\langle...|Z\rangle$ for simplicity, we get the final the coarse-grained density-weighted pdf equation,

$$\frac{\partial f}{\partial t} + \nabla \cdot (f \frac{\langle \rho \mathbf{v} | Z \rangle}{\langle \rho | Z \rangle}) = -\frac{\partial}{\partial Z}(f \frac{\langle \nabla \cdot (\rho \kappa \nabla Z) | Z \rangle + \langle \rho S | Z \rangle}{\langle \rho | Z \rangle}) \tag{A.17}$$

We emphasize that the conditional means on Z are understood as averages over realizations where the concentration field at $\mathbf{x}$ and t is equal to the sampling variable Z.

Appendix B

Moment equations

We derive moment equations of the pdf equation with the diffusivity term given by the closure of Janicka et al. (1979). We concentrate on the diffusivity closure and neglect the advection and source terms,

$$\frac{\partial f(Z)}{\partial t} = \frac{1}{\tau_{mix}}[\int\limits_0^Z dZ_1 f(Z_1) \int\limits_Z^1 dZ_2 f(Z_2) P(Z_1, Z_2; Z) - f(Z)] \tag{B.1}$$

where we set the upper boundary in the metallicity space to be 1 for definiteness. The derivation is unchanged for an arbitrary upper boundary. The contributions to the moment equations from the second term in the square brackets are obvious, in particular, for the first three moments, they are 1, $\langle Z \rangle = \int\limits_0^1 Z f(Z) dZ$ and $\langle Z^2 \rangle = \int\limits_0^1 Z^2 f(Z) dZ$ respectively. The key calculations in the derivation are the moments of the double integral in eq (B1),

$$I_n = \int\limits_0^1 dZ Z^n \int\limits_0^Z dZ_1 f(Z_1) \int\limits_Z^1 dZ_2 f(Z_2) P(Z_1, Z_2; Z) \tag{B.2}$$

We will show that the first two moments $I_0 = 1$ and $I_1 = \langle Z \rangle$ cancel out the contributions from the second term and the total probability and the mean are therefore conserved. We derive an equation for the variance $\sigma^2 = \langle Z^2 \rangle - \langle Z \rangle^2$ by calculating I_2.

We introduce a new variable,

$$\xi = \frac{2}{Z_2 - Z1}(Z - \frac{Z_1 + Z_2}{2}) \tag{B.3}$$

and define a function of this variable, which is a transform of the transition function $P(Z_1, Z_2; Z)$,

$$P_0(Z_1, Z_2, \xi) = \frac{Z_2 - Z_1}{4} P(Z_1, Z_2; Z) \tag{B.4}$$

Using the property $\int\limits_{Z_1}^{Z_2} P(Z_1, Z_2; Z)dZ = 2$, we have,

$$\int\limits_{-1}^{1} P_0(Z_1, Z_2, \xi)d\xi = 1 \tag{B.5}$$

where the integral limits $(-1, 1)$ correspond to the limits (Z_1, Z_2) of Z under the variable change (B3). Another property of the transition function, i.e., $P(Z_1, Z_2; Z) = P(Z_1, Z_2; Z_1 + Z_2 - Z)$, indicates that P_0 is an even function of ξ,

$$P_0(Z_1, Z_2, \xi) = P_0(Z_1, Z_2, -\xi) \tag{B.6}$$

From the definition (B4) we can calculate P_0 for any given P, e.g., if $P(Z_1, Z_2; Z) = \frac{2}{Z_2 - Z_1}$ for $Z_1 < Z < Z_2$ as used in Janicka et al. (1979),

$$P_0(Z_1, Z_2, \xi) = \frac{1}{2} \tag{B.7}$$

for $-1 < \xi < 1$ and if $P(Z_1, Z_2; Z) = 2\delta(Z - (Z_1 + Z_2)/2)$ as adopted in a model for rain droplets by Curl (1963),

$$P_0(Z_1, Z_2, \xi) = \delta(\xi) \tag{B.8}$$

In both cases, $P_0(Z_1, Z_2; \xi)$ is independent of Z_1 and Z_2.

With the variable change (B3), the triple integral (B2) can be written as,

$$I_n = 2 \int\limits_{0}^{1} dZ_1 \int\limits_{Z_1}^{1} dZ_2 \int\limits_{-1}^{1} d\xi P_0(Z_1, Z_2; \xi)(\frac{Z_1 + Z_2}{2} + \frac{Z_2 - Z_1}{2}\xi)^n f(Z_1)f(Z_2) \tag{B.9}$$

where the limits of the integrals are obtained by inspecting the tranformation of the 3-dimenional integral region in (Z_1, Z_2, Z) space into that in the (Z_1, Z_2, ξ) space. It is now straightforward to calculate the integral for different n's.

For $n = 0$,

$$I_0 = 2 \int_0^1 dZ_1 f(Z_1) \int_{Z_1}^1 dZ_2 f(Z_2) \tag{B.10}$$

where eq (B5) is used. To evaluate this integral, we use the identity

$$\int_0^1 dZ_1 f(Z_1) \int_{Z_1}^1 dZ_2 f(Z_2) = \int_0^1 dZ_2 f(Z_2) \int_0^{Z_2} dZ_1 f(Z_1) = \int_0^1 dZ_1 f(Z_1) \int_0^{Z_1} dZ_2 f(Z_2) \tag{B.11}$$

where in the first step we changed the order of the integration with respect to Z_1 and Z_2 and the integral limit changes are based on the integral region on the (Z_1, Z_2) plane. In the second step we exchanged the dumb integral variables. Then we have,

$$I_0 = \int_0^1 dZ_1 f(Z_1) \int_{Z_1}^1 dZ_2 f(Z_2) + \int_0^1 dZ_1 f(Z_1) \int_0^{Z_1} dZ_2 f(Z_2) = 1 \tag{B.12}$$

which implies that eq (B1) conserves the total probability.

For n=1,

$$I_1 = \int_0^1 dZ_1 Z_1 P(Z_1) \int_{Z_1}^1 dZ_2 P(Z_2) + \int_0^1 dZ_1 P(Z_1) \int_{Z_1}^1 dZ_2 Z_2 P(Z_2) \tag{B.13}$$

where we used eq (B5) and $\int_{-1}^{1} P(Z_1, Z_2, \xi) \xi d\xi = 0$ according to eq (B6). Using the same calculation as eq (B11) for the first term, we have

$$\begin{aligned} I_1 &= \int_0^1 dZ_1 P(Z_1) \int_0^{Z_1} dZ_2 Z_2 P(Z_2) + \int_0^1 dZ_1 P(Z_1) \int_{Z_1}^1 dZ_2 Z_2 P(Z_2) \\ &= \int_0^1 dZ_2 Z_2 P(Z_2) = \langle Z \rangle \end{aligned} \tag{B.14}$$

which implies the conservation of the mean.

For n=2,

$$\begin{aligned}I_2 &= \tfrac{1}{2}[\int_0^1 dZ_1 Z_1^2 P(Z_1) \int_{Z_1}^1 dZ_2 P(Z_2)(1+\sigma_P^2) + \int_0^1 dZ_1 P(Z_1) \int_{Z_1}^1 dZ_2 Z_2^2 P(Z_2)(1+\sigma_P^2)] + \\ &\quad \int_0^1 dZ_1 Z_1 P(Z_1) \int_{Z_1}^1 dZ_2 Z_2 P(Z_2)(1-\sigma_P^2)\end{aligned} \tag{B.15}$$

where eqs (B5) and (B6) are used and σ_P^2 is defined as $\int_{-1}^{1} P_0(Z_1, Z_2; \xi)\xi^2 d\xi$. Generally σ_P^2 is a function of Z_1 and Z_2 and the integral depends on the function form. We consider the special case where σ_P^2 is independent of Z_1 and Z_2, as is true for the transition functions used by Janicka et al. (1979) and Curl (1963). In this case, $(1+\sigma_P^2)$ and $(1-\sigma_P^2)$ can be taken out of the integrals. We use the technique in eq (B11) again for the first and third terms and obtain,

$$I_2 = \frac{1+\sigma_P^2}{2}\langle Z^2\rangle + \frac{1-\sigma_P^2}{2}\langle Z\rangle^2 \tag{B.16}$$

Substracting the contribution from the second term on the rhs of eq (B1), which is $\langle Z^2\rangle$, we finally have the variance equation,

$$\frac{d\sigma^2}{dt} = -\frac{1-\sigma_P^2}{2\tau_{mix}}\sigma^2 \tag{B.17}$$

The variance $\sigma_P^2 \leq 1$ with the equality applies only when $P_0(Z_1, Z_2, \xi)$ consists of two delta functions at $\xi = -1$ and $\xi = 1$. Therefore the concentration variance always decreases with time in this closure. For the uniform $P(Z_1, Z_2; Z)$ in Janicka et al. (1979), $\sigma_P^2 = 1/3$ from eq (B7), therefore σ^2 decays exponentially with a timescale of $3\tau_{mix}$. For Curl's model, $\sigma_P = 0$ from eq (B8) and the variance decays with a timescale of $2\tau_{mix}$.

Appendix C

The sweepup mass M_{sw}

In sec 3, we used the total SN rate ν_{SN} and an average sweepup mass M_{sw} representing contributions from both isolated SNe and SBs. Realistically we need to include SNe and SBs separately.

C.1 Isolated SNe

If a fraction f_i of the total SNe are isolated SNe that explode in the field, their contribution to the pdf equation is given by,

$$(\frac{\partial f(Z,t)}{\partial t})_i = -\frac{f_i \nu_{SN} M_{swi}}{M_{gas}}(f(Z,t) - f(Z - \frac{M_Z}{M_{swi}}, t)) \tag{C.1}$$

where M_{swi} is the mass of the ISM gas swept up by an isolated SN.

The sweepup mass M_{swi} can be found in dynamical calculations of SNR evolution, e.g., Cioffi et al (1988) and Thornton et al. (1998). Here we adopt the result by Thornton et al. (1998). In this paper, the final time t_f for the SNR evolution is defined as the time when the SNR luminosity becomes less than 5% of the maximum luminosity in the evolution. They find that this time is earlier than both the onset of the momentum-conserving snow plow phase and the merging of the remnant with the ISM. Therefore the stall radius and the total sweepup mass are expected to be larger than what they derive. However, we point out that their final time is very close to the merging of the shell with the ISM. The shock speed at t_f given by Thornton et al (1998) is

$$V_f = 11.3 E_{51}^{1/14} n_0^{-0.01} (Z/Z_\odot)^{-0.09} \mathrm{km/s} \tag{C.2}$$

where the initial energy of the explosion is $E_{51} = E/10^{51}$ erg, the ambient average ISM particle density is n_0, and the metal fraction relative to the sun is $Z/Z_\odot$. Since the final velocity V_f, which is almost independent of any parameters, is very close to the velocity dispersion $C \simeq 10$ km/s in the ISM, merging is just about to occur after t_f. The total sweepup mass at the merging/ stalling time is therefore not considerably larger than the sweep mass at the final time t_f. If the momentum conserving snow plow starts after t_f, the total sweepup mass at the merging time would be larger by a factor of V/C than that at t_f. This is only a factor of 13% according to eq (C2). Or if after t_f the pressure driven snow plough continues till merging occurs, the total sweepup mass increases by a factor of 16%. Note that eq (C2) only applies when the metallicity relative to solar $Z/Z_\odot$ is larger than 0.01. Thornton et al. obtained a larger speed and a larger sweepup mass at the final time for metallicity $Z/Z_\odot < 0.01$. However, in most chemical evolution models, the mean metallicity approaches $0.01 Z_\odot$ quickly and a larger sweepup mass at extremely early time only gives negligible effect on the present-day metallicity scatter. In our calculations, we will adopt the result of the sweepup mass for $Z/Z_\odot > 0.01$ at any time.

To account for the effect of the magnetic field, we make use of the dependence of the porosity on the magnetic field strength found in 2D MHD simulations by Hanayama and Tomisaka (2006). Their result implies that a 3 microgauss magnetic field reduces the stall radii by a factor of 1.2, or a factor of 1.2^3 for M_{swi} (see their fig. 10b). The reduction factor for 5 μG magnetic field is even larger, about 1.4. We take a conservative reduction factor of 1.2 for $3\mu G$. Applying this factor due to the magnetic field and the factor due to the further expansion after the final time to eq (21) in Thornton et al (1998), we have the merging radius,

$$R_m = 42 E_{51}^{2/7} n_0^{-0.41} (Z/Z_\odot)^{-0.09} \ \mathrm{pc} \tag{C.3}$$

and the total sweepup mass,

$$M_{swi} = 9 \times 10^3 E_{51}^{6/7} n_0^{-0.24} (Z/Z_\odot)^{-0.27} \ M_\odot \tag{C.4}$$

The sweepup mass has a very weak dependence on the ISM density and the metallicity. In principle, the sweepup mass is coupled to the metallicity field and the fluctuations in metallicity give rise to fluctuations in the sweepup mass. However we neglect this coupling for simplicity and use the result at $Z \sim Z_\odot$ since the metallicity arrives at the solar value quickly.

The density variations in the ISM also cause fluctuations in the sweepup mass M_{swi}. One may first neglect the fluctuations and use the average of $\langle M_{swi} \rangle$ to replace M_{swi} in eq(C1). Clearly this approximation underestimates the scatter. The average of M_{swi} is calculated by integrating eq (C3) over the density distribution. For example, if the density distribution of n_0 is log-normal (Padoan and Norlund 1999) with a variance σ_n^2, the average of M_{swi} is equal to $\langle M_{swi} \rangle = 9 \times 10^3 exp(0.15\sigma_n^2)\langle n_0 \rangle^{-0.24}$ $M_\odot$ where we assumed $E_{51} = 1$ and $Z = Z\odot$. According to Padoan et al. (1997), the variance σ_n^2 depends on the Mach number Ma in the ISM as $\sigma_n^2 \simeq ln(1+0.25Ma^2)$. Therefore $\langle M_{swi} \rangle = 9 \times 10^3 (1+0.25Ma^2)^{0.15} \langle n_0 \rangle^{-0.24}$ $M_\odot$ depends on the Mach number very weakly. If the average Mach number is 1, $M_a = 1$, we have $\langle M_{swi} \rangle = 9300 \langle n_0 \rangle^{-0.24}$ $M_\odot$.

To exactly account for the fluctuations of M_{swi}, one needs to integrate the rhs of eq (C1) over the distribution of M_{swi} and solve the integral equation. A simpler approach to see how the fluctuations affect the scatter is to derive the first two moment equations of the integral pdf equation that includes the M_{swi} fluctuations, i.e., the mean and the variance equations, because the ratio of the rms (square root of the variance) of metallicity fluctuations to the mean provides a measure for the metallicity scatter around the mean. Obviously the first order moment equation, i.e., the mean equation, does not contain the sweepup mass, which does not change the mean metallicity. Interestingly, the variance equation only depends on the average $\langle 1/M_{swi} \rangle$ over the distribution of M_{swi}. If we replace M_{swi} in eq (C1) by $\langle 1/M_{swi} \rangle^{-1}$ and then derive its variance equation, we obtain the same equation as derived from the integral pdf equation. This implies that the effect of fluctuations in the sweepup mass can be approximately accounted for by replacing M_{swi} in eq (C1) with $\langle 1/M_{swi} \rangle^{-1}$. We will call $\langle 1/M_{swi} \rangle^{-1}$ the effective sweepup mass. For the log-normal distribution used above, we get $\langle 1/M_{swi} \rangle^{-1} = 9 \times 10^3 (1+0.25Ma^2)^{0.09} \langle n_0 \rangle^{-0.24}$ $M_\odot$. This effective sweepup mass is a little smaller than the average $\langle M_{swi} \rangle$, indicating that fluctuations in M_{swi} give a little increase in the metallicity scatter. For $Ma = 1$, $\langle 1/M_{swi} \rangle^{-1} = 9200 \langle n_0 \rangle^{-0.24}$ $M_\odot$.

We have assumed that the field stars are randomly distributed in the ISM. But it is possible that they tend to locate in the ISM with low density. If most field stars are in the ISM with $n_0 = 0.1$, then sweepup mass we need to use is eq (C3) with $n = 0.1$, i.e., $M_{swi} \simeq 1.6 \times 10^4 M_\odot$. We think this is the upper limit for M_{swi}.

C.2 Superbubbles

We denote as f_c the fraction of the total SNe that are clustered and explode as SBs. Clearly, $f_c = 1 - f_i$. Different SBs may have different number N of massive stars that power their expansion. We define $f(N)$ as the distribution of N so that $f(N)dN$ is the probability of a SB having $(N, N + dN)$ exploding stars. Therefore the number rate $\nu_c(N)$ of SBs that contain N SNe is given by $\nu_c(N) = f_c \nu_{SN} f(N)/\langle N \rangle$ where $\langle N \rangle = \int\limits_{N_l}^{N_u} N f(N) dN$ is the average number of SNe per SB. The lower limit N_l and the upper limit N_u are the minimum and maximum number of SNe in a SB, respectively. The contribution from SBs to the pdf equation is then

$$(\frac{\partial f(Z,t)}{\partial t})_c = -\frac{f_c \nu_{SN}}{M_{gas}} \int \frac{M_{swc}(N)}{\langle N \rangle} (f(Z,t) - f(Z - \frac{M_{Zc}(N)}{M_{swc}(N)}, t)) f(N) dN \quad (C.5)$$

where $M_{swc}(N)$ and $M_{Zc}(N)$ are the ISM mass swept by and the mass of metals produced in a SB that contains N SNe.

The sweepup mass $M_{swc}(N)$ depends on the SB expansion history. The evolution of SB shells is a complicated process where various important effects have to be considered such as the radiative cooling, the scale height of the disk and the magnetic fields in the ISM. The effects of the radiative cooling and the scale height have been studied by McCray and Kafatos (1987), Mac Low & McCray (1988) (for a review, see Tenorio-Tagle and Bodenheimer 1988) and Mac Low, McCray and Norman (1989). The evolution of SBs in magnetized ISM can be found in (Tomisaka 1990, Mineshige et al 1993, Ferriere et al 1991 and de Avillez and Breitschwerdt 2005). In our derivation, we will first neglect the radiative cooling and the hot interior as the shell punches into the halo (McCray and Kafatos 1987). SBs with intermediate number of SNe enter the momentum conservation phase within the disk due to cooling. We carried out a calculation for the sweepup mass of these SBs with the effects of the radiative cooling consistently accounted for. However, here we will give a simpler calculation where we negelct cooling in these bubbles and assume that the expansion is adiabatic before either merging with ISM or blowing out of the disk. This assumption overestimates the average sweepup mass, but only by several percent. A large SB starts the momentum conservation phase as it breaks out of the disk. When blowing out of the disk, the shell starts to accelerate and the Rayleigh-Taylor instability sets in. Simulations by Mac Low, McCray and Norman (1989) (see also Igumentshchev et al 1990) show that this happens when the shell radius exceeds $1.7 - 2.2$ times the scale height H of the disk depending on whether the vertical gas density profile is exponential or Gaussian and whether the SB explodes in the central plane or not. We will take $H = 100$ pc and assume that the blowout happens and the mometum conservation phase starts when the shell radius exceeds twice the scale height, $2H = 200$ pc. Once the momentum conservation phase starts, the expansion decelerates very fast and it takes a short time for the shell velocity to drop below the velocity dispersion in the ISM. Therefore the radius does not grow significantly in the momentum conservation phase and the stall radius is determined mainly by the radius at the transition from the adiabatic phase to the momentum conservation phase.

A complication in the evolution of SBs is the presence of a magnetic field of strength $5\mu G$ in the ISM. Magnetic fields perpendicular to the disk plane can suppress motions in the horizontal direction. In this case, similar to the isolated SNe, the stall radius and the sweepup mass are reduced by the magnetic field. Magnetic fields parallel to the disk plane which suppress the vertical motion (Tomisaka 1990, Mineshige et al 1993) can affect the sweepup mass in two opposite ways depending on the mechanic luminosity of the SB. First, it decreases the stall radius and the sweepup mass of SBs that do not blow out (Ferriere et al 1991). Second it could delay the blow-out of large SBs or even confine some bubbles that can blow out in the absence of magnetic fields, making the adiabatic expansion in the horizontal direction longer. This tends to result in a larger sweepup mass since the transition to momentum conservation phase occurs later. However, we show that the magnetic fields do not significantly change the stall radius and the sweepup mass using the argument by Tomisaka (1990) that the magnetic field starts to be important in the SB evolution only when the internal pressure drops below the magnetic pressure. We find that, assuming adiabatic expansion, the shell velocity decreases to the velocity dispersion in the ISM before the internal pressure drops below the megnetic pressure for typical velocity dispersion $C = 10$ km/s and magnetic strength $B = 5\mu G$. This implies that for small SBs the magnetic field is not important before merging and that for large SBs the internal pressure is larger than the magnetic pressure when they break out

Therefore the magnetic fields do not affect the stall radius and the sweepup mass significantly. This result agrees with the analytical studies and the numerical simulations by Ferriere et al (1991) and de Avillez and Breitschwerdt (2005). Note that in spite of using the same argument, we arrived at a different conclusion from Tomisaka (1990) which claimed that magnetic fields play an important role of confining SBs in the disk. This is because Tomisaka did not consider merging of SB shells with the ISM. When the velocity decreases to about 10 km/s, the shell starts to be destroyed by the turbulent motions in the ISM and lose its identity. In this sense, the turbulent motions provide a confinement that keeps the shell mass in the disk, which we find to occur before the magnetic fields become important.

Since the primary source of variations in the case of SBs is the number of SNe in different SBs, we will neglect the effect of the fluctuations in the density n_0 and the velocity C in the ISM. We assume that $n_0 = 1$ cm^{-3} and $C = 10$ km/s.

We first neglect the the radiative cooling and the magnetic fields, whose effects will be discussed later. We derive the minimum number of SNe that a SB has to have to break out of the disk. In the adiabatic phase, the shell velocity V and radius R, respectively, evolve with time t as (McCray & Kafatos 1987; Weaver et al. 1977),

$$V = 5.7(NE_{51}/n_0)^{1/5} t_7^{-2/5} \text{ km/s} \tag{C.6}$$

and

$$R = 97(NE_{51}/n_0)^{1/5} t_7^{3/5} \text{ pc} \tag{C.7}$$

where t_7 is the time t in unit of 10^7 yr. We define the merging time t_m as the time at which the shell velocity drops to the velocity dispersion C in the ISM, which is obtained by setting V in eq (C6) to C,

$$t_m = 2.4 \times 10^6 C_{10}^{-5/2} (NE_{51}/n_0)^{1/2} \text{ yr} \tag{C.8}$$

where C_{10} is C in unit of 10 km/s. Another important time scale t_b is the time at which a SB shell, if it can, exceeds two times the scale height, $2H$, and breaks out of the disk. We obtain t_b by setting R in eq (C7) to $2H$,

$$t_b = 3.2 \times 10^7 (H/100\ \text{pc})^{5/3} (NE_{51})^{-1/3} n_0^{1/3}\ \text{yr} \tag{C.9}$$

Obviously a SB shell cannot cross the scale height if $t_b > t_m$ and only SBs with $t_b < t_m$ can break out of the disk. Equating eq (C7) to eq (C8) gives a critical number,

$$N_b = 22 C_{10}^3 (H/100\ \text{pc})^2 (n_0/E_{51}) \tag{C.10}$$

SBs can punch into the halo only if they have more than N_b SNe.

We now consider the effect of the radiative cooling. We check whether the radiative cooling is important for SBs with $N \leq N_b$ before they merge with the ISM by comparing the merging timescale estimated above with the cooling timescale. Mac Low and McCray (1988) found that the cooling time scale t_c is,

$$t_c = 4 \times 10^6 (Z/Z_\odot)^{-1.5} (NE_{51})^{0.3} n_0^{-0.7}\ \text{yr} \tag{C.11}$$

Inserting eq (C10) into eq (C11) and eq (C8), we find that for a SB with $N = N_b$, $t_c = 10 \times 10^6 (Z/Z_\odot)^{-1.5} C_{10}^{0.9} (H/100\text{pc})^{0.6} n_0^{-0.4}$ yr, which is smaller than $t_m = 11 \times 10^6 C_{10}^{-1} (H/100\ \text{pc})$ yr, i.e., the radiative cooling becomes important before a SB with $N = N_b$ merges with the ISM. Since the cooling timescale t_c decreases with decreasing N slower than t_m, there is a critical number smaller than N_b at which $t_c = t_m$. Equating eq (C8) with eq (C11), we find the critical number $\simeq 12$. For SBs with more than ~ 12 SNe, the radiative cooling gets the shell into the momentum conservation phase before merging while for SBs that contain less than ~ 12 SNe, cooling does not become important before merging thus does not play a role in the evolution. Radiative cooling does not affect the evolution of very large SBs either, which break out of the disk in the adiabatic phase. Setting t_b equal to t_c, we get another critical number of SNe, $\simeq 28$. For a SB with more than ~ 28 SB, the expansion is adiabatic before the shell arrives at about $2H$ and blows out. SBs with the number of SNe between the two critical numbers start the momentum conservation phase by radiative cooling within the disk. To calculate the stall radius for these SBs, we need to consider the radiative cooling correctly. However, for simplicity we will neglect the radiative cooling and assume that SBs expand adiabatically before they merge with the ISM (for $N < N_b$) or blow out of the disk (for $N > N_b$). Clearly neglecting cooling overestimates the stall radius and the final sweepup mass. We find that this approximation increases the sweepup mass only by several percent. Note that our calculation that neglects cooling is exact for $Z \lesssim 0.5 Z_\odot$ where t_c is larger than t_m by a least a factor of $2-3$ for any SB with $N < N_b$.

We show that the magntic field of $\sim 5\mu G$ in the ISM do not significantly affect the expansion of SBs assuming that the magnetic field becomes important only when the internal pressure drops below the magnetic pressure $P_B = B_0^2/8\pi$ where $B_0 \simeq 5\mu G$ is the average magnetic field in the ISM (Tomisaka 1992). Assuming adiabatic expansion, the evolution of the internal pressure is given by (Weaver et al. 1977),

$$P = 5.2 \times 10^{-13} (NE_{51})^{2/5} n_0^{3/5} t_7^{-4/5} \text{ dyn cm}^{-2} \tag{C.12}$$

Equating it with the magnetic pressure, we obtain the time t_B at which the magetic field starts to be important,

$$t_B = 4.4 \times 10^6 (NE_{51})^{1/2} n_0^{3/4} B^{-5/2} \text{ yr} \tag{C.13}$$

This time scale is a little larger than (but comparable to) the merging timescale t_m, meaning that the shell merges with the ISM before the magnetic fields becomes important. Therefore the magentic fields do not significantly change the stall radius or inhibit the large shells from blowing out of the disk. de Avillez and Breitschwerdt (2005) arrived at a similar conclusion by deriving the maximum radius that SBs can reach condisering the tension of the magnetic fields and confirmed their results with simuations. Ferriere et al. (1991) found that magnetic fields do not modify the shape and dimension of SBs and reduce the volume of the cavity by one third. We will neglect the effects of magnetic fields in the following calculations.

We calculate the stall radius and the sweepup mass for $N \leq N_b$ and $N > N_b$ respectively. For SBs with $N \leq N_b$, the merging radius of the shell is obtained by plugging the merging time (C8) to (C7),

$$R_m = 42 C_{10}^{-3/2} (NE_{51}/n_0)^{1/2} \text{ pc} \tag{C.14}$$

The scaling $R_m \propto N^{1/2}$ is the same as found in Oey and Clark (1997). Note that Oey and Clarke assumed that this scaling applies for SBs with any number of exploding massive stars. However it is only valid for small SBs because, for large SBs, the adiabatic expansion fails at late time when breaking out of the disk. Using the merging radius, we obtain the sweepup mass $M_{swc} = 4\pi\rho R_m^3/3$ where ρ is the density in the ISM,

$$M_{swc} = 8600 C_{10}^{-9/2} (NE_{51})^{3/2} n_0^{-1/2} \ M_\odot. \tag{C.15}$$

For a SB with $N > N_b$, the expansion enters the momentum-conservation phase once it breaks out of the Galactic disk. We assume a 2D geometry for the shell expansion after the radius exceeds twice the scale height. The momentum conservation means that $\rho R^2 H dR/dt$ is constant, which gives $R \propto t^{1/3}$ and $V \propto t^{-2/3}$ thus $R \propto V^{-1/2}$. Using this scaling, we can derive the merging radius R_m from the shell velocity V_{2H} when the shell arrives at twice the scale height and the merging velocity V_m which is equal to the velocity dispersion C, i.e., $R_m/2H = (V_{2H}/C)^{1/2}$. The velocity V_H is obtained by inserting eq (C9) to eq (C6),

$$V_{2H} = 3.5 (H/100 \ \text{pc})^{-2/3} (NE_{51})^{1/3} n_0^{-1/3} \ \text{km/s} \tag{C.16}$$

Therefore the merging radius is

$$R_m = 120 C_{10}^{-1/2} (H/100 \ \text{pc})^{2/3} (NE_{51}/n_0)^{1/6} \ \text{pc} \tag{C.17}$$

Instead of calculating the total sweepup mass from R_m, we derive it by equating the final momentum at merging to the momentum when the shell punches into the halo. This derivation avoids the geometry of the shell, which is not exactly 2D. The final momentum of the shell at merging is equal to the final sweepup mass M_{swc} times the velocity at merging, which is equal to the velocity dispersion C in the ISM. The conservation of momentum $M_{swc}C = 4\pi\rho(2H)^3/3V_{2H}$ gives the final sweepup mass by a SB for $N > N_b$,

$$M_{swc} = 3.2 \times 10^5 C_{10}^{-1} (H/100 \ \text{pc})^{7/3} (NE_{51})^{1/3} n_0^{2/3} \ M_\odot \tag{C.18}$$

which increases with time as $N^{1/3}$, much slower than $N^{3/2}$ in the case of $N < N_b$. Obviously this is because the expansion is less efficient in the momentum conservation phase than in the adiabatic phase.

We now consider $M_{Zc}(N)$ as a function of N. We will neglect the metals lost to the halo from the large SBs so that $M_{Zc}(N)$ is equal to the sum of metals from the N massive stars. We assume that the mass distribution of massive stars in each cluster samples the initial mass function at high masses. The average mass of metals produced in SBs with N SNe is then $\langle M_{Zc}(N)\rangle = N\langle M_Z\rangle$ where $\langle M_Z\rangle$ is the metal yield averaged over the initial mass function. The metal mass from an individual SB with N SNe may deviate from $\langle M_{Zc}(N)\rangle$ due to the finite number of massive stars which incompletely sample the IMF. Thus there are variations in $M_{Zc}(N)$ around the average in different individual SBs containing the same number N of SNe, especially for small N. The amplitude of variations decreases with increasing N. We neglect the variations in the total metal mass produced in different SBs with the same number of SNe and set $M_{Zc}(N) = N\langle M_Z\rangle$. Obviously this underestimates the scatter.

We simplify the integral in eq (C5) by using the average sweepup mass $\langle M_{swc}\rangle = \int_{N_l}^{N_u} M_{swc}(N)f(N)dN$ and the average mass of metals $\langle M_{Zc}\rangle = \int_{N_l}^{N_u} M_{Zc}(N)f(N)dN = \langle N\rangle\langle M_Z\rangle$ per SB to approximate the integral over the distribution of the number of SNe,

$$(\frac{\partial f(Z,t)}{\partial t})_c = -\frac{f_c\nu_{SN}}{M_{gas}}\frac{\langle M_{swc}\rangle}{\langle N\rangle}(f(Z,t) - f(Z - \frac{\langle M_{Zc}\rangle}{\langle M_{swc}\rangle}, t)) \tag{C.19}$$

This is equivalent to assuming that the number N of SNe is single- valued so that $f(N)$ in eq(C5) is a delta function at a certain number, i.e., every SB has this number of SNe, and that each SB sweeps up the same amount, $\langle M_{swc}\rangle$, of interstellar gas. Defining the sweepup mass per SN in SBs

$$\bar{M}_{swc} = \langle M_{swc}\rangle/\langle N\rangle, \tag{C.20}$$

eq (C17) becomes

$$(\frac{\partial f(Z,t)}{\partial t})_c = -\frac{f_c\nu_{SN}\bar{M}_{swc}}{M_{gas}}(f(Z,t) - f(Z - \frac{\langle M_Z\rangle}{\bar{M}_{swc}}, t)) \tag{C.21}$$

which is similar to eq (C1) for the isolated SNe except that f_c and $\bar{M}_{swc}$ replace f_i and M_{swi} respectively.

We need the distribution $f(N)$ to calculate $\bar{M}_{swc}$ using the sweepup mass given by (C10) and (C16) for $N < N_b$ and $N > N_b$ respectively. We take $f(N)$

to be a power law, $f(N) \propto N^{-\beta}$. We experimented with different β around $\beta \simeq 2$ (e.g., Fierrie 1995, Oey and Clark 1997) and different lower and upper limits that satisfy $\langle N \rangle \simeq 30$ (Fierrie 1995). We first take $\beta = 2$ and choose 2 different sets of limits N_l and N_u: $N_l = 4$, $N_u = 7000$ and $N_l = 6$, $N_u = 1000$. If $H = 100$ pc, we get $\bar{M}_{swc} = 1.4 \times 10^4 M_\odot$ and $\bar{M}_{swc} = 1.9 \times 10^4 M_\odot$ for the two sets of limits respectively.

We consider how much $\bar{M}_{src}$ changes with β using two examples $\beta = 1.7$ and $\beta = 2.3$. For $\beta = 1.7$, we take the limits $N_l = 4$ and $N_u = 450$, which satisfy $\langle N \rangle = 30$. For $H = 100$ pc, we get $\bar{M}_{swc} = 1.8 \times 10^4 M_\odot$. For a steeper $f(N)$ with $\beta = 2.3$, the average $\langle N \rangle \simeq 30$ fixes the lower limit $N_l = 8$ but does not constrain the upper limit, provided it is much larger than the lower limit. The average sweepup mass $\bar{M}_{swc}$ per SN is not affected by the upper limit and we get $\bar{M}_{swc} = 2 \times 10^4 M_\odot$ for $H = 100$ pc. Comparing with results from different β and limits, N_l and N_u, we find that the average sweepup mass per SN does not change significantly at different $\beta \simeq 2$ while keeping $\langle N \rangle \simeq 30$. For $H = 100$ pc, $\bar{M}_{swc} \simeq 14000 - 20000 M_\odot$.

The approximation of eq (C17) to eq (C5) neglects the fluctuations in the sweepup mass and the metal mass due to the distribution of numbers of SNe in SBs. Eq (C17) is exact if the metallicity $M_{Zc}(N)/M_{src}(N)$ by which the shell of a SB with N SNe is enriched is independent of N. This is not true under our assumption that all the metals produced in a SB are used to enrich the part of the shell that remains in the disk so that $M_{Zc}(N) \propto N$ while $M_{src}(N) \propto N^{1/3}$ for large N. If a larger fraction of metals are lost to the halo for larger N, $M_{Zc}(N)$ scales with N slower than linearly, the approximation eq (C17) would be better. Since we do not know the exact $M_{Zc}(N)$ as a function of N, we study how the fluctuations in $M_{Zc}(N)/M_{src}(N)$ affect the scatter in the extreme case where no metals are lost to the halo. The effect could be weaker if $M_{Zc}(N)$ goes with N slower than linearly. We use the same approach as in sec C.1 for the fluctuations of M_{swi}, i.e., derive the mean and variance equations of the pdf eq (C5). We find that the variance equation depends on an effective sweepup mass per SNe,

$$\bar{M}_{eff} = \frac{\langle N \rangle}{\int\limits_{N_l}^{N_u} \frac{N^2}{M_{swc}(N)} f(N) dN} \tag{C.22}$$

If we replace $\bar{M}_{src}$ in eq (C19) by $\bar{M}_{eff}$ and then derive the variance equation, we get the same result as derived from the integral eq (C5). In this sense, $\bar{M}_{eff}$ includes the effect of the fluctuations due to the distribution of N. The effective sweepup mass can be calculated given the distribution $f(N)$. Taking $\beta = 2$, $N_l = 4$ and $N_u = 7000$, we get $\bar{M}_{eff} = 4300 M_\odot$ for $H = 100$ pc and if $\beta = 2$, $N_l = 6$ and $N_u = 1000$, $\bar{M}_{eff} = 1.1 \times 10^4 M_\odot$. The effective sweepup mass $\bar{M}_{eff}$ is much smaller than the average sweepup mass $\bar{M}_{swc}$ for the same $f(N)$, meaning that the variations of $M_{swi}(N)$ and $M_{Zc}(N)$ with N have considerable effects on the predicted scatter. The effective sweepup mass is small because the factor N^2 in the integrand in eq (C20), which comes from $M_{Zc}(N) \sim N$, makes the denominator large. If $M_{Zc}(N)$ scales with N slower than $\propto N$, the effective sweepup mass eq(C20) would be larger. Considering the possibility that a larger fraction of metals are ejected into the halo for larger N, the sweepup mass is between $\bar{M}_{swc}$ and $\bar{M}_{eff}$ and we will take the upper limit $\bar{M}_{swc}$ and keep in mind that the effective sweepup mass per SN in SBs can be much lower than $\bar{M}_{swc}$. In summary, the sweepup mass per SN in SBs has a range from $4300 M_\odot - 2 \times 10^4 M_\odot$ accounting for the average sweepup mass $\bar{M}_{src}$ and the effective sweepup mass $\bar{M}_{eff}$.

In our calculations, we will use eq (C1) with $\langle M_{swi} \rangle$ for the isolated SNe and eq (C19) with $\bar{M}_{swc}$ for the superbubbles. The overall average sweepup mass including both isolated SNe and SBs is given by $M_{sw} = f_i \langle M_{swi} \rangle + f_c \bar{M}_{swc}$. We take $f_c = 0.3$ and $f_i = 0.7$. The sweepup mass by isolated SNe is $\simeq 9000 M_\odot$ and the sweepup mass per SN in SBs has much larger uncertainty, $\simeq 4300 - 2 \times 10^4 M_\odot$. Therefore M_{sw} has a range of $6000 M_\odot - 17000 M_\odot$. In our calculations we used M_{sw} from $6000 M_\odot$ to $16000 M_\odot$ with a fiducial $M_{sw} = 10000 M_\odot$.

Appendix D

Distribution of Ratios

Given the joint probability distribution $f(x, y)$ of two variables x and y, we can calculate the distribution of any new variable $z = h(x, y)$ as a function of x and y. The pdf $P(z)$ of z can be written as an integral of a delta function over the joint distribution,

$$P(z) = \int_{-\infty}^{+\infty}\int_{-\infty}^{+\infty} \delta(z - h(x, y)) f(x, y) dx dy \tag{D.1}$$

If the equation $h(x, y) - z = 0$ at given y and z only has single roots, x_i, for x, then we have from the property of delta functions,

$$\delta(z - h(x, y)) = \sum_i \frac{\delta(x - x_i)}{|h'(x_i)|} \tag{D.2}$$

where $h'(x_i)$ is the x derivative of $h(x, y)$ at x_i. The derivatives $h'(x_i) \neq 0$ at single roots. Inserting eq. D(2) to D(1), we have

$$P(z) = \int_{-\infty}^{+\infty}\int_{-\infty}^{+\infty} \sum_i \frac{\delta(x - x_i)}{|h'(x_i)|} f(x, y) dx dy \tag{D.3}$$

Integrating x, we get,

$$P(z) = \sum_i \int_{-\infty}^{+\infty} \frac{1}{|h'(x_i)|} f(x_i, y) dy \tag{D.4}$$

Note that x_i's are functions of y and z. For any given distribution $f(x, y)$ and function $h(x, y)$, $P(z)$ can be calculated from this formula.

We apply the formula to a special case, the ratio of two independent variables, i.e., $h(x, y) = x/y$ and $f(x, y) = f_x(x)f_y(y)$ where $f_x(x)$ and $f_y(y)$ are, respectively, the distributions of x and y. From equation (D4), we have,

$$P(z) = \int_{-\infty}^{+\infty} |y| f_x(yz) f_y(y) dy \tag{D.5}$$

We consider an simple example where x and y are zero-mean Gaussian variables. If the standard deviations of x and y are σ_x, σ_y, respectively, then

$$P(z) = \frac{1}{2\pi\sigma_x\sigma_y} \int_{-\infty}^{+\infty} |y| exp(-\frac{(yz)^2}{2\sigma_x^2}) exp(-\frac{y^2}{2\sigma_y^2}) dy \tag{D.6}$$

Direct integration gives the distribution of z,

$$P(z) = \frac{\sigma_x}{\pi\sigma_y} \frac{1}{z^2 + \frac{\sigma_x^2}{\sigma_y^2}} \tag{D.7}$$

which is a Lorentz distribution.

Appendix E

The She-Leveque Model

In their original paper, She and Leveque (1994) start with the moments of the distribution $P(\epsilon_l)$ and use the ratios of two successive moments, $\epsilon_l^{(p)} = \langle \epsilon_l^{p+1} \rangle / \langle \epsilon_l^p \rangle \propto l^{\tau_{p+1}-\tau_p}$, to characterize a hierarchy of dissipative structures. This ratio can be written as $\epsilon_l^{(p)} = \int \epsilon_l Q_p(\epsilon_l) d\epsilon_l$ where $Q_p(\epsilon_l) = \epsilon_l^p P(\epsilon_l) / \int \epsilon_l^p P(\epsilon_l) d\epsilon_l$. For a typical distribution $P(\epsilon_l)$ that decreases monotonically and faster than any power law at large ϵ_l, $Q_p(\epsilon_l)$ strongly peaks around $\epsilon_l^{(p)}$ for large p. Clearly $\epsilon_l^{(p)}$ increases with p, and $\epsilon_l^{(\infty)} = \lim_{n\to\infty} \langle \epsilon_l^{p+1} \rangle / \langle \epsilon_l^p \rangle$ corresponds to the most intense dissipative structures at scale l. These strongest dissipative structures are the origin of the anomalous scaling and the scaling of $\epsilon_l^{(\infty)}$ with l,

$$\epsilon_l^{(\infty)} \sim l^{-\gamma} \tag{E.1}$$

is of fundamental importance. To determine the parameter γ, we can dimensionally write $\epsilon_l^{(\infty)}$ as an energy scale divided by a time scale t_l. She and Leveque argued that for the most intermittent structures this energy scale is the largest available kinetic energy (which is $\sim v_{rms}^2$, independent of l) and assumed that t_l exhibits a regular Kolmogorov scaling $t_l \sim l^{2/3}$, therefore $\gamma = 2/3$. From eq (E.1), we have $\tau_{p+1} = \tau_p - \gamma$ for $p \to \infty$ or

$$\tau_p = -\gamma p + C, \quad p \to \infty \tag{E.2}$$

where the constant C has a physical interpretation as the codimension of the most intermittent structures. Eq (E.1) means that the dissipation rate in a region of size l that encloses the most intensive structures scales with l as $\epsilon_l \propto l^{-\gamma}$. When calculating $\langle \epsilon_l^p \rangle$ at $p \to \infty$, we need to consider the possibility of a point finding itself within a distance l to the most intermittent structures, which is proportional to $l^{(D-d)}$ where D is the dimension of the system and d is the dimension of the most intensive structures (Frisch 1995). As $p \to \infty$, the contribution to $\langle \epsilon_l^p \rangle$ is dominated by the most intermittent structures, therefore $\langle \epsilon_l^p \rangle \propto l^{-\gamma p + D - d}$. Comparing with eq (E.2), we find that C corresponds to the codimension of the most intermittent structures, $C = D - d$.

In order to determine the entire hierarchy of the dissipative structures, She and Leveque argued that the intensity $\epsilon_l^{(p+1)}$ of the dissipative structures at level $p+1$ depends only on their immediate precursor, the structures of level p, from which the level $p+1$ structures directly develop, and on the most intensive structures, where the structures of all orders tend to end up. Based on this argument, they made an assumption about the hierarchy of the dissipation rates,

$$\epsilon_l^{(p+1)} = A_p (\epsilon_l^{(p)})^{\beta} (\epsilon_l^{(\infty)})^{1-\beta} \tag{E.3}$$

where the coefficients A_p are independent of l but may be flow-dependent and non-universal. The parameter β will be completely fixed by γ and the codimension C. According to She and Leveque, this relation corresponds to a mysterious symmetry of the Navier-Stokes equation, termed "the hidden symmetry".

To derive τ_p from equation (E.3), it is convenient to define a new variable,

$$\pi_l = \epsilon_l / \epsilon_l^{(\infty)} \tag{E.4}$$

which was introduced by Dubrulle (1994). Clearly $\epsilon_l^{(p)} / \epsilon_l^{(\infty)} = \langle \pi_l^{p+1} \rangle / \langle \pi_l^p \rangle$ from the definition of $\epsilon_l^{(p)}$. Then the "hidden symmetry" assumed by She and Leveque becomes,

$$\frac{\langle \pi_l^{p+2} \rangle}{\langle \pi_l^{p+1} \rangle} = A_p \left(\frac{\langle \pi_l^{p+1} \rangle}{\langle \pi_l^p \rangle} \right)^{\beta} \tag{E.5}$$

This recursion relation is solved by,

$$\frac{\langle \pi_l^{p+1} \rangle}{\langle \pi_l^p \rangle} = C_p \langle \pi_l \rangle^{\beta^p} \tag{E.6}$$

where $C_0 = 1$ and $C_p = \prod_{n=0}^{p} A_n^{\beta n}$ for $p > 0$. Eq. (E.6) gives,

$$\langle \pi_l^p \rangle = B_p \langle \pi_l \rangle^{(1-\beta^p)/1-\beta} \tag{E.7}$$

where $B_0 = B_1 = 1$ and $B_p = \prod_{n=1}^{p-1} C_n$ for $p > 1$. Noting that $\langle \pi_l \rangle = \bar{\epsilon}/\epsilon_l^{(\infty)} \propto (\epsilon_l^{(\infty)})^{-1}$ and $\langle \pi_l^p \rangle = \langle \epsilon_l^p \rangle (\epsilon_l^{(\infty)})^{-p}$, eq (A7) gives $\langle \epsilon_l^p \rangle \propto (\epsilon_l^{(\infty)})^{p-(1-\beta^p)/(1-\beta)}$. Using eq (E.1), we have

$$\tau_p = -\gamma p + \gamma \frac{(1-\beta^p)}{1-\beta} \tag{E.8}$$

The parameter β is determined by the asymptotic behavior of τ_p at the $p \to \infty$, eq (E.2). Letting $p \to \infty$ in eq (E.8) and comparing with eq (E.2), we find that $\gamma/(1-\beta) = C = D - d$. Since the most intermittent structures in 3D incompressible turbulence are filamentary, we have $d = 1$ and $C = 2$, thus $\beta = 1 - \gamma/2 = 2/3$ for $\gamma = 2/3$. Finally we arrive at the celebrated She-Leveque formulae,

$$\tau_p = -2p/3 + 2(1 - (2/3)^p) \tag{E.9}$$

and

$$\zeta_p = p/9 + 2(1 - (2/3)^{p/3}) \tag{E.10}$$

which agrees with the experimental result with an accuracy of 1%. Note that this result is consistent with the Kolmogorov's exact result for the third order structure function, i.e., $\zeta_3 = 1$. If the most intense structures are two dimensional, e.g., the dissipation sheets in compressible flows (Boldyrev et al. 2002) or the current sheets in MHD (Muller & Biskamp 2000), $\beta = 1/3$.

Bibliography

[1] Anselmet, F., Gagne, Y., Hopfinger, E. J. & Antonia, R. A. 1984, J. Fluid Mech. 140, 63.

[2] Argast, D., Samland, M., Gerhard, O. E., & Thielemann, F. -K. 2000, A&A, 873, 887

[3] Asplund, M., Grevesse, N., and Sauval, A. J. 2005. The solar chemical composition. In Cosmic Abundances as Records of Stellar Evolution and Nucleosynthesis. ASP Conf. Series, vol. 336, 25-38.

[4] Batchelor, G. K. 1952, Proc. Camb. Phil. Soc., 48, 345

[5] Benner, S. A., Ricardo, A., and Carrigan, M. A. 2004, Curr. Opin. Chem. Biol. 8, 672-689.

[6] Bensby, T. and Feltzing, S. 2006, Mon. Not. R. Astr. Soc. 367, 1181

[7] Biskamp, D. 2003, Magnetohydrodynamic Turbulence. (Cambridge University Press)

[8] Boldyrev, S., Nordlund, A. & Padoan, P. 2002, Phys. Rev. Lett., 89, 031102

[9] Branch, D., Buta, R., Falk, S. W., McCall, M. L., Uomoto, A., Wheeler, J. C., Wills, B. J. & Sutherland, P. G. 1982, ApJ, 252, 61

[10] Branch, D., Lacy, C. H., McCall, M. L., Sutherland, P. G., Uomoto, A., Wheeler, J. C. & Wills, B. 1983, ApJ, 270, 123

[11] Bromm, B. & Larson, R. B. 2004, ARAA, 42, 79

[12] Carigi, L. 2000. Rev. Mex. De Astronomia y Astrofisica 36, 171-184.

[13] Carigi, L., Peimbert, M., Esteban, C., & Garcia-Rojas, J. 2005, ApJ, 623, 213

[14] Cartledge, S. I. B., Lauroesch, J. T., Meyer, D. M., & Sofia, U. J. 2006, ApJ, 641, 327

[15] Cattaneo, A. et al. 2006, MNRAS, 370, 1651

[16] Chaplin, M. F. 2001, Mol. Biol. Educ. 29, 54-59.

[17] Chiappini,C., Matteucci,F. & Gratton,R. 1997, ApJ, 477, 765

[18] Chiappini,C., Matteucci,F. & Romano,D. 2001, ApJ, 554, 1044

[19] Cioffi, D. F. & Shull, J. M. 1991, ApJ, 367, 96

[20] Conselice, C. J. 2006,ApJ, 638, 686

[21] de Avillez, M. A. & Breitschwerdt, D. 2005, ApJ, 634L, 65

[22] de Avillez, M. A. & Mac Low, M-M. 2002, ApJ, 581, 1047

[23] de Donder, E. and Vanbeveren, D. 2005 New Astr. Rev. 48, 861.

[24] De Silva, G. M. et al. 2006, AJ, 131, 455

[25] Dib, S. & Burkert, A. 2005, ApJ, 630, 238

[26] Dominguez, I., Höflich, P. & Straniero, O. 2001, ApJ, 557, 279.

[27] Dubrulle, B. 1994, Phys. Rev. Lett., 73,959

[28] Edvardsson, B., Andersen, J., Gustafsson, B., Lambert, D. L., Nissen, P. E. & Tomkin, J. 1993, A&A, 275, 101

[29] Erb, D. K. et al. 2006 ApJ, 644, 813.

[30] Esteban, C., Garcia-Rojas, J. Peimbert, M., Peimbert, A., Ruiz, M. T., Rodrigues, M., and Carigi, L. 2005. ApJ, 618, L95-L98.

[31] Feltzing, S., Holmberg, J., Hurley, J. R. 2001, A&A, 377, 911.

[32] Finlator, K., Dave, R., Papovich, C., Hernquist, L. 2006, ApJ, 639, 672

[33] Finney, J. L. 2004. Phil. Trans. R. Soc. Lond. B 359, 1145

[34] Fox, R. O. 2003, Computational Models for Turbulent Reacting Flows (Cambridge: Cambridge Univ. Press).

[35] Friel, E. D. & Boesgaard, A. M. 1992, ApJ, 387, 170

[36] Frisch, U. 1995, Turbulence. (Cambridge UniversityPress)

[37] Fuxreiter, M., Mezei, M., Simon, I., and Osman, R. 2005. Biophys. J. 89, 903

[38] Ferriere, K. M. 1995, ApJ, 441, 281. ApJ, 375, 239

[39] Ferriere, K. M., Mac Low, M-M. & Zweibel, E. G. 1991, ApJ, 375, 239

[40] Gaidos, E. J. 2000. Icarus 145, 637

[41] Garczarek, F., Brown, L.S., Lanyi, J.K., and Gerwert, K. 2005, Proc. Natl. Acad. Sci. U S A 102, 3633

[42] Garnett, D. R., Shields, G. A., Peimbert, M., Torres-Peimbert, S., Skillman, E. D., Dufour, R. J., Terlevich, E., and Terlevich, R. J. 1999, ApJ, 513, 168.

[43] Giavalisco, M. 2002, ARAA, 40, 579

[44] Girimaji, S. S. & Pope, S. B. 1990, J. Fluid. Mech., 220, 427.

[45] Gamezo, V. N., Khokhlov, A. M., Oran, E. S., Chtchelkanova, A. Y., Rosenberg, R. O. 2003, Science, 299, 77

[46] Goto, S., & Kida, S. 2003, Fluid Dynamics Res., 33, 403

[47] Governato, F. et al. 2004, ApJ, 607, 688

[48] Gustaffson, B., Karlsson, T., Olsson, E., Edvardsson, O. B., and Ryde, N. 1999, A&A 342, 426.

[49] Hanayama, H. & Tomisaka, K. 2006, ApJ, 641, 90

[50] Haywood, M. 2006, MNRAS, 371, 1760

[51] Henry, R. B. C., Edmunds, M. G., and Koppen, J. 2000 ApJ 541, 660

[52] Höflich, P. 1995, ApJ, 443, 89

[53] Höflich, P., Khokhlov, A. M., Wheeler, J. C. 1995, ApJ, 444, 83

[54] Höflich, P., Khokhlov 1996, ApJ, 457, 500

[55] Hopkins, A. M. 2004, ApJ, 615, 209

[56] Hutchins, J. B. 1976, ApJ, 205, 103.

[57] Igumenshchev, I. V., Shustov, B. M., & Tutukov, A. V. 1990, A&A, 234, 396.

[58] Janicka, J., Kolbe, K. & Kollmann, W. 1979, J. Non-Equilib. Thermodyn., 4, 47

[59] Jimenez, R. & Haiman, Z. 2006, Nature, 440, 501 (JH)

[60] Kennicutt, R. C. 1998, ARAA, 36, 189.

[61] Kennicutt, R. C., Roettiger, K. A., Keel, W. C., van der Hulst, J. M. & Hummel, E. 1987, AJ, 93, 1011.

[62] Keres, D., Katz, N., Weinberg, D. H., Dave, R. 2005, MNRAS, 363, 2

[63] King, J. R., Soderblom, D. R., Fischer, D., and Jones, B. F. 2000, ApJ, 533, 944

[64] Klessen, R. S. & Lin, D. N. C. 2003 Phys Rev. E . 67, 046311

[65] Khokhlov, A. M. 1991, A&A, 245, 114

[66] Khokhlov, A. M. 1995, ApJ, 449, 695

[67] Khokhlov, A. M., Oran, E.S. & Wheeler, J. C. 1997ApJ, 478, 678

[68] Kobulnicky, H. A. and Skillman, E. D. 1998 ApJ 497, 601.

[69] Kolmogorov, A. N. 1962, J. Fluid Mech. 13, 82

[70] Kuchner, M.J. and Seager, S. 2005, astro-ph/0504214

[71] Kulkarni, S. R. & Heiles, C. 1987, in Interstellar Processes, ed. D. J. Hollenbach and H. A. Thronson (Reidel: Dordrecht), p. 87

[72] Laczano, A. C., Holland, H. D., and Dwyer, M. J. 1971. Science 174, 53

[73] Larson, R. B. 1998, MNRAS, 301, 569

[74] Leitherer, C. 2001, in Astrophysical Ages and Time Scales, ASP Conf. 245, ed. T. von Hippel, C. Simpson, N. Manset (ASP Press: San Francisco), p. 390.

[75] Lineweaver, C. H., Fenner, Y., and Gibson, B. K. 2004, Science 303, 59

[76] Lisewski, A. M., Hillebrandt, W & Woosley, S. E. 2000, ApJ, 538, 831

[77] Lisewski, A. M., Hillebrandt, W., Woosley, S. E., Niemeyer, J. C. & Kerstein, A. R. 2000, ApJ, 537, 405 (Lisewski et al. 2000b)

[78] Lodders, K. 2004, ApJ, 611, 587.

[79] Mac Low, M-M., & MaCray, R. 1988, ApJ, 324, 776.

[80] Mac Low, M-M., MaCray, R., & Norman, M. 1989, ApJ, 337, 141.

[81] Mac Low, M-M., & Klessen, R. S. 2004, Rev. Mor. Phys., 76, 125

[82] Malhotra, S. & Rhoads, J. E. 2002, ApJ, 565, 71

[83] Marcillac et al. 2006, A&A, accepted(astro-ph/0605642).

[84] McCray, R., and Kafatos, M. 1987. ApJ, 317, 190.

[85] McKay, C. P. and Smith, H. D. 2005. Icarus 178, 274

[86] Meynet, G. & Maeder, A. 2002, A&A, 390, 561

[87] Minshige, S., Shibata, K., & Shapiro, P. R. 1993, ApJ, 409, 663.

[88] Monin, A. S. & Yaglom, A. M. 1975, Statistical Fluid Mechanics. (MIT press)

[89] Muller, W-C. & Biskamp, D 2000, Phys. Rev. Lett., 84, 475

[90] Naab, T. & Ostriker, J. P. 2006, MNRAS, 366, 899.

[91] Niemeyer, J. C. & Woosley, S. E. 1997ApJ, 475, 740

[92] Niemeyer, J. C. & Kerstein 1997, New Astronomy 2, 239

[93] Nikolic, B., Cullen, H., & Alexander, P. 2004, MNRAS, 355, 874.

[94] Nissen, P. E. 2003, in CNO in the Universe, ASP Conf. Series, Vol.304 (San Francisco, CA: ASP Press), p.60.

[95] Nittler, L. R. 2005, ApJ, 618, 281.

[96] Nomoto, K., Tominaga, N., Umeda, H., Kobayashi, C., Maeda, K. 2006, Nucl. Phy. A., accepted(astro-ph/0605725)

[97] Nordstrom, B. et al. 2004, A&A, 418, 989.

[98] Oboukhov, A. M. 1962, J. Fluid Mech. 13, 77

[99] Oey, M. S. 2000, ApJ, 542, L25.

[100] Oey, M. S. 2003, MNRAS, 339, 849.

[101] Oey, M. S., & Clarke, C. J. 1997, MNRAS, 289, 570

[102] Pan, L. and Scalo, J. 2007, ApJ, L654, 29

[103] Pan, L-B. & Scalo, J. 2008, in preparation

[104] Padoan, P., Nordlund, A., and Jones, B. J. 1997, MNRAS, 288, 145.

[105] Papovich, C., Dickinson, M., & Ferguson, H. C. 2001, ApJ, 559, 620

[106] Paulsen, D. B., Sneden, C., & Cochran, W. D. 2003, AJ, 125, 3185

[107] Pont, F., & Eyer, L. 2004, MNRAS, 351, 487

[108] Pope, S. B. 2000, Turbulent flows. (Cambridge University Press)

[109] Portinari, L., Chiosi, C., & Bressan, A. 1998, A&A, 334, 505

[110] Prantzos, N. 2003, in CNO in the Universe, ASP Conf. Ser. Vol. 304, ed. C. Charbonnel, D. Schaerer, G. Meynet (San Francisco, CA: ASP Press), p. 361.

[111] Quillen, A. C. 2002, AJ, 124, 400

[112] Randich, S., Sestito, P., Primas, F., Pallavicini, R., and Pasquini, L. 2006, A&A, 450, 557

[113] Reddy, B. E., Tomkin, J, Lambert, D. L., Allende Prieto, C. 2003, MNRAS, 340, 304

[114] Reddy, B. E., Lambert, D. L. & AllendePrieto,C. 2006, MNRAS, 367, 1329

[115] Reeves, M. 1972, A&A, 19, 215

[116] Röpke, F. K. 2007, ApJ, 668, 1103

[117] Röpke, F. K. & Hillebrandt, W. 2005, A&A, 431, 635

[118] Saleh, L., Beers, T. C. & Mathews, G. J. 2006, JPhG, 32, 581

[119] Scalo, J. M. 1973, ApJ 184, 801

[120] Scalo, J. & Elmegreen, B. G. 2004, ARAA, 42, 275

[121] Scalo, J. M., Kaltenegger, L. and 13 others 2007, Astrobiology 7, 85

[122] Scannapieco, C., Tissera, P. B., White, S. D. M., Springel, V. 2005, MNRAS, 364, 552

[123] Schaerer, D. 2003, A&A, 397, 527

[124] Shapley , A. E. et al. 2001, ApJ, 562, 95

[125] Sharp, C. M. 1990 Asrophys. Sp. Sci. 171, 185-188.

[126] She, Z-S. & Leveque, E. 1994, Phys. Rev. Lett, 72, 336

[127] She, Z-S. & Waymire, E. C. 1995, Phys. Rev. Lett, 74, 262

[128] Shen, Z.-X. et al. 2005, ApJ, 635, 608

[129] Shimasaku, K. et al. 2006, P.A.S. Japan 58, 313.

[130] Shraiman, B. L. & Siggia, E. D. 2000, Nature, 405, 639.

[131] Simon, D. S. et al. 2006, ApJ, 640, 270

[132] Silk, J. & Langer, M. 2006, MNRAS, 371, 444

[133] Stillinger, F. H. 1980, Science 209, 451

[134] Tenorio-Tagle, G. 1996, AJ, 111, 1641

[135] Tenorio-Tagle, G., and Bodenheimer, P. 1989, ARAA, 26, 145

[136] Thornton, K., Gaudlitz, M., Janka, H. -Th., & Steinmetz, M. 1998, ApJ, 500, 95

[137] Timmes, F. X. & Woosley, S. E. 1992, ApJ, 396, 649

[138] Tinsley, B. M. 1976, ApJ, 208, 797

[139] Tomisaka, K. 1990, ApJ, 361L, 5

[140] Tomkin, J., Wooolf, V. M., and Lambert, D. L. 1995 Astr. J. 109, 2204.

[141] Tsujimoto, T., Shigeyama, T., & Yoshii, Y. 1999, ApJ, 519, L63

[142] Tumlinson, J. 2006, ApJ, 641, 1

[143] van den Hoek, L. B. & de Jong, T. 1997, A&A, 318, 231.

[144] Villermaux, E. 2004, New J. Physics, 6, 125.

[145] Villermaux, E., Innocenti, C., & Duplat, J. 2001, Phys. Fluids, 13.284

[146] Voth, G. A., Haller, G. & Gollub, J. P. 2002,Phys. Rev. Lett., 88, 254501

[147] Wang, L-P., Chen, S., Brasseur, J. G. & Wyngaard, J. C. 1996, J. Fluid Mech. 309, 113

[148] Weaver, R., McCray, R., Castor, J., Shapiro, P. & Moore, R. 1977, ApJ. 218, 377.

[149] White, S. D. M. & Audouze, J. 1983, MNRAS, 203, 603

[150] Wielen, R., Fuchs, B., and Dettbarn, C. 1996 A&A 314, 438.

[151] Wilden,B.S., Jones,B.F., Lin,D.N.C. & Soderblom,D.R. 2002, AJ, 124, 2799.

[152] Woosley, S. E. 2007, ApJ, 668, 1109

[153] Woosley, S. E. & Weaver, T. A. 1995, ApJS, 101, 181

[154] Woosley, S. E., Heger, A. & Weaver, T. A. 2002, Rev. Mod. Phys., 74, 1015

[155] Yaglom, A. M. 1966, Dokl. Akad. Nauk SSSR, 166, 49

[156] Yan, H. et al. 2006, New Astr. Rev. 50, 127

[157] Yeung, P. K., Pope, S. B., Lamorgese, A. G. &Donzis, D. A. 2006, Phys. Fluids. 18, 065103

[158] Zel'dovich, Y. B., Librovich, V. B., Makhviladze, G. M. & Sivashinsky, G. I. 1970, Acta Astron., 15., 313

Vita

Liubin Pan was born and raised in Jiangsu, an eastern province in China. After graduating from Rugao High School, Jiangsu in 1995, he attended the Physics Depertment of The University of Science and Technology of China (USTC). In July 1999, he graduted with a B. S. degree in applied physics. That fall, he entered the graduate school at the center for astrophysics, USTC. In July 2002, he finished his thesis on black hole accretion flows and obtained his M. S. degree. In the fall of 2002, he was admitted to the Ph. D program of the Astronomy Department at University of Texas at Austin.

Permanent Address: Baipu Qianyuan 23 #35
Rugao, Jiangsu, 226511
China

This dissertation was typeset with $\LaTeX\,2_\varepsilon$[1] by the author.

---

[1] $\LaTeX\,2_\varepsilon$ is an extension of $\LaTeX$. $\LaTeX$ is a collection of macros for $\TeX$. $\TeX$ is a trademark of the American Mathematical Society. The macros used in formatting this dissertation were written by Dinesh Das, Department of Computer Sciences, The University of Texas at Austin, and extended by Bert Kay, James A. Bednar, and Ayman El-Khashab.